ULTRA-SHALLOW JUNCTION FABRICATION USING PLASMA IMMERSION ION IMPLANTATION AND EPITAXIAL $CoSi_2$ AS A DOPANT SOURCE

by

Erin Catherine Jones

Memorandum No. UCB/ERL M96/36

16 May 1996

ULTRA-SHALLOW JUNCTION FABRICATION USING PLASMA IMMERSION ION IMPLANTATION AND EPITAXIAL $CoSi_2$ AS A DOPANT SOURCE

by

Erin Catherine Jones

Memorandum No. UCB/ERL M96/36

16 May 1996

ELECTRONICS RESEARCH LABORATORY

College of Engineering
University of California, Berkeley
94720

Abstract

Ultra-Shallow Junction Fabrication using Plasma Immersion Ion Implantation and Epitaxial $CoSi_2$ as a Dopant Source

Erin Catherine Jones

Doctor of Philosophy in Electrical Engineering and Computer Sciences

University of California at Berkeley

Professor Nathan W. Cheung, Chair

Source and drain diffusion regions which are shallow in both the lateral and vertical directions are essential for deep sub-micron metal-oxide-semiconductor field-effect transistors (MOSFETs). Junctions need to be shallow in the lateral direction for process reproducibility, control over the transistor threshold voltage, and reduction of subthreshold leakage. The vertical junction depth needs to be shallow so that the electric field profile in the channel region is confined closely in the area of the gate. It is a challenge to fabricate high-throughput, low-resistivity, low-leakage sub-80 nm junctions for MOSFET source and drain regions.

Plasma immersion ion implantation (PIII) is an emerging technology which can provide high dose-rate, low energy implantation. Shallow junctions are formed using 4-12 kV SiF_4 PIII for preamorphization, 2-5 kV BF_3 PIII for B implantation, and rapid thermal annealing. This preamorphization process yields 80-100 nm pn diodes with area leakage current below 2 nA/cm^2, and shows that preamorphization is effective in reducing both junction depth and diode leakage . 1 kV BF_3 PIII into crystalline Si is used to fabricate p^+ layers of depth 50-90 nm with peak activation above $2x10^{19}$ cm^{-3}.

The study of BF_3 PIII doping includes characterization of substrate etching rates due to sputtering and ion-assisted etching processes during PIII. The BF_3 plasma is shown to have a chemical etch rate less than 2 nm/min at most operating conditions; ion-assisted etching processes during PIII implantation multiply this rate by a factor of 4 for 5kHz, 5kV implantation. The etching is seen to increase with implant energy and frequency in the 1-5 kV, 1-25 kHz regime.

BF_3 PIII dosimetry has been modeled, and a methodology for determining the ion species distribution of the implanted dopant using implanter current and voltage (IV)

waveforms and mass spectrometry data has been developed. After the ion species distribution is determined, this methodology is used to predict the dependence of final implant profiles on implant time, frequency, IV waveform, and substrate etch rate. The ion species distribution in BF_3 PIII is found to be approximately 7.5% B^+, 85% BF_2^+ and 7.5% F^+. Since the substrate is etched during implantation, the dose saturates with time. The saturation dose depends more strongly on energy than frequency, and is found to be ~$3x10^{15}$ cm^{-2} at 1kV and ~$1.4x10^{16}$ cm^{-2} at 5kV.

Junctions are also formed using epitaxial cobalt disilicide as a dopant source for boron. Epitaxial $CoSi_2$ films are made by solid phase epitaxy of a Co/Ti bilayer. B is implanted into the $CoSi_2$ and then outdiffused. This work has produced 110 nm junctions (including the 50 nm silicide thickness) with area leakage current of 12 nA/cm^2 for the epitaxial silicide. B diffusion out of the bilayer-formed epitaxial $CoSi_2$ is shown to be equivalent to diffusion out of polycrystalline $CoSi_2$, as long as the dose is high and the implant is deep enough that dopant buildup at Ti-containing precipitates inside the silicide does not preclude the flow of dopants into the underlying Si.

As ultra-shallow junction diodes with low surface concentration are observed to exhibit thermionic leakage current after short-time annealing, the crossover point between Schottky-like diodes that exhibit thermionic emission leakage and pn junctions which exhibit generation leakage current has been studied. The crossover is a volatile function of the first spatial moment of the doping profile, and is found to occur generally at junction depths on the order of 20-40 nm for $5x10^{18}$-10^{19} cm^{-3} p-type doping. A capacitance-voltage technique for finding the process parameters which will yield the shallowest low-leakage pn junction is presented.

Nathan Cheung
May 15, 1996

Contents

List of Figures

List of Tables

Acknowledgments

I thank my advisor, Professor Nathan Cheung, for allowing my project to evolve and move into different areas of PIII and shallow junction processing when I got excited and wanted to try new things. I have benefitted greatly from his guidance in every direction since I joined the group as an undergraduate. I thank Professor Mike Lieberman for recommending me to the PIII group, way back when. I thank Professor Chenming Hu for help in interpreting the simulations, and for allowing me use of the Device Group computers to run them. I thank Professor Eicke Weber for reviewing the manuscript, and for providing some of the most practical courses, in defects and characterization, that I've taken at the university.

I would like to thank all my collaborators and partners in industry and at other universities whose generous help fleshed out this thesis. I thank my mentor at Intel, David B. Fraser, who generously contributed useful advice, endless encouragement and much-needed project support. I thank Shinichi Ogawa for introducing me to silicides and opening up a whole new world - and a whole new country. I thank Jiqun Shao and Stuart Denholm of Eaton Corp. for exciting and fruitful collaboration. I thank Larry Larson of Sematech and Emi Ishida for both supporting and promoting my work. Paul Chu has also been a great benefactor of the PIII project, providing copious amounts of SIMS analysis. I thank Paul Ameika of Analog Devices for providing conventional implantation, Lawrence Dass of Intel for thorough TEM work, and Robert Mazur and Joe Sherony of Solid State Measurements for providing last-minute spreading resistance analysis. I thank Sue Felch, Michael Current, Larry Larson, Isao Yamada and other members of the "Ion-Beam Mafia" for many interesting technical discussions and for inspiration.

I have enjoyed both working with and sharpening my debating skills on the other residents of 144MA Cory: Tracy Fu, Xiang Lu, James Chan, Crid Yu, Meng-Hsiung Kiang, Sundar Kumar Iyer, Kaustav Banerjee, William Wong, Seongil Im, Jingbao Liu, X.Y. Qian, Carey Pico, and Jiang Tao. I want to thank Barry Linder for hours of fascinating dialogue, technical and not, and for all the little gifts of great data I've fished from the wake of your experiments in the last few months. Most, I owe my gratitude to Bill

En. We met freshman year and have been collaborating ever since. Thank you for lending your expertise in all matters mechanical, and thank you for being a good friend.

I must applaud the efforts of those charged with the maintenance of my sanity over the past few years. I thank Melissa Krance and Joy Schaber for dragging me out of the lab from time to time, and reminding me how colorful the world is through eyes other than my own computer-bleary pair. I thank my sisters, Elisa and Kerri: there is always a feeling of security and comfort in our unshakable, unbreakable roots. I thank my second family, Jeanne and Bob Carson, for allowing me steady withdrawals from their bottomless well of encouragement and warmth. I thank my father for giving me my start. I thank my mother, Judy, for inspiring me: teaching me, by example, how much strength and stamina a human being is capable of. I am thankful I have travelled an easier path so far. Most of all, I thank my husband Sean. You have had the most difficult job, reminding me to eat, to sleep, to breathe. Thank you for *everything*.

1 Ultra-shallow junctions for ULSI

1.1 Introduction

Improvements in the performance and speed of ultra-large-scale integrated (ULSI) circuit devices are made by scaling down device dimensions. As the dimensions of metal-oxide-semiconductor field-effect transistor (MOSFET) devices shrink, suppression of short channel effects in the scaled-down devices requires close attention to doping profiles in the source/drain, use of n^+ and p^+ poly gates, and new methods of well construction and device isolation [1.1, 1.2]. When devices are scaled below 0.1 μm in channel length and power supply voltages are reduced below 2.5 V, short channel effects like threshold voltage lowering and bulk punchthrough may be more critical ULSI scaling limits than hot electron effects [1.3, 1.4]. Doping in the source and drain regions (Figure 1-1) must be optimized to minimize subthreshold leakage while maximizing on-state drain current.

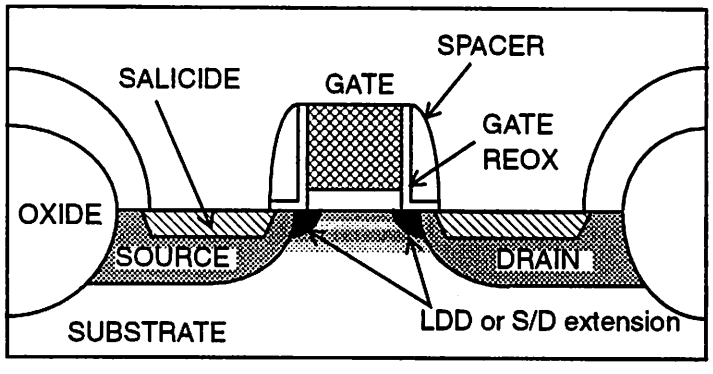

Figure 1-1. Schematic of MOSFET device.

Reduction of the lateral source/drain diffusion junction depth has historically been less aggressive than the scaling of minimum feature size, as the short channel effect is small for channel lengths above 1 μm. Recent scaling projections published by the Semi-

conductor Industry Association [1.5] have proclaimed an end to the slow, cautious shallow junction scaling of the past (Figure 1-2). Over the next two DRAM generations the

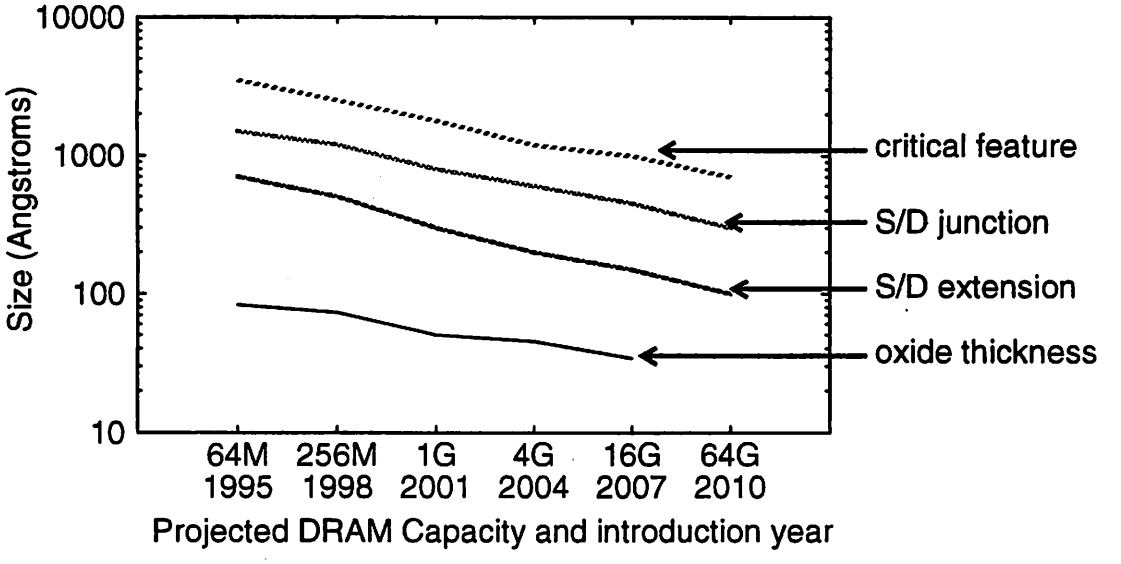

Figure 1-2. Metal-oxide-semiconductor (MOS) device scaling trends

Projected values for minimum critical feature size for MOSFET gates, source/drain extensions (minimum junction depth x_j), source/drain junctions (maximum x_j), and gate oxides, from SIA Technology Roadmap [1.5].

junction depth is expected to halve, from 70-150 nm for the 64M generation to 30-80 nm for the 1G generation. By the year 2010, the SIA technology roadmap predicts that 10 nm junctions will be in use. As junctions this shallow cannot be fabricated by conventional implantation and furnace annealing processes, new shallow doping techniques are being developed and characterized to meet this important scaling goal.

1.2 Device motivation for shallow junctions

Reducing the gate length of a MOSFET is the best way to raise device current and circuit packing density. The goal of shallow junction scaling is to minimize the short-channel effects observed when the MOSFET gate length is reduced. Short-channel effects include MOSFET threshold voltage (V_T) reduction, hot-electron effects, and source-to-drain punchthrough breakdown [1.6]. These effects are directly related to channel length and drain voltage, and all are affected, directly or indirectly, by the dimensions of the source and drain junctions. Junctions must be shallow in the lateral direction for process

reproducibility and threshold voltage control. The vertical junction depth must be shallow to confine the electric field profile in the channel region close to the gate. Properties of the junctions themselves, like resistance and source/drain to substrate leakage currents, can also degrade device performance. A successful MOSFET design will have a minimum V_T high enough to meet off-state leakage requirements, and the variation in V_T among devices on a chip will be small. This section describes these important scaling considerations for shallow junctions.

1.2.1 Drain-induced barrier lowering

For a long-channel MOSFET device, the threshold voltage is a function of the gate capacitance, the channel doping, and the work function of the gate material. When the gate length is reduced, charge sharing and drain-induced barrier lowering (DIBL) cause the threshold voltage to approach zero. Figure 1-3 shows these two effects in a short-channel

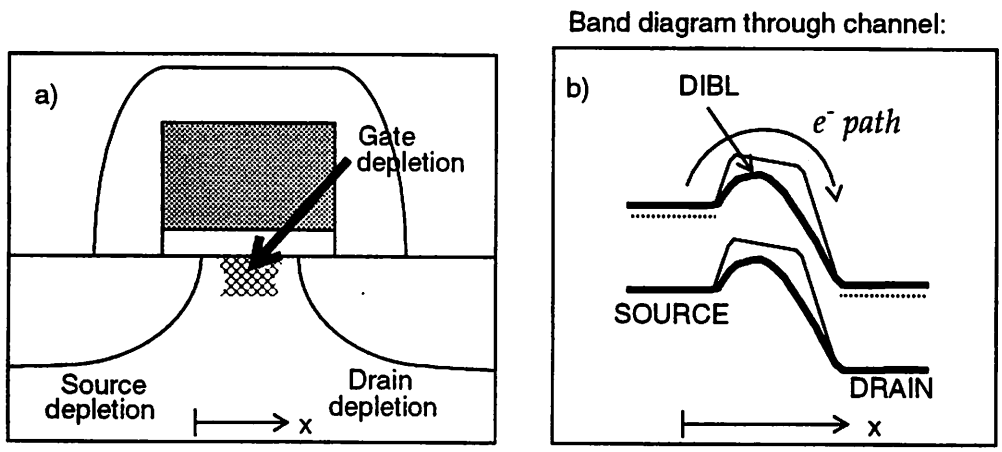

Figure 1-3. Short channel effect in MOSFET

a) Charge sharing. The size of the gate depletion is reduced due to encroachment of the source/drain depletions. b) Drain induced barrier lowering. Both effects reduce the threshold voltage of the device.

device. Charge-sharing is caused by the source and drain depletion regions extending into the channel and reducing the bulk charge that must be created by the gate before inversion occurs [1.7]. This lowers the threshold gate voltage needed for inversion. When the drain voltage increases, the drain depletion extends further into the channel, and the barrier to carrier movement between source and drain is reduced even further (DIBL) [1.8]. The change in threshold voltage due to these short-channel effects is shown in Figure 1-4. It has

been empirically shown that the shift in MOSFET threshold voltage from the long-channel value is $\Delta V_T \propto e^{-L/x}$, where L is the channel length and the relation $x \propto x_j^{1/3} x_{ox}$ is found from graphing the function [1.9]. The parameter x_{ox} is the gate oxide thickness, and x_j is the vertical junction depth.

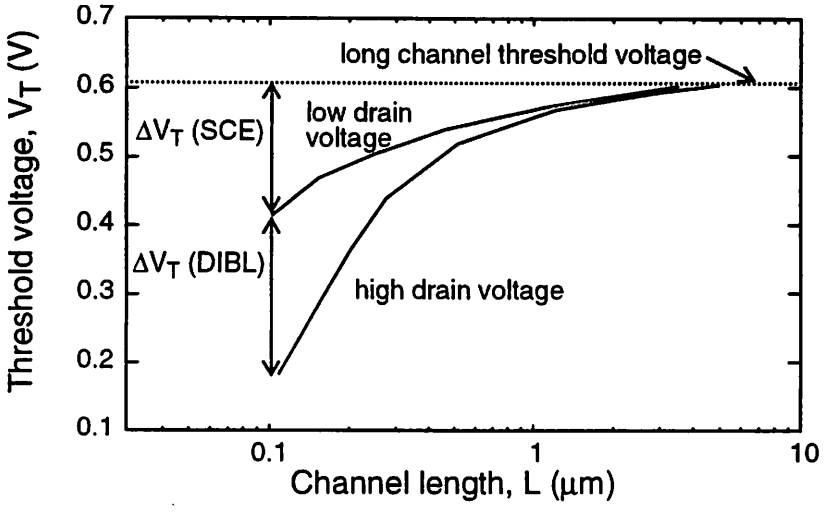

Figure 1-4. Threshold voltage lowering by short-channel effects

Threshold voltage lowered by charge sharing (SCE) and drain-induced barrier lowering. After Ref. [1.10].

Subthreshold slope also demonstrates the quality of a device's turnoff. Below the threshold voltage, the channel is in weak inversion, and the current flowing between source and drain is dominated by diffusion. The current depends on the carrier concentrations in the channel which are proportional to $e^{\eta\Phi_s/kT}$, where Φ_s is the surface potential in the Si along the channel. For an increase of a factor of 10 in the drain current, Φ_s must increase 60 mV. The Si surface potential is coupled to the gate voltage by

$$\Delta V_g = \Delta\Phi_s\left(1 + \frac{\sum C}{C_{ox}}\right), \tag{1-1}$$

where C_{ox} is the oxide capacitance and the summation contains all other capacitors affecting the channel inversion, including body, source and drain capacitors [1.6]. In an ideal, long-channel device the channel is completely controlled by the gate, $\Sigma C=0$, and a decade increase in drain current requires ΔV_g=60 mV. The subthreshold swing is then 60 mV/decade. For short-channel devices with charge-sharing and DIBL, the subthreshold swing is larger than ideal. This indicates a slower turn-off and higher subthreshold leakage

(Figure 1-5). Subthreshold leakage and swing improve when source/drain capacitances decrease.

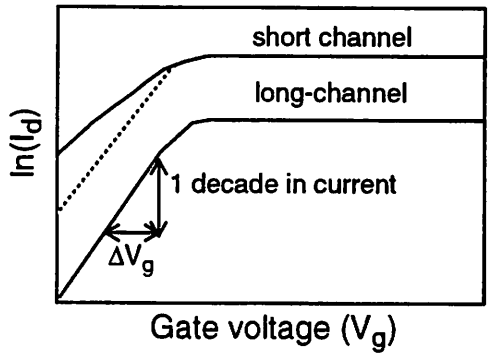

Figure 1-5. Subthreshold slope variation with short-channel effect

The change in subthreshold slope with channel length is shown in the difference between dotted line (ideal) and solid line (real) for the short-channel device.

1.2.2 Punchthrough

Punchthrough is the meeting of source and drain depletion areas under the channel. Punchthrough provides an alternate current path for the drain current. As shown in Figure 1-6, when devices are scaled down without changing the substrate doping, punchthrough leads to the loss of gate control over carriers in the channel: the potential lines in

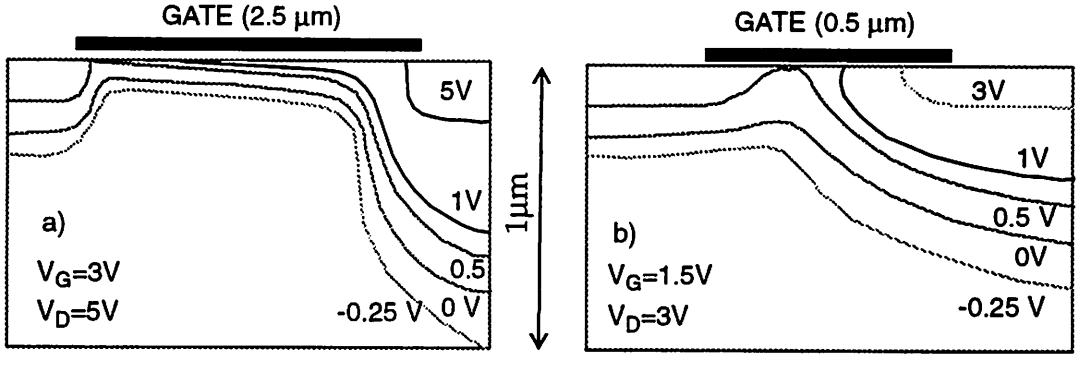

Figure 1-6. Punchthrough in MOSFET

After Ref. [1.6].

the short-channel device are not kept close to the gate, allowing the carriers to spread out into the bulk. The doping cannot be increased throughout the well without decreasing carrier mobility in the channel and exacerbating the body-bias effect, which causes the threshold voltage to be a strong function of the substrate bias. Punchthrough is avoided by

locally changing the doping under the channel, using deep implants or retrograde wells. It is also helped by keeping the source and drain junctions as far apart as possible, by using shallow junctions.

1.2.3 Series Resistance

Reducing x_j can, on the other hand, take its toll on the device ideality. The parasitic source-drain resistances of the device will increase as x_j decreases, causing a reduction in on-state drain current and a decrease in the noise margins of logic circuits using the device [1.11]. The resistances that must be considered are contact resistance (R_{co}), usually due to metal or silicide contact to the doped region, sheet resistance of the doped layer (R_s), spreading resistance where the carrier path turns toward the channel (R_{sp}), and the voltage-dependent resistance at the channel/junction edge due to the graded junction profile (R_{jn}) [1.12]. All of these are dependent on the doping profile, junction depth and activation of dopant in the source/drain junctions. Contact resistance depends on the metallic con-

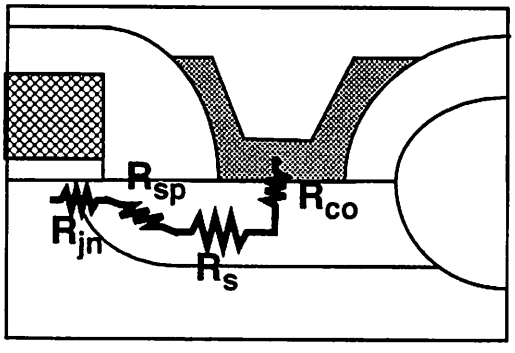

Figure 1-7. Resistances at source and drain junctions
After Ref. [1.12].

tact and surface doping, and may be degraded if the surface doping concentration is small or if the Si surface roughened by previous processing. The sheet resistance is related to the dopant distribution and increases when x_j decreases, unless there is an accompanying increase in carrier mobility (μ) or concentration (n, p):

$$R_S = \left[\int_0^{x_j} q\left(\mu_p p(x) + \mu_n n(x)\right) dx \right]^{-1} . \qquad (1\text{-}2)$$

At the high doping concentrations present in source/drain junctions, the mobility is saturated at a low value due to impurity scattering, and may decrease further due to dopant precipitation or residual implantation damage in the implanted layer. The total series resistance is the sum of all these contributing resistances:

$$R_{tot} = R_{co} + R_S + R_{spr} + R_{jn} . \tag{1-3}$$

This series resistance will raise the saturation drain voltage by $2I_dR_{tot}$, where I_d is the saturation current ignoring series resistance, and reduce the saturation output conductance (gm_0) by a factor of $1+gm_0R_{tot}$ [1.11].

1.2.4 Hot electron effects

Hot electron effects are caused by high electric fields present at the drain edge when the device is driven into the saturation region, at high drain bias. The high electric field creates hot carriers, creates substrate current, and can cause interface and oxide damage [1.13]. *N*-MOSFETs degrade as hot carriers generate interface traps that shift the threshold voltage, reduce the drain current, and degrade the subthreshold swing. *P*-MOSFETs degrade as electrons are trapped in the gate oxide, leading to an effective reduction in channel length, and a corresponding increase in current. At the same time, the *p*-MOS punchthrough voltage moves closer to zero and the subthreshold current increases. The severity of these effects is related to the peak electric field in the (E_m) channel, which is modeled as $E_m = (V_{ds} - V_{dsat})/l$, where V_{ds} is the drain to source bias, V_{dsat} is the voltage at which saturation occurs, and like the short channel effect, l has been empirically found to be related to the junction depth [1.14]:

$$l = 0.22 \cdot x_j^{1/2} \cdot x_{ox}^{1/3} . \tag{1-4}$$

The degradation is even more serious in short-channel devices, for which V_{dsat} is lower. PISCES simulations show that a reduction of x_j from 100 nm to 50 nm can increase the maximum field at the device drain edge by 55%, when assuming a threshold-adjustment implant concentration of 10^{18} cm^{-3} and a Gaussian implant profile in the drain junction with peak concentration of 10^{21} cm^{-3}. Reducing the junction depth from 50 nm to 20 nm increases the peak electric field an additional 30% [1.15].

To reduce the peak electric fields in drain regions, a very shallow, lowly-doped drain region (LDD) may placed between the drain and channel so that the drain voltage

drop is shared between the LDD and channel [1.16]. This reduces the voltage drop and electric field in the channel, reducing hot-electron effects and increasing device lifetime. However, the LDD increases the series resistance of the drain, decreasing the performance as described in Section 1.2.3, especially in the linear region of operation. Typically, LDD structures are used for n-MOSFETS where the drain current is degraded during hot-carrier stressing. Simple source/drains are typically used for p-MOSFETs, as their profiles are less heavily doped and less abrupt than n-type junctions due to the lower solubility and faster diffusion of boron dopants. A key question in the next few generations of devices is whether the supply voltage is lowering enough that an LDD structure is no longer necessary [1.17]. On the other hand, an LDD-like structure with a shallower junction at the channel edge to reduce short-channel effects and a deeper channel nearby for metallization may still be useful for source/drain engineering.

1.2.5 Leakage currents

Keeping the leakage currents small in a scaled-down device is important for correct operation of dynamic memory and other charge-storing circuits where the charge can leak away by junction or subthreshold leakage, causing dynamic errors in the circuit operation. The total leakage current in a shallow junction may increase because the junction depletion regions are closer to the Si surface, and extend to envelop damaged layers from processing, metallic contamination, or stressed Si/SiO_2 interfaces where there deep level traps act as generation-recombination sites for carriers (Figure 1-8). The leakage may increase when the radius of curvature in the spherical corners of the junction decreases, enhancing the electric field in that area, increasing the leakage, and severely reducing the breakdown voltage of the junction.

In the one-dimensional case, the total reverse current density due to diffusion and Shockley-Read-Hall generation currents in a one-sided p^+n junction is given by

$$J_{reverse} = \frac{qn_i^2}{N_D}\sqrt{\frac{D_p}{\tau_p}} + \frac{qn_i}{\tau}\sqrt{\frac{2\varepsilon_{Si}(V_{bi}-V)}{qN_D}} \tag{1-5}$$

where q is the electronic charge, N_D is the doping concentration on the n-side, D_p and τ_p are minority carrier diffusivity and lifetime on the n-side, n_i is the intrinsic carrier concentration, ε_{Si} is the dielectric constant of Si, V_{bi} is the built-in potential of the p^+n junction,

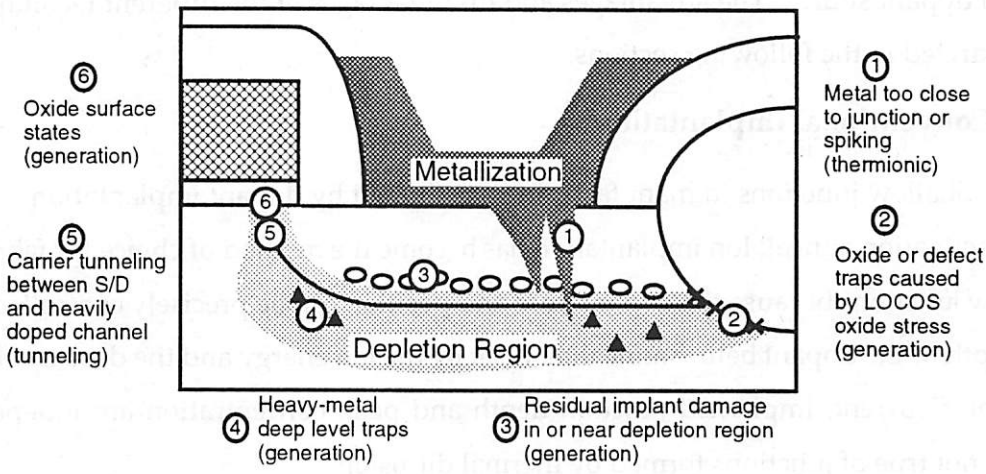

Figure 1-8. Sources of junction leakage currents in MOSFET source/drain junction

and V is the applied bias voltage [1.6]. The effective generation lifetime, τ, includes the effects of generation through deep-level impurities and traps. The slope of the current density-voltage (JV) characteristic is given by

$$\frac{dJ_{reverse}}{dV} = \frac{-qn_i}{2\tau}\sqrt{\frac{2\varepsilon_{Si}}{qN_D(V_{bi}-V)}} \tag{1-6}$$

so that the slope is inversely related to τ. A higher slope of the JV characteristic indicates a lower τ, corresponding to a higher concentration of traps caused by residual implant damage, for example. When making junctions by implantation and annealing, it is especially important that the implant damage be completely annealed and that the junction depletion region be far away from any residual defects that may act as generation centers. In a good shallow junction fabrication process, the generation current in the junction depletion region is not increased by deep level traps introduced into the Si by implantation, other processing damage, or metallic contamination.

1.3 Ultra-shallow junction fabrication techniques

The junctions used in MOSFET devices today are 120-150 nm in depth and relatively easy to process, but the 15-45 nm junctions that are needed for 0.1 μm channel lengths require much more attention to meet leakage, resistivity, and reproducibility standards. These difficulties have led to the invention of a number of new fabrication techniques and the resurgence of a number of old techniques for ultra-shallow junction fabrication. The main categories are implantation, laser doping, and thermal diffusion

from a dopant source. The advantages and disadvantages of the different techniques are summarized in the following sections.

1.3.1 Conventional implantation

Shallow junctions in manufacturing are formed by dopant implantation followed by an activation anneal. Ion implantation has become the method of choice for fabricating shallow junctions because the dopant dose and position can be precisely controlled. Since the depth of the dopant before annealing is set by the ion energy and the dose is set by the implanter current, implanted junction depth and peak concentration are independent. This is not true of junctions formed by thermal diffusion.

Ultra-shallow n^+ junctions are easily made, using dopant atoms such as As or Sb. These atoms are heavy enough that they can be implanted at comfortably high voltages with minimal channeling, and can be annealed at a high enough temperature for good activation with little dopant redistribution using rapid thermal annealing (RTA). Junctions of 10-50 nm have been shown using P and As [1.18, 1.19]. It is not so simple to control p^+ doping. The implantation profile of the primary p-type dopant, $^{11}B^+$, is deeper than the n-type dopants because it has lower mass and because a large portion of the implanted B^+ ions may be scattered into one of the axial or planar channels between rows or planes of Si atoms in the Si crystal. Once in a channel, ions do not experience nuclear collisions as frequently and their energy loss rate decreases, allowing them to travel much further into the Si crystal than they would in an amorphous medium. Further, the diffusivity of B in Si is very high at the annealing temperatures needed to remove implant-induced Si lattice damage. P^+ doping might not be so difficult if heavier p-type dopants were available. However, the main alternatives, Ga and Al, both have unsuitably low solid solubility in Si.

To obtain sub-50 nm p^+n junctions by standard implant and anneal processes, both implant channeling and rapid, transient boron diffusion must be overcome. Other difficulties are implant damage to the substrate and gate oxide edges which may be exposed to the ion beam during lowly-doped drain (LDD) or large-angle-tilt (LATID) implantation, residual defects that remain after annealing, contamination, problems with achieving sufficient activation in a limited thermal cycle, and the extreme difficulty in making a reliable, low-resistance contact to a shallow junction. For boron p^+ junctions, where the large diffusivity of B in Si is greatly enhanced in the presence of residual damage, these problems are difficult to combat, and only 60 nm junctions have been shown with boron dopant [1.20,

1.21]. Reducing the boron junction depths below 60 nm by standard processes requires further reduction of the thermal budget, and a difficult trade-off between junction depth, sheet resistance, contact resistivity, and reverse leakage currents.

1.3.1.1 Energy Limitations

Although conventional implantation machinery improves steadily, there it is not yet a cost-effective tool for high dose-rate, very low-energy implantation (5 keV and below). The conventional implanter current drops precipitously as the energy used to extract ions from the implanter ion source is decreased. A state-of-the-art commercial implanter can provide 5 mA of current at 10 kV, but only 1 mA of current at 2 kV [1.22]. This limits the throughput of the implanter for low-energy implants, a problem for a machine as expensive as a conventional implanter ($3M). Techniques have been developed to deal with this implanter current problem. One technique is to use a BF_2^+ implant species instead of B^+, since BF_2^+ can be implanted at energies higher by a factor of 49/11 without increasing the range of B atoms in the Si. Another technique is to extract ions at a high energy from the ion source, mass-separate them, and then decelerate before implanting. This technique provides a higher implant current, but has the drawback of energetic neutral contamination and BF_2^+ dissociation [1.23, 1.24]. Ions that are extracted at high energy and then experience charge exchange with residual gas molecules will not be decelerated, leading to an undesirable high energy component of the implant.

1.3.1.2 Transient enhanced diffusion

Even more troublesome than variations in the as-implanted profile due to channeling and energy contamination is the rapid movement of the profile due to transient enhanced diffusion. Transient enhanced diffusion is observed whenever dopants are implanted into crystalline Si and annealed at temperatures above 900°C. This enhanced diffusion can cause dopant movement on the order of 100 nm for temperature cycles that should cause no dopant movement according to classical diffusion theory [1.25]. The dopant movement occurs in the tail region of the implant, usually for concentrations below 10^{19} cm^{-3} [1.25, 1.26]. Transient enhanced diffusion is caused by supersaturated concentrations of point defects introduced when implanting ions transfer energy to the lattice and displace substrate atoms. It is observed for both B and P dopant species, whose diffusivities are proportional to the interstitial Si concentration [1.27]. The point defects

will eventually recombine, so the transient only lasts as long as the interstitial concentrations are supersaturated [1.28]. Therefore the transient enhanced diffusion is related to how much damage occurs to the substrate during implantation.

For low-dose implants, point-defect clusters dissociate during an RTA anneal cycle, providing interstitials which enhance the B diffusion [1.29]. For high-dose implantation, the interstitials created by implantation may be present in such quantity they collapse into dislocations. Under RTA, the dislocations are formed and then dissolve, and released interstitials cause rapid diffusion. For a high-dose but non-amorphizing implant, it has been reported that annealing can be done below 950°C without seeing enhanced dopant movement [1-29]. At this temperature the end-of-range (EOR) defects may not form due to point defect cluster dissociation during the temperature ramp. The other option is to implant at lower energy (Figure 1-9). When the implant energy is high the

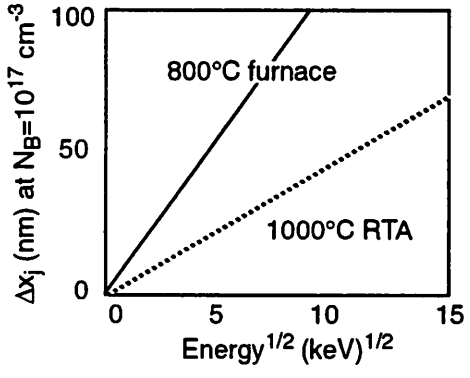

Figure 1-9. Dependence of junction motion on implant energy
Dopant movement during annealing for low dose phosphorus implantation. After Ref. [1.29], p.129.

interstitial and vacancy populations created by the implant are far apart, and the diffusion transient is long. Lower energy implant makes the initial profile shallower, and causes less separation of Frenckel pairs which need to recombine. These two effects combined reduce the junction motion of a low energy implanted sample.

1.3.1.3 Preamorphization

The purpose of preamorphization is two-fold: to stop B channeling into the substrate, and to reduce the implant-induced interstitial concentration which will enhance the B diffusion. As the amorphous silicon is regrown by solid phase epitaxy (SPE) during the

RTA temperature ramp-up, the dopant is incorporated at high levels in the regrown lattice. The activated dopant in this case is usually higher than the activated fraction of boron implanted into a crystalline silicon layer [1.30]. After SPE, the top layer of material is single-crystal, with few interstitials present to help B diffuse. This was shown in Ref. [1.25], where the diffusion of B implants into crystalline Si, preamorphized Si, and post-amorphized Si were compared. In this experiment, the amorphous layers were thick enough that all the boron was contained within them. Transient enhanced diffusion was observed in the B tail region in the samples without amorphization. The transient lasted less than 3 s at temperatures less above 950°C, and caused as much as 100 nm of dopant motion. The dopant movement increased with dose, as higher dose implantation caused greater interstitial supersaturation. Samples with post-amorphization only showed diffusion which matched with classical diffusion theory. Samples with pre-amorphization rather than post-amorphization were even shallower, because the pre-amorphization reduces implant channeling as well as enhanced diffusion.

There are difficulties with preamorphization as well. The dopant must be entirely contained in the amorphized-Si layer. Any dopant located beyond the α-Si before annealing will be in a region of high damage and will experience enhanced diffusion. Also it has been observed that it is more likely for B in high concentration regions to form precipitates in amorphized samples [1.25]. It is theorized that in crystalline samples, rapid diffusion of the B dopant occurs before the precipitates can form or that the solubility limit may be altered in the heavily damaged, crystalline sample. Another problem is the presence of the end-of-range (EOR) extrinsic dislocation loops that form below any α-Si layer during annealing. These are formed because the area below the α-Si is supersaturated with interstitials that gained energy from implanting ions and have recoiled from the surface layer. The loops form to reduce the compressive strain caused by the large interstitial concentration [1.31]. Strain fields remaining even after loop formation cause the EOR loops to be preferred sites for dopant and impurity gettering. Both B [1.25] and F (Section 5.8) gettering has been observed. This defect pinning makes the loops harder to dissolve. In shallow junctions, EOR loops need to be removed, as they may provide deep level traps if present in a junction depletion region, and make a junction leaky. As the activation energy for defect removal (~5 eV [1.32]) is higher than the activation energies for dopant diffusion

(~3.46 eV for B in Si [1.27]), rapid thermal annealing must be used to remove these defects without causing excessive dopant movement.

EOR loops are removed faster when the defect layer is closer to the surface, when the amorphized layer is thinner [1.29,1.33]. This may be due to the proximity of the surface providing a sink for point defects, or may be related to the energy effect observed in Figure 1-9. When the implant energy is lower, the ion range will be lower, the amount of implant damage will be lower, and the EOR layer will be more shallow. This is another reason to employ lower energy implantation for shallow junction formation.

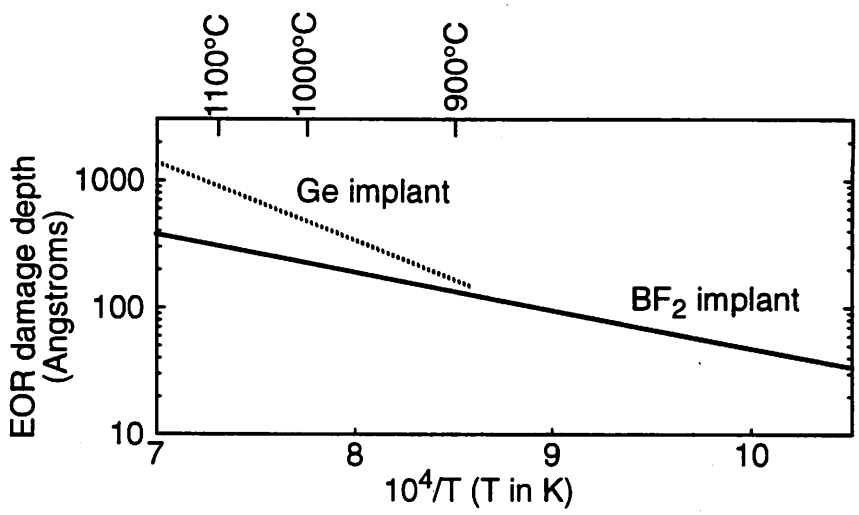

Figure 1-10. Dependence of end-of-range damage removal on damage depth
The line shows the depth of damage that can be removed in a 10 s RTA at the specified temperature. It is easier to remove shallower defects. After Ref. [1.29].

1.3.1.4 New techniques

There are other techniques to lower the junction depth with conventional implantation. One is using a higher dopant dose rate. There have been reports in the 2-20 keV range for B implantation that higher dose rate can lead to higher damage accumulation in the Si substrate. This means that if implanted at higher dose rate, the amorphous layer caused by an implant may be thicker than usual, or the amorphous layer may be formed at lower dose [1.34, 1.35]. The advantages of using an amorphized layer to reduce transient diffusion increase when the layer is thicker, or when the interstitial concentrations beyond it are lower because the amorphizing dose was kept small. It has also been reported that two-step annealing can reduce enhanced diffusion by reducing the point defect concentra-

tion in a pre-anneal step. Furnace annealing in the 550-600°C range for 30 minutes and low temperature (750-800°C RTA) have shown some improvement in junction depths of As [1.26] and B [1.34, 1.36, 1.37]. Although the junction depth measured by secondary ion mass spectroscopy may be reduced tens of nm by two-step annealing, little improvement is seen in the electrical junction depth [1.34].

If the junction depth cannot be reduced by changing the implant energy and diffusion, another option is to change the background doping. Since increasing well doping decreases the carrier mobility, increases the subthreshold slope, and increases the body effect, implantation under the source/drain extension regions may be used to locally increase the doping and decrease the electrical junction depth [1.38]. These "pocket" implant regions also serve to reduce the extension of source/drain depletion regions into the channel and to increase the punchthrough resistance of the device.

1.3.2 Plasma Immersion Ion Implantation (PIII)

PIII is a very high-current, high-throughput alternative to conventional implantation for ULSI doping [1.39 - 1.42]. PIII has the advantage of being easily integrated into a CMOS process in place of conventional implantation. PIII and conventional implanters are both capable of the very low energy, 10^{15} cm^{-3} dose implants required to achieve acceptable, low resistivity shallow junctions. However, the throughput of PIII is much higher because the PIII current is only very weakly dependent on the implant energy. Implant current of 1 mA/cm^2 can be delivered (80 mA for a 100 mm wafer) regardless of implant energy or wafer size.

The PIII concept is shown in Figure 1-11. A plasma containing the dopant ions to be implanted is generated, and the wafer is immersed in it. When a negative bias is applied to the wafer holder, the plasma electrons are repelled, and the dopant ions are accelerated across the sheath region and implanted at a voltage approaching the applied bias. The applied bias may be either dc or pulsed; for microelectronic applications a pulsed bias is used to minimize thin oxide charging stress [1.43]. In this type of implanter, a high implant current can be obtained for energies above the plasma potential, around 100 eV or greater. The PIII apparatus is a very simple and inexpensive system, built like a reactive-ion etcher with the addition of a high voltage pulser. Additional advantages are an implant current density and throughput which are independent of wafer size. Disadvantages of the PIII shallow junction process are similar to those of conventional implantation: transient

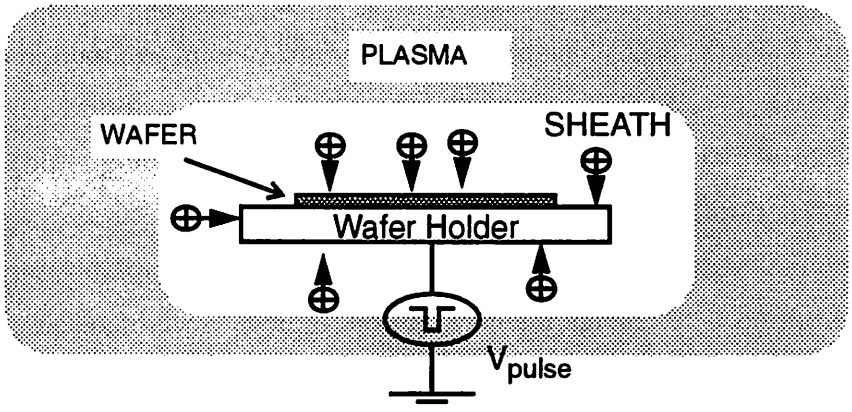

Figure 1-11. Plasma Immersion Ion Implantation

enhanced diffusion (TED), B channeling, and annealing of implant damage. Other difficulties to consider are etching of the substrate during implantation, non-mass-selective implantation, and possibly non-monoenergetic implantation due to finite rise and fall times of the substrate bias waveforms. All ion species generated in the plasma may be implanted. The PIII process, projects, dosimetry, and shallow junction fabrication are described in detail in Chapter 2 - Chapter 6.

50-60 nm p^+n junctions made with PIII have been reported using a 1kV implant in a BF_3 plasma, and a two-step rapid thermal annealing cycle of 5 s at 800°C and 10 s at 1050°C [1.37, 1.44]. Spreading resistance analysis of the profiles shows a peak activation around 10^{20} cm^{-3}. Ultra-shallow p^+n junctions can also be formed by PIII using a two-step implant: heavier ions (SiF_x (x=1-4), Si, or F) from a SiF_4 plasma are implanted into the Si substrate to form a 10-20 nm amorphous layer, and then boron is implanted at 2kV with a BF_3 plasma [1.45 - 1.48]. The two steps are performed sequentially without breaking vacuum. Using this two-step PIII process, no end-of-range dislocation loops or stacking faults are detected after annealing (1060°C, 10 s) due to the proximity of the Si surface which acts as a sink for implantation-induced interstitial point defects [1.46]. The fluorine concentration is below the detection limit of SIMS after annealing [1.49]. *N*-type PIII doping has been demonstrated using PH_3 plasma source gas [1.50].

1.3.3 Dopant Outdiffusion from Thin Films

The category of rapid thermal diffusion (RTD) from a solid source includes outdiffusion of dopant from polysilicon films [1.51], silicides [1.52 - 1.54], oxides [1.19], and other films like B-doped Ge or SiGe [1.55, 1.56]. Dopant may be introduced into these films

by implantation, or they may be doped in situ. Since there is no lattice damage done to the Si substrate in either case, lower temperatures may be used for dopant activation and drive-in cycle. RTD techniques have been used to form the shallowest junctions with the highest dopant activation: 10 nm junctions have been reported for B, P and As using out-diffusion from doped films. Using poly-Si or selectively depositing epi-Si for the dopant source makes a raised source/drain structure possible [1.2].

The difficulties in using solid source diffusion for shallow junctions are insufficient reproducibility and process control. Diffusion from a doped film is subject to the properties of the interface between the film and the Si surface, which is difficult to keep free from oxide precipitates and contamination, especially in ever-shrinking contact holes. The incorporated dose, then, cannot be well-controlled. Since the maximum concentration is dopant solid solubility at the anneal temperature, and since the junction depth is set by the anneal time and dopant diffusivity at the anneal temperature, surface concentration and junction depth are not entirely independent. Diffusion from a doped polysilicon or oxide film produces a junction whose shape resembles an error function, as expected from classical diffusion theory. Diffusion from silicide films may produce a different profile, as dopant has been shown to build-up at some silicide/Si interfaces [1.52]. Current research is devoted to finding new solid source materials, especially those that can be selectively deposited, or be used in raised source/drain structures. The use of epitaxial and polycrystalline cobalt disilicide as a dopant source for ultra-shallow boron junctions is discussed in Chapter 7 and Chapter 8.

1.3.4 Gas-Phase Doping

Gas-phase or rapid thermal vapor-phase doping is related to solid-source doping, except here the dopant is deposited in the form of desorbed gas molecules over the wafer surface instead of a thin film (Figure 1-12). Since the gas layer cannot be patterned like a thin film diffusion source, a hard nitride mask layer which can withstand the rapid thermal annealing temperatures must be put down on the wafer before processing. Advantages of the technique are that no damage is done to the substrate, and that the dopant can be predeposited and driven-in without opening the system (by flushing gas). It is a cluster-tool compatible technique that could be combined with a surface-cleaning step so that the Si surface/interface effects which are a problem for solid-source diffusion can be minimized. Gas-phase doping has the same process control problems as the solid-state diffu-

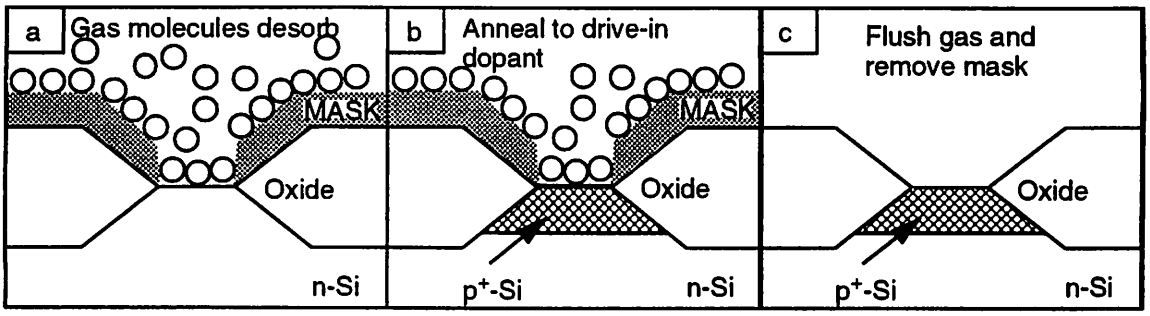

Figure 1-12. Gas-phase doping

sion source technique: that the profile is constrained to be exponential, that the dose control is difficult, and that the surface concentration and junction depth cannot be controlled separately. The junction depth x_j depends on anneal time and temperature, and the surface concentration depends on temperature and gas flow. B junctions 30-70 nm in depth with surface concentration above 10^{20} cm^{-3} have been reported using a B_2H_6 gas source [1.57 - 1.59].

1.3.5 Laser Doping

Laser doping can produce the highest activated dopant concentrations and almost constant concentration profiles in the doped regions [1.60, 1.61]. The laser doping technique is described in Figure 1-13. Gas molecules desorb on the wafer surface, as in the gas-

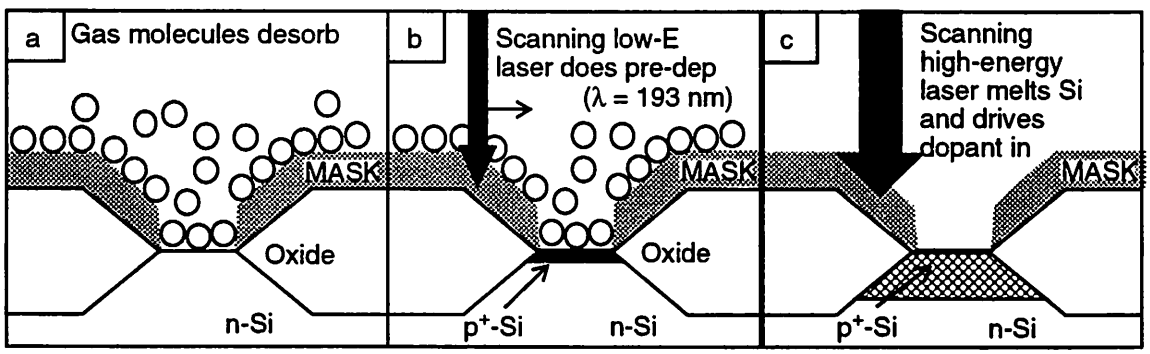

Figure 1-13. Laser doping

phase doping process, but here the predeposition step is performed by B_2H_6 photolysis by a low energy (0.05 J/cm^2) scanning ArF excimer laser at 193 nm. The incorporated dose is controlled by the number of pulses and the gas flow rate. The dopant drive-in is a second

step, where the laser fluence (energy density) is large enough to melt the Si (0.7 J/cm^2). The laser energy and number of pulses control the melt time and melt depth. Dopant atoms are incorporated in the Si lattice as it regrows by solid-phase epitaxy (SPE). No additional annealing is needed. 50 nm B junctions and 60 nm As junctions with surface concentration above 10^{20} cm^{-3} have been reported. Additional advantages are that no damage to the substrate is observed during melting / regrowth and that no oxide damage or charging occurs.

One difficulty with laser doping is that a hard, reflective mask is required to absorb the laser energy where dopant incorporation is unwanted. Usually Al masks are used. The technique has very low throughput, as the small spot-size laser must be scanned across the whole wafer twice. The most difficult issue is process integration, however. Simulations of the melt region in Si show that the thermal gradients due to melting at a MOSFET gate edge prevent the melt from extending under the gate region [1.62]. This means there is little or no electrical overlap of the gate and source/drain, leading to high series resistance and bad coupling. Additionally, the poly-gate is expected to melt during source/drain doping, leading to resizing of poly-Si grains and possible oxide stressing.

1.3.6 Gas-Immersion Laser Doping

Gas-immersion laser doping (GILD) is a variant of the laser doping technique where a single laser scan is done with a high energy excimer laser at 308 nm while the wafer is immersed in the doping gas [1.63, 1.64, 1.44]. Like laser doping, a box-like doping profile with high concentration from the surface to the junction depth can be achieved. The dose is controlled by the number of pulses and dopant gas pressure. The junction depth is equal to the depth of Si melted, which is determined by the laser fluence (energy density) of a 40 ns laser pulse. In GILD, the laser wavelength is in the optical region. Current research focuses on integrating the technique into an optical lithography wafer stepper system. If that were to occur, laser doping could be performed using a mask in the stepper optical column, instead of using a hard mask on the wafer surface. It would eliminate the masking steps needed to define source and drain regions, and increase the source/drain process module throughput. To date, Al masks are still needed to reflect the laser energy away from regions that do not require doping. With this technique, junctions of 25 nm have been reported for boron.

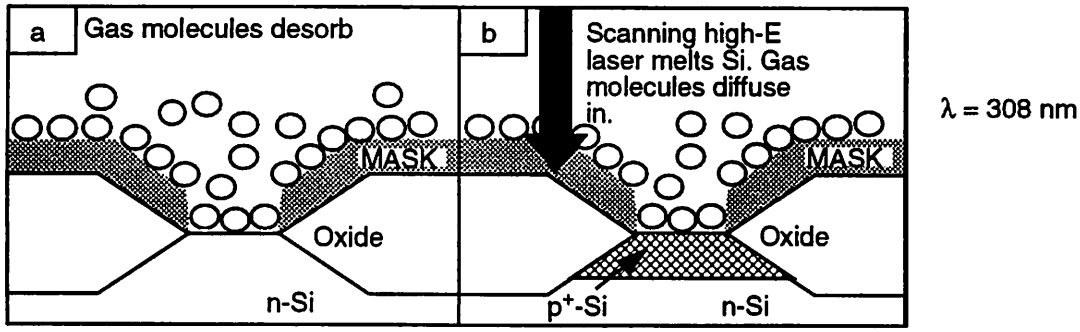

Figure 1-14. Gas-immersion laser doping

1.4 Objective of this work

This thesis details the development and characterization of two techniques for shallow junction fabrication. Plasma immersion ion implantation (PIII) and epitaxial $CoSi_2$ as a doping source are two methods which are easily integrated into standard CMOS processing, and have unique properties that can be exploited in making shallow junctions for ULSI. Shallow junction optimization is studied using a combination of physical materials analysis techniques, electrical measurements, and modeling. Materials techniques are used to monitor the movement of dopant in shallow junction systems, and to monitor the effect of doping processes on the Si substrate and thin films on the wafer. Electrical characterization is used to predict which doped structures will behave more ideally in a circuit, and new electrical techniques are developed for optimizing the doping sequence. Modeling is used to explain the evolution of well-behaved junctions from leaky metal-Si contacts as dopant diffuses and becomes active. The materials and shallow junctions made with PIII and epitaxial $CoSi_2$ are described in depth in the following chapters.

1.5 References

[1.1] J.O. Borland and R. Koelsch, "MeV implantation technology: next-generation manufacturing with current-generation equipment," Sol. St. Tech., 36 (12), pp. 28-29, 1993.

[1.2] P. Singer, "Trends in ion implantation," Semicond. Int., 18 (9), pp. 58-60, 62, 64, 1995.

[1.3] C. Hu, "MOSFET scaling in the next decade and beyond," Semicond. Int., 17 (6), pp. 105-106, 108, 110, 112,114, 1994.

[1.4] C. Hu, "Ultra-large-scale integration device scaling and reliability," J. Vac. Sci. Tech., B12 (6), pp. 3237-3241, 1994.

[1.5] R. Burger and W. Howard, eds., "Semiconductor Industry Association Semiconductor Technology Workshop Working Group Reports," Santa Clara: SIA, 1993.

[1.6] S.M. Sze, *Physics of Semiconductor Devices*, New York: Wiley and Sons, 1981.

[1.7] L.D. Yau, "A simple theory to predict the threshold voltage of short-channel IGFET's," Sol. St. Electron., 17 (10), pp. 1059-1063, 1974.

[1.8] S. G. Chamberlain, S. Ramanan, "Drain-induced barrier-lowering analysis in VLSI MOSFET device using two-dimensional numerical simulations," IEEE Trans. on Electron Dev., 33 (11, pt.1), pp. 1745-1753, 1986.

[1.9] Z.-H. Liu, C. Hu, J.-H. Huang, and T.-Y. Chan, "Threshold voltage model for deep-submicrometer MOSFETs," IEEE Trans. on Electron Dev., 40 (1), pp. 86-95, 1993.

[1.10] C. M. Osburn, SRC / Sematech Review, 1995.

[1.11] P.K. Ko, "Approaches to Scaling" in *VLSI Electronics Microstructure Science 18*, ed. by N. G. Einspruch, New York: Academic Press, 1989.

[1.12] K. K. Ng and W. T. Lynch, "The impact of intrinsic series resistance on MOSFET scaling," IEEE Trans. on Electron Dev., 34 (3), pp. 503-511, 1987.

[1.13] C. Hu, "Hot-carrier effects," in *VLSI Electronics Microstructure Science 18*, ed. by N. G. Einspruch, New York: Academic Press, 1989.

[1.14] T. Y. Chan, P. K. Ko and C. Hu, "Dependence of channel electric field on device scaling," IEEE Electron Dev. Lett., 6 (10), pp. 551-553, 1985.

[1.15] M. Ching and E.C. Jones, "Effects of variations in doping profiles on 0.1 μm channel length MOSFETs", unpublished.

[1.16] C. Hu, S. C. Tam, F.-C. Hsu, P.-K. Ko, T. Y. Chan and K.W. Terrill, "Hot-electron-induced MOSFET degradation-model, monitor, and improvement," IEEE Trans. on Electron Dev., 32 (2), pp. 375-385, 1985.

[1.17] P. H. Singer, "Trends in CMOS development," Semicond. Int., 15 (5), pp. 56-58, 60, 1992.

[1.18] M. Ono, M. Saito, T. Yoshitomi, and C. Fiegna, "A 40 nm gate length n-MOSFET," IEEE Trans. on Electron Dev., 42 (10), pp. 1822-1830, 1995.

[1.19] B.G. Park, J. Bokor, H.S. Luftman, C.S. Rafferty, and M.R. Pinto, "Ultrashallow junctions for ULSI using As_2^+ implantation and rapid thermal anneal," IEEE Elec. Dev. Lett., 13 (10), pp. 507-509, 1992.

[1.20] S. Ando, H. Horie, M. Imai, K. Oikawa, H. Kato, H. Ishiwari, and S. Hijiya, "Very shallow p^+-n junctions and subquarter micron gate p-channel MOSFETs," in *Proc. 1990 Symp. VLSI Tech.*, New York: IEEE, pp. 65-66, 1990.

[1.21] S.N. Hong, G.A. Ruggles, J.J. Wortman, E.R. Myers, and J.J. Hren, "Characterization of ultra-shallow p^+-n junction diodes fabricated by 500-eV boron-ion implantation," IEEE Trans. on Elec. Dev., 38 (1), pp. 28-31, 1991.

[1.22] L. Rubin, private communication.

[1.23] C. Jaussaud, F. Jourdan, A. Soubie, and R. Simonton, "Monitoring of High Energy contamination in ion implantation by Thermawave measurements," in *Ion Impl. Tech. 92*, Amsterdam: North-Holland, pp. 571-574, 1993.

[1.24] D. F. Downey, R. B. Liebert, "Control of BF_2 dissociation in high-current ion implantation," Nucl. Instr. Meth. in Phys. Res., B55 (1-4), pp. 49-54, 1991.

[1.25] T. O. Sedgwick, A. E. Michel, V. R. Deline, S. A. Cohen, and others, "Transient boron diffusion in ion-implanted crystalline and amorphous silicon," J. of Appl. Phys., 63 (5), pp. 1452-1463, 1988.

[1.26] R.B. Fair, J.J. Wortman, and J. Liu, "Modeling rapid thermal diffusion of arsenic and boron in silicon," J. Electrochem. Soc., 131 (10), pp. 2387-2394, 1984.

[1.27] S. Wolf and R. Tauber, *Silicon processing for the VLSI era*, Sunset Beach: Lattice Press, 1990.

[1.28] A. E. Michel, W. Rausch, P. A. Ronsheim, R. H. Kastl, "Rapid annealing and the anomalous diffusion of ion implanted boron into silicon," Appl. Phys. Lett., 50 (7), pp. 416-418, 1987.

[1.29] R.B. Fair, "Junction formation in Silicon by Rapid Thermal Annealing," in *Rapid Thermal Processing Science and Technology*, ed. by R. B. Fair, Boston: Academic Press, pp. 169-226, 1993.

[1.30] M. Y. Tsai and B. G. Streetman, "Recrystallization of Implanted Amorphous Silicon Layers I, Electrical Properties of Silicon Implanted with BF_2^+ or $Si^{++}B^+$," J. Appl. Phys., 50 (1), pp.183-192, 1979.

[1.31] K.S. Jones, S. Prussin, and E.R. Weber, "A systematic analysis of defects in ion-implanted silicon," Appl. Phys. A, A45 (1) pp. 1-34, 1988.

[1.32] K.S. Jones and G.A. Rozgonyi, "Extended defects from Ion Implantation and Annealing," in *Rapid Thermal Processing Science and Technology*, ed. by R. B. Fair, Boston: Academic Press, pp. 123-168, 1993.

[1.33] E. Myers, J.J. Hren, S.N. Hong, and G.A. Ruggles, "Damage Removal of low energy ion implanted BF_2 layers in Silicon," in *Ion Beam Processing of Advanced Electronic Materials*, ed. by N.W. Cheung, Pittsburgh, PA: Mater. Res. Soc., pp. 27-32, 1989.

[1.34] M. Craig, A. Sultan, K. Reddy, and S. Banerjee, "Dose rate and thermal budget optimization for ultrashallow junctions formed by low-energy (2-5 keV) ion implantation," J. Vac. Sci. Tech., B14 (1), pp. 255-259, 1996.

[1.35] J. R. Liefting, J. S. Custer, R. J. Schreutelkamp, F. W. Saris, "Dislocation formation in silicon implanted at different temperatures," Mat. Sci. Engin., B15 (2), pp. 173-186, 1992.

[1.36] A. Sultan, M. Craig, K. Reddy, and S. Banerjee, "The dependence of ultrashallow junction depths on impact dose rates," Appl. Phys. Lett., 67 (9), pp. 1223-1225, 1995.

[1.37] S. B. Felch, D. L. Chapek, S. M. Malik, and P. Maillot, "Comparison of different analytical techniques in measuring the surface region of ultrashallow doping profiles," J. Vac. Sci. Tech., B14 (1), pp. 336-340, 1996.

[1.38] A. Hori, H. Nakaoka, H. Umimoto, K. Yamashita, M. Takase, N. Shimizu, B. Mizuno, and S. Odanaka, "A 0.05 μm-CMOS with ultra shallow source/drain junctions fabricated by 5 keV ion implantation and rapid thermal annealing," in Proc. IEEE IEDM 94, pp. 485-488, 1994.

[1.39] E.C. Jones, B.P. Linder, and N.W. Cheung, "Plasma Immersion Ion Implantation for Electronic Materials," Japan. J. Appl. Phys, 35 (2B, pt. 1), pp. 1027-1036, 1996.

[1.40] P.K. Chu, S. Qin, C. Chan, N.W. Cheung, L.A. Larson, "Plasma Immersion Ion Implantation - A fledgling technique for semiconductor processing," to be published.

[1.41] N.W. Cheung, W. En, E. Jones, and C. Yu, "Plasma immersion ion implantation of semiconductors," in *Beam Solid Interactions: Fundamentals and Applications*, ed. by M. Nastasi, Pittsburgh: Mat. Res. Soc., pp. 297-306, 1993.

[1.42] C. Yu and N.W. Cheung, "Plasma immersion ion implantation, a perspective," in *Proc. of the NATO Advanced Study Institute on Semicond. Mat. and Proc. Tech.*, Dordrecht, Netherlands: Kluwer Academic Publishers, pp. 245-249, 1992.

[1.43] S.B. Felch, T. Sheng and C.B. Cooper III, "Characterization of a plasma doping system" in *Ion Impl. Tech. 92*, Amsterdam: North-Holland, pp. 687-690, 1993.

[1.44] E. Ishida, "Study of electrical measurement techniques for ultra-shallow dopant profiling," J. Vac. Sci. Tech., B14 (1),pp. 397-403, 1996.

[1.45] X.Y. Qian, N.W. Cheung, M.A. Lieberman, S.B. Felch, "Plasma immersion ion implantation of SiF_4 and BF_3 for sub-100 nm p^+/n junction fabrication," Appl. Phys. Lett., 59 (3), 348-350, 1991.

[1.46] E.C. Jones and N.W. Cheung, "Characteristics of sub-100-nm p^+/n junctions fabricated by plasma immersion ion implantation," IEEE Elec. Dev. Lett., 14 (9), pp. 444-446, 1993.

[1.47] E C. Jones, S. Im and N. W. Cheung, "Ultra-shallow P^+/N junctions formed by SiF_4 preamorphization and BF_3 implantation using plasma immersion ion implantation," in *Beam Solid Interactions: Fundamentals and Applications*, ed. by M. Nastasi, Pittsburgh: Mat. Res. Soc., pp. 255-259, 1993.

[1.48] E. C. Jones, S. Im and N. W. Cheung, "Characterization of ultra-shallow p^+n diodes fabricated using plasma immersion ion implantation" in *Proc. Ion Impl. Tech. 92*, Amsterdam: North-Holland, pp. 373-376, 1993.

[1.49] S.B. Felch, T. Sheng and C.B. Cooper III, "Characterization of a plasma Doping System," in *Proc. Ion Impl. Tech. 92*, Amsterdam: North-Holland, p. 687-690, 1993.

[1.50] B. Mizuno, I. Nakayama, N. Shimizu, M. Kubota, and K. Yano, "Plasma Doping," in *Ion Impl. Tech 94*, Amsterdam: North-Holland, pp. 985-988, 1995.

[1.51] K. Park, S. Batra, S. Banerjee, G. Lux, and T.C. Smith, "Analysis of ion-implanted amorphous and polycrystalline silicon films as diffusion sources for ultrashallow junctions," J. Appl. Phys. 70 (3), pp. 1397-1404, 1991.

[1.52] E.C. Jones, D.B. Fraser, and N. W. Cheung, "Low-temperature processing of shallow junctions using epitaxial and polycrystalline $CoSi_2$," J. Elec. Mat., 24 (7), pp. 863-73, 1995.

[1.53] E.C. Jones, S. Ogawa, P. Ameika, M.L.A. Dass, D.B. Fraser, P. Chu and N.W. Cheung, "Rapid thermal processing of shallow junctions using epitaxial $CoSi_2$ as a doping source," in *Rapid Thermal and Integrated Processing III*, ed. by J.J. Wortman, Pittsburgh: Mat. Res. Soc., pp. 339-343, 1994.

[1.54] S. Ogawa, J.A. Fair, T. Kouzaki, R. Sinclair, E.C. Jones, N.W. Cheung, and D.B. Fraser, "Direct solid state phase transformation from Co to epitaxial $CoSi_2$ in Co/thin Ti(100)/Si structure and its application for shallow junction formation," in *Silicides, Germanides, and Their Interfaces*, ed. by R.W. Fathauer, Pittsburgh: Mat. Res. Soc., pp. 355-360, 1994.

[1.55] B.G. Park, C.A. King, D.J. Eaglesham, T.W. Sorsch, B. Weir, H.S. Luftman, and J. Bokor, "Ultrashallow p^+-n junctions formed by diffusion from an RTCVD-deposited B, Ge layer," in Proc. Soc. Opt. Eng. (SPIE) 2091, pp. 122-131, 1994.

[1.56] F. Honma, J. Murota, K. Goto, T. Maeda, and Y. Sawada, "Ultrashallow junction formation using low-temperature selective $Si_{1-x}Ge_x$ chemical vapor deposition," Japan. J. Appl. Phys. Part 1, 33 (4B), pp. 2300-2303, 1994.

[1.57] P. A. O'Neil, K. E. Violette, M. C. Ozturk, I. C. Ivanov, "Formation of ultra-shallow junctions in silicon by rapid thermal vapor phase doping in an ultrahigh vacuum rapid thermal processing system," in *Rapid Thermal and Integrated Processing IV*, ed. by S. R. J. Brueck, Pittsburgh: Mater. Res. Soc., pp. 395-400, 1995.

[1.58] Y. Kiyota, T. Onai, T. Nakamura, and T. Inada, "Ultra-thin-base Si bipolar transistor using rapid vapor-phase direct doping(RVD)," IEEE Trans. on Electron. Dev., 39 (9), pp. 2077-2081, 1992.

[1.59] J. Nishizawa, K. Aoki, T. Akamine, "Ultrashallow, high doping of boron using molecular layer doping," Appl. Phys. Lett., 56 (14), pp. 1334-1335, 1990.

[1.60] T. Akane, T. Nii, and S. Matsumoto, "Two-step doping using excimer laser in boron doping of silicon," Jpn. J. Appl. Phys., 31 (12B), pp. 4437-4440, 1992.

[1.61] S. Matsumoto, S. Yoshioka, J. Wada, S. Inui, and K. Uwasawa, "Boron doping of silicon by ArF excimer laser irradiation in B_2H_6," J. Appl. Phys. 67 (12), pp. 7204-7210, 1990.

[1.62] K.H. Weiner, P.G. Carey, A.M. McCarthy and T.W. Sigmon, "An excimer-laser-based nanosecond thermal diffusion technique for ultra-shallow pn junction fabrication," Microelec. Eng., 20 (1-2), pp. 107-130, 1993.

[1.63] K. H. Weiner, P. G. Carey, A. M. McCarthy, T. W. Sigmon, "Low-temperature fabrication of p^+-n diodes with 300 A junction depth," IEEE Elec. Dev. Lett., 13 (7), pp. 369-71, 1992.

[1.64] E. Ishida, T. W. Sigmon, K. H. Weiner, M. R. Frost, "Ultra-shallow boxlike profiles fabricated by pulsed ultraviolet-laser doping process," J. Vac. Sci. Tech., B12 (1), pp. 399-404, 1994.

2 Plasma Immersion Ion Implantation

2.1 Introduction

Plasma immersion ion implantation (PIII) is a versatile technology for large area, high current, high dose rate implantation at both medium and low implantation energies (100 eV - 100 keV) [2.1-2.3]. PIII, also called plasma source ion implantation or plasma doping, was originally developed for metallurgical applications like high dose-rate implantation of wear- and corrosion-resistant surface alloys by ion beam bombardment [2.4-2.7]. Metallurgical applications exploit the conformal implantation capability of PIII: it can be used to implant all sides of three-dimensional objects simultaneously, without ion beam scanning or sample rotation. The physical principle of plasma immersion ion implantation is illustrated in Figure 2-1. A substrate is placed on a holder which is immersed in a uniform plasma of density n_0 containing the implant ion species. A bias

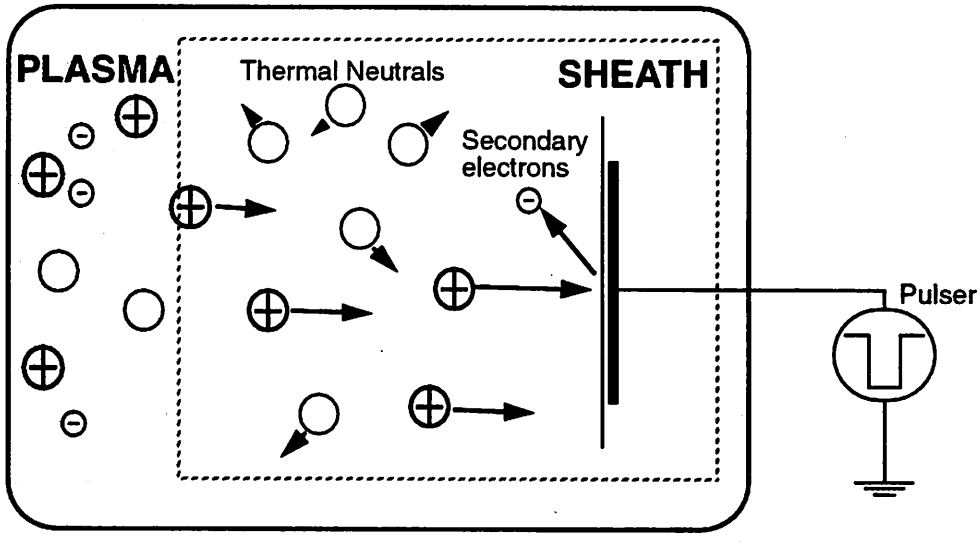

Figure 2-1. Schematic drawing of PIII process

waveform or DC voltage is applied to the wafer holder for implantation. When this negative voltage waveform is applied to the target wafer, electrons are repelled away from the target surface and a "sheath region" of positive ions is established around the wafer holder. Positive ions inside the sheath region are attracted by the negative potential of the target and accelerate toward it. The ions gather kinetic energy while traversing the sheath, and implant at energies up to the potential difference across the sheath. When the wafer bias is turned off, electrons from the plasma collapse the sheath region and neutralize the accumulated surface charge.

2.2 PIII Dynamics

Understanding the dynamics of sheath movement, ion current, and electron current during PIII is essential for controlling the implant dose, dose rate, surface charging, and contamination. A model for the plasma sheath and implant currents during PIII has developed [2.8-2.10] from analytical relations used to describe the time dependent plasma currents and the flux of ions across a moving sheath edge [2.11]. The total current drawn from the system power supply consists of four components: ion, secondary electron, plasma electron, and displacement currents:

$$I_{total} = I_i + I_{se} + I_e + I_{disp} . \tag{2-1}$$

With efficient remote plasma sources, the sheath thickness is kept below 10 cm, even under a bias of 100 kV. The ECR PIII system usually works in the low pressure regime (0.1-10 mTorr), to minimize collisional scattering between the accelerating ions and neutral atoms or molecules in the sheath. In the low pressure regime, where the mean free path is larger than the sheath thickness, the sheath may be described as collisionless. The ion current density (J_i) is then described by the quasi-static collisionless Child Law:

$$J_i = \frac{4}{9}\varepsilon_0 \left(\frac{2q}{M}\right)^{1/2} \cdot \frac{V^{3/2}}{s^2} \tag{2-2}$$

where ε_0, q, M, V, and s are the free space permittivity, ion charge, ion mass, sheath voltage and sheath thickness, respectively. This analysis assumes the value of electric field seen by an ion does not change as the ion crosses the sheath. This has been shown to be a good approximation [2.12] when the timescale of the voltage pulse (rise time, on time, and fall time) is longer than the inverse ion plasma frequency, ω_{pi}^{-1}. ω_{pi}^{-1} is a measure of how fast

the plasma ions can react to the applied bias, and is equal to $(\varepsilon_0 M/q^2 n_0)^{1/2}$. For a BF_2^+ ion in a plasma with n_o=10^{10} cm^{-3}, ω_{pi}^{-1} is about 53 ns. If the voltage is slowly varying in comparison, it can be assumed that the ions see the instantaneous potential V across the sheath.

The positive ion supply is replenished by diffusion from the bulk plasma across the sheath boundary. These ions move at velocities approximately equal to the Bohm velocity, ($u_B \approx 10^5$ cm/s). The ion current is then also equal to the ion flux across the sheath boundary:

$$J_i = qn_0(\frac{ds}{dt} + u_B) \tag{2-3}$$

where n_o is the ion density. Equation 2-2 and Equation 2-3 together provide a complete description of both the ion current and the sheath motion. Plasma electron current density is assumed to follow a Boltzmann distribution,

$$J_e = -\frac{1}{4} q n_0 v_e e^{-V_s/T_e} . \tag{2-4}$$

v_e is the average electron velocity, $v_e = (8kTe/\pi m_e)^{1/2}$, T_e is average electron temperature, k is Boltzmann's constant, and m_e is electron mass. The plasma electron current is the only source of electrons available to neutralize the accumulated positive surface charge due to the bombarding ions and emitted secondary electrons. Displacement current is due to the time variation of sheath potential and capacitance [2.13, 2.14]:

$$J_{disp} = C_s \frac{dV_s}{dt} + V_s \frac{dC_s}{dt}. \tag{2-5}$$

Accurately accounting for the last current component, secondary electron current, is essential for predicting charging damage to the substrate. Ion bombardment of the wafer surface generates secondary electrons which are accelerated away by the sheath potential, amplifying the surface charge accumulation. The secondary electron current is related to the ion current which generates the electrons. Since the secondary electron yield (γ) is a function of the incoming ion energy, for a collisionless sheath, it can be related to the bias voltage:

$$J_{se} = \gamma(V) J_i . \tag{2-6}$$

The secondary electron yield is proportional to $V^{1/2}$ for moderate ion energies (above a few keV for BF_2^+), when the secondary electrons are created by kinetic energy transfer. In the

lower energy regime the yield may saturate at a constant value due to potential emission. Potential emission is the release of a secondary electron that gains energy when another electron jumps from the target surface into a lower energy state in the approaching ion and neutralizes it. This potential secondary electron emission pins γ at a small value for low energy incoming ions.

The above equations are valid whether the substrate bias waveform is pulsed or dc. In either case, while the wafer bias is negative, electrons are repelled from the surface. Positive charge will build up on insulating layers on the substrate during the implantation. When an implant pulse ends, the barrier to electrons is reduced, and electrons from the plasma will flood the surface according to Equation 2-4 to neutralize the positive charge built up by implanting ions. To avoid dielectric breakdown or thin-oxide stressing, a pulse waveform must therefore be used to capacitively couple the applied bias to the surface potential for wafers containing insulating layers [2.15, 2.16]. The oxide stressing is minimized by using short implant pulses, around 1 μs, and low duty factors. If the implant frequency is too high, in the range of 20 kHz, the implant charge neutralization by electrons between pulses may not be complete [2.17]. PIII can be used with a dc waveform for samples for which charging damage is not a concern.

Using only a few experimentally measured parameters, the ion density (n_0), electron temperature (T_e), plasma potential (V_p) and floating potential (V_f), the above equations can be solved to predict the PIII currents during implantation of an arbitrary substrate or device structure. Comparison of the model with measured PIII current during implant pulses shows good agreement [2.17]. Work with this model has explained a number of heretofore anomalous device and process-related charging effects during PIII: for example, the insulator charging which occurs during the substrate bias pulse and the electron neutralization of the surface when the pulse ends [2.17]. The charging is also affected by device structures on the substrate. The model has predicted that reverse-biased well structures on ULSI wafers may exacerbate gate-oxide charging [2.18]. For microsecond pulses, this modeling and experimental work has verified that thin-oxide charging effects can be minimized by keeping the duty factor small and pulsing frequency below several kHz.

2.3 Uses of PIII

Currently researched semiconductor applications of PIII shown in Figure 2-2 include plasma doping of source/drain, polysilicon, and trenches, SIMOX and Ge-Si-C buried layer formation, and surface modification of metals. A number of these applications are described in the following sections.

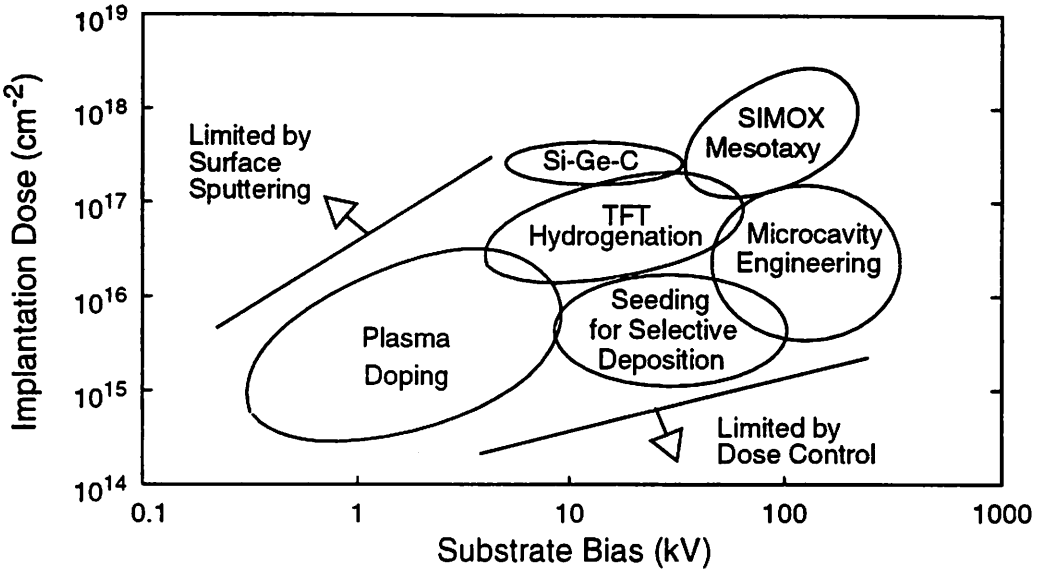

Figure 2-2. Semiconductor applications of PIII

2.3.1 Plasma Doping

Conventional implantation is the primary technique used for high dose doping applications like doped polysilicon gates, polysilicon emitters for bipolar transistors, dopant source layers like silicides, and raised source-drain dopant source layers for ULSI devices. However, conventional beamline implanters are very expensive, and have lower throughput and higher per-wafer costs when compared to PIII for shallow junction formation [2.19]. Since there is no drop-off in PIII implant current at low energy, as observed in conventional implanters, PIII can perform these implants much faster.

The large-area capability of PIII makes it a viable alternative to conventional implantation for large-area, high-throughput doping of thin-film transistors (TFT) for flat-panel displays, as well. TFT material doping with P has been reported using RF plasma [2.20, 2.21] and ECR plasma doping [2.22], using PH_3 diluted in H or He as a plasma source gas. P-type doping of polysilicon has been performed with BF_3 gas in an ECR source [2.23,

2.24]. Another emerging technique for high dose doping with a plasma source is ion shower doping. Ion shower doping systems differ from PIII in that grids are placed between the plasma source and wafer to extract and accelerate the ions from the plasma, instead of using a substrate bias. Ion shower doping apparati have reported ion implantation energies from 50 eV - 100 keV and implant currents comparable to PIII, in the 0.1-2 mA/cm^2 range [2.25-2.27]. Unlike PIII, ion shower systems require electron flood guns to neutralize the built-up charge on the substrate during implantation. They do retain the non-mass selective and large-area implant properties of PIII. These systems have been used for TFT material doping using diluted PH_3 [2.21, 2.25-2.28] and B_2H_6 [2.27].

One consideration when evaluating plasma doping systems is whether additional ions implanted along with the dopant degrade device characteristics. As plasma and ion shower doping are both non-mass-selective, all ions generated in the plasma are implanted. This leads to high concentrations of H or F in the material after implantation, depending on the gas source. It has been reported [2.26, 2.15] that these atoms largely diffuse out of a Si film during annealing, yielding low resistivity films even under low temperature annealing. Figure 2-3 shows polysilicon film resistivity versus dopant annealing

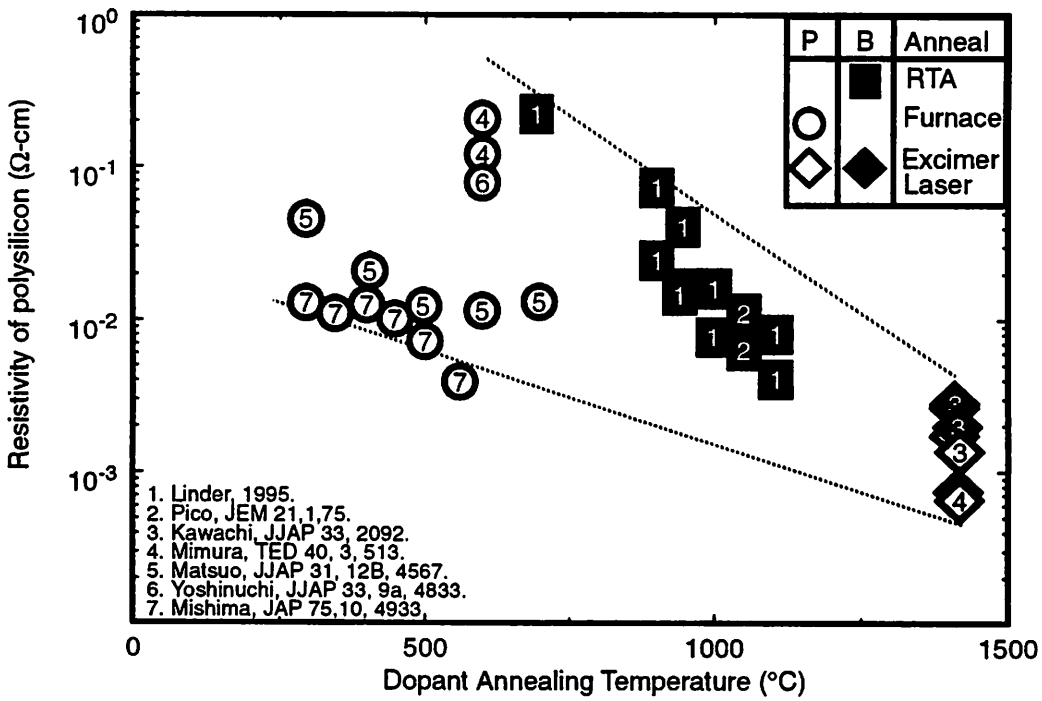

Figure 2-3. Comparison of poly-doping by PIII and Ion Shower techniques
Data from Refs. [2.21, 2.23-2.28].

temperature for a number of plasma doping and ion shower systems and various annealing techniques. The trends for B and P film resistivity track well among the groups, and show that non-mass selective doping of P-doped polysilicon layers can be quite effective, even coupled with low-temperature furnace annealing. No information on furnace annealing of B layers was found. If the carrier gas is changed from H_2 to He, a significant difference in resistivity results. Implants done with PH_3 in a He carrier likely show lower resistivity for the same implant conditions due to the higher ionization potential of He and its smaller contribution to the ion current. For the same implant current and implant time, a substrate doped in a PH_3/He plasma will contain a higher dose of P than one processed in a PH_3/H_2 plasma.

A comparison of doping efficiency and activation between ion shower and conventional ion implantation shows that these resistivity values are comparable to the conventional process [2.26]; in fact, the activated carrier concentrations and conductivity are slightly higher for the ion shower system when both samples undergo a 300°C furnace anneal. The difference may be due to the excess damage caused by the molecular implant species in the ion shower case, and by hydrogen termination of dangling bonds when hydrogen carrier and hydrogen-containing gases are used. Ion shower and conventional implant processes appear equivalent after a 450°C anneal. Another concern of ion shower doping is the introduction of heavy metal atoms that are sputtered off the extraction grid into the substrate. Since TFTs fabricated with PH_3/He have been shown to have comparable electrical characteristics to conventionally implanted devices [2.25], with no obvious deficiencies that might be due to deep level centers [2.21, 2.27], control of dopant activation appears a more pressing issue in the process development.

2.3.2 Plasma Doping of Trenches

PIII also be applied to the difficult problem of conformal doping of three-dimensional, non-planar topographies like pre-oxidation field implants in recessed oxide structures and the deep, high aspect ratio trenches that need to be highly doped on the sides and bottom to maximize the storage capacitance of high density DRAM cells [2.29]. With conventional implantation, doping the sidewalls of trenches requires multiple implants at varying tilt and rotation [2.30, 2.31]. Even with multiple reflections of dopants off the trench sidewalls, conformal doping of very high aspect ratio trenches is not possible with conventional techniques. Plasma doping is capable of conformal implants if the system

pressure and implant energy are chosen correctly [2.32-2.36]. The angular distribution of implanting ions is caused by collisions with neutrals in the sheath and by some randomization in the direction of ion paths before entering the sheath. The angular distribution of ions $\rho(\theta)$, and its centroid Θ are therefore functions of the plasma pressure and the energy gained by ions crossing the sheath. The angular divergence among the ions in a PIII implant has been shown to be large enough to conformally dope a trench with an aspect ratio of 12 and top opening of 1 μm [2.35], yielding a uniform electrical junction depth

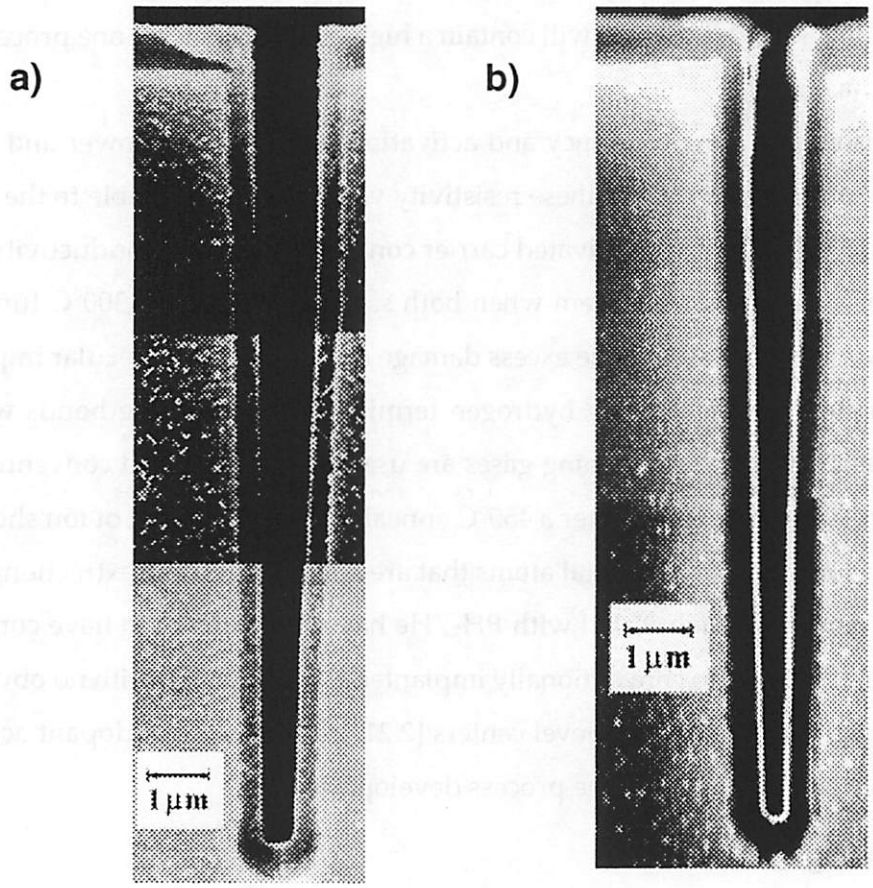

Figure 2-4. Conformal Trench Doping using PIII

SEM cross-section of 12:1 aspect ratio trenches conformally doped by 5 mTorr BF_3 PIII at a) 10 kV and b) 7.5 kV. After Ref. [2.35].

along the sidewalls of the trench [2.36] with no evidence of beam shadowing (Figure 2-4). Varying the implant energy alters the junction depth on the bottom of the trench, confirming that for the same neutral gas pressure, the centroid of the angular distribution (Θ) of

ions in the plasma sheath is reduced by increasing the applied bias. In the pressure range of 0.8-8 mTorr, no effect of the plasma pressure on the dopant distributions is apparent.

2.3.3 PIII for Buried Layer Synthesis

Buried layers of many kinds are being explored for use in devices: subsurface SiGe layers for heterojunction bipolar transistors [2.37], subsurface silicide and other conducting layers for metal-base transistors, and buried layers of dopants [2.38, 2.39] or insulators for VLSI device isolation [2.40]. These layered structures were originally formed by successive deposition steps onto a silicon substrate. If the materials formed are equivalent, implantation is the preferred synthesis method due to its higher throughput and lower cost per wafer than molecular beam epitaxy (MBE) or metal-organic chemical vapor deposition (MOCVD). To achieve proper stoichiometry of subsurface compounds, the implantation step must introduce atom concentrations above the solubility limit, requiring a dose larger than 10^{17} cm^{-2}. Silicon-on-insulator structures for ULSI have been formed by wafer bonding and polishing, and by SIMOX, where a high dose of oxygen (> 10^{17} cm^{-2}) is implanted into the Si wafer and a high temperature annealing step is used to create a buried oxide layer under the crystalline Si surface. The development of a PIII SIMOX process is aimed at lowering the cost of SIMOX wafers for SOI electronics by reducing the implantation time. A two order-of-magnitude reduction in implantation time is possible by PIII [2.41].

High-dose rate SIMOX synthesis using an oxygen plasma has been demonstrated in the PIII system [2.41-2.44]. The high voltage demanded by SIMOX (> 50 kV) can be maintained across the plasma sheath when using extremely low gas pressure (sub-mTorr). The implant time for an oxygen dose of $3x10^{17}$ cm^{-2} is less than 3 minutes for PIII; hours are required by conventional ion implantation. Three different modes of SIMOX microstructures (oxide precipitates, single SIMOX layers and double SIMOX layers) are observed when the relative concentrations of O_2^+ and O^+ changes. Single, continuous buried oxide layers are obtained when the relative abundance of O_2^+ to O^+ is above 9:1 as shown in Figure 2-5.

2.4 References

[2.1] N.W. Cheung, W. En, E. Jones, and C. Yu, "Plasma immersion ion implantation of semiconductors," in *Beam Solid Interactions: Fundamentals and Applications*, Pittsburgh: Mat. Res. Soc., pp. 297-306, 1993.

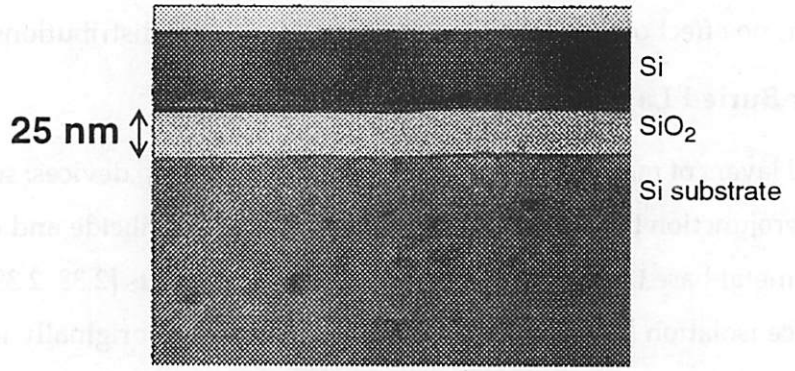

Figure 2-5. Buried oxide (SIMOX) layer formed by PIII

Cross-sectional transmission electron microscopy (XTEM) of a continuous SIMOX structure was obtained by a 60 kV PIII oxygen plasma implant, followed by 1270°C annealing.

[2.2] B. Mizuno, I. Nakayama, N. Shimizu, M. Kubota, and K. Yano, "Plasma Doping," in *Ion Impl. Tech. 94*, Amsterdam: North-Holland, pp. 985-988, 1995.

[2.3] E. C. Jones, B.P. Linder, and N.W. Cheung, "Plasma immersion ion implantation for electronic materials," Japan. J. Appl. Phys, 35 (2B, Pt. 1), pp. 156-165, 1996.

[2.4] J.R. Conrad and C. Forest, "Plasma source ion implantation," in *IEEE Int. Conf. on Plasma Sci. Abstracts*, pp. 28-29, 1986.

[2.5] J.R. Conrad, J.L. Radtke, R.A. Dodd, F.J. Worzala, et al, "Plasma source ion-implantation technique for surface modification of materials," J. Appl. Phys., 62 (11), pp. 4591-4596, 1987.

[2.6] J.R. Conrad, S. Baumann, R. Fleming, and G.P. Meeker, "Plasma source ion implantation dose uniformity of a 2*2 array of spherical targets," J. Appl. Phys., 65 (4), pp. 1707-1712, 1989.

[2.7] J. Tendys, I.J. Donnelly, M.J. Kenny, and J.T.A. Pollock, "Plasma immersion ion implantation using plasmas generated by radio frequency techniques," Appl. Phys. Lett., 53 (22), pp. 2143-2145, 1988.

[2.8] M. A. Lieberman, "Model of plasma immersion ion implantation," J. Appl. Phys. 66(7), pp. 2926-2929, 1989.

[2.9] M. Shamim, J. T. Scheuer and J. R. Conrad, "Measurements of spatial and temporal sheath evolution for spherical and cylindrical geometries in plasma source ion implantation," J. Appl. Phys., 69 (5), pp. 2904-2908, 1991.

[2.10] R. A. Stewart and M. A. Lieberman, "Model of plasma immersion ion implantation for voltage pulses with finite rise and fall times," J. Appl. Phys., 70 (7), pp. 3481-3487, 1991.

[2.11] J. K. Chester, "Effects of expanding sheaths on the operation of mercury-arc rectifiers," J. Sci. Tech., 37 (1), pp. 2-10, 1970.

[2.12] W.G. En, Ph.D. thesis, University of California at Berkeley, 1996.

[2.13] W. En and N. W. Cheung, "Modelling of charging effects in plasma immersion ion implantation," Nucl. Instr. & Meth., B96 (1-2) pp. 435-439, 1995.

[2.14] W. En, M.A. Lieberman, and N. W. Cheung, "Comparison of experimental target currents with analytical model results for plasma immersion ion implantation," IEEE Trans. Plasma Sci., 23 (3), pp. 415-421, 1995.

[2.15] S.B. Felch, T. Sheng and C.B. Cooper III, "Characterization of a plasma doping system" in *Ion Impl. Tech. 92*, Amsterdam: North-Holland, pp. 687-690, 1993.

[2.16] W. En and N. W. Cheung, "Modeling and Experiments of Waveforms on Oxide Charging in Plasma Immersion Ion Implantation," in review for IEEE Trans. Elec. Dev. (1996).

[2.17] W. En and N. W. Cheung, "A new method for determining the secondary electron yield dependence on ion energy for plasma exposed surfaces," to be published in IEEE Trans. Plasma Sci, 24 (6), 1996.

[2.18] W. En, B. P. Linder and N. W. Cheung, "Modeling of oxide charging effects in plasma processing," J. Vac. Sci Tech., B14 (1), pp. 552-559, 1996.

[2.19] D.J. Rej and R.B. Alexander, "Cost estimates for commercial plasma source ion implantation," J. Vac. Sci. Tech., B12 (4) pp. 2380-2387, 1994.

[2.20] R. Kakkad, T. Shimano, and N. Ibaraki, "Effect of ion doping conditions on electrical conductivity of amorphous silicon films and its application to thin transistors," Jpn. J. Appl. Phys., 31 (12B) pp. 4563-4566, 1992.

[2.21] M. Matsuo, T. Nakazawa, and H. Ohshima, "Low-temperature activation of impurities implanted by ion doping technique for poly-Si thin-film transistors," Jpn. J. Appl. Phys. 31 (12B), pp. 4567-4569, 1992.

[2.22] H. Kakinuma, M. Mohri, and T. Tsuruoka, "Phosphorous doping using electron cyclotron resonance plasma for large-area polycrystalline silicon thin film transistors," Jpn. J. Appl. Phys., 33 (1B), pp. 654-658, 1994.

[2.23] C.A. Pico, M.A. Lieberman, and N.W. Cheung, "PMOS integrated circuit fabrication using BF_3 plasma immersion ion implantation," J. Electron. Mater., 21 (1), pp. 75-79, 1992.

[2.24] B.P. Linder, unpublished.

[2.25] A. Mimura, G. Kawachi, T. Aoyama, T. Suzuki, Y. Nagae, N. Konishi, and Y. Mochizuki, "A 10-s doping technology for the application of low-temperature polysilicon TFTs to giant microelectronics," IEEE Trans. Elec. Dev., 40 (3), pp. 513-520, 1993.

[2.26] Y. Mishima and M. Takei, "Non-mass-separated ion shower doping of polycrystalline silicon," J. Appl. Phys., 75 (10, pt. 1), pp. 4933-4938, 1994.

[2.27] G. Kawachi, T. Aoyama, A. Mimura, and N. Konishi, "Application of ion doping and excimer laser annealing to fabrication of low-temperature polycrystalline Si thin-film transistors," Jpn. J. Appl. Phys., 33 (4A), pp. 2092-2099, 1994.

[2.28] A. Yoshinouchi, A. Oda, Y. Murata, and T. Morita, "Formation of sources/drains using self-activation technique on polysilicon thin film transistors," Jpn. J. Appl. Phys., 33 (9A), pp. 4833-4836, 1994.

[2.29] N.C.C. Lu, "Advanced cell structures for dynamic RAMs," IEEE Circ. and Dev. Mag., 5 (1), pp. 27-36, 1989.

[2.30] G. Fuse, H. Ogawa, K. Tamura, Y. Naito, and H. Iwasaki, "Indirect trench sidewall doping by implantation of reflected ions," Appl. Phys. Lett., 54 (16), pp. 1534-1536, 1989.

[2.31] R. Kakoschke, R.E. Kaim, P.F.H.M. van der Meulen, and J.F.M. Westendorp, "Trench sidewall implantation with a parallel scanned ion beam," IEEE Trans. Elec. Dev., 37 (4), pp. 1052-1056, 1990.

[2.32] B. Mizuno, I. Nakayama, N. Aoi, M. Kubota, and T. Komeda, "New doping method for sub half micron trench sidewalls by using an electron cyclotron resonance plasma," Appl. Phys. Lett., 53 (21), pp. 2059-2061, 1988.

[2.33] X.Y. Qian, N.W. Cheung, M.A. Lieberman, and R. Brennan, "Conformal implantation for trench doping with plasma immersion ion implantation," Nucl. Inst. & Meth., B55 (1-4), pp. 898-901, 1988.

[2.34] C. Yu, M.S. Thesis, University of California at Berkeley, 1993.

[2.35] C. Yu and N.W. Cheung, "Trench doping conformality by plasma immersion ion implantation (PIII)," IEEE Elec. Dev. Lett., 15 (6), pp. 196-198, 1994.

[2.36] C. Yu, Z. Huang, and N.W. Cheung, "Conformal doping of high aspect ratio trenches by plasma immersion ion implantation (PIII)," in *Ion Impl. Tech. 92*, Amsterdam: North-Holland, pp. 369-372, 1993.

[2.37] S.P. Voinigescu, C.A.T. Salama, J.-P. Noel, and T.I. Kamins, "Optimized Ge channel profiles for VLSI compatible Si/SiGe p-MOSFET's," in *Int. Elec. Dev. Meet. 40*, New York: IEEE, pp. 369-372, 1994.

[2.38] J.O. Borland and R. Koelsch, "MeV implantation technology: next-generation manufacturing with current-generation equipment," Solid State Technol., 36 (12) pp. 28-29, 1993.

[2.39] P. Singer, "Trends in ion implantation," Semicond. Int., 18 (9), pp. 58-64, 1995.

[2.40] J.-P. Colinge, *Silicon-on-insulator technology: Materials to VLSI*, Boston: Kluwer Academic Press, 1991.

[2.41] J.B. Liu, S.S.K. Iyer, J. Min, P. Chu, R. Gronsky, C. Hu and N.W. Cheung, "Formation of buried oxide in silicon using separation by plasma implantation of oxygen," Appl. Phys. Lett., 67 (16), pp. 2361-2363, 1995.

[2.42] J.B. Liu, Ph.D. dissertation, University of California at Berkeley, 1995.

[2.43] J.B. Liu, S.S.K. Iyer, J. Min, P. Chu, R. Gronsky, C. Hu, and N.W. Cheung, "Formation of silicon on insulator (SOI) with separation by plasma implantation of oxygen (SPIMOX)," in *Beam-Solid Interactions for Materials Synthesis and Characterization*, Pittsburgh: Materials Research Society, pp. 117-122, 1995.

[2.44] J.B. Liu, S.S.K. Iyer, J. Min, P.K. Chu, R. Gronsky, C. Hu, and N.W. Cheung, "Competitive oxidation during buried oxide formation using separation by plasma implantation of oxygen (SPIMOX), in *Film Synthesis and Growth Using Energetic Beams*, ed. by H. Atwater, Pittsburgh: Mater. Res. Soc, pp. 385-391, 1995.

3 Plasma and PIII Diagnostics

3.1 Introduction

The U.C. Berkeley PIII apparatus is shown in Figure 3-1. Microwave power from a 2.45 GHz, 1500 W microwave power supply is routed by waveguides and is fed through a TE 10 rectangular to TM 01 circular mode converter into the electron cyclotron resonance (ECR) source chamber through a quartz window. Process gas enters near the quartz microwave input window, and the gaseous by-products leave the chamber through turbomolecular and mechanical pump systems. The chamber has a base pressure of 10^{-7} Torr before processing. Typical process gas pressures are in the 0.2 to 5 mTorr range. The plasma is generated inside an 875 Gauss magnetic field in a mirror configuration created in the source chamber by current coils with 100 - 300 Amperes DC current [3.1, 3.2]. The plasma density is varied by altering the microwave power, input gas pressure, or mag-

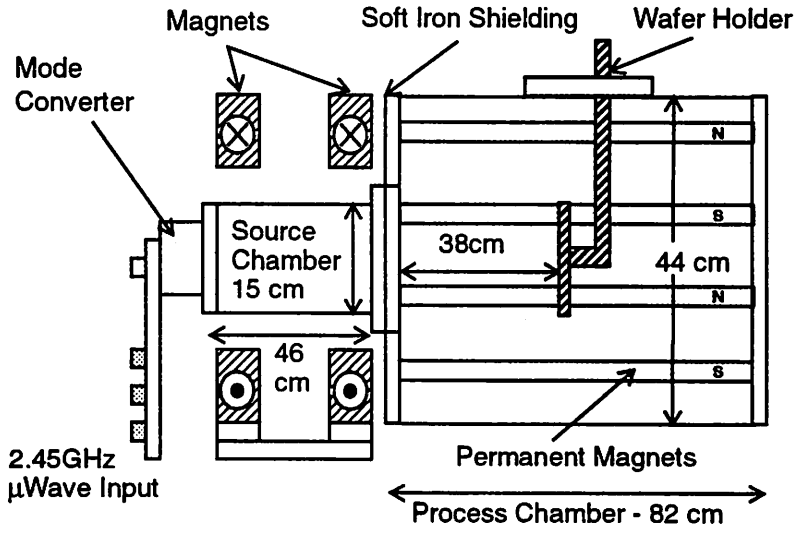

Figure 3-1. Schematic of U.C. Berkeley PIII system

netic field configuration. The plasma flows into a 44 cm diameter processing chamber surrounded by lines of permanent magnets. These magnets effect a magnetic bucket inside the chamber to improve the uniformity of the spreading plasma as it enters the processing chamber from the smaller 15 cm diameter source chamber. Uniformity of the ion density of an Ar plasma has been measured by Langmuir probe measurements as ±2% across 8 inches [3.3]. Single or multiple-wafer holders up to 10 inches in diameter can be located 20-50 cm away from the source chamber in the 82 cm long process chamber, so the system is compatible with both single wafer cluster tools and large-area implantation.

3.2 BF_3 Plasma Diagnostics

3.2.1 Mass spectrometry of neutral and ionized species

The plasma used for boron doping is generated from BF_3 source gas. The energy of some of the dissociation and ionization processes in the BF_3 system are listed in Table 3-1. The lowest energy process is dissociation of BF_3 into BF_2 + F. Mass spectrometry

Dissociation Reaction	Energy (eV)	Ref.	Ionization Reaction	Energy (eV)	Ref.
$BF_3 \rightarrow BF_2+F$	6.48	[3.4]	$B \rightarrow B^+$	8-8.3	[3.6]
$BF_3 \rightarrow BF+F_2$	10.58	[3.4]	$BF \rightarrow BF^+$	11-12	[3.6, 3.7]
$BF_3 \rightarrow BF_2^*+F$	11.44	[3.4]	$BF_2 \rightarrow BF_2^+$	8-9	[3.6, 3.7]
$BF_3 \rightarrow BF+F+F$	12.22	[3.4]	$BF_3 \rightarrow BF_2^++F$	15.9-16	[3.6]
$BF_3 \rightarrow BF_2^{**}+F$	13.18	[3.4]	$BF_3 \rightarrow BF_3^+$	15.25-16	[3.5, 3.6, 3.7]
$BF_3 \rightarrow BF^*+F_2$	14.19	[3.4]	$F \rightarrow F^+$	16.92	[3.6]
$BF_3 \rightarrow BF^*+F+F$	15.83	[3.4]	$F_2 \rightarrow F_2^+$	15.7	[3.6]
			$F_2 \rightarrow F+F^+$	19.01	[3.6]

Table 3-1. Energy of dissociation and ionization processes in BF_3 plasma

in Figure 3-2 shows that BF_2 is the most prevalent neutral species in the plasma. Data taken by a high mass-resolution CMA/quadrupole mass spectrometer measures the BF_2 fraction at 78% (Figure 3-2a), and data from a Ferran micropole mass spectrometer measures 97% BF_2 (Figure 3-2b). Both micropoles employ ionizers to ionize the neutral beam for analysis. The measurements are taken for a 900 W, 0.8 mTorr plasma.

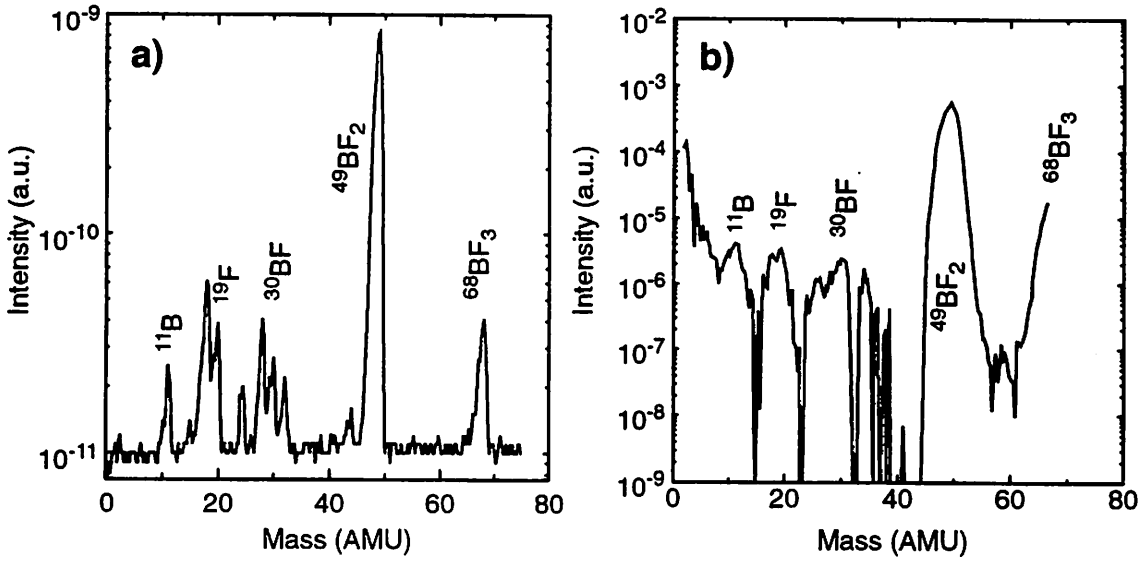

Figure 3-2. Mass spectra of neutrals in BF_3 plasma

a) CMA/quadrupole and b) Ferran micropole measurements of neutrals in 0.8 mTorr, 900W BF_3 plasma. Extra peaks seen at mass 24, 28, 32, 44 due to a few percent N, O, H gaseous contamination.

In the CMA/quadrupole, the ionizer may be turned off to measure ionized species in the plasma. A mass spectrum of ionized boron is shown in Figure 3-3. The wide peak reflects the presence of two boron isotopes. Dividing the peak among the two masses shows the B^+ is 23% $^{10}B^+$ and 77% $^{11}B^+$. This is close to the naturally occurring fraction,

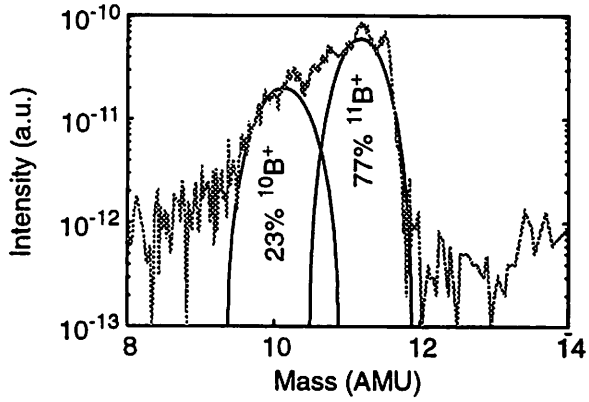

Figure 3-3. Mass spectrum of boron ions in BF_3 plasma

CMA/quadrupole measurement in 0.8 mTorr, 900 W BF_3 plasma.

19% ^{10}B. Unfortunately, this mass spectrometer cannot be used to measure the ionized species fractions at normal operating conditions (gas pressure above 1 mTorr). There is no differential pumping, so at high gas pressure, the ion signal diminishes. Additionally, the

system has a very long, 1 meter column between the ion entrance port in the plasma chamber and the channeltron detector. Wall losses and collisional losses of the ions are very high along this path. The ionized species signal is already much lower than the neutral signal, and these losses make the measured ion species mass spectrum unreliable at typical BF_3 plasma operating conditions.

3.2.2 Langmuir probe measurements of ion density

The BF_3 plasma conditions are dependent on the input power, gas pressure, current in the magnet coils, and arrangement of the permanent magnets on the process chamber. The following observations have been made by Langmuir probe measurements in the BF_3 plasma, and are used to choose a plasma condition for implantation. The Langmuir probes used to measure the BF_3 plasma are etch-resistant cylindrical probes made from Pt wire. The ion density can be calculated from the current-voltage (IV) characteristic of the probe (Figure 3-4) in the region where the probe voltage is negative and ions are collected [3.8]. The ion density can be found by plotting the square of the ion current versus the

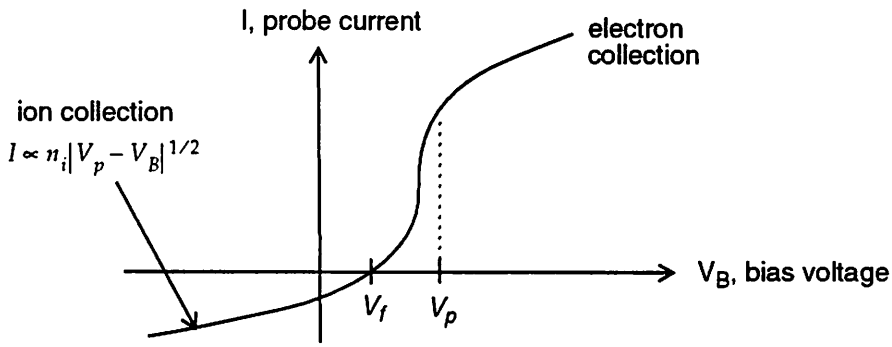

Figure 3-4. Langmuir probe current-voltage characteristics
After Ref. [3.8].

applied probe bias. In the region where the ion current is saturated, the slope of this graph will be

$$\frac{dI_{sat}^2}{dV} = 8q^3n^2a^2d^2/m \qquad (3\text{-}1)$$

where V is the applied bias, q is the electronic charge, n is the ion density, a is the probe radius, d is the probe length, and m is the ion mass.

Langmuir probe measurements show that the ion density increases with microwave power (Figure 3-5a). The BF_3 plasma ion density peaks at a gas pressure between 1-2 mTorr. Below this, the density is limited by gas supply. Above this, the density falls rapidly due to plasma collisionality and ambipolar ion diffusion to chamber walls (Figure 3-5b). For ion density above $10^{10}cm^{-3}$ at 500W and 125 A magnet current, operation between 0.6 mTorr and 8 mTorr is necessary. Plasma uniformity is measured by moving the Lang-

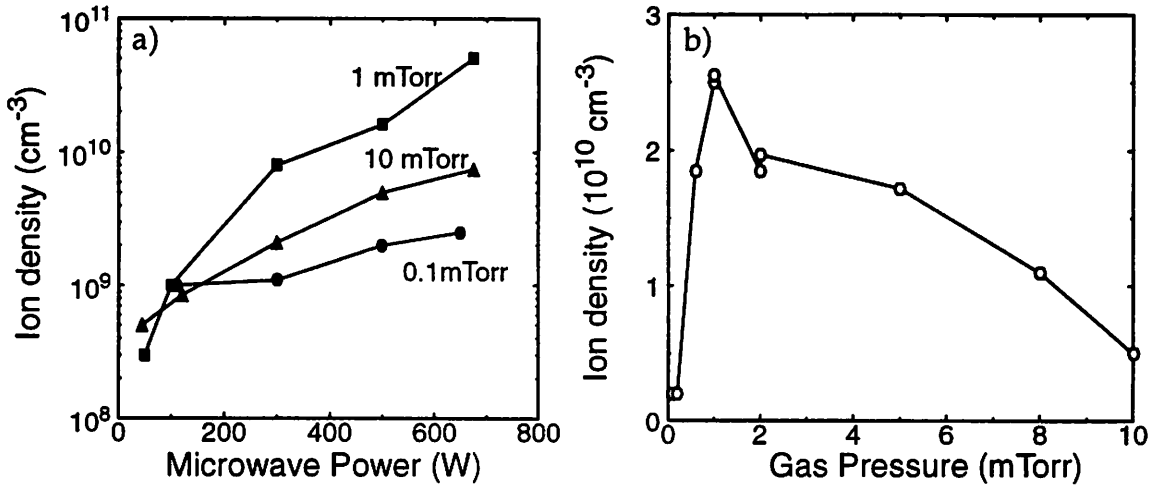

Figure 3-5. BF_3 plasma density in PIII reactor

BF_3 plasmas generated in ECR source with 125 A magnet current, measured by Langmuir probe. a) shows variation in density with input power, and b) shows the peak ion density at 1 mTorr, with 500 W input power. From Ref. [3.1].

muir probe across the chamber. Uniformity has been measured using Ar gas, showing the uniformity percentage of the plasma density across a 200 mm diameter at 1 mTorr improves from 15% to 2.5% with the addition of the permanent magnets on the process chamber [3.9]. The uniformity improves for lower gas pressures, higher input power, and by moving further away from the source chamber [3.10]. Uniformity can also be varied by changing the magnet coil current. The best BF_3 PIII implant uniformity in this chamber, 3% across an 8 inch wafer, is achieved at 220 A [3.11].

3.2.3 Optical Emission Spectroscopy of ion species

Optical emission spectroscopy is a non-invasive technique for identifying ion and neutral species present in the plasma. The apparatus used to measure the light intensities versus frequency is shown in Figure 3-6. As the wavelength controller steps through the

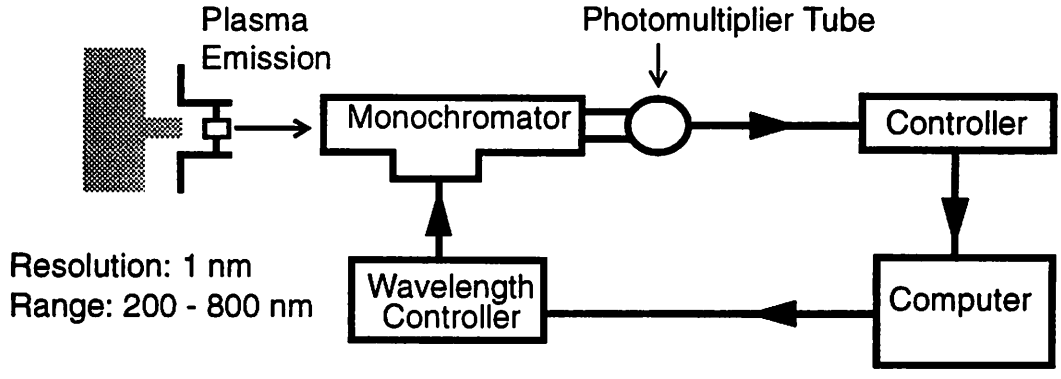

Figure 3-6. Optical emission spectroscopy apparatus

optical spectrum, intensity peaks are seen. Their wavelengths correspond to the energy emitted when an excited ion or neutral falls from a high energy state, usually caused by energy gain during collisions with electrons in the plasma, to a lower one. Since the transition energies depend uniquely on the energy levels of individual atoms and ions, the spectrum of light emitted can be used to identify to the species that caused it. As a typical plasma from the ECR source will have neutral density orders of magnitude higher than the ion density, the neutral peaks usually have higher intensities.

Calibration of the monochromator is the limiting factor in correct measurement of peak locations: the wavelength step is 0.1 nm, but the actual peak positions may be off by more than 10 nm. Therefore, in this work a small leak of Ar tracer gas (~100 μTorr) is fed into the plasma so the wavelength position and scale can be calibrated by matching a set of four well known Ar peaks at 738.4, 750.4, 751.47, and 763.5 nm. The intensity peaks from BF_3 can then be identified and studied. Unfortunately, BF_3 plasma optical emission spectra are difficult to analyze due to a high intensity background peak from 300-520 nm (Figure 3-7). Some of these transitions have been identified as BF and BF^+ species, but most are due to BF_2 ions and neutrals. The large number of possible vibrational and rotational modes of the BF_2 molecular species leads to this broadband radiation. The individual peaks are listed in Appendix A.

The best use of OES is actinometry, where the ratio of intensity of a characteristic peak from the plasma (I_x) to a peak from an inert tracer gas (I_t) is used to measure the variation in the density of species x in the plasma. This technique can only be used if the excitation cross section of species x has the same functional form as the species t. The commonly used F peak at 704 nm that is known to have a cross section similar to Ar is too small to be observed in this work. What can be seen are changes in the intensity of the

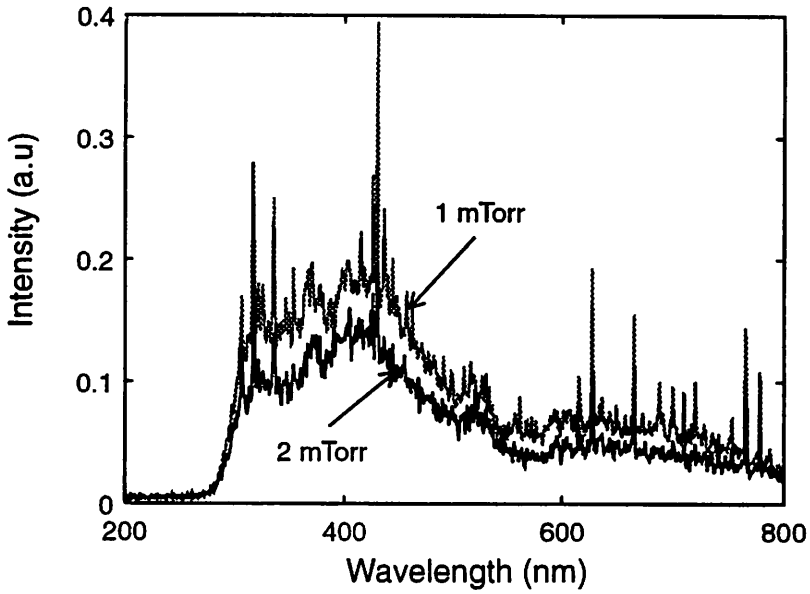

Figure 3-7. Optical emission spectroscopy of BF_3 plasma

OES spectra for 500 W BF_3 plasmas at 1 mTorr and 2 mTorr. Higher radiation intensity at 1 mTorr indicates higher dissociation and/or ionization at that condition.

background and individual peaks with power and pressure. Figure 3-7 shows the decrease in signal intensity from both the molecular species radiation band and from individual peaks when the pressure is raised from 1 mTorr to 2 mTorr. This indicates that either fewer excited neutrals and ions are being formed at the higher pressure, or that their lifetime is lower as the plasma becomes more collisional. Both possibilities affect the species available during PIII implantation. In Figure 3-8, a few trends are shown for identified peaks in the BF_3 plasma. All of the peaks decrease in magnitude between 1 mTorr and 2 mTorr. Additionally, these BF, F^+ and B^+ peaks are seen to peak at 700 W for both pressures, and the largest to smallest peak magnitudes are seen for BF, B^+ and F^+, in that order, for both pressures. These points cannot be used for actinometry, since the cross-sections are not known. However, the relative intensities can be easily measured to check the reproducibility and stability of a plasma condition.

3.3 PIII Diagnostics

The PIII implant is controlled by setting the plasma condition, which controls the ion density and ion supply, and by setting the external parameters of implant bias, frequency, and implant time. The dose incorporated in the substrate may be smaller than expected from the aforementioned parameters if the exposed surface is eroded during

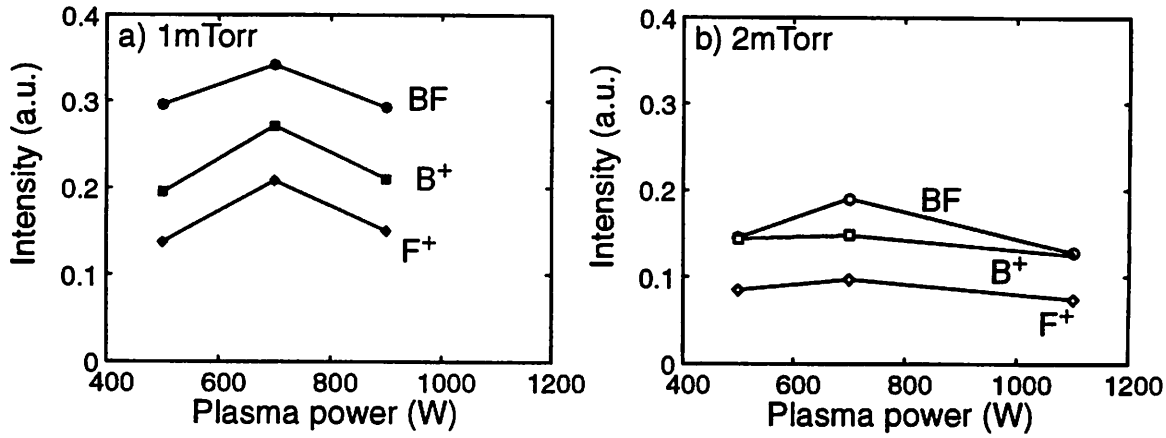

Figure 3-8. BF, B^+ and F^+ OES peak variation in BF_3 plasma

Variation in intensity of BF, B^+ and F^+ peaks in BF_3 plasma measured by OES when power and pressure changed. BF peak intensity measured at 325.5 nm, B^+ at 345.1 nm, F^+ at 485.9 nm.

implantation. It may be difficult to predict the surface erosion for implantation runs as the etching rate of the substrate and surface films are functions of all the other parameters: the plasma conditions, source gas, implantation energy and frequency. During plasma doping, substrates are subject to corrosive plasma etching, reactive ion etching and sputter etching by ions and radicals (Figure 3-9). Fluorine-containing gases have very high reac-

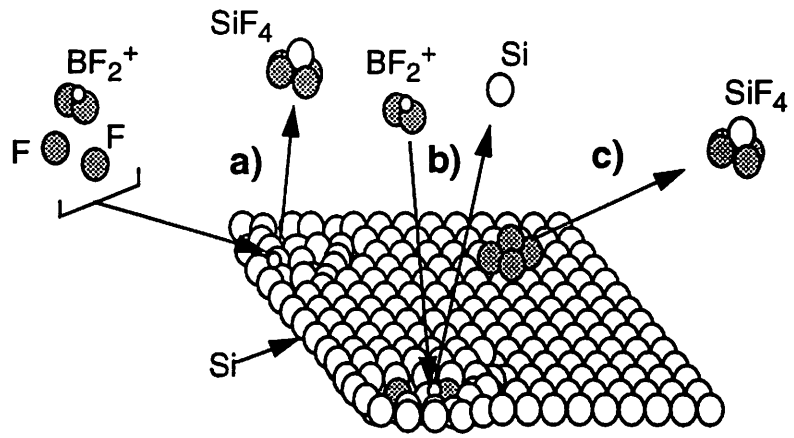

Figure 3-9. Etching mechanisms in PIII

a) Chemical sputtering, b) physical sputtering, and c) chemical etching.

tive ion etching rates of Si [3.8]. Switching to a non-corrosive gas source like B_2H_6 does not preclude Si etching, as carrier gases like H_2 have exhibited Si etch rates as high as BF_3 during PIII [3.12] and sputtering can be caused by any gas at low energy. The following

experiments study sputter etching of oxide and poly-Si during Ar PIII, and chemical sputter etching during BF_3 PIII of oxides, Si and $CoSi_2$.

3.3.1 Ar PIII etching rates

Oxide and polysilicon etching during Ar PIII is investigated to see PIII ion beam sputtering rate in an unreactive plasma, in which the plasma alone will not cause etching. The following experiments are run with a 1 mTorr, 900 W Ar plasma. PIII is performed for 10 min at 4 kV with repetition rates from 100 Hz to 25 kHz. Control samples are exposed to the plasma without pulsing. One sample set is implanted with a 30 s DC implant pulse to see the steady-state etching rate.

A Nanospec spectrophotometer is used to measure the oxide and polysilicon layer thicknesses after PIII exposure, which are compared to the thicknesses in regions covered by a clip during the processing. The data are plotted in Figure 3-10. The figure shows that there is no difference between the polysilicon and oxide etch rates, as is expected for non-reactive ion sputter etching of similar materials. The etch rate is very small for the plasma

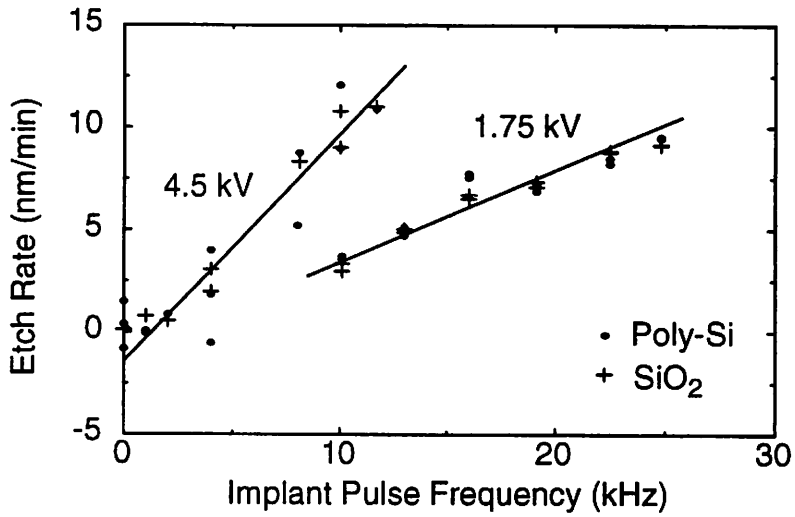

Figure 3-10. Etching rates of poly-Si and SiO_2 during Ar PIII

Etching rates during Ar PIII are the same for poly-Si and SiO_2. Etching rate increases with implant energy. 900W, 1 mTorr Ar plasma.

alone and at low frequency. The etch rate increases linearly to almost 10 nm/min for 25 kHz pulsing. The two lines show the etch rate increasing as implant energy is raised from 1.75 to 4.5 kV, as expected since the peak sputter yield for Si with Ar^+ occurs at energy

higher than 5 kV [3.13]. The etch rate during DC implantation is much higher, 52.4 nm/min of polysilicon and 38 nm/min of oxide. To keep substrate material loss below 2 nm during non-reactive 4 kV PIII, maximum implant times are 30 sec at 10 kHz, 13 sec at 25 kHz and 2 sec for DC.

3.3.2 BF_3 etching rates

F ions and radicals that are formed in the BF_3 plasma are efficient Si and SiO_2 etching agents, since the chemically active F will attach to dangling Si surface bonds and create volatile molecules of SiF_4 and SiF_2, which can easily desorb. The combination of chemical etching due to the F-containing BF_3 plasma and sputter etching due to accelerated, implanting ions can be expected to lead to higher etch rates than sputter etching alone. These etch rates must be controlled for BF_3 PIII, so that loss of implanted dose due to surface erosion is kept small. This can be done by using low etch-rate conditions and by performing the implantation as quickly as possible. It is also possible to get deposition from the plasma on the substrate. Often when working at low power and at high pressure, a brownish tinge is detected after processing, indicating deposition. If PIII is run under a depositing condition, much of the dopant will be located in a surface polymer layer. If this layer is thick, much of the implanted dopant will be contained in this layer rather than in the substrate. The dopant incorporated during annealing then depends upon how well the surface is cleaned before annealing. Therefore, it is important that deposition be avoided for dose reproducibility. Even if high etch-rate chemical sputtering is expected during the implantation pulse, a visible deposited layer can build up between pulses since the PIII duty factor is typically less than 2%. The etching rates must be monitored to make sure implantation takes place in a slowly etching plasma.

3.3.2.1 Oxide

Figure 3-11 shows that the chemical oxide etching rate due to the plasma alone (no pulsing) is controlled by the plasma power and gas pressure. The etch rate increases linearly with microwave power and decreases with pressure. As plasma ion density falls slowly with increasing pressure, operating at a pressure above 1 mTorr and at moderate power is recommended in this system to minimize etching. If the pressure approaches 5 mTorr, the plasma sheath may become collisional.

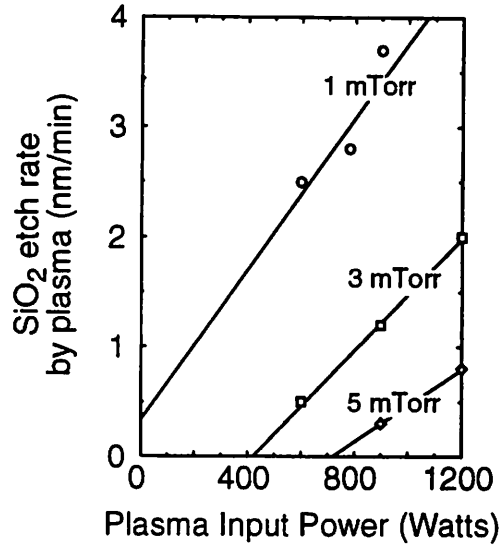

Figure 3-11. Etching rate of SiO_2 in BF_3 plasma

SiO_2 samples etched in BF_3 plasma with no pulsing for 30 min. show the etch rate decreasing when power is decreased or gas pressure is increased.

In Figure 3-12, the variation of etch rates with PIII implant conditions are measured at one of the highest plasma etching conditions in Figure 3-11, using a 900W, 1.5 mTorr plasma. The etch rate for plasma etching alone (no pulsing) at this condition is about 3 nm/min, in good agreement with Figure 3-11. During pulsing, chemical sputtering mechanisms are seen to magnify the oxide etching rate. The oxide etch rate increases

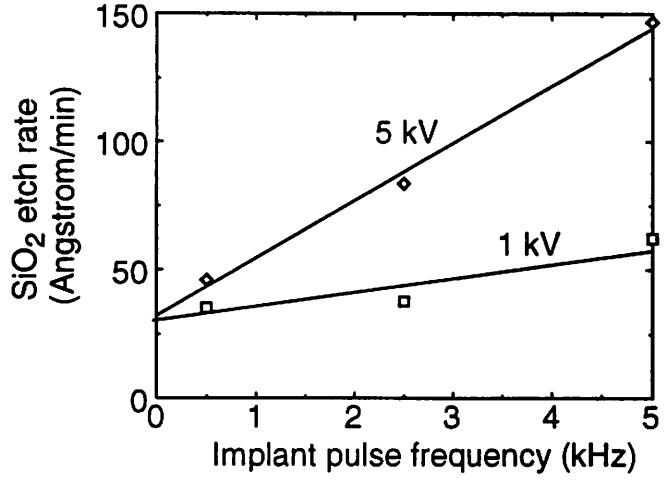

Figure 3-12. Etching rate of SiO_2 during BF_3 PIII

SiO_2 samples etched during BF_3 PIII for 10 min. at 900 W, 1.5 mTorr pressure show etch rate increasing with BF_3 PIII substrate bias and frequency.

with both implant energy and frequency, as seen for Ar PIII. With Ar PIII, the plasma etch rate is zero and the sputter etch rate of 4 kV, 5 kHz implanting ions is 5 nm/min. In BF_3 PIII the implanting ions increase the etch rate from 3 nm/min for plasma only to 15 nm/min for 5kV, 5kHz PIII. To avoid more than 2 nm of SiO_2 loss from a poly-gate spacer oxide during implant, a 5kV, 5kHz BF_3 implant step must be performed in less than 8 seconds.

Another fact which recommends high frequency operation is the observed increase of plasma etch rate with increasing exposure time. This is observed in both SiF_4

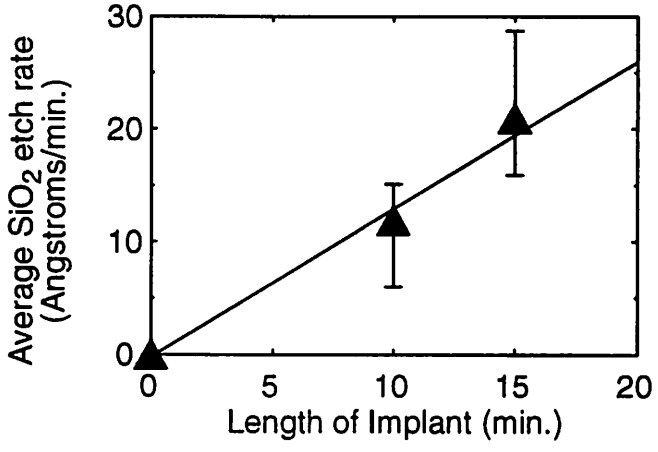

Figure 3-13. Time-dependence of oxide etch rate during SiF_4 PIII
Samples etched during SiF_4 PIII in 300W, 0.2 mTorr plasma. PIII bias is 4-6 kV and pulse frequency is 1-2 kHz.

(Figure 3-13) and BF_3 plasmas [3.9] due to increasing substrate temperature aiding surface diffusion and chemical desorption of etch products from the wafer surface. The wafer temperature can exceed 150°C after a few minutes of PIII processing, if wafer cooling is not employed.

3.3.2.2 Silicon

Since the etching rate has a significant effect on the shape and incorporated dose of a PIII profile, an experiment is performed to measure the Si etch rate during PIII. Because oxide charging may cause trenching around oxide patterns, here a pattern of Al lines is formed on a Si test wafer. After etching, the Al is selectively removed and the Si etching measured by a profilometer. The plasma conditions during this test are 900 W

input power and 1.5 mTorr BF_3 gas pressure. Again, this is the highest etch rate condition observed in ECR PIII system, as seen in Figure 3-11. The results in Figure 3-14 show that the base etch rate of Si due to plasma etching alone is about 2.5 nm/min at this worst-case condition. The etch rate is highly dependent on frequency, showing the importance of

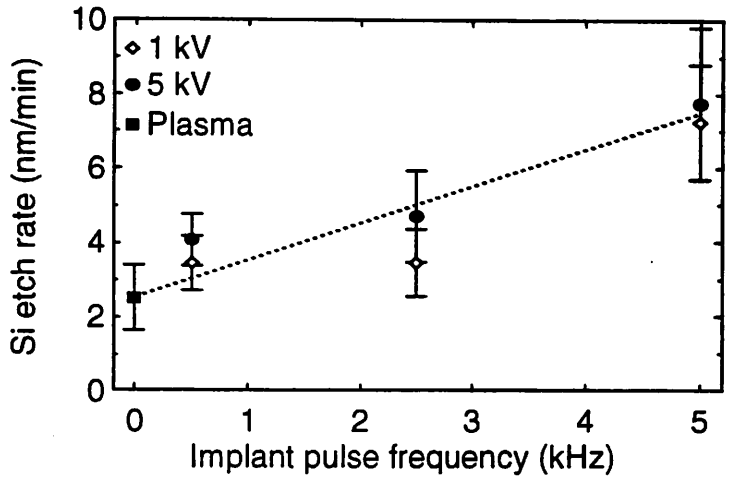

Figure 3-14. Etching rate of Si during BF_3 PIII

Si samples etched during BF_3 PIII for 10 min. at 900W, 1.5 mTorr pressure show etch rate increasing with BF_3 PIII frequency. Effect of energy cannot be resolved.

chemical sputtering during the implant pulses. The etch rate approximately doubles when increasing the pulse frequency from 500 Hz to 5 kHz. The difference in etch rates due to implant energy is within the error of the profilometer measurement. Figure 3-15 shows the selectivity of SiO_2/Si etching during BF_3 PIII. The Si and SiO_2 etch rates are almost the same at low energy and frequency, but oxide etches almost twice as fast as Si in the 5kV, 5kHz case.

3.3.2.3 $CoSi_2$

Fast $CoSi_2$ etching has been reported with Cl etchants, as Co forms a very volatile gaseous compound with Cl, $CoCl_3$ [3.14]. Co may form a gaseous compound with fluorine, CoF_3, but this compound is not as volatile as $CoCl_3$. $CoCl_3$ is reported to be volatile in the presence of F_2 gas only at temperatures above 600°C [3.15]. Reported reactive-ion etching rates of $CoSi_2$ in F-containing plasmas are quite low. However, it has also been observed that Si/Co ratios of $CoSi_2$ films increase to 3.3-3.4 when etched in CF_4 and 2.8-2.9 when etched in F-contaminated Ar [3.14]. When F is present, Co appears easier to

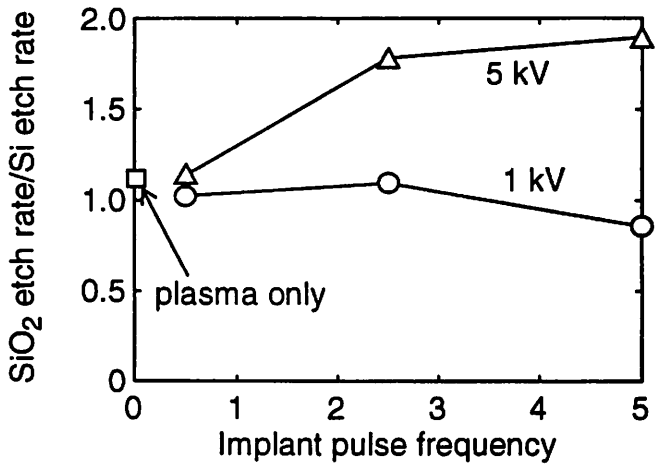

Figure 3-15. BF_3 PIII etch selectivity

Data from Figure 3-12 and Figure 3-14 are used to find selectivity of SiO_2 over Si during BF_3 PIII at 900W, 1.5 mTorr. The etch is more selective for higher energy.

remove than Si from the surface layer, perhaps due to the ion bombardment causing CoF_3 formation or aiding CoF_3 desorption [3.8]. Significant Co loss is also possible due to sputtering during PIII. The Co loss during BF_3 implantation is monitored since the films used for shallow junction processing are thin.

The silicides used to produce the following graphs are 30 nm thick, epitaxially-grown, single crystal $CoSi_2$ films grown by single-step annealing of a Co-Ti bilayer (Chapter 7). Blanket-deposited and patterned wafers are exposed to a BF_3 plasma for 7 minutes and then implanted by BF_3 PIII with accelerating voltages of 3.5 kV and 14 kV for 10 minutes. A grounded control sample is exposed to the plasma for 17 minutes for comparison. The amount of $CoSi_2$ etching is measured by measuring the Co peak signal from Rutherford backscattering (RBS). The etch rates in Figure 3-16 are calculated by converting the Co signal width to a $CoSi_2$ layer thickness,. assuming no stoichiometry change during implantation, and are therefore approximate. The figure shows that plasma exposure alone has little effect on the silicide: within experimental error, no Co is removed. Samples that are PIII-implanted in the BF_3 plasma, however, are severely etched. The 3.5 kV and 14 kV implanted samples lose 69% and 83% of the original Co atoms, respectively. The data is comparable to RIE etching rates reported for $CoSi_2$ etched by CF_4 and CF_4+O_2 at 500 V RF bias: 2.2 and 2.0 nm/min [3.14]. The fluorine RIE etching rates are comparable to the pure sputtering rate reported for $CoSi_2$ in Ar: 1.1 nm/min [3.14]. The Ar sputter etch rate reported in Figure 3-10 si about 4 nm/min for 6.7 kHz, 4.5 kV PIII. As the sputter yield is

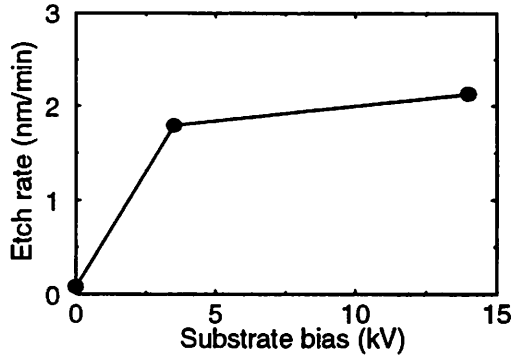

Figure 3-16. Etch rate of $CoSi_2$ during BF_3 PIII

Data from samples exposed to BF_3 plasma for 17 minutes. PIII pulsing lasted 10 min. BF_3 implantation at 900 W, 1.6 mTorr, 6.7 kHz.

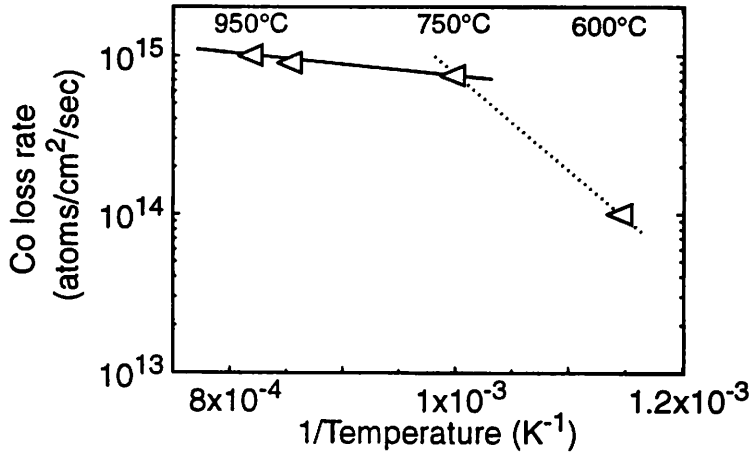

Figure 3-17. Co loss from BF_3 PIII-implanted $CoSi_2$ during annealing

$CoSi_2$ films have smaller Co content after BF_3 PIII and rapid thermal annealing in forming gas. Activation energy of high temperature (750°C-950°C) points is 0.15 ± 0.03 eV.

expected to peak at incident ion energy near 10 kV, it is possible the maximum etch rate lies between the 3.5 and 14 kV data points reported.

Although in this work the $CoSi_2$ removal rate is consistent with sputtering, volatilization of the Co is observed during rapid thermal annealing, as shown in Figure 3-17. This graph shows the loss rate of Co atoms from the silicide film per second of rapid thermal annealing. The drop in the Co areal density is monitored by RBS. The loss rate is highest for 750°C and higher, and the activation energy in this regime is calculated from the Arrhenius plot as 0.15 eV. This low activation energy may indicate a CoF_x compound is formed which is quite volatile above 750°C, perhaps CoF_3. This result indicates that F-con-

taining etches and implants should be kept to a minimum in the presence of $CoSi_2$. Therefore, for conventional implantation of $CoSi_2$, the work in following chapters uses a $^{11}B^+$ implant species.

3.3.3 Surface Roughening during PIII

Atomic force microscopy (AFM) is used to look at the surface roughness after PIII implantation and annealing steps of all materials. The AFM root-mean-square (RMS) factor is the chosen measure of average surface roughness. If the Si surface is rough, the contact material during subsequent metallization steps may form local spike features, creating shorts, leakage, or premature junction breakdown. For both Si and silicide surfaces, implanted dopants may go deeper in one area than another if the surface is rough. Figure 3-18 shows the effects of plasma exposure and PIII on Si and SiO_2 surface roughness. Si exposed to the BF_3 plasma and Si etched during PIII implantation have roughness larger than unprocessed Si. After implantation, the roughness is greater than that of unprocessed Si by a factor of 4-5, but still on the order of a few monolayers of Si. Rapid thermal annealing is also shown to increase the roughness slightly. The proximity of the roughness values for PIII and plasma etched samples suggests that surface etching during

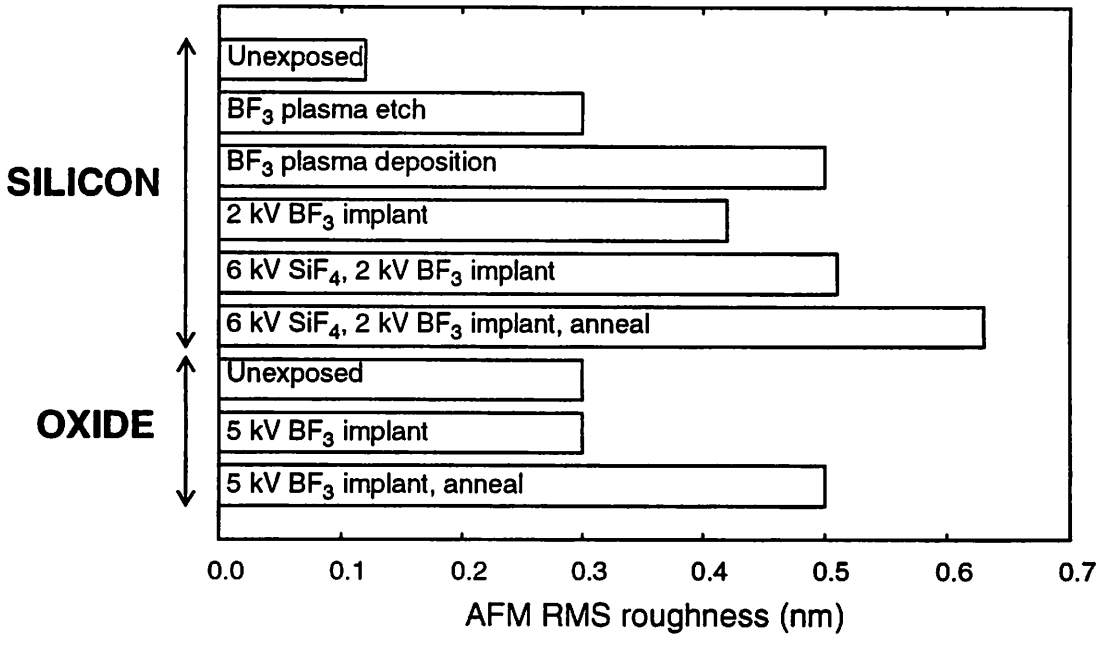

Figure 3-18. Surface roughness of Si and SiO_2 after PIII processing

Samples exposed to plasma or implanted for 30 min. Rapid thermal annealing performed at 1060°C, for 10 s in N_2. The AFM sampling window is 5μm by 5μm.

implantation is quite uniform. For SiO_2, the RMS roughness before and after implantation is comparable. Oxide roughness increases during RTA annealing as well.

AFM of $CoSi_2$ raises different concerns. The initial roughness of $CoSi_2$ is higher than Si or SiO_2, at 2.7 nm. Plasma exposure and 14 kV PIII do not affect the surface greatly, as shown in Figure 3-19. The 3.5 kV PIII sample, however, shows a great increase in the surface roughness. This suggests non-uniform etching of the silicide film, perhaps due to micro-patches of remaining surface contamination preventing local etching, or due to preferential etching of facets or grains of the silicide. Either of these would explain why etching is more uniform for the 14kV PIII, where higher energy bombardment is expected to be more successful in removing surface oxide and material of varying crystalline orientation. After annealing, the roughness of the 3.5 kV and 14 kV implanted samples is reduced substantially.

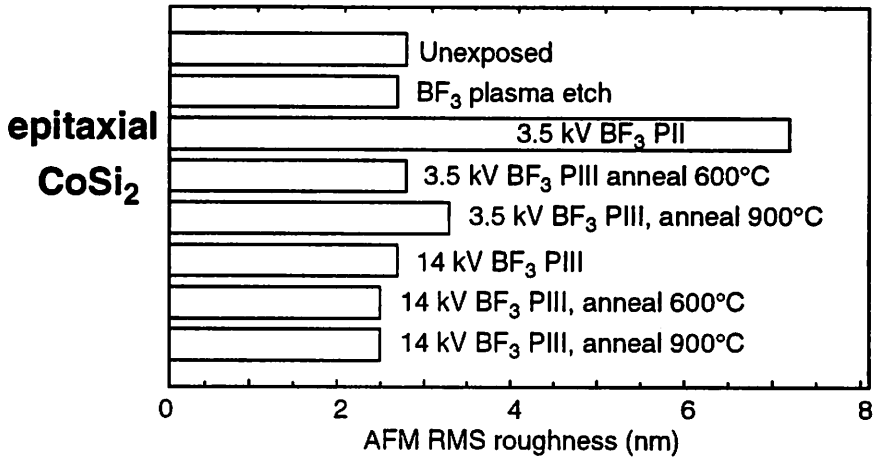

Figure 3-19. Surface roughness of epitaxial $CoSi_2$ after PIII processing

3.3.4 Contamination

For PIII to be considered as a replacement for conventional implantation for high-dose ULSI steps, it has to be proven to be a clean technique. It cannot introduce heavy metal or other impurities into the Si substrate that might act as deep level centers. Impurities that act as carrier traps have energy levels around the midgap of the Si energy band and are efficient at aiding the generation and recombination of holes and electrons. In the source/drain depletion regions they can make the device leaky. In the channel, they reduce the carrier lifetimes.

The impurities Mg, Al, Cr, Fe and Cu are studied by secondary mass ion spectroscopy (SIMS). The graph in Figure 3-20a shows impurities in the wafer after a 3.5 kV, 14 min. BF_3 PIII implant. Figure 3-20b is a control sample from the same wafer. The SIMS secondary ion data is collected from the center 30 μm of a 300 μm diameter rastered crater sputtered by a 5.5 keV O_2^+ primary ion beam. The concentrations are expected to be accurate within a factor of two and the depth scale within 7%. The penetration depth of the primary O_2^+ beam for this analysis is about 8.8 nm (see Appendix C), so the high surface concentrations in the top 10 nm of the material can be ignored. The results show higher concentrations (3-4 orders of magnitude above background) and deeper penetration of the impurities for the PIII sample. The contours of Al and Mg follow the curvature of the implanted B and F profiles, indicating that these light mass impurities are likely sputtered off the wafer holder or walls, ionized in the plasma, and implanted. Al and Mg come from the Al used to construct the chamber walls and wafer holder. The Fe and Cu profiles show a more Gaussian shape, indicating diffusion of these species occurred during the BF_3 PIII where the wafer temperature can approach 100-200°C. The Fe diffusion depth into the substrate is 78 nm from Figure 3-20a. For Fe to diffuse this deep ($x = \sqrt{Dt}$) during the 14 min. implantation step, the average diffusivity (D) must have been at least 7×10^{-14} cm^2/s. Using the reported temperature dependence of Fe diffusivity in Si [3.16], this indicates the substrate temperature was at least 114°C. The observed Cu diffusion would indicate a lower temperature. Fe and Cu come from the stainless steel clips and screws used to hold the wafer pieces onto the holder. The Fe and Cu may have been sputtered off the clips, redeposited on the wafer surface, and diffused in from there. This may explain why the Fe and Cu concentrations are higher than Al and Mg. For IC processing, this Cu contamination must be eliminated.

Fortunately, none of these contamination sources are intrinsic to the PIII process, and can be easily eliminated in a commercial machine. The inside walls and wafer holder can be coated with a number of materials which will not contaminate Si: SiO_2, BN, Si_3N_4, poly-Si coatings or a quartz liner can be used. The coatings can be deposited by plasma-enhanced chemical vapor deposition (PECVD) and plasma-cleaned in the PIII chamber itself, daily if necessary to keep contamination to a minimum.

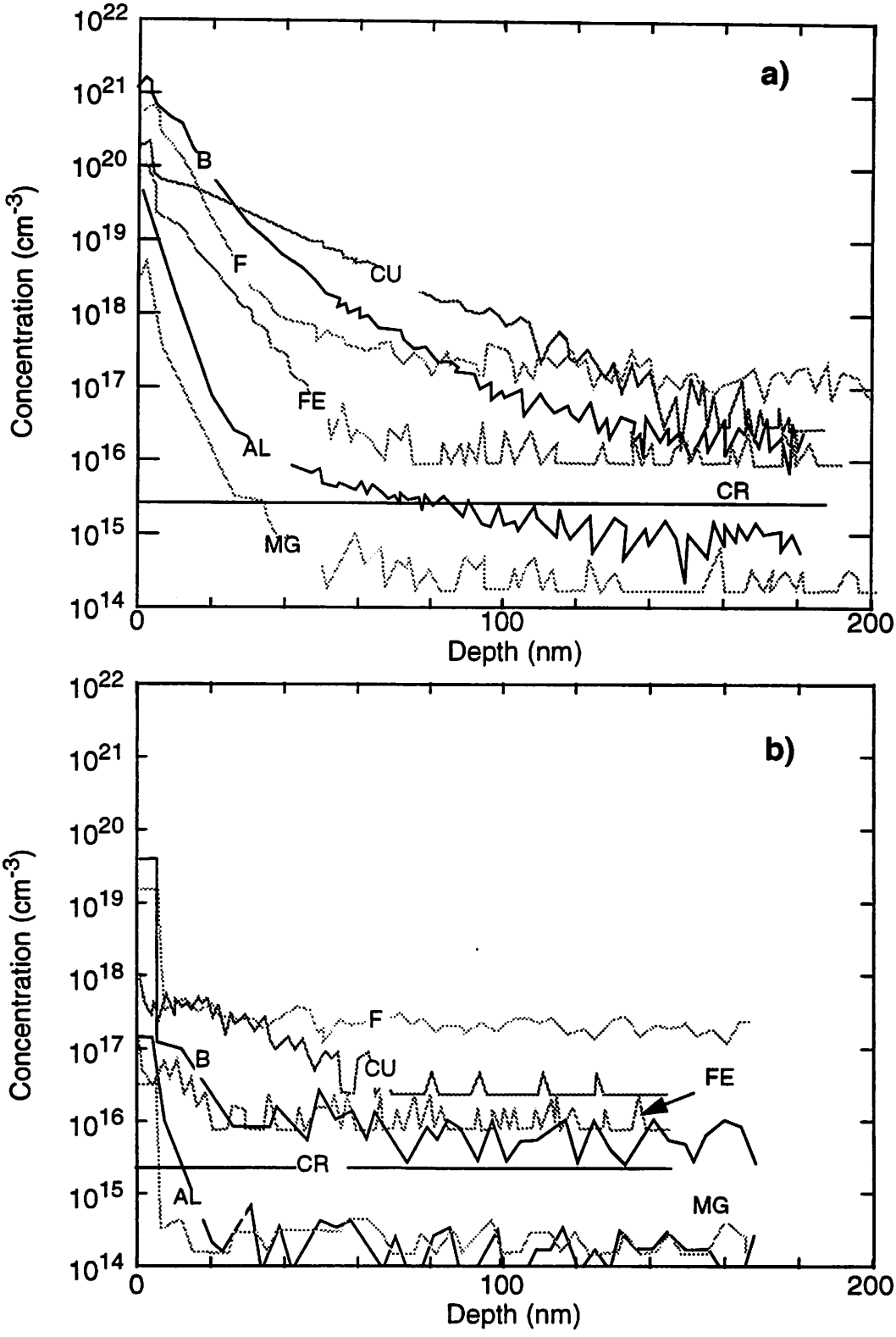

Figure 3-20. Metallic contamination during BF_3 PIII in U.C. Berkeley system

a) Impurities introduced by 3.5 kV BF_3 PIII for 14 minutes, measured by SIMS. b) Impurities in control Si sample. Cr levels below SIMS detection limits for both.

3.4 Conclusions

The etching of Si and other materials during BF_3 PIII may be unavoidable, but the rates can be controlled. For maximum incorporated dopant dose, the Si etch rate must be kept small. Si is seen to etch up to twice as slow as SiO_2 for the process parameters discussed in this paper. Roughness of Si surfaces increases by a factor of 4-5 during plasma exposure or PIII, so a screen oxide may be helpful in preserving the Si surface quality during PIII steps. It is equally important that SiO_2 etching, especially the etching of spacer and screen oxides, be controlled for reproducibility. This requires a careful choice of plasma conditions. As seen for the cobalt disilicide, material chemistry must be considered when a sample is exposed to a reactive plasma like BF_3, and the process window for each material must be determined. In all of these cases, the length of plasma or PIII exposure is important and should be minimized by short time (1-30 s) and higher frequency (25 kHz, in our system) pulsing.

3.5 References

[3.1] X.Y. Qian, N.W. Cheung, and M.A. Lieberman, "Plasma Immersion Ion Implantation for VLSI Fabrication," Report UCB/ERL, M90/84, 13 Sept. 1990.

[3.2] X.Y. Qian, D. Carl, J. Benasso, N.W. Cheung, M.A. Lieberman, I.G. Brown, J.E. Galvin, R.A. MacGill, and M.I. Current, "A plasma immersion ion implantation reactor for ULSI fabrication," Nucl. Instrum. Meth. Phys. Res., B55 (1-4), pp. 884-887, 1991.

[3.3] R.A. Stewart, X.Y. Qian, D. Carl, B. Lake, Jr., J. Benasso, R. Lynch, C.A. Pico, M.A. Lieberman, and N.W. Cheung, "Characterization of the Processing Plasma in an Engineering prototype reactor for plasma immersion ion implantation," Report UCB/ERL, M90/100, 1990.

[3.4] M. Suto, C. Ye, L. C. Lee, "Photoabsorption and fluorescence spectroscopy of BF_3 in the extreme-vacuum-ultraviolet region," Phys. Rev. A, 42 (1), pp.424-431, 1990.

[3.5] C. F. Batten, J. A. Taylor, B. P. Tsai, G. G. Meisels, "Photoionization processes at threshold. II. Threshold photoelectron photoionization, and coincidence ion-threshold photoelectron spectra of BF_3," J. of Chem. Phys., 69 (6), pp. 2547-2552, 1978.

[3.6] R. D. Levin and S. G. Lias, *Ionization potential and appearance potential measurements, 1971-1981*, Washington, DC: U.S. Dept. of Commerce, National Bureau of Standards, 1982.

[3.7] M. Farber and R.D. Srivastava, "Electron and thermal dissociation of BF_3 (g)," J. Chem. Phys., 81(1) 241-244, 1984.

[3.8] M.A. Lieberman and A.J. Lichtenberg, *Principles of plasma discharges and materials processing*, New York: Wiley and Sons, 1994.

[3.9] N.W. Cheung, M.A. Lieberman, C.A. Pico, R.A. Stewart, J.Tao, M.H. Kiang, C. Yu, V. Vahedi, B. Troyanovsky, W. En, E. Jones and J. Benasso, "Plasma Immersion Ion Implantation (PIII) for Integrated Circuit Manufacturing: Second Quarterly Progress Report," Report UCB/ERL, M91/63, 1991.

[3.10] M.A. Lieberman, R.A. Stewart, and B. Troyanovsky, "PIII Uniformity," internal communication.

[3.11] C.A. Pico, unpublished.

[3.12] J.D. Bernstein, S. Qin, C. Chan, J. Shao, and S. Denholm, to be published in Surf. Coat. Tech., 1995.

[3.13] S. Wolf and R. N. Tauber, *Silicon Processing for the VLSI Era*, Sunset Beach: Lattice Press, 1986.

[3.14] F. Fracassi, R. d'Agostino, R. Lamendola, and A. Filippo, "Plasma assisted dry etching of cobalt silicide for microelectronics applications," J. Electrochem. Soc., 143 (2), pp. 701-707, 1996.

[3.15] P. G. Stetcher, *The Merck Index*, Rahway, NJ: Merck, p. 380, 1968.

[3.16] E.R. Weber, "Transition metals in silicon," Appl. Phys. A, A30 (1), pp. 1-22, 1983.

4 PIII Doping Dosimetry

4.1 Introduction

PIII depends on the principle that the large negative bias applied to the wafer holder is capacitively coupled to the plasma sheath. The entire wafer bias is expected to be dropped across the sheath so that the ions that cross the sheath are implanted with that energy. If the rise and fall times of the wafer bias waveform are short, the majority of the ions are implanted at the peak energy. Even so, the as-implanted PIII profile is a function of many process variables: the substrate etch rate during implantation, the thin film deposition rate on the surface during implantation, the capacitive coupling of the applied bias to the sheath region, the rise and fall times of the applied bias, the time-varying implant current, the fractions of different ion species in the plasma, and ion-neutral collisions in the plasma. This distinguishes them from conventional implant profiles, where mono-energetic, mono-species implant beams lead to profiles which are better described by Gaussian or Pearson IV distributions with sub-surface peaks. PIII has been shown to produce profiles with peak concentration at the surface and exponential shape for energies below 5 kV (Figure 4-1).

In this chapter, a methodology is developed to use in situ measurements of the implanter current (I) and implant voltage (V) to derive an energy spectrum for a single implant pulse. If the ion species concentrations in the plasma are known, this energy spectrum can be used to construct a per-pulse implant profile. If the ion species distribution is not known a priori for a multi-species plasma, secondary ion mass spectroscopy (SIMS) data from an implanted sample can be used to estimate the distribution and calibrate the IV-generated profile. Data from 1 - 5 kV, 2.5 - 5 kHz BF_3 PIII implants are used to demonstrate the concept. The implant profile for a single pulse can be used to project the final

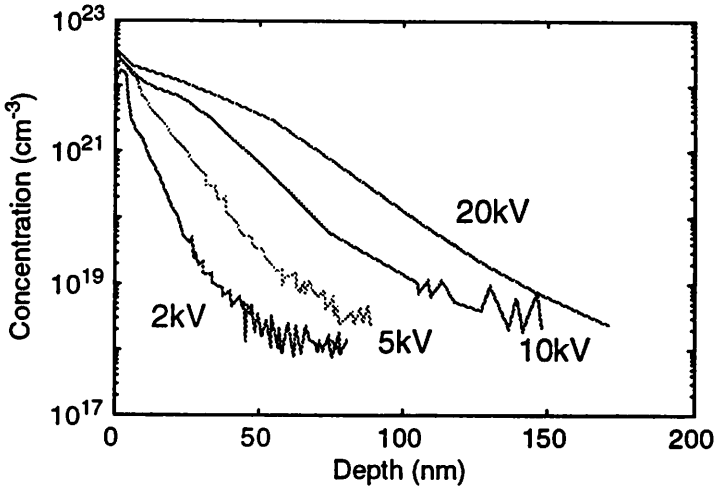

Figure 4-1. BF_3 PIII implantation profiles

BF_3 PIII profiles with 2 kV to 20 kV applied bias voltage.

implant profile and total implanted dose as a function of implant time, PIII pulse frequency, and substrate etching.

4.2 Model of PIII implantation

4.2.1 General Model

The previous chapter discussed the processes of deposition, etching and polymer deposition that can occur concomitantly during SiF_4 or BF_3 PIII. Since operating in a region of deposition nullifies the advantages of controllable depth and dose of ion implantation, implantation is generally performed in a slowly etching plasma.

When implanting in a slowly etching plasma, the surface of the substrate is steadily removed. If the surface at time t=0 is at x=0, then the surface at time t>0 is located at x'=x-vt, where v>0 is the velocity of interface movement determined by the rate of surface removal due to sputtering and plasma etching (Figure 4-2a). If the distribution of ions implanted per second into the substrate is $g(x)$ in the absence of etching, then in the presence of etching, $g(x')$ describes the ions added to the substrate at time t. The total accumulated implantation profile after time t is

$$C(x,t) = \int_0^t g(x')\,dt' = \int_0^t g(x-vt')\,dt' \quad . \tag{4-1}$$

The total incorporated dose in the substrate is the integral of the concentration profile from the surface to the maximum implant depth:

$$Q = \int_{vt}^{\infty} C(x,t)\,dx \tag{4-2}$$

Since, as shown in Figure 4-2a, the etching removes the implanted species along with the substrate surface, dopant is lost from every implant pulse, and the incorporated dose decreases as the etch rate increases. In the case of deposition, the equations are similar, using $v<0$ (Figure 4-2b):

$$C(x,t) = \int_{0}^{t} g(x-vt')\,dt' \qquad \text{for } x>0 \tag{4-3}$$

$$C(x,t) = \int_{x/v}^{t} g(x-vt')\,dt' \qquad \text{for } 0>x>vt. \tag{4-4}$$

Equation 4-3, for $x>0$, is the dopant profile in the substrate, and Equation 4-4 gives the profile inside the deposited layer.

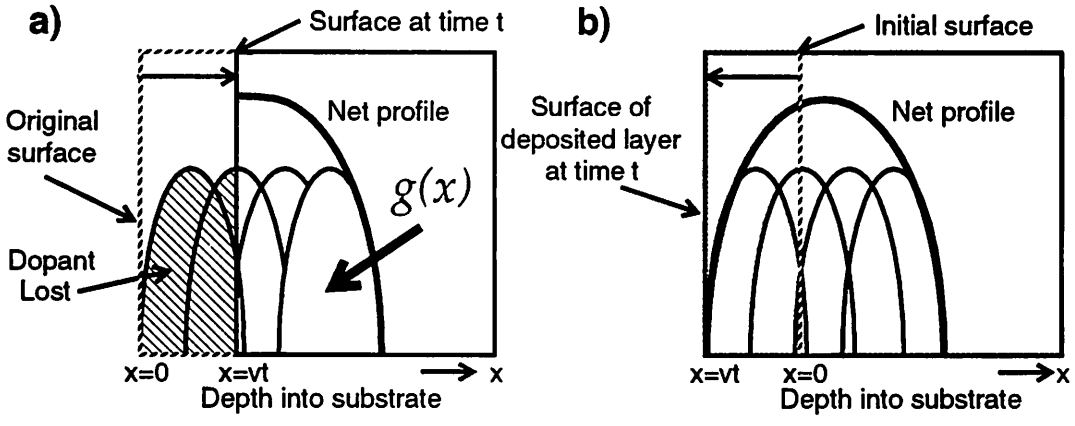

Figure 4-2. Implantation during etching or deposition

Schematic illustration of simultaneous plasma a) etching or b) deposition during PIII, and the effect on incorporated dose in the substrate.

4.2.2 Model for Shallow Implantation of BF_3

The equations are easily solved for the case of a shallow implant in an etching BF_3 plasma, where the as-implanted profile can be approximated by an exponential function [4.1]. In this case the following equations apply:

$$g(x') = \frac{\Phi}{L} e^{-(x-vt)/L} \tag{4-5}$$

$$C(x,t) = \frac{\Phi}{v}(e^{vt/L} - 1)e^{-x/L} \tag{4-6}$$

$$Q = \frac{\Phi L}{v}(1 - e^{-vt/L}) \tag{4-7}$$

where Φ is the implant dose rate ($cm^{-2}sec^{-1}$), L (cm) is a characteristic depth determined by the implant species and energy, and x is the depth in cm. When the implant length t (in seconds) becomes large in comparison with L/v, the implant dose Q (Equation 4-7) will saturate, and further implantation will not increase the incorporated dopant. For shallow junctions, the junction depth (and therefore L) must be small, so careful processing is necessary to make the etch-rate parameter v small. Using ECR-source PIII, the dose rate (Φ) is higher than 10^{12} cm^{-2} sec^{-1}, which helps achieve a high incorporated dose in shallow implanted junctions, even in the presence of etching.

4.3 Extracting per-pulse implant profiles from SIMS data

Since PIII dopant is usually introduced during short, microsecond pulses with a duty factor less than 10%, the mathematical description of the implant profile in Equation 4-1 lends itself to a discrete formulation:

$$C(x,t) = f\Delta t \sum_{n=0}^{t/\Delta t} g(x - nv\Delta t)\,\Delta t = g(x) * f\Delta t \sum_{n=0}^{t/\Delta t} \delta(x - nv\Delta t)\,\Delta t \tag{4-8}$$

which is merely a convolution of the function $g(x)$ with a series of $t/\Delta t$ Dirac delta functions spaced $v\Delta t$ apart (Figure 4-3). The time step Δt is the actual time between pulses, or to

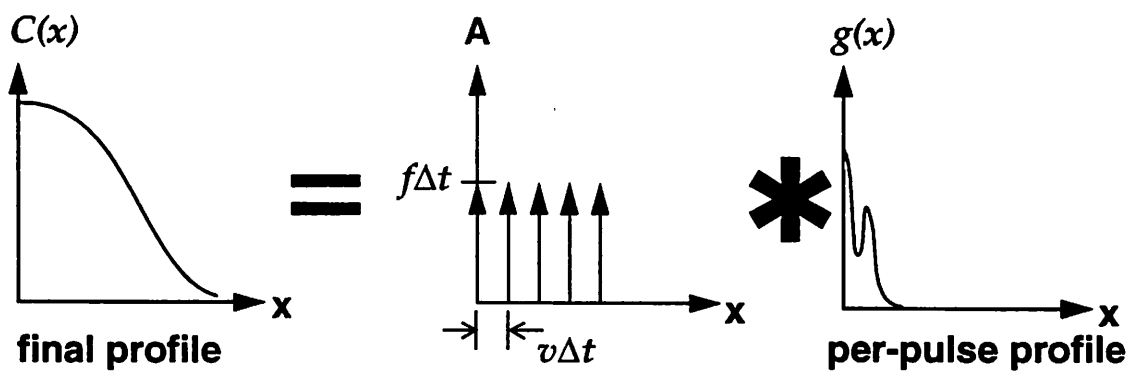

Figure 4-3. Schematic picture of per-pulse profile deconvolution

Total concentration profile of implant (C(x)) is the convolution of a series of delta functions (A(x)) with the dopant implanted per-pulse, g(x).

reduce computation time, can be defined as the time required for the etching to remove a chosen incremental thickness ($x_{inc} = v\Delta t$) of the substrate, perhaps several Angstroms. In this case, it is assumed that every implant pulse that occurs in the time it takes to etch away x_{inc} Angstroms of Si is implanted at the same time.

In Ref. [4.2], the discrete nature of the function was recognized and used to solve for the concentration profile $C(x, t)$ and the dose, assuming a Gaussian profile for $g(x)$. A profile for $g(x)$ does not need to be assumed to fit the profile of $C(x, t)$, as all the information regarding the substrate etch rate (v), the length of the implant (t), the time step (Δt), and the implant frequency (f), is entirely contained in the series of delta functions, $f\Delta t \cdot \delta(x - nv\Delta t)$. Equation 4-8 has been implemented in Matlab [4.3] using a matrix representation for the convolution:

$$C = Ag \tag{4-9}$$

where C is a vector containing the final concentration depth profile, g is a vector representing the per-pulse implant profile, and A contains all the information on the convolution. Using this algorithm, the per-pulse profile g is determined from the final profile C, if the etch rate, pulse repetition rate, and implant time are known and used to construct the matrix A. Since g is independent of the etching rate, the final profile C and dose incorporated in the substrate can be simulated for any etching conditions or implant times by altering A. The advantage of this technique is that the per-pulse profile g is extracted experimentally, without any need for an implant model. This reduces error in the simulated profiles. The programs used are described in Appendix B.

Secondary ion mass spectrometry (SIMS) data from a 10 kV as-implanted PIII sample is shown in Figure 4-4a. Since the jagged roughness of the data is due to noise in the SIMS measurement, the data read into vector C was smoothed as shown in the thicker line to resemble the real profile in Si. The incremental thickness used in the extracted per-pulse profile is 5 Angstroms, which is much smaller than the depth resolution of the SIMS profiling (Appendix C). As the etch rate (2 nm/min), implant time (20 min), and repetition rate (1 kHz) are known for this sample, the matrix A is constructed, and the vector g is calculated (Figure 4-4b). The graph of g shows that even for this 10 kV implant most of the dopant is very close to the surface. The main peak at 20 nm is shallower than the expected 37 nm projected range for a 10 kV B^+ implant [4.4]. For B introduced from a 10 kV BF_2^+ implant, one would expect that the B peak would be found closer to about 10 nm. This

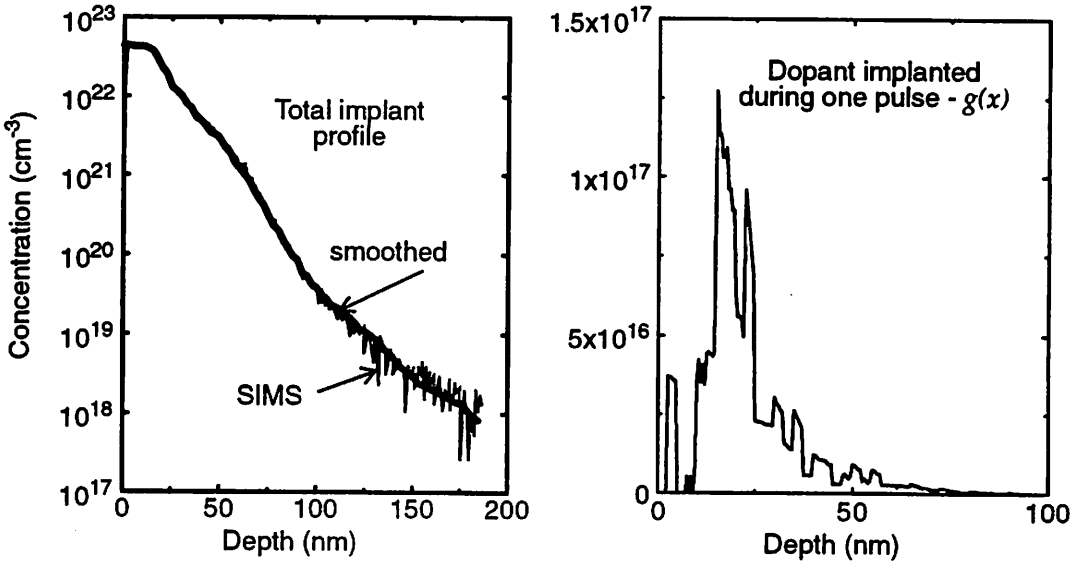

Figure 4-4. Per-pulse profile extracted from 10 kV BF_3 PIII SIMS profile

a) SIMS profile from an as-implanted 10 kV BF_3 sample is shown with the thin line, and a smoothed version used for extraction of implant per-pulse profile is shown with the thick line. b) Extracted per-pulse implant profile.

implies that most of the dopant implanted in this case is implanted as a BF^+ ion species at 10 kV or as a B^+ species at an energy lower than the 10 kV peak energy.

This algorithm is used to extract per-pulse profiles from as-implanted SIMS data from BF_3 PIII samples in the following sections. The extracted profiles are used to calibrate and double-check the results of implant profile modeling.

4.3.1 Data from 1 kV and 5 kV BF_3 PIII implants

In the presence of etching, the dose per pulse is higher than what would be predicted by simply dividing the final SIMS profile by the number of pulses. Since etching during BF_3 implantation is expected, the profile of the dose implanted per pulse must be found first, before comparing to the profile determined by the IV characteristics. For this work, 1 kV and 5 kV BF_3 PIII implants are done at 900 W microwave power, 1.5 mTorr pressure, for 10 minutes. Ten minutes was long enough that the saturation dose was reached for all samples and the etching of the substrate material was deep enough to be measured. The incremental thicknesses were chosen to make sure the etch rate used in the extraction was as close as possible to the measured etch rate. This is necessary because of the assumption that all the dopant implanted in the time it takes to remove x_{inc} Angstroms of Si is implanted at the same depth. The etch rate must be rounded up so that it will

remove exactly x_{inc} angstroms in t seconds. The etch rates used in the deconvolution are listed in Table 4-1. All are well within the experimental variation of the measured etch rates.

Sample	Measured etch rate	Optimal incremental thickness	Etch rate used in deconvolution
1 kV, 5 kHz	7.25 nm/min	6 A	7.2 nm/min
5 kV, 500 Hz	4.1 nm/min	4 A	4.0 nm/min
5 kV, 2.5 kHz	4.7 nm/min	4 A	4.8 nm/min
5 kV, 5 kHz	7.75 nm/min	4 A	8.0 nm/min

Table 4-1. Approximate etch rates used in SIMS profile extraction

4.4 Constructing per-pulse profile from implanter IV waveforms

The approach taken here to explain and model the implant profiles is the opposite of Ref. [4.7], where points from as-implanted profiles were used to approximate an ion energy distribution for the ions. The present work takes a direct approach: since measurement of the bias voltage (V) and implanter current (I) waveforms versus time is already a common diagnostic tool in PIII systems, we use these measured waveforms to derive the energy spectrum of dopant implanted during each implant pulse. If the fraction of different ion species in the implanting flux is known, the implant profile can be constructed from the energy spectrum of implanted dopant (IV per-pulse profiles). If the ion species distribution is unknown, secondary ion mass spectroscopy (SIMS) data can be used to determine it.

4.4.1 I and V waveforms

Substrate current (I) and applied bias (V) are typically measured in situ during PIII. For most plasma doping systems, the measured peak current and peak voltage are used as a reproducibility check, to compare whether the current run is comparable to a previous run at the same condition. Most dose calibration is done ex situ, by running a number of samples at different conditions, measuring the dose by SIMS or by four point probe after annealing, and then plotting those results against integrated current delivered by the implanter. The present work uses the measured IV waveforms in a more precise manner, first deducing what part of the total current is due to ions, and then using the voltage

waveform to derive an energy spectrum for the ions. From this energy spectrum, the implant profile can be constructed. In this way, the IV waveforms can be developed into a diagnostic tool for dopant dose and profile control during PIII.

The current and voltage waveforms measured during a 5kV, 5kHz BF_3 implant are shown in Figure 4-5. The current waveform is the total current drawn by the implanter, and the bias waveform is measured on the wafer holder. It is usually assumed that the large negative bias applied to the wafer holder is capacitively coupled to the sheath region of the plasma, and that the entire wafer bias is dropped across the sheath [4.9]. Ions crossing the sheath are then implanted with that energy. For the ECR source, the plasma density is ~10^{10} cm^{-3}, and the sheath width is on the order of 1 cm. Since oxide thicknesses on

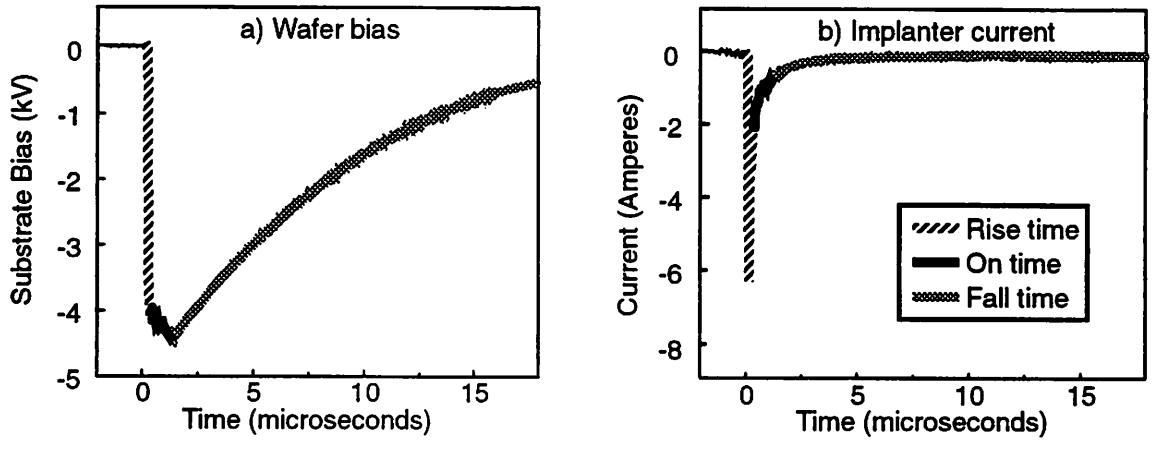

Figure 4-5. PIII implant current and substrate bias voltage waveforms

a) Bias waveform applied to PIII wafer holder during implantation showing duration of rise time, on time and fall time of pulse. b) Total current drawn by implanter during application of voltage pulse shown in a). Total current is approximately equal to the ion current plus secondary electron current.

Si wafers for ULSI are on the order of 1 micron = 10^{-4} cm, the capacitances on the wafer are much larger than the sheath capacitance, and practically all the applied bias is dropped across the sheath. This may not be true for implants of glass substrates for TFT devices, where the insulating layer thickness is much larger. If the insulator thickness is on the order of 1 mm, a significant, time-dependent error will be introduced into the implant energy, as much of the applied bias will be dropped across the substrate [4.10]. For the ULSI wafers used in this experiment, the sheath voltage can be equated to the applied bias.

Since the time-scale of interest in the plasma pulsing is microseconds and ions cross the sheath on the nanosecond time-scale, it can be approximated that the ions cross the sheath instantaneously. The dose of ions at time t will then be proportional to the ion current at time t, and their energy will be given by the bias at time t. This approximation is invalid if the ions cross the sheath much slower than the time-scale of the pulse, or if the plasma sheath is collisional, as in the case of Ref. [4.7]. If the neutral gas pressure is too high, charge-exchange between neutrals and accelerated ions in the sheath leads to an additional implantation component of fast neutrals. In this case, the implant dose will be higher due to the fast neutrals, although there may be no change in the implanter current. In this work, the gas pressure is kept near 1 mTorr, low enough that the plasma can be described as non-collisional, and fast-neutral implantation is negligible.

4.4.2 Secondary electron yield

As described in section 2.2, the total current drawn by the implanter is the sum of the ion current, electron current, displacement current, and secondary electron current. Previous work has shown that the displacement current is negligible for the operating conditions used in this experiment [4.9]. Whenever the wafer holder is at negative bias, during the rise-time, on-time, and fall-time of the pulse, the barrier to electrons is very high, resulting in negligible electron current. Therefore, the only currents that must be accounted for in this work are ion current and secondary electron current. Secondary electron yield is a function of ion species and target composition. All the ion species in the BF_3 plasma (B^+, F^+, BF^+, and BF_2^+) may be expected to have different yields. It complicates matters further that the surfaces exposed to the ions during doping tests include regions of Si, SiO_2 and Al on the test wafers and Al on the wafer holder. As a first order approximation to the average secondary electron yield versus energy in these experiments, a number of observations have been culled from the literature.

Most secondary electron yield (γ) information is collected from noble gas ions, like Ar^+, on clean metal surfaces like Al. When a clean, atomically-flat surface begins to oxidize or roughen, the secondary electron yield increases. In Figure 4-6, it can be seen that in the energy range of interest in this paper, 0 - 5 keV, the secondary electron yield of B is close to that of Ar, while the yield of F is higher by an average of 0.2 [4.11]. Ref. [4.12] shows that the secondary electron yield of a molecule is typically as large as the sum of the yield of its components. Ref. [4.13] has shown that the secondary electron yield of Ar on Al is, on

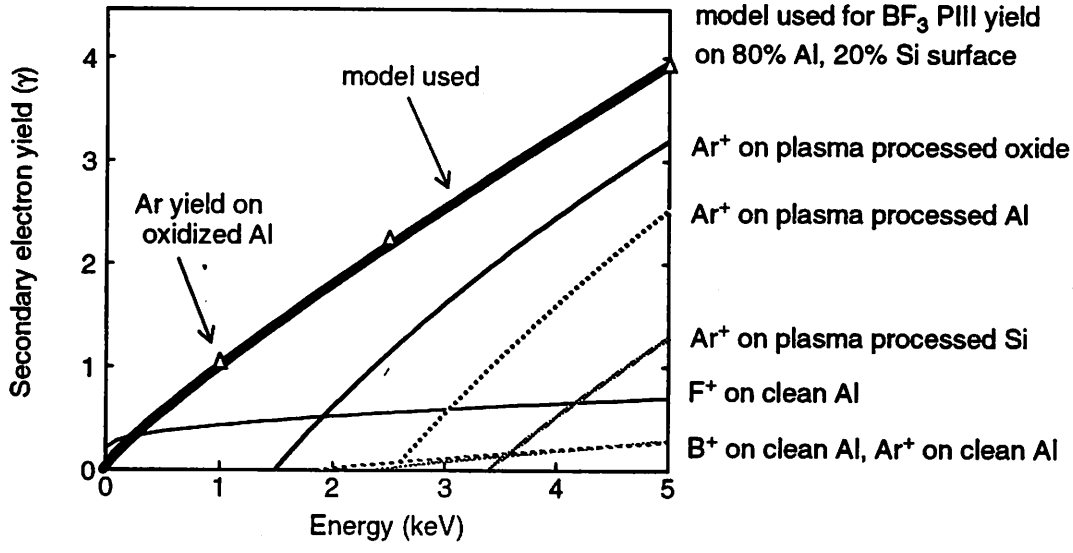

Figure 4-6. Secondary electron yields on surfaces bombarded by Ar, F and B.
Yield from Ar-bombarded, plasma-processed Si, SiO_2 and Al from Ref. [4.13]. Yield from F, B and Ar-bombardment of pristine Al from Ref. [4.11]. On clean surfaces, the yield of F ions is larger than Ar or B. On processed surfaces, the yields from Si and Al are comparable. As these models are only valid for energies above 1.5-2 keV, the yield model used in this work (thick line) is based on data on low-energy Ar bombardment of oxidized Al (triangles) from Ref. [4.14].

average in this energy range, 1.9 larger than Si and 1.25 larger than SiO_2. For this work, the average secondary yield is calculated starting with the yield of Ar on oxidized Al measured in Ref. [4.14], adjusting for the ion species B and F using approximate proportions of B^+, BF^+, BF_2^+ and F^+ in the plasma and the data of Ref. [4.11], and adjusting for the target material by gauging the percentage of Si, SiO_2 and Al present on the wafer surface and using the data of Ref. [4.13]. The data are fit with the function $\gamma_{se} = A^*\text{Energy}^m$ for the conditions in this study, where energy is in eV. As shown in Figure 4-6, once the higher yield of F ions and the lower yield of Si are taken into account, this secondary electron yield approximation is not very different from the original data in Ref. [4.14]. Values of the fitting factors A and m are given in Table 4-2 for different plasma compositions, assuming that the material exposed is 20% Si and 80% Al. This fit estimates kinetic secondary electron emission only, so the secondary electron yield and current at very low energies, where potential electron emission usually dominates, are somewhat underestimated. This means the dose of low energy ions (< 1 keV) may be overestimated in the IV profiles.

Figure 4-7 shows the energy spectrum of implanted ions during the 1 microsecond, 5 kV PIII pulse shown in Figure 4-5. This energy spectrum is obtained assuming the sec-

Plasma ion species	A	m
100 % Ar^+	0.0026	0.86
7.5 % B^+, 7.5 % F^+, 85 % BF_2^+	0.001	0.965
80% B^+, 20% BF_2^+	0.004	0.82

Table 4-2. Approximate secondary electron yield fitting factors for PIII

ondary electron yield as described above, assuming a non-collisional sheath, and assuming that 50 eV is the minimum energy an ion must have to be implanted. The energy resolution in the figure is 100 eV; resolution of 10 eV is used for the actual profile construction. It was expected that the high current during the rise time of the pulse would be an important factor in the energy spread. The ion current is very high at the beginning of the

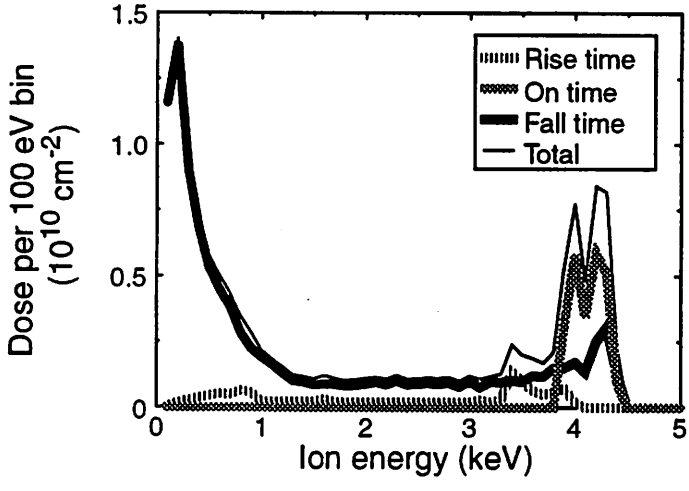

Figure 4-7. Energy spectrum of 5 kV PIII implant

Energy spectrum of PIII implant, showing dose of ions implanted per energy, assuming ions see instantaneous bias and sheath is collisionless. Energy resolution in figure 100 eV, minimum energy for ion to implant taken as 50 eV. Secondary ion yield adjusted for ion species present and substrate material.

pulse when the electrons are repelled and a large concentration of ions is left in the sheath region. The current falls to a steady-state value as the initially high ion concentration in the sheath is depleted, and the current is maintained by ions diffusing from the plasma to the sheath edge. Figure 4-7 shows that the energy spread due to the rise time is not nearly as severe as that due to the fall time. As can be seen from the figure, the long fall time of the wafer bias contributes most to the energy spread of the implant, even though the

implant current during the fall time is low and exponentially decreasing. To reduce this spread in the energy the pulse fall time must be reduced. The slow fall time in this PIII system is a function of the matching network, which can be improved to yield more monenergetic implants. Increasing the pulse on time to make the high energy ions a greater faction of the total implant dose is not a good solution: when the on-time is increased beyond 1-2 μs, the positive charge deposited on the surface by the implant may be large enough to cause thin oxide charging damage or breakdown [4.8].

4.4.3 Multiple ion species

Once the ion energy spectrum is determined, an ion species or collection of ion species must be specified before calculating the profile. When the ion fractions are chosen, the profile is constructed using tables of projected range (R_p) and straggle (ΔR_p) data from the implant simulator TRIM [4.4]. Figure 4-7 gives the dose implanted in an energy range, E-$\Delta E/2$ to E+$\Delta E/2$. The energy resolution ΔE, the energy bin size, is 10 eV in the following simulations. The dose in each bin is then divided up among the ion species present in the ion flux incident on the wafer. Once the dose is divided among the implanted species, a Gaussian profile is constructed for each ion species within each energy bin. Interpolation between the values from TRIM is used to find $R_p(E)$ and $\Delta R_p(E)$, and the height of the Gaussian is calculated by integrating the function from the Si surface to infinity and setting that value equal to the dose for the current species in the current bin. The individual profiles are added up to make a total profile. Results are shown for three different cases inFigure 4-8, assuming the ions are 100% B^+, 100% BF^+, or 100% BF_2^+. The profiles all show a peak right under the surface due to the high concentration of very low energy ions implanted during the fall time of the pulse. The profiles show the B^+ profile extending a few hundred Angstroms deeper than the BF_2^+ profile, as expected. As TRIM data assumes implantation into an amorphous solid, the effects of ion channeling are not accounted for.

4.5 Comparison of per-pulse profiles from IV waveforms and SIMS deconvolution

Per-pulse profiles for the 5 kV, 5 kHz BF_3 PIII implant are derived in Figure 4-9a for boron and Figure 4-9b for fluorine using both SIMS deconvolution and IV-construction. The per-pulse profiles from SIMS data were derived using an etch rate of 8 nm/minute and an incremental thickness of 4 Angstroms. A systematic and constant error is

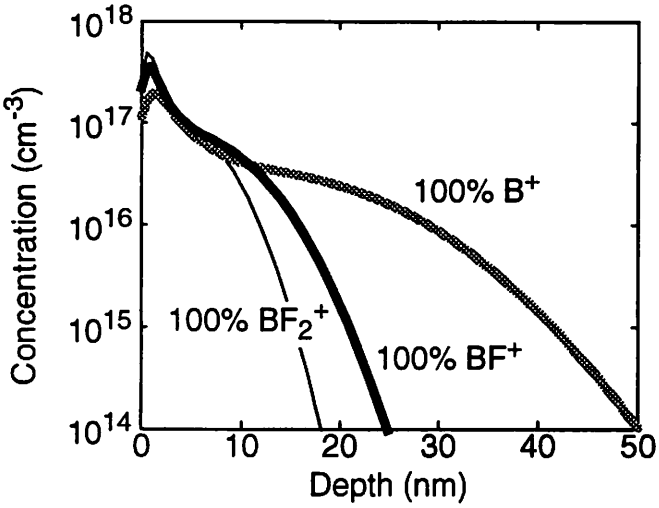

Figure 4-8. Per-pulse profiles from IV waveforms assuming B^+, BF^+ or BF_2^+ ion species

Per-pulse implant profiles generated by IV method for 5 kV, 5 kHz BF_3 PIII implant at 900 W, 1.5 mTorr, using energy spectrum as shown in Figure 4-7.

present in the B and F concentrations and dose, due to uncertainty in the relative sensitivity factor (RSF) used to convert the raw SIMS data to concentration. The uncertainty in the RSF factor is estimated at 20% for B in Si, but may be more than 100% for F in these profiles. This means that although the shape of the profile may be correct, the absolute concentration at each point will be off by a constant factor. There will be a corresponding error in the integrated dose from the SIMS profile. In the first 5 nm of material removal, SIMS has not attained a steady-state removal rate, so the shape of the profile may not be reliable that close to the surface. Reproducibility between samples is estimated at 5% for B and 50% for F. Therefore, when using the SIMS profiles to compare to the IV profiles, it is more useful to compare the profile shapes than the actual concentrations, especially for fluorine.

Also shown in the figure are per-pulse profiles constructed using the IV method, using the IV waveforms and energy spectrum shown in Figure 4-5 and Figure 4-7. To account for the distribution of ion species, the ion current is divided among the ion species according to their fraction:

$$I_{ion} = I_{ion}\left(X_B + X_{BF} + X_{BF_2} + X_F\right) \tag{4-10}$$

where the X terms are the fractional contribution of each ionized species to the total ion flux. This is not necessarily the same as the ion species distribution measured by optical emission or mass spectrometry in the bulk plasma, so it may not be possible to measure

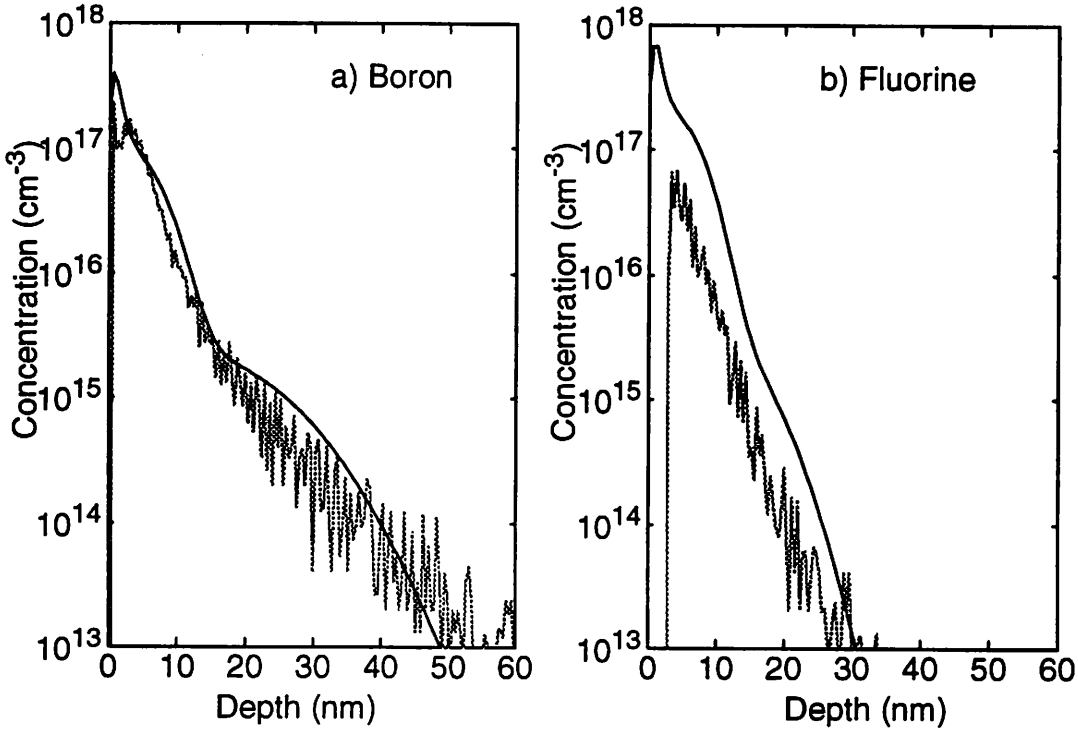

Figure 4-9. Per-pulse profiles for 5 kHz, 5kV BF_3 PIII implant

Comparison of per-pulse profiles from IV method (dark line) and from SIMS deconvolution method (gray line) for a) boron b) fluorine profiles from 5 kV, 5 kHz BF_3 PIII at 900 W, 1.5 mTorr. Ion species distribution used for simulation is 7.5% B^+, 0% BF^+, 85% BF_2^+, and 7.5% F^+.

them directly. In that case, the X terms can be used as fitting parameters. As B^+, BF^+, BF_2^+ and F^+ are the main ion species detected by mass spectrometry in the bulk BF_3 plasma, the sum of the four X terms is approximately 1. Assuming that the ion species distribution does not change during the pulse, the ion dose per energy is then divided up among the ions according to their fraction X. The boron dose and fluorine doses are then written:

$$\Phi_B = \Phi_{total}(X_B + X_{BF} + X_{BF_2}) \tag{4-11}$$

$$\Phi_F = \Phi_{total}(X_F + X_{BF} + 2X_{BF_2}) \tag{4-12}$$

where the total dose Φ_{total}, is the ion dose per energy summed over all energies.

The per-pulse profiles in Figure 4-9 show how the ion species distribution can be used to fit the IV profile to the profile extracted from SIMS. For the 5 kV, 5 kHz profile, at least 5% of the ion species must be B^+ to fit the tail of the boron profile. Less than 10% F^+

is needed to fit the tail of the fluorine profile. The contribution of BF^+ is 0-10%. Variation of the X_{BF} parameter has shown that the total profile is insensitive to this contribution. The data shows that the implant contains about 85% BF_2^+. This gives a peak concentration near the surface, and causes the dopant concentration to fall two orders of magnitude in the first 15 nm.The ion species distribution shown is the result of fitting the IV energy spectrum to the SIMS profiles for the three different implants: 5 kV at 5 kHz (Figure 4-9), 5 kV at 2.5 kHz (Figure 4-10), and 1 kV at 5 kHz (Figure 4-11). The distribution which best fits

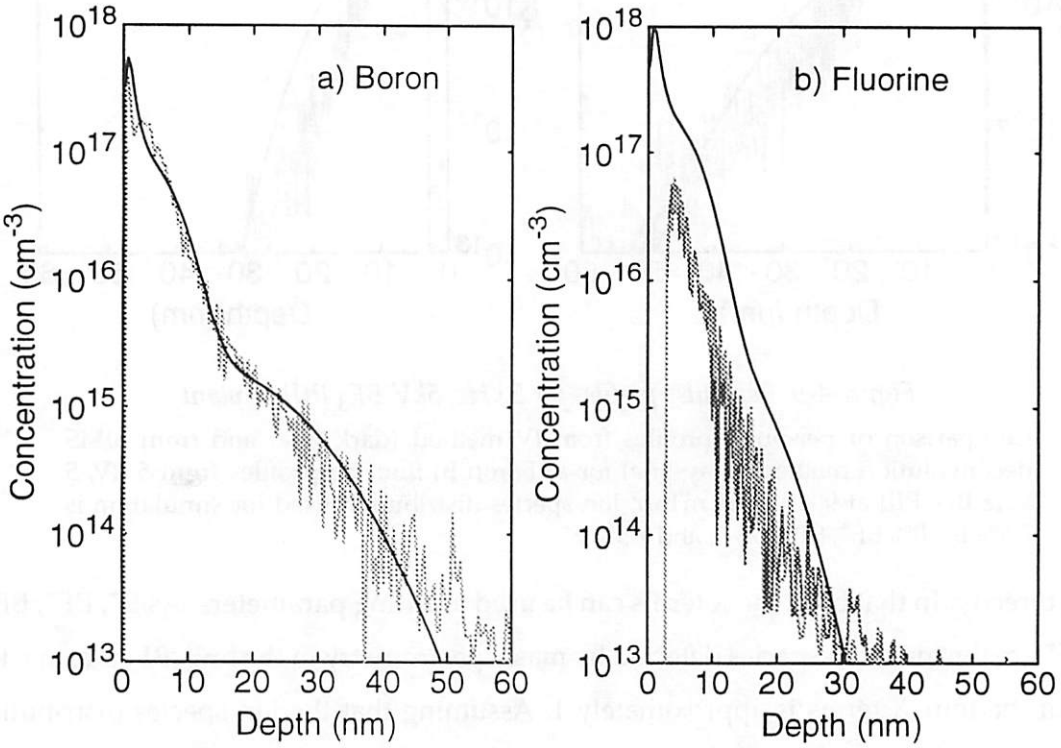

Figure 4-10. Per-pulse profiles for 2.5 kHz, 5kV BF_3 PIII implant

Comparison of per-pulse profiles from IV method (black line) and from SIMS deconvolution method (gray lines) for 5 kV, 2.5 kHz BF_3 PIII at 900 W, 1.5 mTorr. a) are boron profiles and b) are fluorine. Ion species distribution is 7.5% B^+, 0% BF^+, 85% BF_2^+, and 7.5% F^+.

all three is 7.5% B^+, 0% BF^+, 85% BF_2^+ and 7.5% F^+. This distribution is close to values that have been reported for BF_3 plasmas in other PIII systems and spectroscopy work [4.5, 4.6].

The SIMS for this work was done using a Cameca IMS4f instrument. The primary beam was an O_2^+ beam at 64 degrees to the normal, with an impact energy of 2 keV. The analysis was performed with the chamber backfilled with oxygen to a pressure of 5 μTorr for better resolution near the surface. Even so, as can be seen in the first 5-10 nm of the B

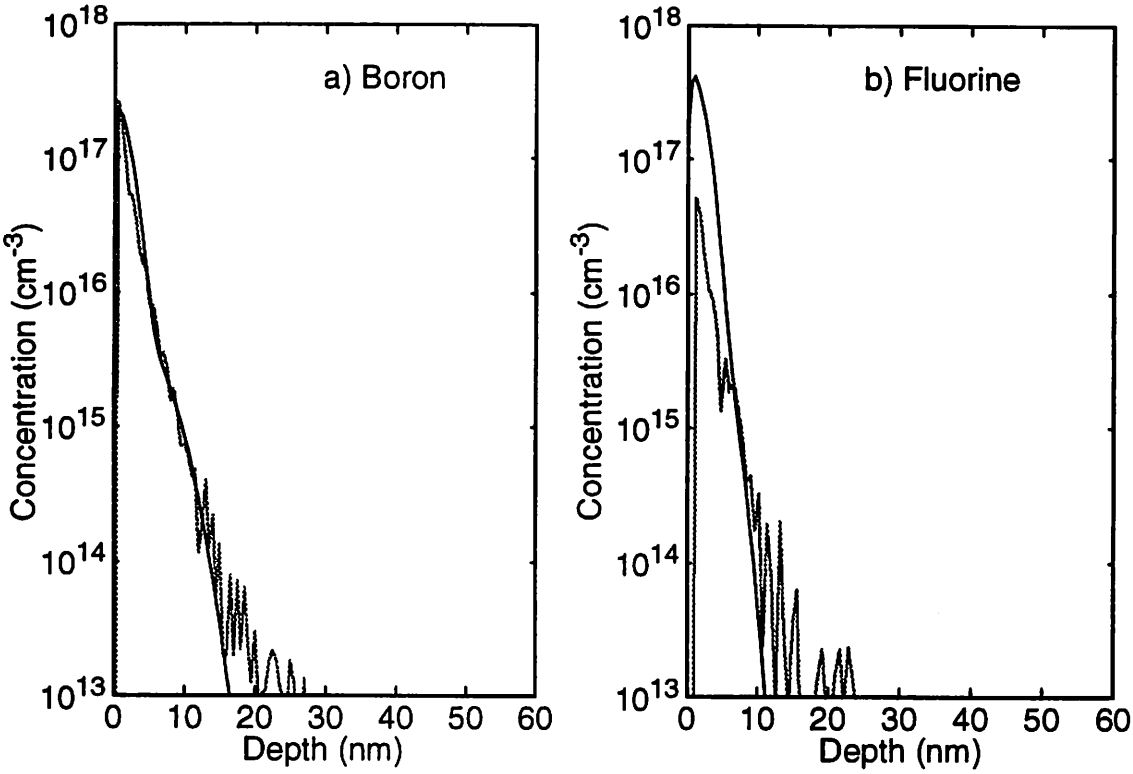

Figure 4-11. Per-pulse profiles for 5 kHz, 1 kV BF_3 PIII implant

Comparison of per-pulse profiles from IV method (black line) and from SIMS deconvolution method (gray line) for 1 kV, 5 kHz BF_3 PIII at 900 W, 1.5 mTorr. a) are boron profiles and b) are fluorine. Ion species distribution is 7.5% B^+, 0% BF^+, 85% BF_2^+, and 7.5% F^+.

profiles in Figure 4-9 and Figure 4-10, the IV and SIMS profiles do not match very well close to the surface. This is expected due to the SIMS transient at the surface, before the primary O_2^+ beam and oxygen bleed have time to convert the surface to a steady-state SiO_x layer. It is impossible to tell whether the high surface concentrations predicted by the IV method are truly present, as SIMS cannot measure the surface concentration. The simulated surface concentration is mainly due to very low energy ions implanted during the fall time of the implant bias. It is also possible that many of these low energy ions were reflected or contributed to the surface etching rather than being implanted.

The boron profile shapes, however, are fit very well by the *IV* profile in all three cases, predicting the high concentrations near the surface and the rapidity of the dopant fall-off. The shape of the fluorine profiles is fit well for the 5 kV cases, although the concentrations are off by more than a factor of two in places. This error in concentration is comparable to the uncertainty in the SIMS concentration calibration. The boron doses

from IV vary from the SIMS doses by the factors listed in Table 4-3. The dose error reflects errors in the secondary electron yield function, the etch rates used, and the ion species distribution. In these examples, it is shown the IV method can be used to generate per-pulse profiles that can be used to predict absolute doses in PIII within a factor of 2. With better SIMS concentration calibration, this factor can be reduced.

Sample	SIMS dose (cm^{-2})	IV dose (cm^{-2})	ratio (SIMS/IV)
5 kV, 5 kHz	2.2×10^{10}	3.2×10^{10}	0.69
5 kV, 2.5 kHz	3.0×10^{10}	3.1×10^{10}	0.97
1 kV, 5 kHz	1.8×10^{9}	1.6×10^{9}	1.13

Table 4-3. Dose from SIMS and IV per-pulse profiles, excluding top 5 nm

4.6 Using per-pulse profiles for dose prediction

During PIII implantation in the presence of etching, a steady state condition will develop where the dopant etched away is balanced by the dopant implanted. The IV-generated per-pulse profile developed in this chapter is useful for predicting the as-implanted dose and profile, as it requires no assumption about the shape of the per-pulse profile. It can predict the profile shape, dose, and profile changes due to changes in the implanter current or voltage waveform. The data needed for these predictions are the current and voltage waveforms, etch rate, and the ion species distribution.

Figure 4-12 and 4-13 show how the IV profiles can be useful for choosing the best implant parameters for a run, by determining the dose saturation behavior under a number of different PIII conditions. To construct these figures, the IV per-pulse profiles from Figs. 4-9 to 4-11 have been multiplied by matrices containing the information on implant time, etch rate and pulse frequency, as described in Equation 4-9, to yield final concentration profiles. The dose saturates after a steady-state condition of implantation and removal is reached. Figure 4-12 shows the dependence of dopant saturation on the implant energy. This graph takes into account the actual measured etch rates during 1 kV and 5 kV implantation at 5 kHz. The graph shows clearly that the dose in the 1 kV case reaches its saturation value faster, in about 30 s. The saturation behavior here is due to the differences in profile. Saturation occurs more quickly when the dose is located nearer the surface. Also shown is the maximum dose possible at each condition. The 1 kV implant can deliver a maximum dose of 4×10^{15} cm^{-2}, in 30 s, but the 5 kV implant delivers a dose

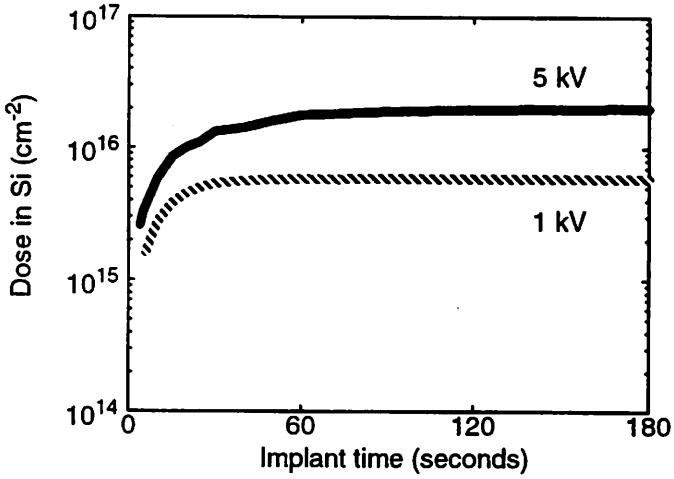

Figure 4-12. Dependence of dopant saturation on implant energy

Dependence of dose saturation on implant energy in 5 kHz BF_3 PIII. Generated using IV per-pulse profiles from Figure 4-9 and Figure 4-11, and measured etch rates for 5 kHz, 1 and 5 kV implantation. Dose saturates faster and at lower dose for lower energy implant, when dopant is closer to Si interface.

over $2x10^{16}$ cm^{-2} when it saturates in about 60 s. Both of these doses are in excess of what is typically needed for a ULSI source/drain implant. Using the 5 kV, 5 kHz implant, a worst-case shallow junction dose of $5x10^{15}$ cm^{-2} can be achieved in a 10 seconds. In this short time, less than 13 Angstroms of Si will be lost due to etching, even at the highest Si etch rates reported here.

Figure 4-13 shows the dependence of the dose saturation on implant pulse frequency. Since the dose implanted per time increases proportionally to the frequency, but the etch rate only increases a factor of 2 as frequency increases a factor of 10, using higher frequency is an effective way to increase the incorporated dose in the substrate. The time required for saturation depends more on the profile than on the etch rate, so the dose saturation is reached in about one minute for all frequencies. From this figure, the time to reach $5x10^{15}$ cm^{-2} for the 2.5 kHz case is twice as long the 5 kHz case. Taking into account the smaller etch rate of Si at 2.5 kHz, the Si loss is approximately the same for each, less than 13 Angstroms. This etching loss should not cause a problem in ULSI devices, as it is comparable to Si loss during cleaning processes.

Modeling of PIII plasma currents has shown that it takes milliseconds for equilibrium to be re-established after the implant pulse ends, for typical plasma conditions [4.8]. This means that if the pulsing frequency is too high, positive charges deposited on the surface by the implanting ions may not be totally neutralized by plasma electrons before the

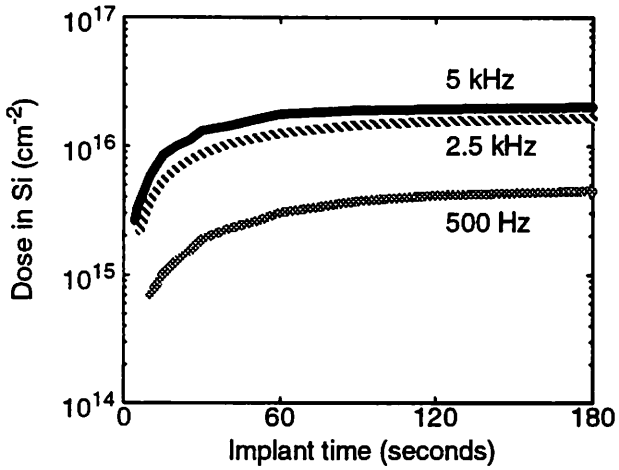

Figure 4-13. Dependence of dopant saturation on implant frequency

Dependence of dose saturation of 5 kV BF_3 PIII on pulse frequency. Generated using IV per-pulse profiles and measured etch rates for 5 kV, 0.5-5 kHz implantation. Time required for dopant saturation not a strong function of etch rate. Since etch rate does not increase as fast as dose rate does with increasing frequency, higher frequency can still be used to increase dose incorporated.

next implant pulse begins. Although individual implant pulses may only deposit enough charge on the surface to change the surface potential by a fraction of a volt, over a series of pulses, a potential large enough to cause oxide damage may develop. If the pulsing frequency is too high, the charge built up on the surface can become large enough that the oxide breakdown field will be exceeded. So although using higher implant pulse frequency is useful for increasing the dose rate and reducing the total amount of substrate etching, the frequency must be kept low enough to protect thin oxides on the wafer. For a $4x10^{10}$ cm^{-3} Ar plasma implant using a 2 μs implant pulse with infinitely fast fall time, the maximum frequency that should be used is 20 kHz. The peak frequency that can be used without oxide breakdown may be increased by lowering the pulse on time, lowering the pulse fall time, or changing plasma conditions. These same steps will lead to lower etch rates and lower energy spread in the implanted ions.

4.7 Conclusions

Implanter current and voltage waveforms can be used to construct implant profiles for single-species plasma immersion ion implantation. The ion species distribution in multiple-species implantation can be found by comparing constructed per-pulse profiles with SIMS profile data. Once the ion species distribution is known, per-pulse profiles can

be generated for various implantation conditions and can be used to project the dependence of implant profile and dose on other process parameters, like implant time, substrate etch rate, and frequency. By monitoring and tailoring the implant bias waveforms, the plasma implant profiles can be predicted, controlled, and optimized for specific implant applications.

4.8 References

[4.1] X.Y. Qian, N.W. Cheung, M.A. Lieberman, S.B. Felch, R. Brennan, and M.I. Current, "Plasma immersion ion implantation of SiF_4 and BF_3 for sub-100 nm p^+/n junction fabrication," Appl. Phys. Lett., 59 (3), pp. 348-350, 1991.

[4.2] J. Shao, M. Round, S. Qin, and C. Chan, "Dose-time relation in BF_3 plasma immersion ion implantation," J. Vac. Sci. Tech., A13 (2), pp. 332-334, 1995.

[4.3] S.C. Johnson and C. Moler, "Compiling MATLAB," *Proc. of USENIX Symp.Very High Lev. Lang.*, Berkeley: USENIX Assoc., pp. 119-127, 1994.

[4.4] J.F. Ziegler, J.P. Biersack, and U. Littmark, *The Stopping and Range of Ions in Solids*, vol. 1, New York: Pergamon, 1985.

[4.5] P.K. Chu, S. Qin, C. Chan, N.W. Cheung and L. Larson, "Plasma Immersion Ion Implantation - A Fledgling Technique for Semiconductor Processing," unpublished.

[4.6] J. E. Hesser, J. Chem. Phys., 47(9), pp. 3443-3450, 1967.

[4.7] S. Qin, C. Chan, and N.E. McGruer, "Energy distribution of boron ions during plasma immersion ion implantation," Plasma Sources Sci. Tech., 1 (1), pp. 1-6, 1992.

[4.8] W. En and N. W. Cheung, "Modeling and Experiments of Waveforms on Oxide Charging in Plasma Immersion Ion Implantation," in review for IEEE Trans. Elec. Dev., 1996.

[4.9] W. En and N. W. Cheung, "Comparison of experimental target currents with analytical mode results for plasma immersion ion implantation," IEEE Trans. Plasma Sci., 23 (3), pp. 415-421, 1995.

[4.10] B.P. Linder and N.W. Cheung, "Plasma Immersion Ion Implantation with Dielectric Substrates," unpublished.

[4.11] E.V. Alonso, R.A. Baragiola, J. Ferron, M.M. Jakas, and A. Oliva-Florio, "Z_1 dependence of ion-induced electron emission from aluminum," Phys. Rev. B, 22 (1), pp. 80-87, 1980.

[4.12] J. Axelsson, C.T. Reimann, and B.U.R. Sundqvist, "Electron emission from conducting surfaces impacted by multiply-charged polyatomic ions," Nucl. Instrum. Meth. Phys. Res., B101 (4), pp. 343-356, 1995.

[4.13] W. En and N.W. Cheung, "A new method for determining the secondary electron yield dependence on ion energy for plasma exposed surfaces," to be published in IEEE Trans. Plasma Sci, 24 (6), 1996.

[4.14] B. Szapiro and J.J. Rocca, "Electron emission from glow-discharge cathode materials due to neon and argon ion bombardment," J. Appl. Phys, 65 (9), pp. 3713-3716, 1989.

5 Shallow junction fabrication with PIII

5.1 Introduction

Shallow semiconductor doping with PIII was first reported by Mizuno in 1987 [5.1, 5.2]. That process used an ECR plasma source with 5% B_2H_6 in He to generate ions, and an RF bias to effect an implant energy of 700 eV for p-type doping. The U.C. Berkeley reactor was constructed in 1988 for impurity gettering implants [5.3], and the first shallow junction doping using BF_3 source gas was reported in 1990 [5.4-5.6]. Since then, *p*-type shallow junction doping by PIII has been achieved on prototype systems at a number of companies and universities [5.7-5.23]. The work of Felch et al has produced the shallowest p^+n junctions made with PIII, using a 1 kV implant in a BF_3 plasma, and a two-step rapid thermal annealing cycle of 5 s at 800°C and 10 s at 1050°C [5.15, 5.16]. Spreading resistance analysis of the profiles shows a peak activation near 10^{20} cm^{-3} and junction depth of 50-55 nm at background doping 10^{18} cm^{-3}.

This chapter evaluates the use of PIII as a replacement for conventional ion implantation for shallow junction formation. Properties of p^+ implants and p^+ junctions made in the U.C. Berkeley PIII reactor are studied. The results are compared to a number of conventional BF_2^+ implanted samples and BF_3 PIII-implanted samples prepared by off-campus vendors.

5.2 Effect of PIII substrate bias on as-implanted profiles

5.2.1 As-implanted profiles

Boron implant profiles from BF_3 PIII performed with a 900 W power, 1.5 mTorr pressure, and 220 A magnet current plasma are shown in Figure 5-1. The implants were done with 1 kV and 5 kV bias at a repetition rate of 5 kHz. SIMS analysis was performed with a 2 keV primary O_2^+ beam at 64° to the normal. The O_2^+ primary beam is used

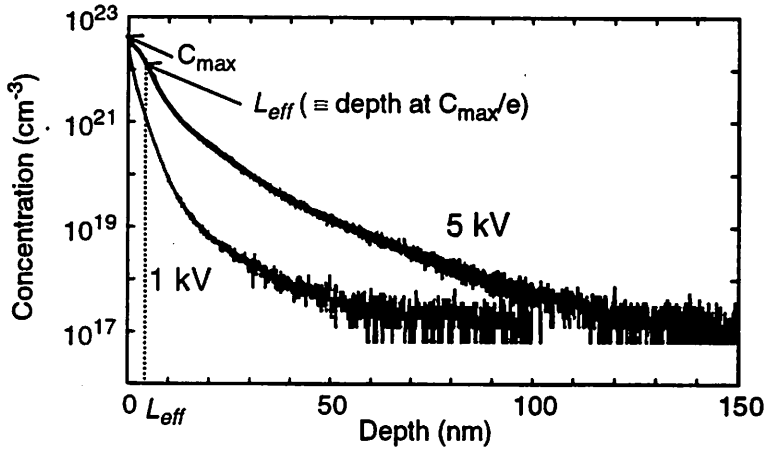

Figure 5-1. UCB PIII implant profiles at 1 kV and 5 kV

Si implanted by 1kV and 5kV, 5 kHz BF_3 PIII, at 900W, 1.5 mTorr pressure. The effective characteristic length of the implant, L_{eff}, is defined as the point at which the concentration falls to 1/e of its peak value.

because the secondary B^+ concentration is higher when the surface matrix is SiO_2, not Si. An O_2^+ beam and O_2 bleed are used to convert the surface to SiO_2 for accurate SIMS measurement. In addition to having a higher dose, the 5 kV profile shows a dopant concentration an order of magnitude higher than the 1 kV implant as deep as 65 nm. If the source of the B dopant were a surface deposition layer, the dopant concentrations would not be this high so deep in the wafer, since SIMS ion mixing for the samples measured here should be less than 19 Angstroms (Appendix C). This shows that the dopant is implanted, not just deposited on the surface. As described in the previous chapter, the features of the implant profile are caused by the implanter current-voltage waveforms, and the simultaneous implantation of multiple ion species.

Most PIII systems in use are prototype machines for which quantitative correlation of depth and substrate bias have not been shown. Most published PIII implantation profiles closely resemble the exponential curve in Figure 5-1 before annealing. It is therefore proposed to characterize implants by a parameter L_{eff}. L_{eff} is defined in Figure 5-1 as the exponential fall-off parameter, the depth at which the dopant concentration falls to 1/e of its maximum value. The depths at which these profiles fall to 1/e of their peak concentrations are 13 A for 1 kV, and 43 A for 5 kV. Figure 5-2 shows a plot of L_{eff} for a number of groups performing boron implants with different plasma sources and source gases. The correlation is quite good, showing a marked relation of the wafer bias voltage to the effec-

tive depth of the implant profile, which was measured by secondary ion mass spectrometry (SIMS) in each experiment.

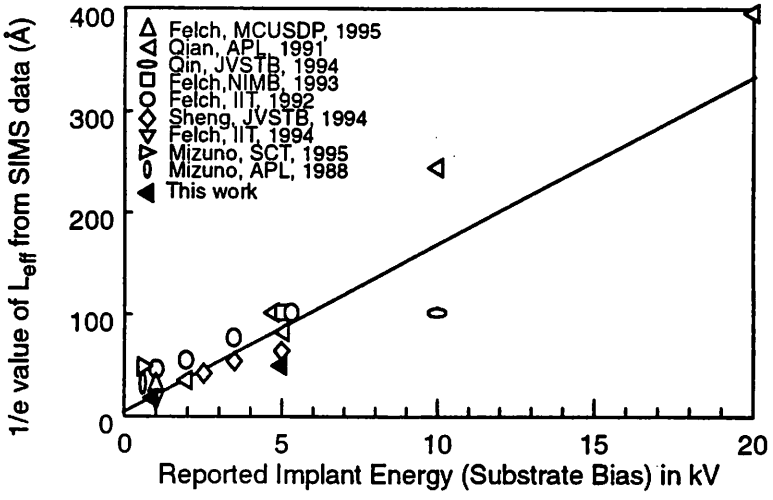

Figure 5-2. Application of exponential PIII model to other PIII groups

L_{eff} values for different plasma doping groups showing a good correlation between L_{eff} measured from SIMS data and the reported implant bias voltage. Data from Refs. [5.15, 5.6-5.11, 5.19, 5.24].

5.2.2 As-implanted dose

Since the highest current occurs when the sheath is first formed, and the sheath width increases with increasing applied bias, the dose per pulse is expected to increase with bias as well. The ion current before the sheath reaches a steady-state thickness is related to the maximum sheath width and the velocity of the sheath edge as it expands. Both of these are larger when a higher bias is applied. With a larger bias, a larger volume of ions are uncovered as the sheath forms. If the pulse and fall time are short, these ions implanted as the sheath expands may be a larger fraction of the total dose than ions that diffuse to the sheath edge and become accelerated. The PIII implant models given in Chapter 2 describe the ion current during a PIII pulse in a low-pressure, collisionless plasma as

$$J_i = q n_0 \left(\frac{ds}{dt} + u_B\right) = K \cdot \frac{V^{3/2}}{s^2} \qquad (5\text{-}1)$$

where K is a constant, n_0 is the ion density, V is the applied bias, and s is the sheath thickness. u_B is the Bohm velocity, which is constant. In steady state, the ion current will be con-

stant, and depend only on the ion density, $J_i = qn_0u_B$. However, since steady state takes many microseconds to be established, almost as long as the period of the implant pulse, most of the dopant is introduced in the transient stage. Using Equation 5-1, the total charge implanted is

$$Q_{tot} = \int_{pulse} J_i \cdot dt = Q_{ss} + qn_0(s_{final} - s_{initial}) \quad . \tag{5-2}$$

The contribution due to ions diffusing to the sheath edge from the bulk plasma is the steady state component $Q_{ss} = qn_0u_Bt_p$, where t_p is the pulse length. The charge due to the transient current component is $Q_{trans} = qn_0s_{final}$ if the initial sheath width is comparatively small. The functionality of Q_{trans} is found from Equation 5-1 by setting *ds/dt* to zero, as the maximum sheath width is attained at the end of the transient:

$$Q_{trans} = qn_0s_{final} \propto K_2 \cdot V^{3/4} \cdot n_0^{1/2} \quad . \tag{5-3}$$

If the total implanter current is given by the sum of ion current and secondary electron current, then $J_{tot} = J_i + J_{se} = J_i(1+\gamma)$. The total charge drawn by the implanter during a pulse is then $Q_{tot} = Q_{trans}(1+\gamma)$ when $Q_{trans} >> Q_{ss}$, during a short pulse. As γ also has bias voltage dependence, $\gamma \propto V^{0.5}$, the functionality of the integrated charge dose of the implanter should be

$$Q_{tot} = \gamma Q trans = K_3 \cdot n_0^{1/2} \cdot V^{5/4} \tag{5-4}$$

for $\gamma >> 1$. This functionality is seen in measurements of the total charge per pulse drawn from the implanter in Figure 5-3, which show a super-linear dependence on substrate bias,

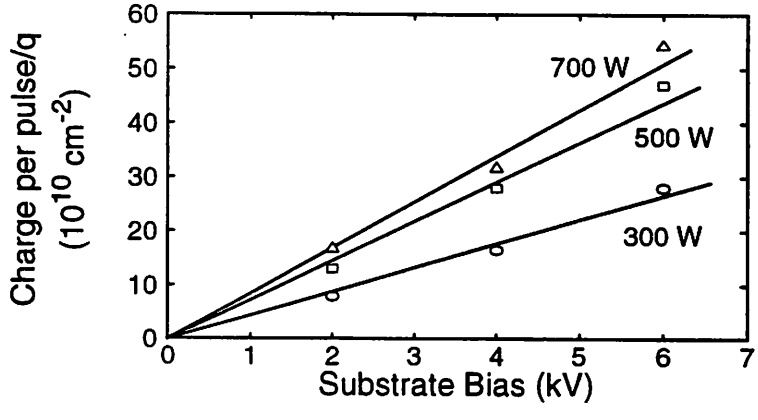

Figure 5-3. PIII integrated implanter charge dose per pulse
BF_3 PIII at 1 mTorr pressure with 125 A magnet current.

and a sub-linear dependence on the plasma power, which is related to ion density. The actual ion dose per pulse can only be found by separating the secondary electron current from the ion current, a method for which was discussed in Chapter 4. The total ion dose per pulse is plotted versus substrate bias in Figure 5-4. According to the dosimetry work in Chapter 4, approximately 92.5% of the ions implanted contain B. The expected sub-linear dependence of ion dose versus substrate bias can be seen in this data.

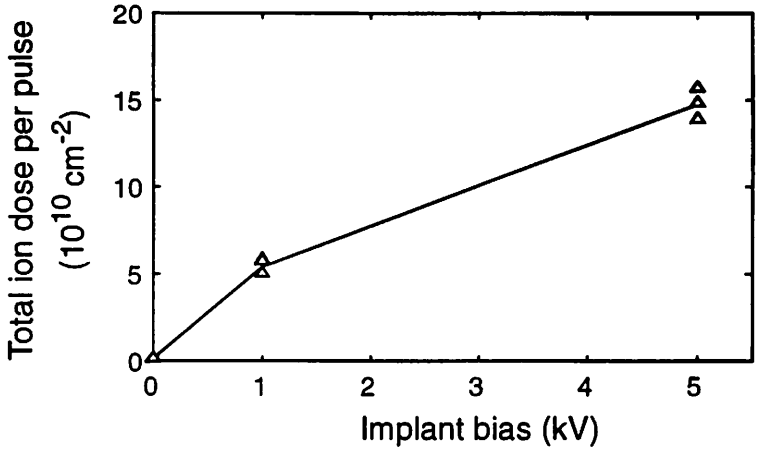

Figure 5-4. Total ion implant dose per pulse for BF_3 PIII pulses

BF_3 PIII at 1.5 mTorr pressure, 900 W power, 220 A magnet current. Dose values found by measuring total ion current and eliminating secondary electron component as in Chapter 4. Boron dose per pulse is approximately 92.5% of the total.

5.2.3 Dose saturation

As described in the previous chapter, the dose in Si will saturate after about one minute of implantation, as dopant introduction and removal due to etching reach a steady-state. The expected and measured saturation doses are shown in Figure 5-5. The saturation doses measured by SIMS are 1.4×10^{16} cm^{-2} for 5 kV and 3×10^{15} cm^{-2} for 1 kV, with a pulse repetition rate of 5 kHz. A combination of two effects makes the 5kV saturation dose higher: first, less dopant is lost to surface etching because the peak ion energy is higher and the profile is deeper. Second, the dose is higher because a higher dose of ions is implanted during the transient portion of the implant pulse (higher Q_{trans}). The saturation doses for the implant conditions in Figure 5-5 are large enough for MOSFET source/drain implants, and can be reached in less than 60 s implant time. The saturation dose can be raised by using plasma conditions with slower etch rates, higher implant bias voltage, or higher frequency.

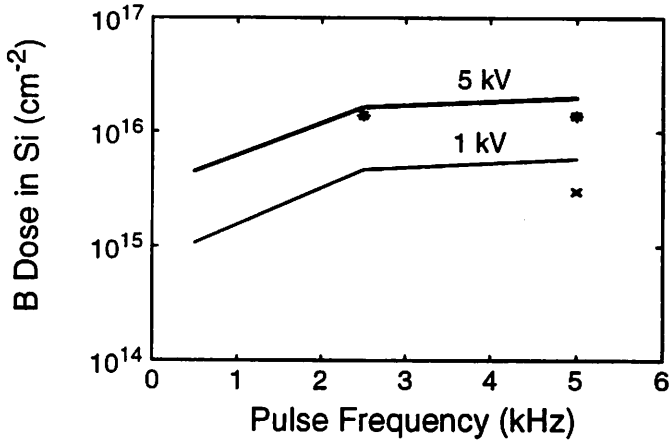

Figure 5-5. Dependence of dose saturation on substrate bias

BF_3 PIII implants at 1 kV and 5 kV with 900W, 1.5 mTorr pressure BF_3 plasma. Implanted for 10 min. to reach saturation dose. Solid lines are dose saturation levels calculated from implanter IV waveforms using measured Si etch rates. Stars (5kV) and cross (1kV) are integrated doses measured by SIMS.

5.3 Effect of implant pulse frequency on incorporated dose

Figure 5-5 predicts that higher frequency implantation will increase the incorporated dose. However, since both dose rate and etch rate increase with increasing ion frequency, the etch rate must be checked to confirm that a net dose gain will result. A 20% increase in dose between the 5 kV, 2.5 kHz and 5 kHz implants is expected from the simulation, but can not be resolved by the SIMS measurement. Figure 5-6 shows the estimated throughput of PIII for frequencies above those measured in the UCB system. The BF_3 PIII etching rates measured at 0-5 kHz are extrapolated to estimate etch rates for 10 kHz and above. Above 10 kHz, about 3 seconds is required to reach a $5x10^{15}cm^{-2}$ dose for 5 kV. For this energy, a repetition rate above 10 kHz need not be used. A higher repetition rate implant will require approximately the same time, but will attack the Si surface faster. For 1 kV implants, the highest possible repetition rate is required to approach the $5x10^{15}cm^{-2}$ dose mark. To do a low dose implant, below 10^{15} cm^{-2}, at these dose rates only a fraction of a second of implantation is needed. Sheet resistance measurements of the 1 kV and 5 kV BF_3 samples after 1060°C, 20 s RTA annealing in nitrogen confirm that the effect of the pulse frequency on incorporated saturation dose is slight (Figure 5-7).

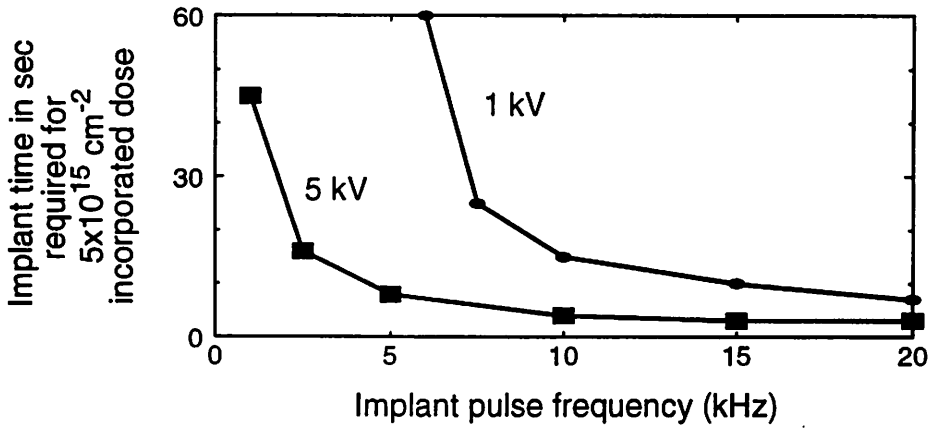

Figure 5-6. PIII throughput dependence on implant bias and frequency

Simulated time to reach $5x10^{15}$ cm^{-2} incorporated dose using measured etch rates for low frequencies and estimated etch rates for frequencies above 5 kHz. Per-pulse profiles generated from implanter IV waveforms used to predict behavior.

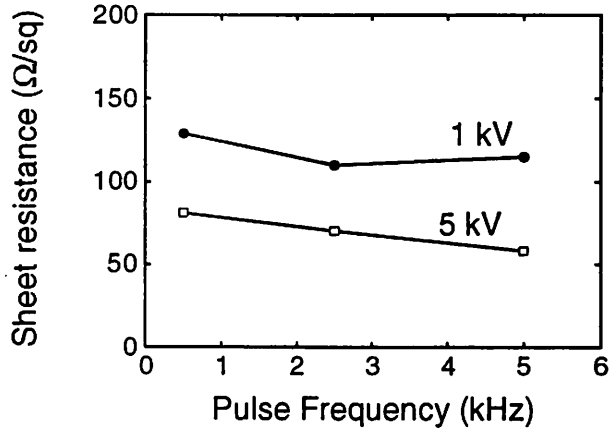

Figure 5-7. Variation in active dose with implant frequency

Measured sheet resistance values for UCB PIII samples implanted at varying energies and frequencies. Implantation done for 10 min. to reach saturation dose. Samples annealed at 1060°C for 20 s.

5.4 Effect of substrate bias on annealed profiles

With an eye toward meeting the predicted target of 10-45 nm junction depth for 0.1 μm VLSI devices, the junction depths of PIII-formed diodes at a background concentration of 10^{18} cm^{-3} made by different groups are shown in Figure 5-8. A correlation between junction depth and implantation voltage is apparent, even though the data come from three different junction profiling methods. The spread of the data is due mostly to variation in

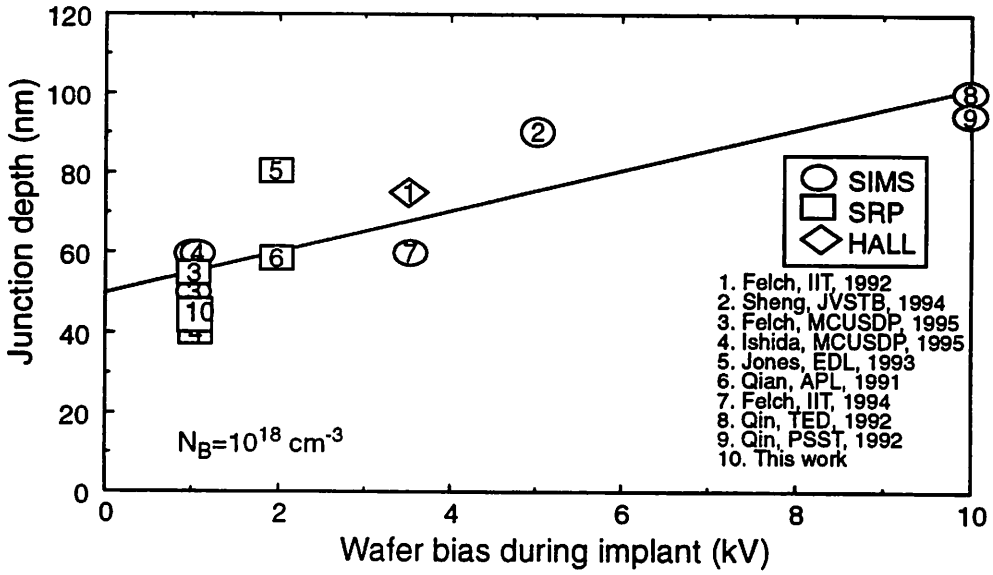

Figure 5-8. Correlation of junction depth after annealing to substrate bias
Junction depth defined at background (N_B) doping level 10^{18} cm^{-3}. Data from Refs. [5.6, 5.7, 5.9-5.11, 5.15, 5.16-5.18].

annealing cycles. The trend recommends the use of implant energies as low as possible for shallow junction formation, regardless of annealing cycle and whether preamorphization is used.

5.4.1 Junction depth

Spreading resistance profiles are shown in Figure 5-9 for shallow junction samples implanted with BF_3 PIII at 1kV and 5 kV and annealed identically, at 800°C for 20 s and then at 1000°C for 20 s. The deeper junction depth for the 5 kV implanted sample is caused by a number of factors. First is the higher dose of dopant in the 5 kV sample. The samples were implanted for 10 minutes, and each has reached the saturation dose, which is a function of substrate bias. The 5 kV sample has a dose 4.7 times higher than the 1 kV sample, and its as-implanted tail region extends about 50 nm deeper than the 1 kV sample, as shown in Figure 5-1. As 85% of the implanted species are BF_2^+, both of the implants are at high enough dose to cause amorphization of the substrate. As discussed in Section 1.3.1.2, transient enhanced diffusion is a function of the amount of substrate damage present after implantation, which can be expected to be sizable under the amorphous layer of these high-dose implants. This damage is a function of the implant energy and dose, and is expected to be more severe in the 5 kV case.

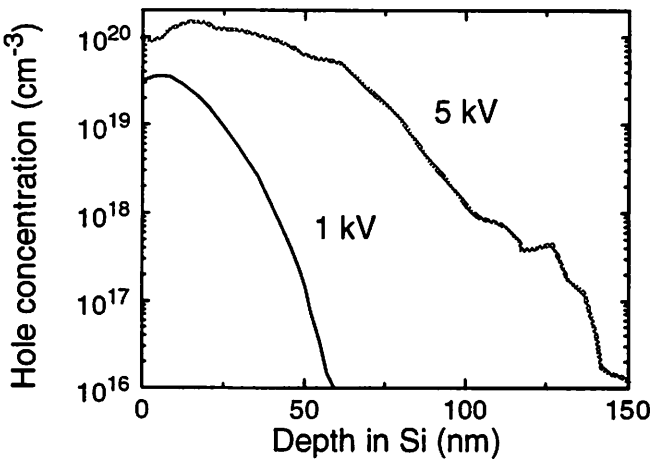

Figure 5-9. SRP junction depth dependence on substrate bias at saturation dose
Samples implanted at UCB with 1 kV and 5 kV BF_3 PIII to saturation dose. Annealed in two steps: 20 s at 800°C, and 20 s at 1000°C. Profiles measured by spreading resistance.

5.5 Effect of surface cleaning after PIII

As described in Section 5.2.1, a shallow dopant profile may be observed by SIMS whether the dopant was implanted at low energy or deposited on the surface. During low-power, low-frequency implantation, a B and F containing film may deposit on the wafer [5.25]. Films may also occur when the chamber has been contaminated with water. It is important to avoid deposition, as it can lead to reproducibility problems. The dose in Si after annealing is then a function of how the wafer is cleaned before annealing. Figure 5-10 shows this effect for 1 kV and 5 kV BF_3 PIII implanted wafers implanted by Vendor A and cleaned in by different procedures before annealing. Vendor A has a PIII chamber with an ICP ion source which operates at a nominal condition of 0.8 mTorr, 350-500 W RF power. This system uses 4 μs pulses with frequency up to 12.5 kHz. In Figure 5-10, either a de-ionized water rinse or normally non-Si attacking HF dip affect the resistivity. Hydrofluoric (HF) acid has been reported to etch heavily n^+ doped poly-Si at an extremely low rate of 0.7 nm/min., so the dopant removed in this short 10 second dip is more likely in the form of a deposited layer or B-Si alloy. Wafers that are cleaned in sulfuric acid/peroxide and then HF dipped lose a greater deal of dose, as this clean oxidizes and removes about the top 4 nm of Si. The resistivity of the 5 kV wafer increases sharply after HF dip but is the same for sulfuric acid oxidation plus HF dip. This indicates a surface film on this wafer, which is removed in an HF dip or acid clean. The deep H_2SO_4/H_2O_2 clean does not

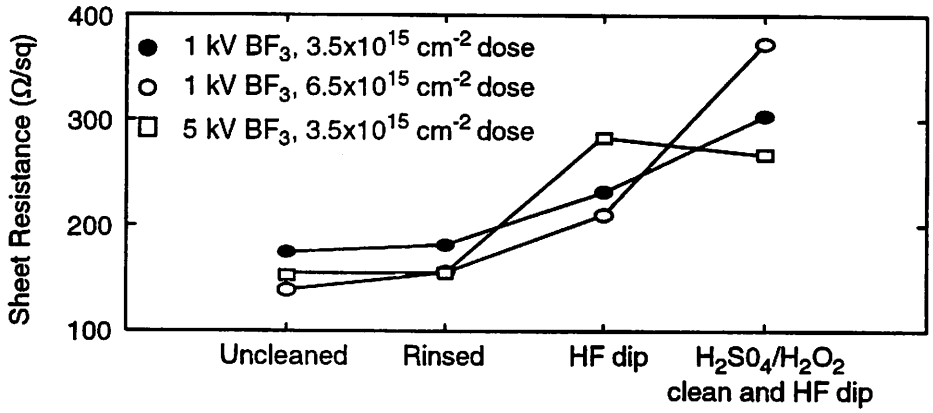

Figure 5-10. Effect of wafer cleaning and substrate bias on incorporated dose
Samples are cleaned with either a 5 min. de-ionized (DI) water rinse, 10 s hydrofluoric (HF) acid dip and DI water rinse, or standard 10 min. H_2S0_4/H_2O_2 clean, HF acid dip and DI water rinse

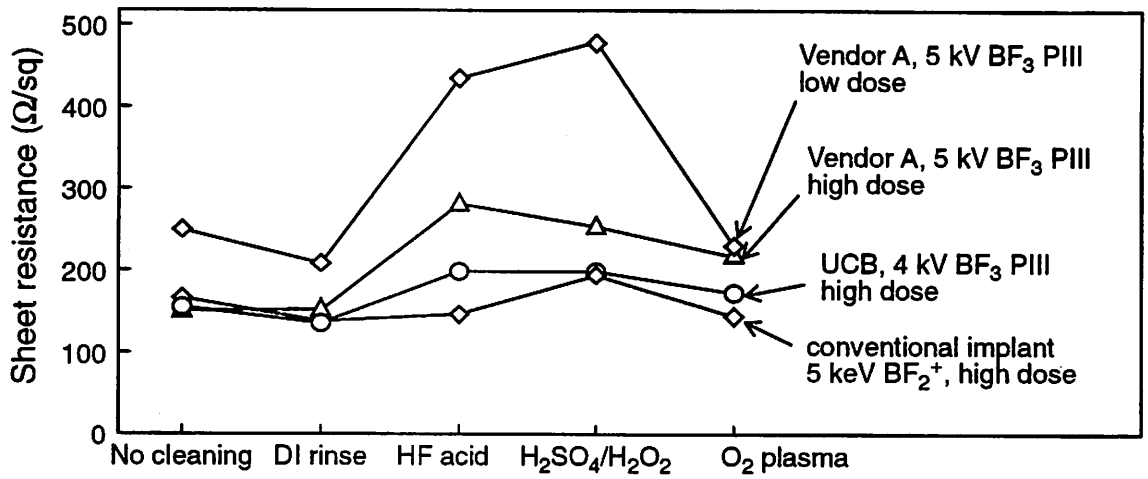

Figure 5-11. Effect of wafer cleaning and type of implant on incorporated dose
High implant dose ~$3x10^{15}$ cm^{-2}. Low implant dose ~ $2x10^{15}$ cm^{-2}.

change the resistivity from the HF case because the projected range of B implanted as a 5 kV BF_2^+ ion is more than 5 nm, and so most of the implanted dopant is deeper than the etch can reach. The dopant in the 1 kV case is much closer to the surface than 4 nm, so the dose is more seriously affected by the sulfuric acid clean.

A commonly used alternative to the H_2SO_4/H_2O_2 clean for removing residual organic material is an oxygen plasma scourge at 300 W for 2.5 minutes. The effect of the plasma cleaning process on dopant retention is shown in Figure 5-11. This figure compares the sheet resistance of a conventionally implanted sample, a sample from Vendor A,

and a UCB PIII sample, all implanted at approximately the same dose and substrate bias. With no cleaning or just a DI rinse, the three samples show approximately the same sheet resistance. With an HF dip or O_2 plasma clean, the resistivity of the conventional implant does not change. The UCB sample, which is implanted in a etching plasma condition and has little surface deposition, loses a small amount of dose. The Vendor A sample loses more. This indicates that the Vendor A sample either has more surface deposition or a lower effective energy of implant. For the sample with lower dose, the variations in dose retention with cleaning are more pronounced.

5.6 Effect of annealing conditions

The main factor determining the final junction depth is the anneal sequence. Choosing an annealing sequence for ultra-shallow junctions implanted by PIII must take into account the considerations of activation, damage removal, and junction movement. The first two require a significant thermal budget, and a shallow junction depth requires a minimal one. The doses implanted by PIII are typically above the amorphization threshold, so the annealing cycle for the PIII-implanted junctions must be sufficient to dissolve end-of-range (EOR) defects which are formed when the supersaturated concentrations of Si self-interstitials below the amorphous/crystalline interface collapse into extrinsic dislocation loops. The annealing behavior of the defects depends on the annealing ambient, the defect concentration, the surface proximity, stress at wafer pattern edges, and the concentration of contaminants in the Si [5.26]. Contaminants like O and F have been reported to pin EOR defects, making them harder to anneal out (see Section 5.8). Elimination of these defects is especially important for ultra-shallow junctions, for which the *pn* junction depletion region may be only a few hundred angstroms from the EOR defect sites. The defects are likely sources of deep-level generation centers that will increase the leakage current of junctions. According to Figure 1-10, the advantage of PIII implanted junctions is their surface proximity. The time needed for complete defect annealing decreases when the defects are close to the surface, which can act as a sink for the excess interstitials [5.27, 5.28].

As mentioned in Section 1.3.1.2, increasing the dose rate to get deeper amorphization during implant and utilizing two-step annealing profiles are two ways that small decreases in junction depth can be achieved using conventional implantation. With PIII, the dose rates are already much higher than conventional implantation. The following sec-

tions show effects of one- and two-step annealing on implant resistivity and junction depth.

5.6.1 One-step annealing

Junction properties with annealing are studied by sheet resistance and spreading resistance measurements. Figure 5-12 shows the sheet resistance of samples annealed for 20 s at varying temperatures. For 5 kV, the difference between annealing at 1000°C and 1060°C is small, but for 1 kV samples, 1060° C is needed to minimize the resistance. For both samples, the active dose after annealing at 1100°C is shown to be smaller than after 1060°C. This could be due to some dopant evaporation from the near-surface layers at the elevated temperature, but is more likely due to gettering of the dopant in electrically inactive B precipitates near the implant peak. B precipitation has been shown to occur in con-

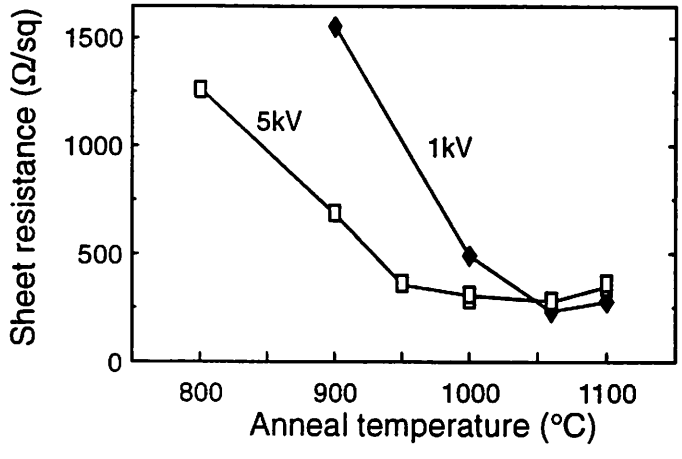

Figure 5-12. Isochronal annealing of BF_3 PIII implants

Annealing for 20 s in nitrogen. Samples implanted by Vendor A with BF_3 PIII at dose 3.5×10^{15} cm^{-2}. RF plasma power 350-500W, pulsing at 12.5kHz.

ventionally implanted samples in which the dopant exceeds the solubility limit (0.8-1.7×10^{20} cm^{-3} at 1000°C) [5.26]. Precipitation is more likely for higher temperature annealing, for higher implant doses, and in samples which have been amorphized. Figure 5-13 shows isothermal annealing of samples implanted at 4 kV and annealed at 1000-1050°C. 1050°C is more effective for activating dopant. Dopant activation increases only slowly after the first few seconds. Since increasing the anneal time from 10 to 20 seconds only slightly improves the sheet resistance for 1000°C and may degrade it at 1050°C, using an

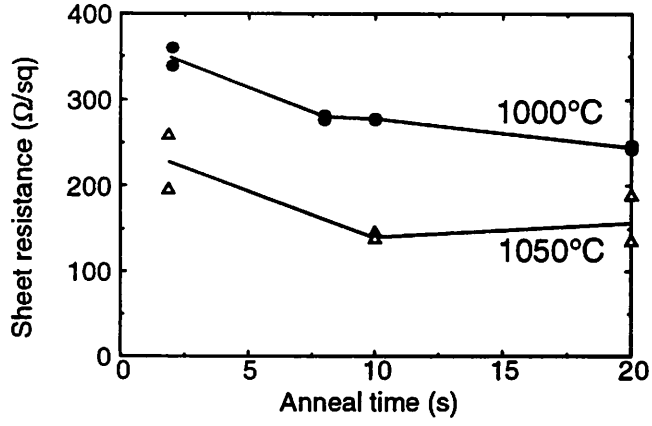

Figure 5-13. Isothermal annealing of BF_3 PIII implants

Samples implanted in UCB reactor with 4 kV, 5 kHz BF_3 PIII, in 900 W, 1.5 mTorr plasma, for 30-60 s. Rapid thermal annealing in N_2.

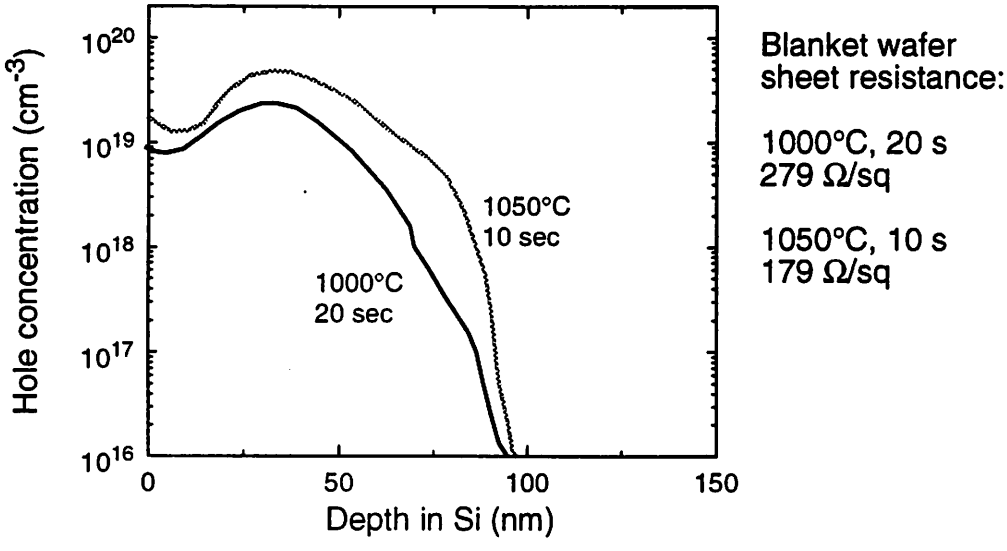

Figure 5-14. Variation in junction depth with anneal temperature

Samples implanted with 1kV BF_3 PIII at $3x10^{15}cm^{-2}$ dose at UCB. Implantation in 900 W, 1.5 mTorr plasma. Annealed in nitrogen RTA.

anneal of 8-10 seconds is preferred to minimize diffusion. Two-second annealing is not enough to ensure sheet resistance below 200 Ω/sq.

Spreading resistance profiles are shown in Figure 5-14 for 1 kV BF_3 implanted samples that are annealed for 20 s at 1000°C or 10 s at 1050°C. The short 1050°C anneal causes higher activation and larger dopant movement than the longer anneal at lower temperature, as expected from the sheet resistance data. The drop in the hole concentration near the surface is caused by an increase in the measured sheet resistance of the samples, and

may be due to B precipitation in the area of the implant peak. Transient enhanced diffusion below the 10^{19} cm^{-3} level, high concentration enhanced diffusion, and increased activation at 1050°C are seen to make the profile more uniform without increasing the junction depth by much. The junction depth at background concentration of 10^{17} cm^{-3} is 90 nm for the 10 s 1050°C anneal, and 84 nm for the sample annealed at 1000°C for 20 s.

5.6.2 Two-step annealing

Two-step annealing has been reported for both PIII and conventional implant profiles, with improvements in junction depth up to 10 nm. An RTA pre-anneal at 750-800°C [5.11] or furnace pre-anneal at 600°C for 30 min. have been explored [5.29]. These works postulated that the pre-anneal cycle allows some movement and recombination of point-defects at a temperature too low for dopant diffusion. In this work, a pre-anneal cycle of 800°C for 20 s was used to test the application of two-step annealing to the PIII samples. It was shown in Figure 5-12 that the 800°C anneal only causes a small amount of activation of the dopant. Figure 5-15 shows the effect of the two-step anneal on sheet resistance. In all cases, the use of a pre-anneal reduces the sheet resistance, in most cases, by 100 Ω/sq. For both 1 kV and 5 kV, the pre-anneal reduces the resistance after a 1000°C anneal to a value comparable to the value after a 1050°C one-step anneal.

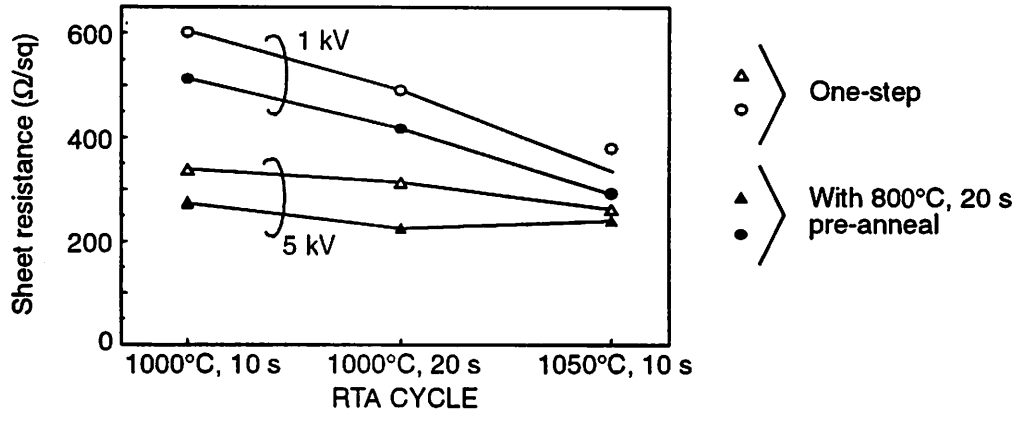

Figure 5-15. Effect of two-step anneal on sheet resistance
Samples implanted with 1 kV and 5 kV BF_3 PIII by Vendor A. Dose=$3.5x10^{15}cm^{-2}$.

SRP profiles are shown in Figure 5-16 for the 1000°C one-step and two-step annealed samples. The profiles show that the two-step anneal cycle does yield a shallower junction for these implant conditions. The pre-annealed junction has a depth of 50-60 nm

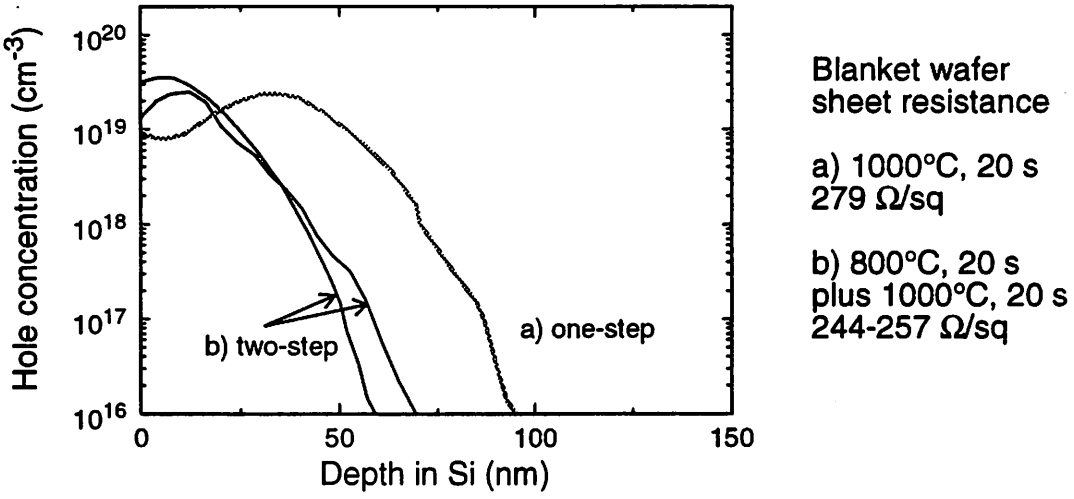

Figure 5-16. Variation in junction depth with two-step anneal

Spreading resistance profiling of samples implanted with 1 kV BF_3 PIII at $3x10^{15}cm^{-2}$ dose at UCB. Implantation in 900W, 1.5 mTorr plasma. Annealed in nitrogen RTA for a) 20 s at 1000°C, and b) 20 s at 800°C and 20 s at 1000°C. The two profiles for the two-step annealed sample were provided by different spreading resistance vendors.

at a background concentration of 10^{17} cm^{-3}, 24-34 nm shallower than the sample annealed in a 1000°C cycle only. No sign of precipitation is seen, and the dopant activation is high almost all the way to the surface. The small dip in the carrier concentration near the surface of the two-step samples can be attributed to spreading resistance surface effects. It is clear from Figure 5-16 that transient enhanced diffusion is drastically reduced in two-step annealing of these samples. According to Figure 1-10, a 10 s 800°C anneal cycle can remove EOR damage 8 nm deep from BF_2^+ implants. If EOR loops were to form in the 1 kV PIII samples, they would be slightly deeper than the projected range of most of the dopant in the PIII samples. The dopant in the 1 kV PIII samples should be closer to the surface than the projected range of a 1 kV $^{11}B^+$ ion, which is about 5 nm. This means that the 800°C pre-anneal cycle is likely sufficient for the EOR loops to dissolve and for the excess interstitials to migrate to the Si surface. When the high temperature anneal step begins, the interstitial concentrations are low, and the diffusion transient is minimal, leading to a significantly shallower junction. This improvement in the junction depth after annealing is due to the shallowness of the implanted dopant and the length of the pre-anneal. If the pre-anneal were shorter or the implant deeper, the 800°C cycle might not be sufficient to remove the implant damage.

5.7 Effect of machinery

As described in Chapter 4, the as-implanted distribution of dopant is a function of the implant waveforms, ion species and density in the plasma, collisionality in the plasma, and substrate etching rates. All these parameters vary from system to system, as different plasma sources, reactor geometry, operating conditions, and pulsers may be used. Figure 5-17 shows 5 kV as-implanted BF_3 PIII profiles from three different reactors. The integrated dose of these profiles has been normalized to $2.6x10^{15}$ cm^{-2} to show the differences in the profile shapes. The Vendor A sample is implanted in a ICP ion source with pulse width of 4 μs, gas pressure of 0.8 mTorr and repetition rate of 12.5 kHz. The Vendor A profile is similar in shape to the UCB profile, which was implanted in ECR plasma at pressure around 2 mTorr using 1 μs pulses and a repetition rate of 5 kHz. As described

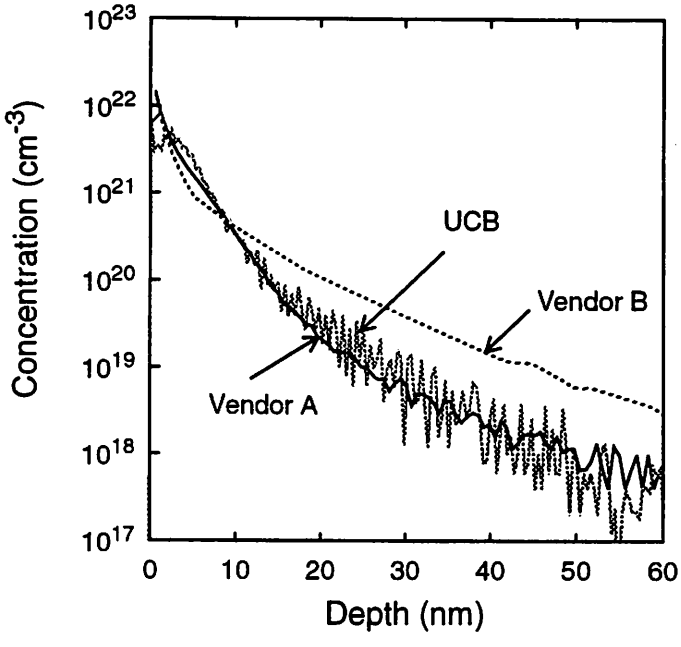

Figure 5-17. Comparison of as-implanted profiles from different PIII apparatuses
SIMS profiles of B implanted by 5 kV BF_3 PIII at UCB, Vendor B [5.10]and Vendor A. Dose normalized to $2.6x10^{15}$ cm^{-2} for Vendor A sample. UCB profile generated from per-pulse profile extracted from SIMS data of 5kV, 5kHz BF_3 PIII implant at 10^{16} cm^{-2} dose.

previously, the UCB profile is influenced by a long pulse fall time causing a low mean implant energy and 85% BF_2^+ implant species. The Vendor B sample is implanted in a PIII reactor with a dc plasma source with gas pressure of 1 mTorr, using 20 μs pulses with 1

kHz repetition rate. This profile indicates that the implanted boron in the Vendor B system have either higher peak implant energy, a greater fraction of high energy components, lower collisionality, or a greater fraction of B^+ ion species than the other two. The 20 μs long implant pulse probably raises the mean energy of the implant. Collisional effects are not expected at the relatively low pressures used in these systems.

5.8 Effect of fluorine

Use of BF_2^+ conventional implantation or BF_3 PIII results in high concentrations of F in the substrate. As F is has very low solubility in the Si lattice, a high fluorine concentration can cause defects in the Si during annealing. Two kinds of defects have been observed. One type occurs during SPE regrowth of the amorphized surface during annealing. The SPE proceeds from the amorphous/crystalline (α/c) interface and proceeds toward the surface. As F cannot be incorporated in the lattice due to low solubility, it is pushed up into the remaining α-Si. When the concentration of F in the α-Si grows too high, the F may precipitate. This can cause stacking errors in the growing layer and local "bubbles" of trapped F. These F precipitates usually occur near the projected range of the implant. F which is implanted below the α/c interface may be gettered by the EOR range loops as they form [5.30].

Figure 5-18 shows the as-implanted F position (a - c) and F movement during annealing (d - f) in samples implanted by BF_3 PIII from 5-20 kV. All samples show a B surface peak after annealing, due to SIMS artifacts, some surface deposition, or precipitation. For samples implanted below 20 kV, the 20 sec., 1000°C annealing cycle used is sufficient for all F to diffuse out of the substrate. After annealing, the F concentrations are below the SIMS detection limit. The effect of F can only be seen in the 20 kV BF_3 PIII implant, where a second, sub-surface B and F peak develop during annealing. This peak is located about 30 nm deep. As the projected range for a B atom implanted as BF_2^+ is about 16 nm and the range of a F atom from BF_2^+ is 18 nm, this is likely the location of the EOR defects. It can be plainly seen that F is gettered at these sites. The EOR loops may be harder to anneal out in this sample because they are larger, due to the higher damage done by a higher energy implant, or because the F at the EOR sites pins the defects, making them even more difficult to dissolve.

As F supersaturation in an implanted sample can cause extended defects or defects that affect the effective diffusivity of B, it is preferable to implant at as low an energy as

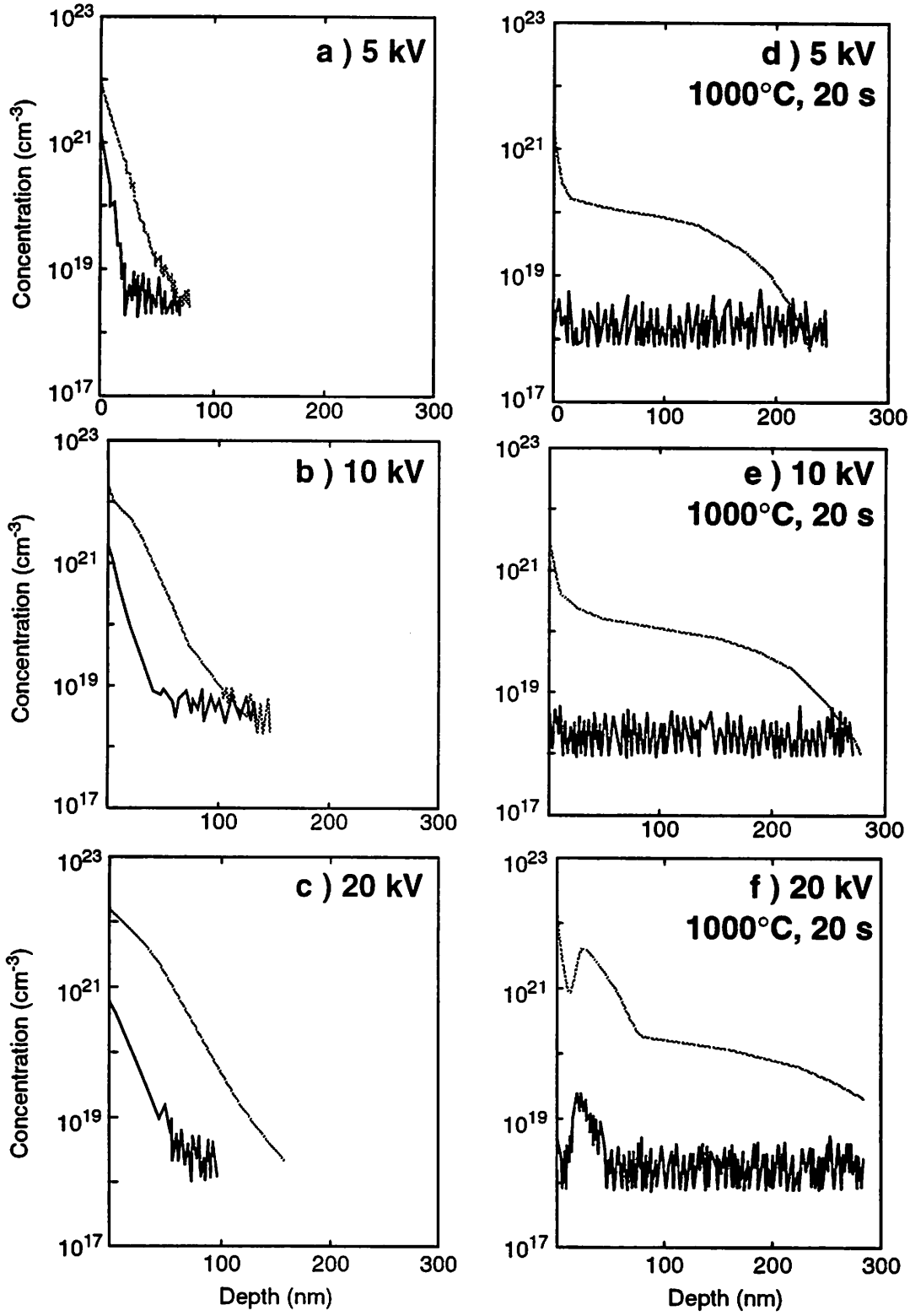

Figure 5-18. Dependence of fluorine outdiffusion on substrate bias in BF_3 PIII

Samples implanted at UCB with BF_3 PIII at varying bias voltage. a) - c) are as-implanted samples, and d) - f) are rapid thermal annealed at 1000°C for 20 s. Dashed line is boron, solid line is fluorine.

possible when a high implant dose is needed. When a BF_3 PIII implant is done below 10 kV, the F diffuses out of the Si entirely in a 1000°C, 20 s RTA cycle, and there is no observed impact of the F on the dopant profile.

5.9 PIII vs. conventional implantation

For very low energy implantation, conventional implantation exhibits many of the complications that are perceived as problems in PIII implantation. Low-energy conventional implant beams often contain a significant fraction of energy contamination and metallic contamination, and exhibit non-uniformity due to beam broadening. Figure 5-19 is a comparison of implant profiles from 5kV BF_3 PIII and 5 keV conventional BF_2^+ implantation from [5.31]. Since a low-energy conventional implant profile at the same high PIII dose was not available, the PIII concentrations are normalized to the same dose using an

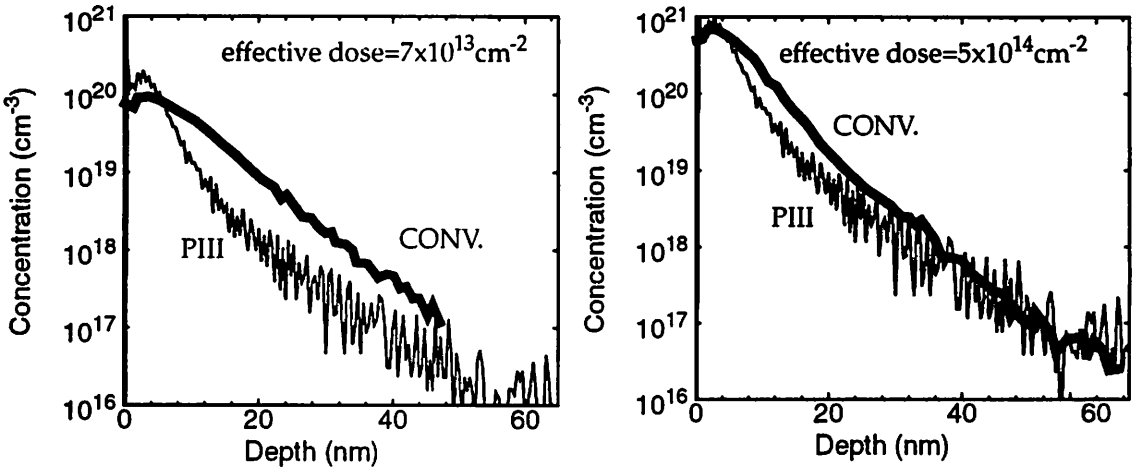

Figure 5-19. Comparison of PIII and conventional implant profiles at 5 kV
Conventional BF_2^+ implant profiles from $7x10^{13}cm^{-2}$ and $5x10^{14}$ cm^{-2} implants [5.31]. PIII profiles calculated from per-pulse profile extracted from 5kV, 5kHz, $1.4x10^{16}$ cm^{-2} dose BF_3 PIII.

extracted per-pulse profile. The comparison is not perfect, as the PIII profile is based on 10^{16} cm^{-2} implantation, which is far above the necessary dose for amorphization. For the conventional implant profiles, the $7x10^{13}cm^{-2}$ dose is well below the amorphization threshold and $5x10^{14}$ is the threshold dose. It can be seen that the tail region of the conventional profiles does not change appreciably as the dose is raised to $5x10^{14}$ cm^{-2}. For higher dose, the tail profile of the conventional implant should not change further. The implant

tail regions in the conventional and PIII profiles match in the $5x10^{14}$ cm^{-2} case, so it can be inferred that the small fraction of B^+ ion species that exist in the BF_3 PIII plasma does not make the profile deeper than a 5 keV conventional BF_2^+ implant. From 8-36 nm in depth, the PIII profile has a lower concentration. This is because of the high surface concentrations measured for the PIII sample, which may not be precise. As mentioned, these profiles were normalized to the same dose, and so the high surface peak seen by SIMS may skew the profiles. In any case, as the dose increases, the conventional implant profile looks more like the PIII implant profile.

Profiles for conventional BF_2^+ and BF_3 PIII implants at 1kV are shown in Figure 5-20. These are as-measured, un-normalized SIMS plots. The conventional implant was done to a dose of $10^{15}cm^{-2}$, and the PIII implant was done to the saturation dose. From the

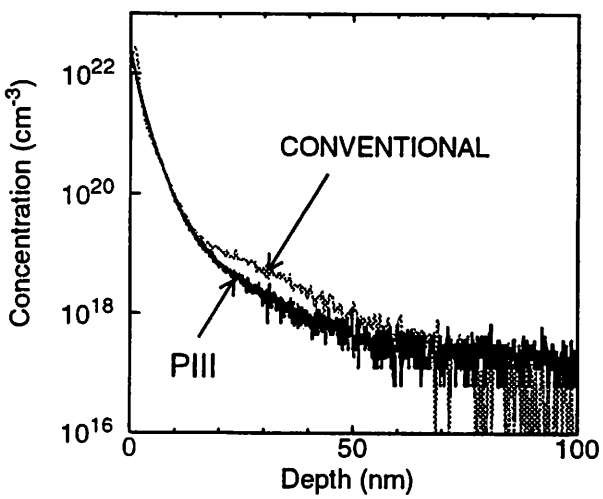

Figure 5-20. Comparison of PIII and conventional implant profiles at 1 kV
PIII sample implanted by 1 kV UCB BF_3 PIII, 900W, 1.5 mTorr, to saturation dose, measured by SIMS at $3.11x10^{15}cm^{-2}$. Conventional implant is 1 kV BF_2^+ implanted to expected dose $10^{15}cm^{-2}$ [5.32]. SIMS measures dose at $3.7x10^{15}cm^{-2}$.

integrated SIMS data, the doses are estimated at $3.1x10^{15}$ cm^{-2} for PIII and $3.7x10^{15}$ cm^{-2} for the conventional implant. As the SIMS data was provided by the same vendor, the SIMS dose errors should be reproducible (± 5%), and so it is valid to compare the characteristics of the profiles, especially in the tail regions. If SIMS had not been provided by the same vendor it would be difficult to compare the profiles, as most of the dose is contained within the first few tens of Angstroms, where the SIMS measurement is in its transient stage, and concentration conversion factors are not reliable. As shown in Figure 5-21, more

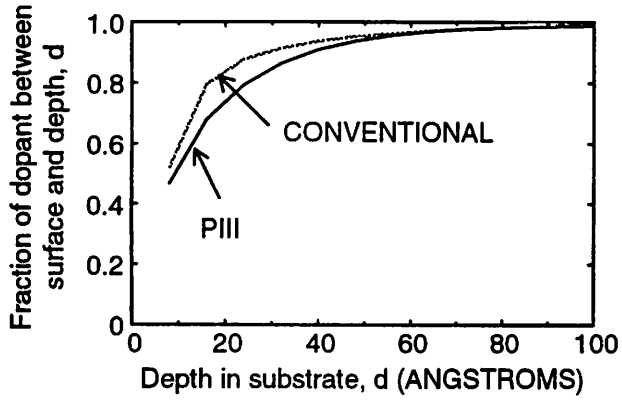

Exclusion	Conv.	PIII
total dose	371	311
4 nm	24.0	28.0
10 nm	4.4	3.1

dose in 10^{13} cm^{-2}

Figure 5-21. Proximity of dopant to surface in 1 kV implantation

More than 90% of dopant in Figure 5-20 is located within 4 nm of Si surface for both conventional and PIII implant.

than 93% of the conventionally implanted dopant is located within 4 nm of the surface; for PIII, 91% of the dopant is in this region. Below 10 nm, there is less than $5x10^{13}$ cm^{-2} dopant present in both samples. The implant profiles look very similar in the top 20 nm, especially between 10-20 nm in depth where the dose conversions should be consistent for both samples. From 20-50 nm in depth, the conventional profile has a higher concentration, which may be due to B channeling or neutral contamination of the implanting ion beam. This component may be absent in the PIII implant because the higher dose rate causes faster preamorphization and reduces channeling. PIII will not have any high energy contamination, because the ions are extracted from the plasma by the implant bias. The shallowness of the PIII profile is encouraging, given that 10% of the dopant implanted with PIII may have been implanted as B^+ ion species. Apparently, even with the complexities of multiple ion species implantation and waveform-dependent energy distribution, PIII produces a profile which is very similar to the conventional implanter in this energy range.

5.10 Conclusion

The preceding sections show the ease of using PIII processing in place of conventional implantation for shallow junctions. Since the dose rate of PIII can be very high, advantages seen for high dose-rate conventional implantation are seen for PIII. Dose rate is increased by increasing plasma power or increasing implant substrate bias. As final junction depth is tied to implant energy, low energy should be used. To maintain reproducibility of shallow PIII implant doses, it is important that surface deposition be avoided.

This is done by controlling plasma parameters and performing the implant at high frequency, for a total implant time of a few seconds. Shallow junctions with electrical junction depth of 50 nm and surface concentration above $2x10^{19}$ cm^{-3} can be made simply, by 1 kV implantation and two-step annealing at 800°C for 20 s and 1000°C for 20 s.

5.11 References

[5.1] B. Mizuno, I. Nakayama, N. Aoi, and M. Kubota, "Plasma doping into the side-wall of a sub-0.5 mu m width trench," in Ext. Abstr. of 19th Conf. Sol. St. Dev. Mater., Tokyo, Japan: Bus. Center Acad. Soc. Japan, pp. 319-322, 1987.

[5.2] B. Mizuno, I. Nakayama, N. Aoi, and M. Kubota, and T. Komeda, "New doping method for sub-half-micron trench sidewalls by using an electron cyclotron resonance plasma," Appl. Phys. Lett., 53 (21), pp. 2059-2061, 1988.

[5.3] H. Wong, X.Y. Qian, D. Carl, N.W. Cheung, et al, "Plasma immersion ion implantation for impurity gettering in silicon," in *Ion Beam Processing of Advanced Electronic Materials*, ed. by N.W. Cheung, Pittsburgh: Mater. Res. Soc., pp. 91-96, 1989.

[5.4] X. Y. Qian, D. Carl, J. Benasso, N. W. Cheung, et al, "A plasma immersion ion implantation reactor for ULSI fabrication," Nucl. Instrum. Meth. Phys. Res., B55 (1-4), pp. 884-887, 1991.

[5.5] X. Y. Qian, N. W. Cheung, M. A. Lieberman, and M. I. Current, "Sub-100 nm p^+n junction formation using plasma immersion ion implantation," Nucl. Instrum. & Meth. in Phys. Res., Section B, B55 (1-4), pp. 821-825, 1991.

[5.6] X. Y. Qian, N. W. Cheung, M. A. Lieberman, and S. B. Felch, "Plasma immersion ion implantation of SiF_4 and BF_3 for sub-100 nm p^+/n junction fabrication," Appl. Phys.Lett., 59 (3), pp. 348-350, 1991.

[5.7] E.C. Jones and N.W. Cheung, "Characteristics of sub-100-nm p^+/n junctions fabricated by plasma immersion ion implantation," IEEE Electron Dev. Lett., 14 (9), pp. 444-446, 1993.

[5.8] S. B. Felch, R. Brennan, S. F. Corcoran, and G. Webster, "A Comparison of three techniques for profiling ultra-shallow p^+-n junctions," Nucl. Instrum. Meth. Phys. Res., B74 (1-2), pp. 156-159, 1993.

[5.9] S. B. Felch, T. Sheng, C. B. Cooper III, "Characterization of a plasma doping system" in *Ion Impl. Tech. 92*, Amsterdam: North-Holland, pp. 687-690, 1993.

[5.10] T. Sheng, S. B. Felch, C. B. Cooper III, "Characteristics of a plasma doping system for semiconductor device fabrication," J. Vac. Sci. Tech., B12 (2), pp. 969-972, 1994.

[5.11] S.B. Felch, T. Sheng, E. Ganin, K.K. Chan, D.L. Chapek, R.J. Matyi, and J.R. Conrad, "Studies of ultra-shallow p^+-n junction formation using plasma doping," in *Ion Impl. Tech. 94*, Amsterdam: North-Holland, pp. 981-984, 1995.

[5.12] S. B. Felch, R. Brennan, S. F. Cororan, and G. Webster, "A comparison of three techniques for profiling ultra-shallow p^+-n junctions," Sol. St. Tech., 36 (1), pp. 45-47, 50-51, 1993.

[5.13] D. L. Chapek, J. R. Conrad, R. J. Matyi, and S. B. Felch, "Structural characterization of plasma-doped silicon by high resolution X-ray diffraction," J. Vac. Sci. Tech., B12 (2), pp. 951-955, 1994.

[5.14] R. J. Matyi, D. L. Chapek, J. R. Conrad, and S. B. Felch, "Structural analysis of silicon doped by plasma source ion implantation," In *Materials Synthesis and Processing Using Ion Beams Symposium*, ed. by R. J. Culbertson, Pittsburgh: Mater. Res. Soc, pp. 1017-1022, 1994.

[5.15] S. B. Felch, D. L. Chapek, S. M. Malik, P. Maillot, et al, "Comparison of different analytical techniques in measuring the surface region of ultra-shallow doping profiles," J. Vac. Sci. Tech., B14 (1), pp. 336-40, 1996.

[5.16] E. Ishida, "Study of electrical measurement techniques for ultra-shallow dopant profiling," J. Vac. Sci. Tech., B14 (1), pp. 397-403, 1996.

[5.17] S. Qin, C. Chan, and N. E. McGruer, "Energy distribution of boron ions during plasma immersion ion implantation," Plasma Sources, Sci. and Tech., 1 (1), pp. 1-6, 1992.

[5.18] S. Qin, N. E. McGruer, C. Chan, and K. Warner, "Plasma immersion ion implantation doping using a microwave multipolar bucket plasma," IEEE Trans. on Electron Dev., 39 (10), pp. 2354-2358, 1992.

[5.19] S. Qin and C. Chan, "Plasma immersion ion implantation doping experiments for microelectronics," J. Vac. Sci. Tech., B12 (2), pp. 962-968, 1994.

[5.20] J. Shao, S. Qin, Z. Zhao, C. Chan, "Etching and charging effects on dose in plasma immersion ion implantation," in *Beam-Solid Interactions for Materials Synthesis and Characterization*, ed. by D. C. Jacobson, Pittsburgh: Mater. Res. Soc., pp. 111-116, 1995.

[5.21] J. Shao, M. Round, S. Qin, C. Chan, "Dose-time relation in BF_3 plasma immersion ion implantation," J. Vac. Sci. Tech., A13 (2), pp. 332-334, 1995.

[5.22] T. Hara, S. Nakagawa, K. Shinada, S. Nakamura, "Formation of shallow p^+ layer in silicon by plasma doping," Appl. Phys. Lett., 63 (1), pp. 90-92, 1993.

[5.23] T. Hara, K. Shinada, S. Nakamura, "Damage formed by plasma boron doping in silicon," Jpn. J. of Appl. Phys., 33 (10, pt. 1), pp. 5608-5611, 1994.

[5.24] B. Mizuno, to be published in Surf. Coat. Technol., 1996.

[5.25] N.W. Cheung, M.A. Lieberman, C.A. Pico, R.A. Stewart, J.Tao, M.H. Kiang, C. Yu, V. Vahedi, B. Troyanovsky, W. En, E. Jones and J. Benasso, "Plasma Immersion Ion Implantation (PIII) for Integrated Circuit Manufacturing: Second Quarterly Progress Report," Report UCB/ERL, M91/63, 1991.

[5.26] T.O. Sedgwick, A.E. Michel, V.R. Deline, and S.A. Cohen, and J.B. Lasky, "Transient boron diffusion in ion-implanted crystalline and amorphous silicon," J. Appl. Phys, 63 (5), pp. 1452-1463, 1988.

[5.27] R.B. Fair, "Junction formation in Silicon by Rapid Thermal Annealing," in *Rapid Thermal Processing Science and Technology*, ed. by R.B. Fair, New York: Academic Press, pp. 169-226, 1993.

[5.28] E. Myers, J.J. Hren, S.N. Hong, and G.A. Ruggles, "Damage Removal of low energy ion implanted BF_2 layers in Silicon," in *Ion Beam Processing of Advanced Electronic Materials*, Pittsburgh: Mat. Res. Soc., pp. 27-32, 1989.

[5.29] M. Craig, A. Sultan, K. Reddy, S. Banerjee, et al, "Dose rate and thermal budget optimization for ultrashallow junctions formed by low-energy (2-5 keV) ion implantation," J. Vac. Sci. Tech., B14 (1), pp. 255-259, 1996.

[5.30] K.S. Jones and G.A. Rozgonyi, "Extended defects from Ion Implantation and Annealing," in *Rapid Thermal Processing, Science and Technology*, ed. by R.B. Fair, New York: Academic Press, pp. 123-168, 1993.

[5.31] K.B. Parab and A.F. Tasch, "Analysis and Modeling of Low Energy Implanted Ultra-Shallow Dopant Profiles," in Proc. of National Implant Users Meeting, 1995.

[5.32] A. Sultan, private communication.

6 Shallow junction formation with PIII using preamorphization

6.1 Introduction

Preamorphization is studied for two reasons: first, when dopant is implanted into an amorphous layer, B channeling is suppressed. Second, the amorphous silicon is regrown by solid phase epitaxy (SPE) during an annealing step. The SPE-regrown Si should have fewer defects than Si implanted at a sub-amorphizing dose, so transient enhanced diffusion should be lower in that layer. These effects have been observed in many experiments: activated dopant in pre-amorphized and re-crystallized Si is usually higher than the activated fraction of boron implanted into a crystalline silicon layer [6.1], and many groups have reported shallower junctions using pre-amorphized Si. The challenge of this project is to demonstrate the use of PIII for shallow junction preamorphization, and design a process flow for an ultra-shallow P^+/N junction that minimizes residual damage in the Si and keeps it away from the metallurgical junction to achieve a leakage current as low as the industry standard of 1 nA/cm^2.

6.2 Experiment

Shallow junctions are formed with PIII using a two-step implant: first, heavy ions (SiF_x^+ (x=1-4), Si^+ and F^+) are implanted into the crystalline Si substrate using SiF_4 PIII. A dose on the order of 10^{15} cm^{-2} is sufficient to convert the Si surface to amorphous Si (α-Si) with this implant. The SiF_4 implants are done with a 300 W, 5 mTorr plasma, with etch rates during pulsing around 1.2 nm/minute for oxide. In this chapter, SiF_4 PIII is performed with bias voltages from 4 - 8 kV and with pulse frequency 1 - 2 kHz. The implants are done for 10 min. to reach the saturation dose. Boron is then implanted into the α-Si with substrate bias 1 - 5 kV. Dopant is implanted for 15 min. to reach the saturation dose either with 5 kHz pulsing or DC implantation. The nominal BF_3 plasma condition is 1

mTorr, 650-750 W. The Si etching rate at this condition is lower than the values cited at 1-3 mTorr, 900 W in Chapter 3. The amorphous layer is recrystallized and the dopant is activated in a single rapid thermal annealing (RTA) cycle in nitrogen.

Since amorphization can be caused by any of the species in the SiF_4 PIII implant, the depth of the amorphous layer is related to the projected range of Si^+ or F^+ ions, which penetrate the deepest. Projected range values from the simulator TRIM are listed in Table 6-1 for the energies used in this experiment [6.2]. The amorphous layers are expected to be about 85 - 150 A deep for the 4 - 6 kV SiF_4 PIII. The 1 - 5 kV bias for BF_3 PIII is chosen so that most of the dopant, which should be within $R_p + 2\Delta R_p$ of the surface, will be located inside the amorphous layer. The majority of the dopant in a PIII implant should be even shallower than these values suggest since the multiple species present and the energy distribution of the PIII implant introduce low energy components, as described in Chapter 4.

Implant Energy	Si^+ ion R_p /R_p+2ΔR_p	F^+ ion R_p /R_p+2ΔR_p	B^+ ion R_p /R_p+2ΔR_p	B from BF_2^+ R_p /R_p+2ΔR_p
1 keV			53 / 131 A	19 / 49 A
2 keV	52 / 112 A	62 / 138 A	91 / 217 A	32 / 82 A
4 keV	85 / 177 A	105 / 225 A	162 / 368 A	49 / 123 A
5 keV	100 / 206 A	126 / 266 A	198 / 440 A	57 / 141 A
6 keV	115 / 233 A	146 / 306 A	233 / 511 A	66 / 162 A

Table 6-1. Maximum possible range and straggle in Angstroms of implanted ions in Si

6.3 Preamorphization Depth

Rutherford backscattering (RBS) channeling and transmission electron microscopy were used to measure the depth of the amorphous layer created by SiF_4 PIII. Channeling results using a 1.95 MeV $^4He^+$ beam with 105° backscattering angle are shown for 4 kV and 6 kV implants in Figure 6-1. The peak at the right hand side is due to the α-Si layer. Using the width of this peak, the amorphous layer thickness is calculated as 10 nm for 4kV, and 14 nm for 6 kV SiF_4 implantation. The small surface peak seen on a pristine Si wafer with native oxide is about 4 nm, so the height and width of these peaks can be ascribed to disorder caused by implantation. TEM micrographs confirm the amorphous layer thickness for the 4 kV case in Figure 6-2, where the lighter region at the top of the bright-field TEM

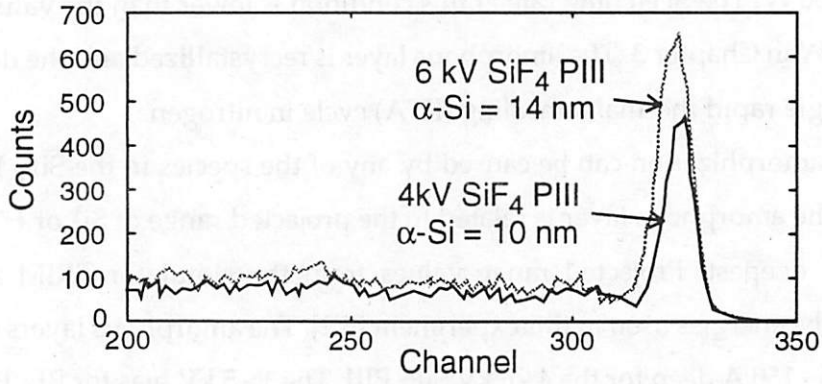

Figure 6-1. RBS channeling spectrum of Si preamorphized by SiF_4 PIII

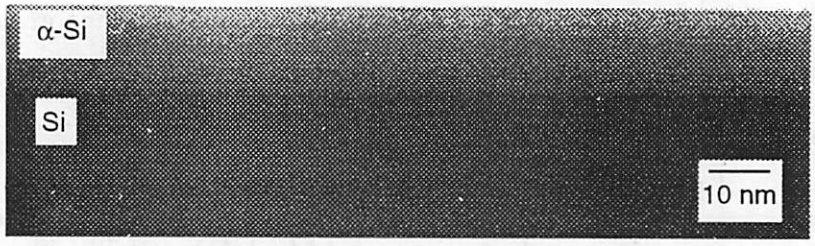

Figure 6-2. TEM micrograph of α-Si layer formed by 4 kV SiF_4 PIII

micrograph is a 10 nm layer of α-Si. The transition between the amorphous and crystalline regions is quite abrupt. The layer thicknesses measured from RBS channeling and TEM are close to the projected range of 4 and 6 keV F^+ ions shown in Table 6-1.

6.4 Incorporated dose

The sheet resistance of PIII-doped samples after 1060°C, 10 s annealing is higher for the samples that have been preamorphized (Figure 6-3). The dose, $\sim(R_s\mu q)^{-1}$, has similar functional dependence on plasma power for preamorphized and non-preamorphized samples if mobility is assumed constant. The ratio of active dose in the two cases is approximately 2.3. Higher sheet resistance can be caused by lower incorporated dose, lower activation, shallower junctions, or lower mobility of carriers. The reduction in active concentration may be due to lower retained dose in the preamorphized samples caused by a higher etching rate of the amorphous Si during BF_3 PIII. Another possibility is that the very high concentrations of B near the Si surface have formed precipitates. Precipitates form at lower concentrations in samples that have been amorphized [6.3], and their presence in the surface region can reduce the mobility of carriers.

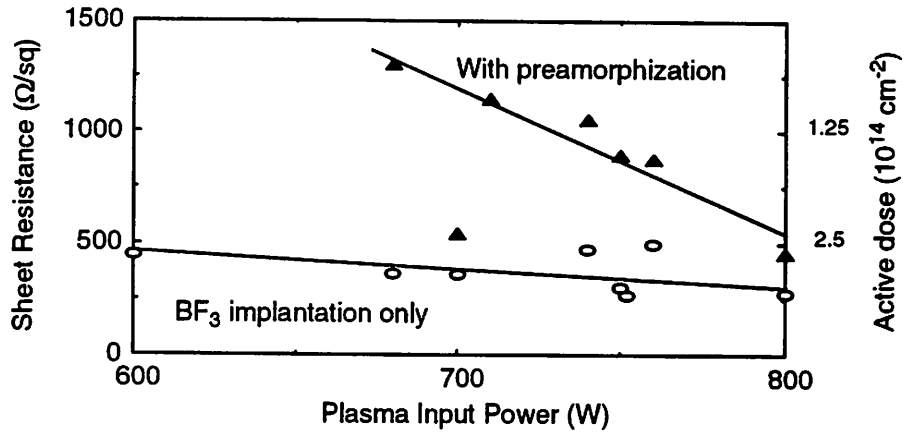

Figure 6-3. Dependence of sheet resistance on preamorphization

Samples implanted with 4-6 kV SiF_4 PIII and 2 kV BF_3 PIII, and annealed at 1060°C for 10 s.

6.5 Annealed profiles

The preamorphized and BF_3-implanted samples in Figure 6-4 are annealed at 1060°C for 10s. Spreading resistance (SRP) profiles show that the PIII two-step 5kV SiF_4 PIII and 2 kV BF_3 PIII implant creates a 100 nm junction (~ 75 nm at 10^{18} cm^{-3} concentration), whereas devices fabricated without the SiF_4 preamorphization step are more than 20 nm deeper. Figure 6-4 shows that even a thin, 10 nm amorphous layer is useful for reducing the junction depth with PIII, since the B implant peak is at the surface. Again, active dopant concentrations are lower in the preamorphized case, due to precipitation or lower dopant incorporation in the substrate. Transient enhanced diffusion is observed to be the main cause of the junction depth extending to 100 nm. In a sample with thin (10 nm) preamorphization, this enhanced diffusion may be caused by incomplete containment of the B in the α-Si before annealing, or may be due to the small end-of-range (EOR) defects providing an insufficient sink for interstitials. The concentration of interstitials available to enhance the diffusion becomes smaller as preamorphization energy and dose are reduced [6.4].

Figure 6-5 summarizes the effect of a thicker amorphous layer reducing the junction depth. The diodes which were implanted with ions from a SiF_4 plasma at 7-8 kV and in a BF_3 plasma at 2 kV with implant doses $5x10^{14}$ to 10^{16}/cm^2 have junction depths of 77±10 nm after a 1060°C, 1-10 second rapid thermal anneal. This is likely due to thicker amorphous layer containing a greater amount of the dopant. When the amorphous layer

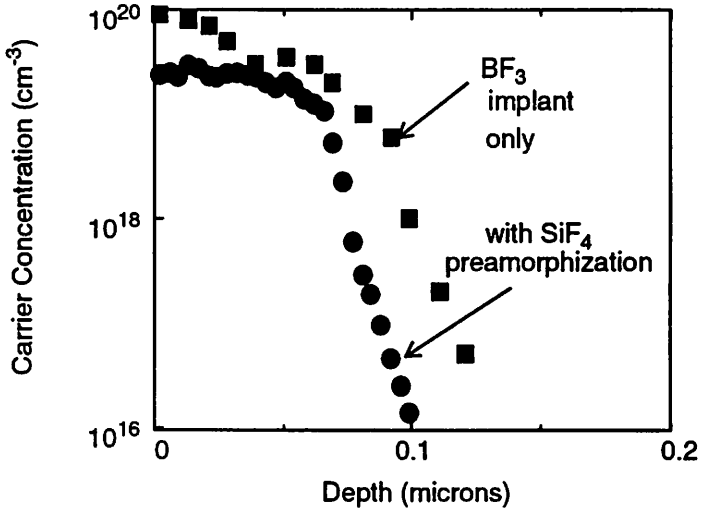

Figure 6-4. Effect of pre-amorphization on junction depth for 2kV BF_3 PIII

Spreading resistance (SRP) profiles of diodes processed with and without SiF_4 preamorphization step. The error in junction depth is 3-10 nm. The SiF_4 preamorphization voltage is -5 kV, with dose 10^{15} cm^{-2}, and the BF_3 implant voltage is -2 kV, with dose $5x10^{14}$ cm^{-2}.

is thicker, the tail will extend a smaller distance beyond it. The fraction of the B which is affected by the initial transient will be reduced.

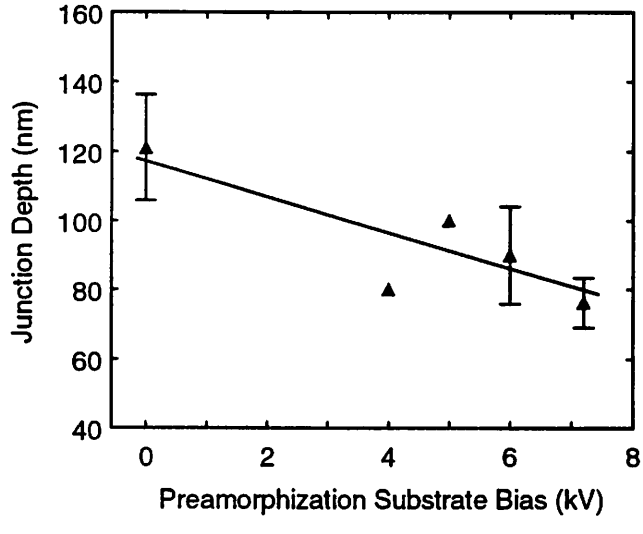

Figure 6-5. Variation in electrical junction depth with preamorphization energy

Preamorphization by SiF_4 PIII at varying substrate bias, and BF_3 implantation at 2 kV. Annealing at 1060°C for 10 s. Junction depth measured by spreading resistance profiling.

6.6 Substrate Damage

The thermal cycle used to activate dopant must also be long enough to dissolve the layer of end-of-range defects that forms underneath the amorphous-crystalline interface when the wafer is heated. If incompletely removed, the end-of-range (EOR) defects may act as deep-level traps in the pn junction depletion region. Extrinsic defects are more likely to form and are harder to remove in locations in the sample that are under stress, like LOCOS oxide edges. The following studies were done to show that the 1060°C, 10 s annealing cycle is long enough to remove all traces of the defects.

6.6.1 Channeling data

Figure 6-6 shows channeling data from samples implanted with SiF_4 at 6 kV and/or BF_3 at 2 kV. Shallow angle channeling was performed with 1.95 MeV $^4He^+$ ions with a backscattering angle of 105°. When implanted with BF_3 only, an 8 nm deep damage layer is formed. The depth of the damage is slightly lower than the projected range of a 2 kV B^+ ion, or the $R_p+2\Delta R_p$ value for a B atom implanted as a BF_2^+ ion. The curve for implantation

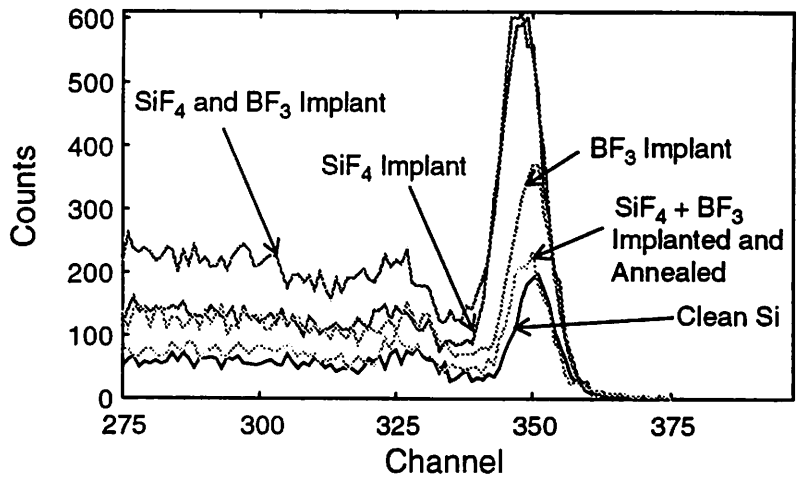

Figure 6-6. Substrate damage with and without preamorphization

RBS channeling performed with 1.95 MeV $^4He^+$ beam and 105° backscattering. Scale is 3.8 keV per channel. SiF_4 implants at 6 kV and BF_3 implants at 2 kV. Annealing at 1060°C for 10s.

of both SiF_4 and BF_3 shows a damage profile identical to the SiF_4-only case. Comparison of the channeling spectra of implanted, annealed and unprocessed Si in Figure 6-6 shows that the crystalline quality of the implanted sample is recovered after annealing.

The amount and depth of surface damage can be measured by integration of the counts in the channeling surface peaks. These numbers are compared to the nominal peak size for a clean Si wafer in Figure 6-7. The size of the surface peak increases with the implantation energy and α-Si depth, but after annealing, all samples have a peak comparable to that of unprocessed Si. There is no detectable surface damage remaining after anneal.

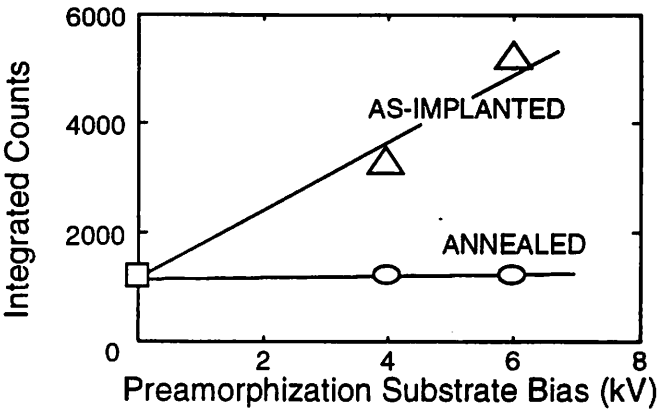

Figure 6-7. Recovery of Si quality after amorphization and anneal

Integrated counts from Si surface peak of RBS channeling data before and after RTA annealing at 1060°C, 10 s. Samples implanted by SiF_4 PIII at 4-6kV and BF_3 at 2 kV. Sample at zero is unprocessed Si.

6.6.2 Transmission electron microscopy (TEM)

After annealing at 1060°C for 10 seconds, the amorphous Si region is recrystallized and no end-of-range (EOR) dislocation loops due to SiF_4 implant damage or extended defects remain (Figure 6-8a). A thin layer of residual damage exists within 2-3 nm of the Si surface in blanket-implanted samples. In diode device samples, this surface layer is removed during wafer cleaning and further processing. TEM studies show that the actual, low-leakage diode samples in the active device center and at the diode edge below the field oxide are as good as the blanket samples. No EOR dislocation loops or stacking faults are observed in the active device region (Figure 6-8a), or in the diode perimeter region (Figure 6-8b), where stress in the LOCOS oxide might be expected to promote defect nucleation. No extended defects exist after this anneal cycle because the amorphous layer is less than 20 nm, and the thermal cycle required to remove EOR damage decreases with the depth of the damage. In a 10 s anneal cycle, 20 nm deep EOR defects would require 970°C annealing to dissolve, while defects 10 nm deep only require 850°C annealing [6.4].

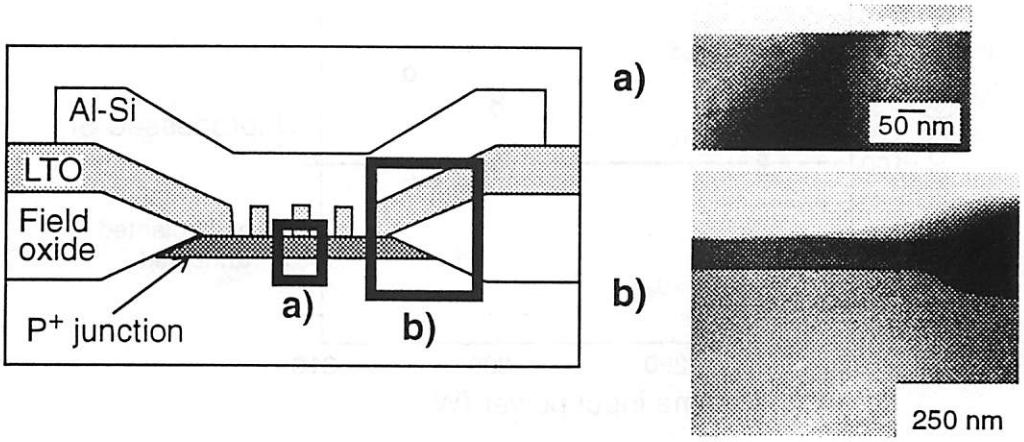

Figure 6-8. TEM of Si in active device areas after implantation and anneal

TEM micrographs of Si show no extended defects: a) under the active device, and b) at the device edge. Samples are implanted with SiF_4 at 4 kV, with dose 10^{15} cm^{-3}, and with BF_3 at 2 kV, and dose $5x10^{14}$ cm^{-3}. Rapid thermal annealing was performed for 10 s at 1060°C.

For the 4 - 6 kV PIII preamorphized samples with 10-15 nm deep amorphous layers, the 1060°C, 10 s annealing is sufficient to remove extrinsic EOR loops. The F which might pin EOR dislocation loops or bubbles diffuses out during annealing for these low implant energies, as observed by SIMS.

6.6.3 Reflectance

A third measurement that testifies for the recovery of crystalline quality in PIII implanted and annealed Si is a reflectance measurement using an optical source of wavelength 400-800 nm. Figure 6-9 shows the measured optical reflectance of samples with a surface α-Si layer created by 4-6 kV SiF_4 PIII, and the reflectance of the same samples after annealing. The as-implanted samples have a reflectance value 25% greater than the reference value of 100 measured for a clean, unprocessed Si wafer. After annealing, the surface reflectance is indistinguishable from that of pure Si, given the measurement error of 2%.

6.7 Electrical behavior of preamorphized devices

6.7.1 Diode process flow

The process flow for *pn* junctions using PIII is shown in Figure 6-10. Substrates are CZ-grown, (100) *n*-type wafers with resistivity 8-12 Ω-cm. Active diode areas are defined using the local-oxidation (LOCOS) process to reduce the volume of the depletion region

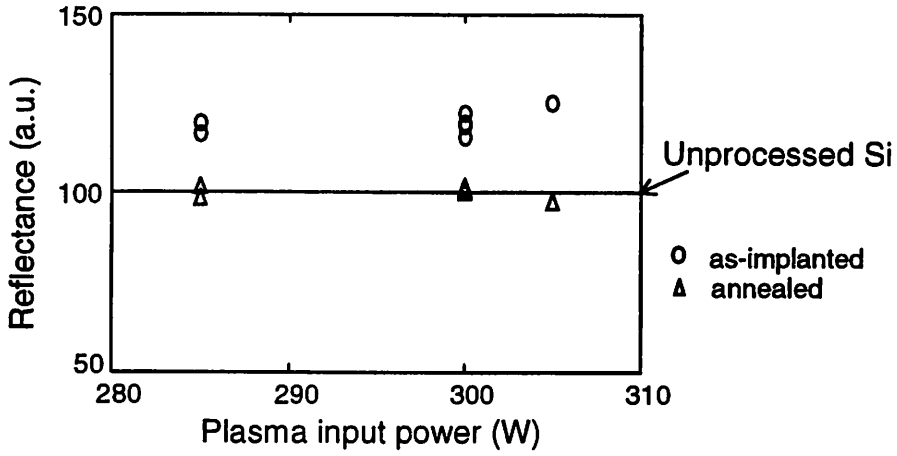

Figure 6-9. Reflectance measurements of implanted and annealed Si

around the diode perimeter and reduce the generation leakage currents. For comparison, a second set of diodes is fabricated with active areas etched into a 500 nm field oxide (No LOCOS). All wafers are doped using a two-step PIII implant directly into the exposed Si substrate, using SiF_4 for preamorphization and BF_3 for doping. The amorphous layer is recrystallized and the dopant is activated in a rapid thermal anneal (RTA) cycle of 10 seconds at 1060°C in N_2. Chemical vapor deposition is used to put down a low temperature (CVD-LTO) oxide at 400°C. Contact holes are patterned in this oxide before deposition of 800 nm of Al-2% Si. The wafers are sintered at 400°C for 20 minutes to make good electrical contact between the Al and p^+ Si.

6.7.2 Diode characteristics

To study the current-voltage characteristics of the shallow junctions, diodes of sizes from 625 to $4x10^6$ μm^2 and with width-to-length ratios from 1:1 to 16:1, were fabricated on the test chip. Electrical characteristics of forward-biased diodes with various preamorphization conditions were measured. The ideality factors of the diodes range from 1.05 to 1.06 for all diode sizes. The total forward current (sum of bulk area diode current and current from periphery or perimeter of diode) is proportional to (diode area)$^{0.88}$. Forward current is more strongly dependent on area than perimeter for diode areas up to $4x10^6$ μm^2. The linear dependence of current on area indicates there is no spiking of the Al-2% Si through the shallow junction.

Measurements of the reverse-bias leakage currents of the diodes are also encouraging. The forward and reverse *J-V* characteristics of a diode made with 5kV SiF_4

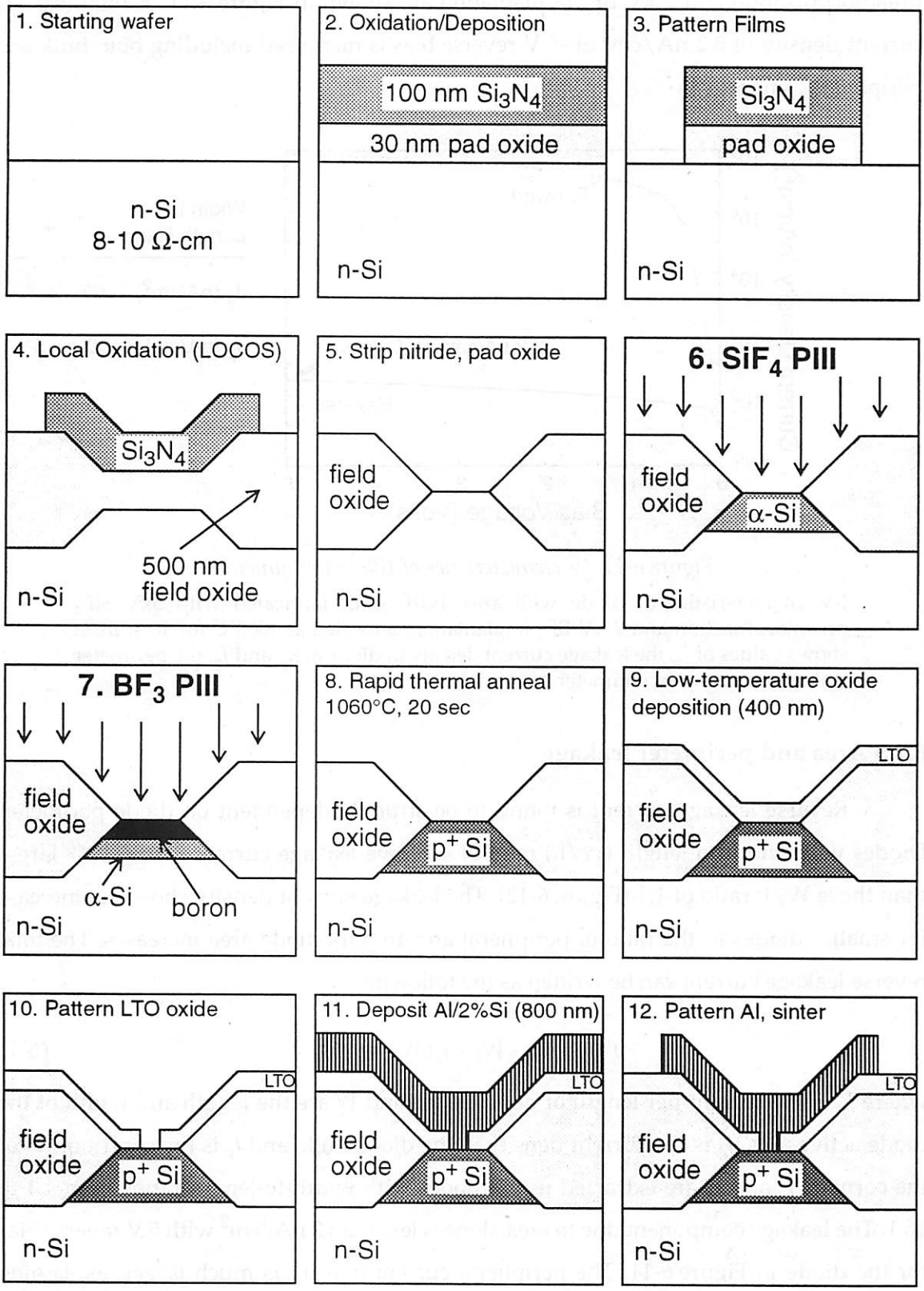

Figure 6-10. Process flow for low-leakage p^+n diode structures

preamorphization and 2 kV BF_3 implantation are shown in Figure 6-11. A total leakage current density of 3.2 nA/cm^2 at -5 V reverse bias is measured including both bulk and peripheral components.

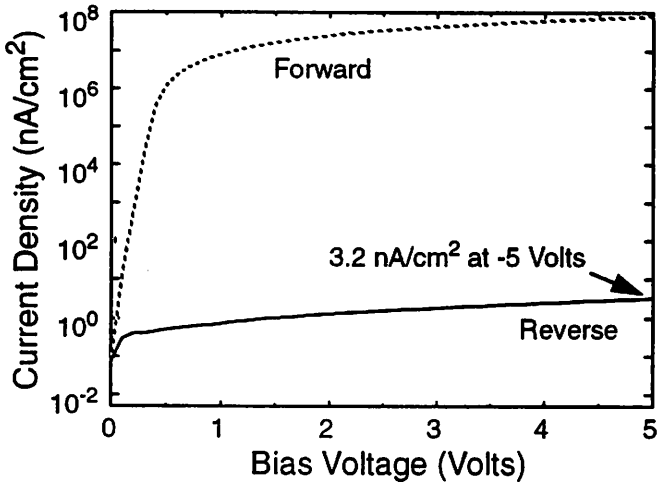

Width to Length Ratio	1	4
J_a (nA/cm^2)	1.7	1.7
J_p (pA/cm)	90	95

Figure 6-11. JV characteristics of 100 nm pn junction

J-V characteristics of diode with area 4x10^6 μm^2, fabricated with 5kV SiF_4 preamorphization and 2 kV BF_3 implantation, annealed at 1060°C for 10 s. Inset shows values of J_a, the leakage current density in diode area, and J_p, the perimeter leakage current per centimeter of perimeter.

6.7.3 Area and perimeter leakage

Reverse leakage current is found to be strongly dependent on diode perimeter. Diodes with width-to-length (W/L) ratio of 4:1 have leakage current nearly 20% larger than those W/L ratio of 1:1 (Figure 6-12). The leakage current density shows an increase for smaller diodes as the ratio of peripheral area to bulk diode area increases. The total reverse leakage current can be written as the following:

$$I = 2J_p(L+W) + J_aLW + 4J_c \qquad (6\text{-}1)$$

where J_p is the current per length of perimeter, L and W are the length and width of the diode active area, J_a is the current density in the diode bulk, and J_c is the contribution of the corners. J_a and J_p are extracted using diodes with width-to-length ratios from 1:1 to 16:1. The leakage component due to area alone is less than 2 nA/cm^2 with 5 V reverse bias for the diode in Figure 6-11. The peripheral current density is much larger, explaining increased leakage for smaller area diodes. The peripheral leakage component is greater than 90 pA/cm for all diodes (or 20 nA/cm^2 using the metal overlap value of 50 μm). The

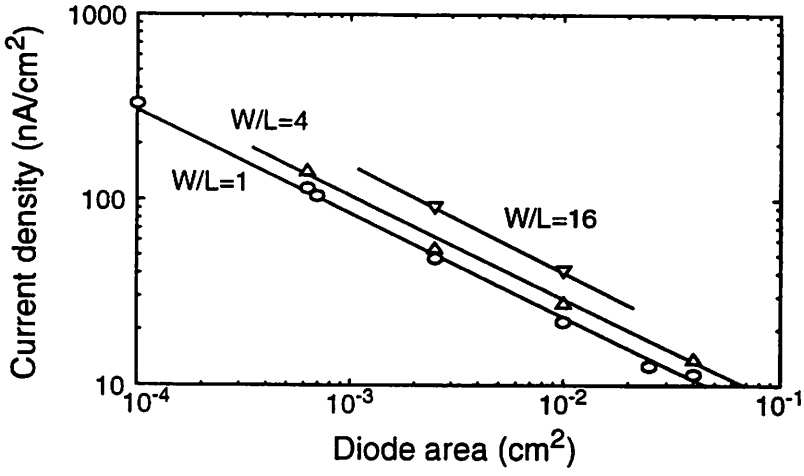

Figure 6-12. Effect of perimeter on diode leakage

Increase in current density when perimeter leakage becomes more important. Diodes preamorphized with 4kV SiF_4 PIII, and implanted with 2kV BF_3 PIII.

low leakage of the diode bulk shows that the PIII process is intrinsically capable of producing extremely low-leakage junctions.

6.7.4 Leakage dependence on preamorphization and device structure

Electrical measurements of diodes with and without a 4-8 kV SiF_4 preamorphization step show that the reverse leakage currents at 5V reverse bias and ideality factors of preamorphized and non-preamorphized samples are similar. The diode reverse characteristics for preamorphized and non-preamorphized samples are equivalent below reverse breakdown (Figure 6-13), but the onset of breakdown occurs at a lower voltage for the preamorphized samples. This early breakdown is expected in the shallower preamorphized diodes, where higher junction curvature causes increased electric field in the diode corners.

Figure 6-14 shows the effect of preamorphization energy and device structure on junction leakage. The two diodes fabricated with LOCOS structures, preamorphized with 4 kV and 5 kV SiF_4 PIII, have similar values of J_p (52 pA/cm and 90 pA/cm). The value of J_a is found to be higher for the 4 kV samples regardless of their diode isolation structure. The area leakage density is 14.8 nA/cm^2 for the 4 kV preamorphized samples, which is higher than the 2 nA/cm^2 at -5V bias found in the 5 kV preamorphized samples. For diodes fabricated without LOCOS, perimeter leakage is much higher, about 300 pA/cm, due to an increase in the volume of the junction depletion region and in the surface area of Si/SiO_2 interface states around the perimeter. This illustrates the limiting effects of

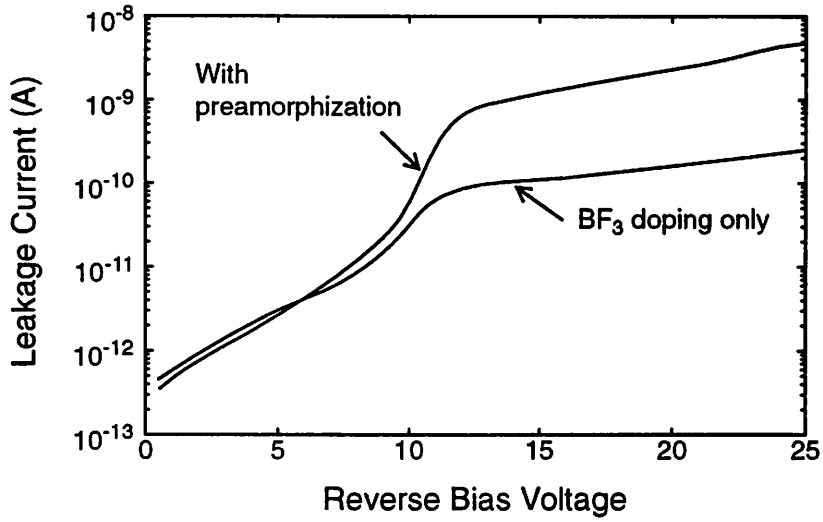

Figure 6-13. Leakage of diodes with and without preamorphization

Preamorphization with 7.2 kV SiF_4 PIII, doping with 2kV BF_3 PIII. Samples annealed 1s at 1060°C. Leakage current density at -5V is 25 nA/cm^2 for preamorphized sample, 28.5 nA/cm^2 for non-preamorphized sample.

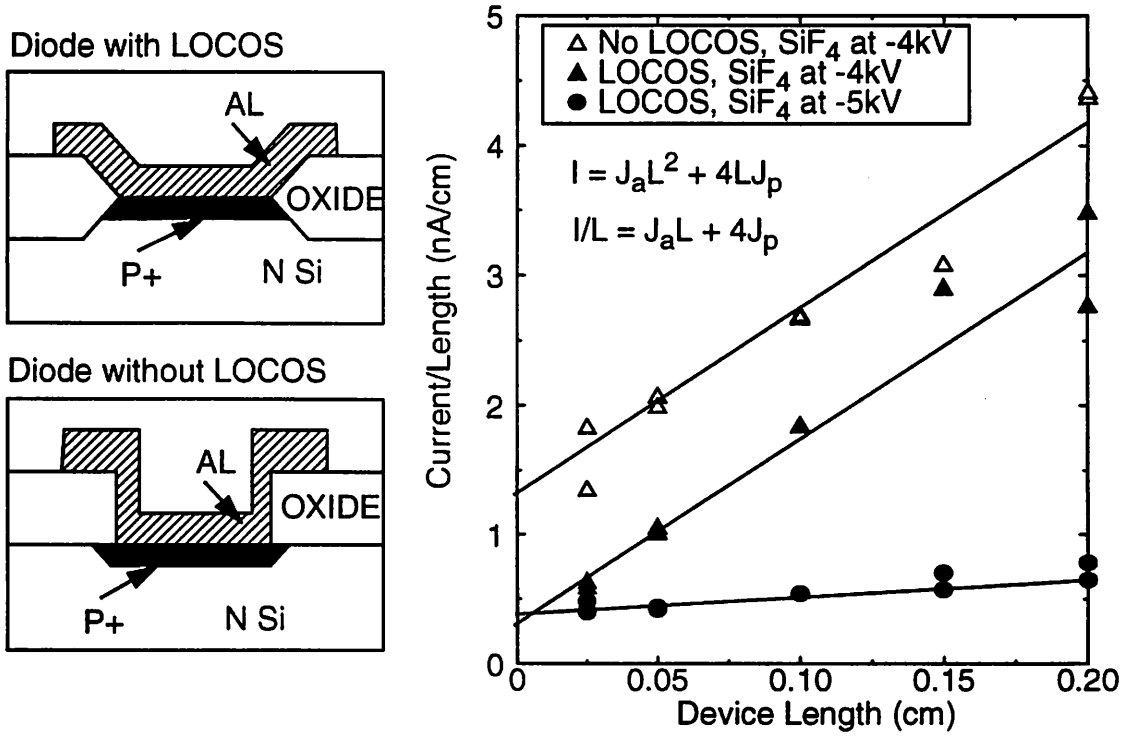

Figure 6-14. Effect of device structure and preamorphization on area and perimeter leakage

Plot of current (I) divided by diode length (L) versus length (L), to show effects of preamorphization energy and device structure on bulk leakage current density (J_a) and perimeter leakage current density (J_p) of square diodes (W/L=1).

device structure on shallow diodes: the intrinsic leakage of the PIII junction, ignoring edge and device design effects is below 2 nA/cm^2. Table 6-2 contains a summary of the area and perimeter leakage components of diodes made with different preamorphization and annealing conditions. The sample with 6 kV SiF_4 implant and annealed for only 1s shows

Sample	E10	E15	E19	E2-21-3	E2-21-5
SiF_4 implant voltage (kV)	4.1	4.2	5	6.2	6.1
Structure	No LOCOS	LOCOS	LOCOS	LOCOS	LOCOS
Anneal time at 1060°C	10	10	10	1	10
J_a (nA/cm^2)	19	16	2	9	2
J_p/50 µm (nA/cm^2)	29-60	18-40	21	10-14	90-94

Table 6-2. Summary of preamorphized diode area and perimeter leakage

higher area leakage than comparable samples that are annealed for 10s. The shallower junction depth and lower activation of the sample annealed for 1 sec may cause higher leakage due to higher junction curvature or incomplete removal of defects. The minority carrier lifetime extracted for Si under the junction area is about 250 µs [6.5], indicating that few additional deep-level centers are introduced by the PIII technique.

6.8 Conclusion

Using a two-step PIII implantation process is an efficient method of fabricating very low leakage, ultra-shallow pn junctions. The low-energy PIII preamorphization and dopant implantation sequence can be used to keep the junction shallow without causing extended defects or implantation EOR loops. In this processing sequence, residual crystal damage from the SiF_4 implantation is kept more than 80 nm from the metallurgical junction, which is 75 - 100 nm deep after annealing. Electrical measurements show the total leakage of the diode bulk can be less than 3. 2 nA/cm^2 at -5 V applied bias. Diodes with varying areas and width-to-length ratios show that most leakage current is produced at the diode edges. Data extraction shows that leakage due to diode bulk alone (J_a) is as low as 2 nA/cm^2, while peripheral leakage (J_p) is greater than 90 pA/cm, and varies according to field oxide thickness.

6.9 References

[6.1] M. Y. Tsai and R. G. Streetman, "Recrystallization of Implanted Amorphous Silicon Layers 1: Electrical Properties of Silicon Implanted with BF_2^+ or Si^++B^+," J. Appl. Phys., 50 (1), pp.183-187, 1979.

[6.2] J.F. Ziegler and J.P. Biersack, *The Stopping and Range of Ions in Solids*, New York: Pergamon Press, 1985.

[6.3] T.O. Sedgwick, A.E. Michel, V.R. Deline, S.A. Cohen, and J.B. Lasky, "Transient boron diffusion in ion-implanted crystalline and amorphous silicon," J. Appl. Phys, 63 (5), pp. 1452-1463, 1988.

[6.4] R.B. Fair, "Junction formation in Silicon by Rapid Thermal Annealing," in *Rapid Thermal Processing Science and Technology*, ed. by R. B. Fair, New York: Academic Press, pp. 169-226, 1993.

[6.5] H. Wong, N. W. Cheung, and S. S. Hong, "Electronic defects in silicon induced by MeV carbon and oxygen implants," Nucl. Instrum. Meth., B37-38, pp. 970-974, 1989.

7 Epitaxial Cobalt Disilicide for ULSI

7.1 Silicides for ULSI

Silicides are used in a number of ULSI processing steps, as interconnects, Schottky barriers, ohmic contacts, and low-resistivity gate contacts. Typical silicides have resistivity ten times lower than polysilicon, and so are used to reduce RC delays in short interconnects previously fabricated from poly-Si. These chapters focus on a process used to make ohmic salicide contacts to heavily doped source and drain regions of ULSI devices. Silicide contacts to n^+ or p^+ Si regions have lower contact resistivity than Al or barrier layer contacts. They reduce the sheet resistivity of the source/drain region and do not suffer from junction spiking like Al-Si contacts [7.1]. Electric field simulations of source/drain areas have shown that voltage drops due to the parasitic contact resistance are responsible for most of the loss of current-driving capability of small-dimension MOS devices; thus, the lower contact resistance of a silicide-Si contact can make a significant increase in the speed of a circuit [7.2].

Silicide contacts need low resistivity, good thermal stability, low stress, to be compatible with existing fabrication processes, to exhibit no overgrowth on field and spacer oxides, and to be un-reactive with dopant atoms. The most commonly used silicide is $TiSi_2$ since it has the lowest resistivity of the silicides, 13-16 μΩ-cm [7.2]; however, it meets few of the other qualifications of a good silicide. Although it has a slightly higher resistivity (15.8-20 μΩ-cm) [7.1], $CoSi_2$ is studied as an alternative to $TiSi_2$ because it outperforms $TiSi_2$ in all other categories (Table 7-1). Silicide growth can proceed either by Si diffusing into the metal and reacting, or by metal diffusing into the Si substrate and reacting. If the growth occurs by Si movement, then the silicide grows up onto the field and spacer oxides, and can cause electrical shorting between the shallow junctions and the gate, called bridging. $TiSi_2$ grows by Si movement unless the annealing temperature is below 620°C. A

Property	C54 - $TiSi_2$	$CoSi_2$	epitaxial $CoSi_2$
Resistivity	13-16 μΩ-cm	15.8-20 μΩ-cm	
Tensile stress (dynes/ cm^2)	$1.6x10^{10}$	$0.8x10^{10}$	$1.9\text{-}3.3x10^{10}$
Temperature range for which Si is diffusing species	T > 600°C	T < 600°C	T < 600°C
B diffusion	Reacts with B	Fast	Fast
As diffusion	Reacts with As	Fast	grain boundary diffusion only
P diffusion		Reacts with P	Reacts with P
Lattice structure	Orthorhombic	CaF_2 (fcc)	CaF_2 (fcc)
Lattice parameter	a=0.8252 nm b=0.4783 nm c=0.8540 nm	0.5367 nm	0.5367 nm
Atomic density		$7.7622x10^{22}$ cm^{-3}	$7.7622x10^{22}$ cm^{-3}
Barrier height to n-Si	0.6 eV	0.64 eV	
Thermal expansion coefficient, α=3 ppm/ °C for Si	12.5 ppm/°C	10.1 ppm/°C	

Table 7-1. Summary of important properties of silicides for ULSI

second annealing step must then be used to convert the $TiSi_2$ into a lower resistivity phase. The resistivity of $TiSi_2$ is critically dependent on these steps, while low-resistivity $CoSi_2$ can be formed for temperatures higher than 400°C. $CoSi_2$ grows by Co movement except between 550° and 650°C, so overgrowth is less problematic, and single-step annealing above 650°C is possible. For efficient processing, it is preferred that silicide growth be self-aligned, so that extra masking steps are not necessary (Figure 7-1). For self-aligned silicidation to be successful, the recipe must be perfected to eliminate silicide overgrowth on oxides. This can be done in a single step with cobalt silicide.

Probably the most important advantage of $CoSi_2$ over $TiSi_2$ for shallow junctions is its stability with respect to the prevalent Si dopants. During high temperature annealing steps, $TiSi_2$ will react with B or As, forming Ti-B or Ti-As precipitates at the $TiSi_2$ grain boundaries. These precipitates block dopant diffusion in the silicide and raise the resistivity of the material [7.3]. The formation of these precipitates is so favorable that B may be

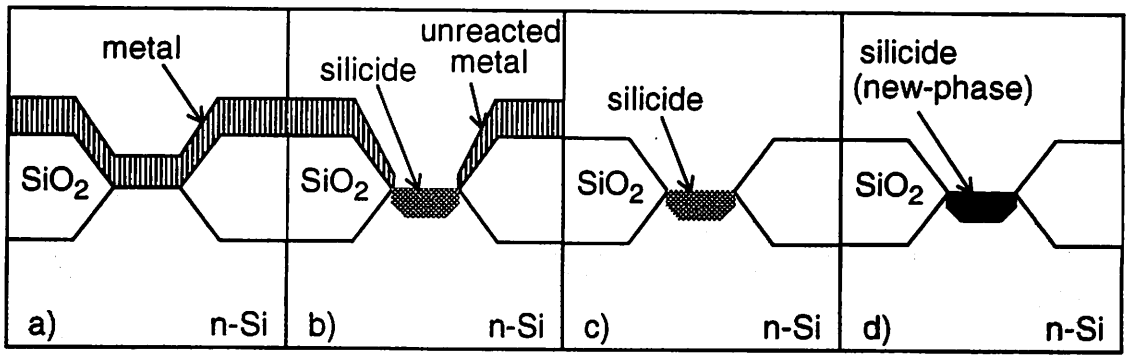

Figure 7-1. Self-aligned silicidation

a) Blanket deposition of metal, b) RTA or other anneal cycle to form silicide, c) selective metal etch to remove un-reacted metal on oxide, and d) second anneal to reduce resistivity (for $TiSi_2$).

depleted from the $TiSi_2$/Si interface during annealing, increasing the contact resistance [7.4]. $CoSi_2$ does not react with B, and although it is energetically favorable for $CoSi_2$ to react with As, such a reaction has not been observed [7.3]. Since the solubility of B and As in $CoSi_2$ is lower than in Si, dopant in these structures diffuses to the $CoSi_2$ interfaces, where a buildup of dopant can seen during annealing, further reducing the contact resistance of $CoSi_2$/Si interfaces [7.5].

The difficulty in using any silicide is reproducibility. The properties of the material and the junction under it depend on many variables: surface cleaning before metal deposition, metal deposition technique, annealing ambient, annealing temperature and ramping rate, temperature gradients, substrate doping, and contact size, to name a few. All of these will affect the silicide resistivity, contact resistance, thickness, and lateral growth. A few general guidelines exist for making a good-quality polycrystalline $CoSi_2$ layer. The annealing ambient must be carefully controlled, because self-passivating Co_3O_4 may form if O_2 is present during heating [7.6]. Precipitates of this material in the silicide will increase the resistivity of the silicide. Rapid thermal annealing, with high flows of N_2 or forming gas in the chamber during annealing, can create silicides with lower O content and lower resistivity [7.7]. Good $CoSi_2$ films can also be made using a capping layer or vacuum tube [7.8, 7.9]. Presence of a native oxide on the Si substrate is another problem during $CoSi_2$ formation. Co cannot reduce oxide like Ti can, rather it balls up on an oxide surface. Silicide will only form where the oxide is thin enough that Co can diffuse through it [7.10],

leading to patchy and discontinuous films. Surface cleaning must be careful and uniform so the silicide may grow evenly.

There are also problems inherent in the scaling of silicide films. Overgrowth on oxides is more likely as contact hole sizes are reduced. $CoSi_2$ resistivity increases when the metal thickness is decreased, regardless of annealing temperature [7.2, 7.1]. Films with $CoSi_2$ thickness below 40 nm have been shown to agglomerate, balling up into highly resistive islands during silicide formation [7.10]. Thicker films are typically more stable, allowing long-time, high temperature annealing steps before they agglomerate. Recent work has reduced the minimum thickness of $CoSi_2$ that can be used without agglomeration to 25nm [7.20].

7.2 Epitaxial cobalt disilicide

Using an epitaxially grown silicide is one way of avoiding the problems of rough interface [7.11], moderate thermal stability [7.2], and large grain-boundary dopant out-diffusion [7.12] of poly-crystalline $CoSi_2$. $CoSi_2$ has a fcc-based lattice (CaF_2) structure and a low (1.19%) lattice-mismatch to (100) Si, so it is possible to grow epitaxially. If Co metal is deposited directly on Si and growth proceeds by solid-phase diffusion, the film will not grow epitaxially because the metal diffuses to the interface quickly and unevenly due to oxide patches, and the material grows too fast. The first epitaxially grown $CoSi_2$ on (100) Si was reported in Ref. [7.13]. This method uses a 10-30 nm Ti layer under the 20-30 nm Co layer to retard the Co diffusion to the Si interface, where the growth occurs by solid-phase epitaxy (SPE). Epitaxial, single-crystal $CoSi_2$ growth has since been achieved on (100) Si using bilayers of Co/Ti [7.14-7.16, 7.9, 7.12], Co/Zr [7.17], and Co/Ta [7.11], multilayers of Co/Ti [7.16], and CoW alloys [7.18]. In all of these cases, the epitaxial growth of $CoSi_2$ is aided by the second material in two ways: the Ti, Ta, Zr, and W all serve to reduce the native oxide at room temperature, so the Si surface is atomically clean before growth begins, and they all form an intermediate layer between the Co and Si which drastically reduces the Co diffusion into the Si. When the growth proceeds slowly, $CoSi_2$ grows epitaxially, without any intermediate phases (CoSi or Co_2Si), for temperatures above 400°C [7.15]. Low-resistivity, single-crystal $CoSi_2$ is grown by fine-tuning this process, choosing correct layer thicknesses and annealing conditions.

7.3 Experiment

The cobalt silicide process used for the samples in this chapter is based on the well-optimized process developed in Refs. [7.14, 7.15, 7.9]. These processes utilize a Co/Ti bilayer to force the silicide to grow epitaxially. The $CoSi_2$ layer is a single crystal, has the most planar interface, and has the lowest resistivity with a 2 nm Ti layer. Since it is difficult to deposit a continuous 1 nm thick layer of Ti, there may still be some SiO_2 left on the surface, and films grown under this condition are polycrystalline with a preferred (200) orientation and a rough interface. With a 5 nm Ti layer, the interface has pronounced <100> and <111> facets. Thicker Ti layers lead to a rough layer of TiN on top of the $CoSi_2$ after annealing [7.21]. In all cases, the Co/Ti growth leaves a surface layer of fine Ti-Co-Si-O-N precipitates on top of the silicide. The $CoSi_2$ film made with 2 nm Ti is very stable: it can withstand 900°C, 30 min. annealing without degradation.

The samples described in this chapter were grown on 4-inch diameter, CZ-grown, (100) n-type wafers with resistivity 8-12 Ω-cm. Active diode areas were defined using the local-oxidation (LOCOS) process on some of the wafers. After wet cleaning and a 300 W, 60 s oxygen plasma scourge, a 2 nm layer of Ti and a 15 nm layer of Co were sputter deposited in a Perkin-Elmer 4410 sputtering system. These are the metal thicknesses that have been shown in Ref. [7.14] to yield the lowest resistivity and most planar, uniform epitaxial silicide film. To make polycrystalline silicide samples for comparison, some wafers were deposited with only the 15 nm of Co. Silicides are grown in an AG Associates Heatpulse 210T rapid thermal annealing (RTA) chamber in a forming gas ambient (N_2/12% H_2). Since annealing temperatures above 900°C have been reported to cause silicide agglomeration [7.1, 7.15, 7.23], the silicides were formed at 900°C in a 30 s cycle. Excess Co and Ti metals were removed in standard selective etches: Co was removed in a 1:1 HNO_3:H_2O solution, and Ti was removed in a 2:1:1 H_2O_2:NH_4OH:H_2O solution.

7.4 Metal layer thicknesses

7.4.1 X-ray fluorescence (XRF)

The X-ray fluorescence measurements were performed on a Kevex Omicron machine at 10 keV with 0.084 mA beam current for 100 s. Since calibration curves were not available for Co or thin Ti, the thicknesses were found by comparing to a standard with 2 nm Ti under 15 nm Co whose layer thicknesses had been measured by TEM. The layers

were measured to be 12.9 nm Co and 1.9 nm Ti on the Co/Ti sample, and 14.3 nm Co on the sample without Ti.

7.4.2 Rutherford Backscattering (RBS)

Rutherford backscattering and channeling are used to check the thickness and composition of the Ti, Co and $CoSi_2$ layers, and gauge their crystalline quality. RBS data is shown for the Co/Ti and Co layers before annealing in Figure 7-2. Measuring the width

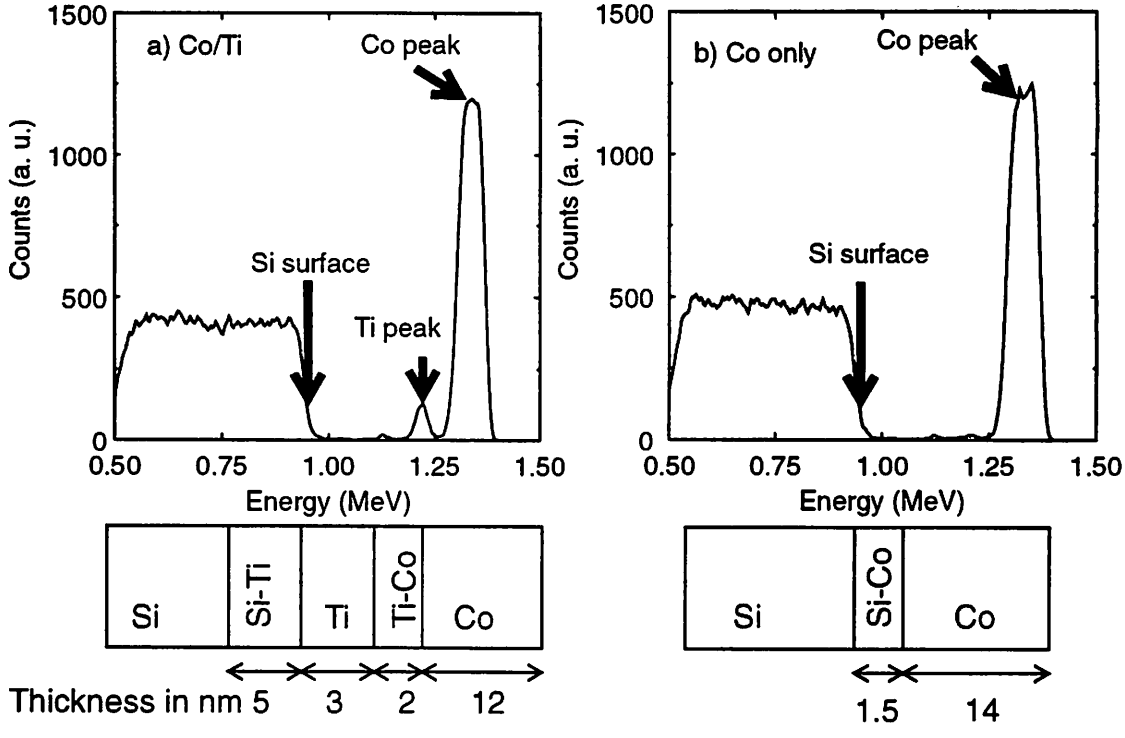

Figure 7-2. RBS of unannealed Co/Ti and Co samples

RBS performed with 1.8 MeV $^4He^+$ primary beam and angles θ_1=65°, θ_2=80° and θ=165° is shown for the Co/Ti and Co metal layers before annealing

of the energy peaks at 50% of their maximum height, the analysis in Appendix C is used to calculate a thickness of 14 nm for the Co layer and 10 nm for the Ti layer in Figure 7-2a. The difference between the right edge of the Ti and Si peaks and the values of the Ti and Si kinematic factors show that the Ti layer begins 12 nm from the surface, and the Si layer begins about 17 nm from the surface, indicating either large transition layers between the Si/Ti/Co materials or rough interfaces. For the sample without Ti in Figure 7-2b, the Co thickness is calculated at 15.5 nm. The difference between the right edge of the Si peak and

the position expected from its kinematic factor implies a transition layer or interface roughness of 1.5 nm.

7.5 Silicide layer thickness and composition

Random Rutherford backscattering (RBS) and channeling measurements are shown in Figure 7-3a for the Co-Ti and Figure 7-3b for the Co samples after annealing. The area of the RBS Co peak and the Si peak from the silicide are used to find the composition of the silicides made with and without Ti. The Co-Ti silicide is $CoSi_{2.2}$ with a thickness of 47.8 nm from the Co peak and 45.4 nm from the Si peak. The silicide made from Co alone is $CoSi_{2.1}$ with a thickness of 44.9 nm from the Co peak and 45.3 nm from the Si peak.

RBS channeling measurements were performed by aligning the beam with the <100> direction and performing RBS with a backscattering angle of 105°. For a perfect Si crystal, the ratio of the backscattered ion yield from the Co signal when the beam is aligned to the yield when the beam direction is random (χ_{min}) would be less than 5%. For the silicide grown from Co-Ti, χ_{min} is 28%. This relatively high value of χ_{min} indicates that

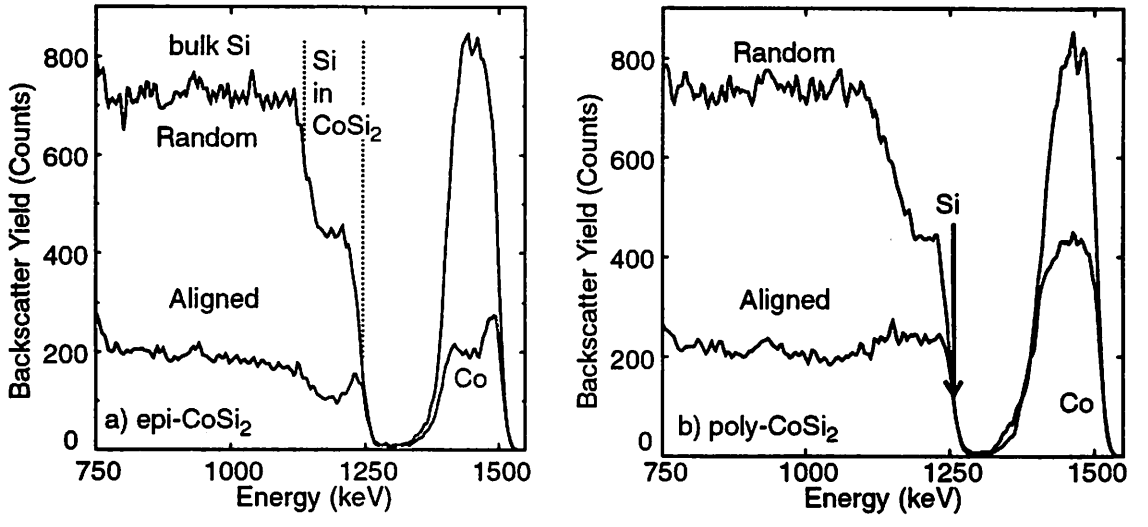

Figure 7-3. RBS of annealed silicide films

RBS spectra of A) epi-$CoSi_2$ with χ_{min}=28% and B) poly-$CoSi_2$ with χ_{min}=60%. RBS performed with 1.8 MeV $^4He^+$ ions, 65° sample tilt and normal incidence. <100> channeling performed at an angle of 105°.

while the sample is highly epitaxially grown, it is not perfectly single-crystal. It is, however, of very good crystalline quality for a silicide made from sputtered metal. Some of the

scattering in the silicide may be due to surface oxide, isolated residual Ti impurities or precipitates. Previous work in Ref. [7.21] on similar silicides reported a 17% channeling χ_{min} when the Ti precipitates and TiN material on the top of the silicide were etched off. The high χ_{min} for this sample is probably due to the Ti-containing precipitates at the silicide surface. The silicide made without a Ti interlayer, the sample referred to as polycrystalline $CoSi_2$, has a channeling χ_{min} of 60%. For a material made up of small, randomly oriented grains, the χ_{min} is expected to be higher. This data indicates that the grains of the poly-$CoSi_2$ film are highly textured, although grains of many orientations are present, as shown by x-ray diffraction.

7.6 Silicide structure

7.6.1 X-ray diffraction

X-ray diffraction (XRD) data supports the conclusion that $CoSi_2$ films made from a Co/Ti bilayer grow epitaxially and that films grown without Ti have a number of differently-oriented grains. As described in Appendix C, it is expected that for an epitaxially grown $CoSi_2$ film on (100) Si, only planes from the {100} family will be detected. A polycrystalline film will have a number of randomly oriented grains, so other planes should meet the Bragg condition as the sample is tilted. The collected data are shown in Figure 7-4. The intensities of the peaks are fairly low, as expected when a very thin film is measured. The scan of the sample grown from a Ti/Co bilayer shows only (200) and (400) $CoSi_2$ peaks, identified using Table C-2. Usually the (200) Si peak cannot be seen due to interference from radiation scattering off atoms in the Si diamond structure. In the Co/Ti sample, the high stress at the interface has apparently caused enough rearrangement of the surface Si that the (200) peak may be seen. The sample grown from a Co layer without Ti appears somewhat polycrystalline, as many higher index planes can be seen, including (220), (222), and (311) $CoSi_2$. The (400) peak is the largest, implying the film has predominantly a (100) texture. The three small extra peaks between the (200) and (220) $CoSi_2$ peaks in Figure 7-4b are best identified as Co_xN or Co_xO peaks, probably due to the annealing of the $CoSi_2$ samples in a N_2/H_2 ambient which may have contained some oxygen contamination. The 2 nm of Ti used to grow the film in Figure 7-4a does not appear to be enough to cause nucleation of any $TiSi_x$ or TiO_x phases large enough to be identified.

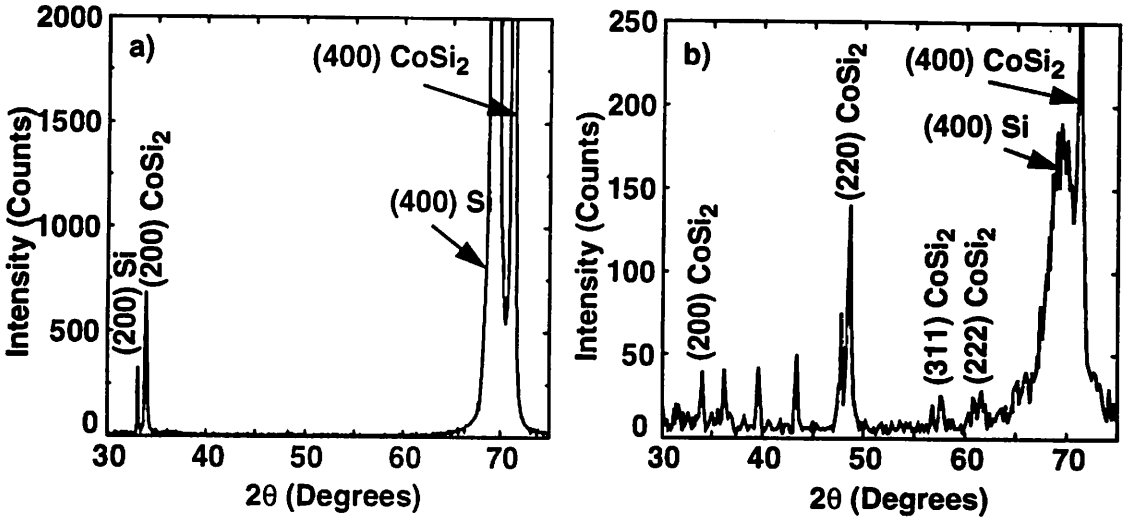

Figure 7-4. X-ray diffraction of epitaxial and polycrystalline $CoSi_2$.

XRD spectra of the a) epi-$CoSi_2$ sample and b) poly-$CoSi_2$ sample after silicide formation and selective metal etch. 2θ scan performed by tilting the samples to vary the diffraction angle from 25 to 75°. The 2θ resolution is 0.1°, and the mechanical tilting of the sample takes 1 second per data point.

The distance between the same-index $CoSi_2$ and Si peaks can be used to measure the strain present in the $CoSi_2$ thin film. Since un-strained $CoSi_2$ and Si will have lattice parameters of 0.5367 nm and 0.543 nm, respectively, $CoSi_2$ grown on Si will be under tensile stress, forcing the lattice parameter in the direction perpendicular ($a_{f\perp}$) to the surface to contract. The perpendicular lattice parameter is calculated from the XRD peak using equations listed in Appendix C. The location of the (200) and (400) $CoSi_2$ and Si peaks near 33° and 70° are used to calculate values for a_s and a_f (Table 7-2). The peak locations are averages from three XRD runs. Values of strain are calculated assuming that the substrate

Si peak 2θ	Co peak 2θ	a_s (A)=$a_{f\parallel}$	$a_{f\perp}$ (A)	$\varepsilon_{\parallel}$	$e_{\perp}$	ε_T
33.175	33.9	5.404	5.284	-0.69%	-1.55%	2.24%
69.217	71.167	5.425	5.295	-1.08%	-1.34%	2.42%

Table 7-2. Strain in epitaxial cobalt disilicide

and film are pseudomorphic. Using a reported value of the Poisson ratio, ν=0.33 [7.22], it can be seen that the measured values of tetragonal strain are very close to the theoretical maximum strain (ε_{max})in the silicide film:

$$\varepsilon_{max} = \frac{1+\nu}{1-\nu} \cdot \frac{a_s - a_f}{a_f} = 0.0233 \quad . \tag{7-1}$$

Assuming that none of the lattice mismatch is relieved through misfit dislocations, the stress in the plane of the film (σ) can be written:

$$\sigma = \left(\frac{Y}{1-\nu}\right)\varepsilon_{II} = \left(\frac{2\mu\,(1+\nu)}{1-\nu}\right)\varepsilon_{II} \tag{7-2}$$

where μ is the shear modulus, 4.85×10^{11} dyn/cm^2. Using this equation, the stress in the epitaxial film is found to be between 1.33×10^{10} dyn/cm^2 and 2.08×10^{10} dyn/cm^2, in reasonable agreement with values reported by in Ref. [7.21] (1.9×10^{10} dyn/cm^2) and Ref. [7.22] (3.32×10^{10} dyn/cm^2) for epitaxial $CoSi_2$ films.

7.6.2 Transmission Electron Microscopy

A cross-sectional transmission electron micrograph (XTEM) of the as-formed epitaxial silicide is shown in Figure 7-5. The film is approximately 52 nm thick with a standard deviation of less than 5 nm. The interface is coherent with the substrate and very planar, interrupted every 100 nm or so by ledges edged with (111) facets as observed previously [7.21, 7.14, 7.15]. Silicides made at the same annealing temperature but in a shorter,

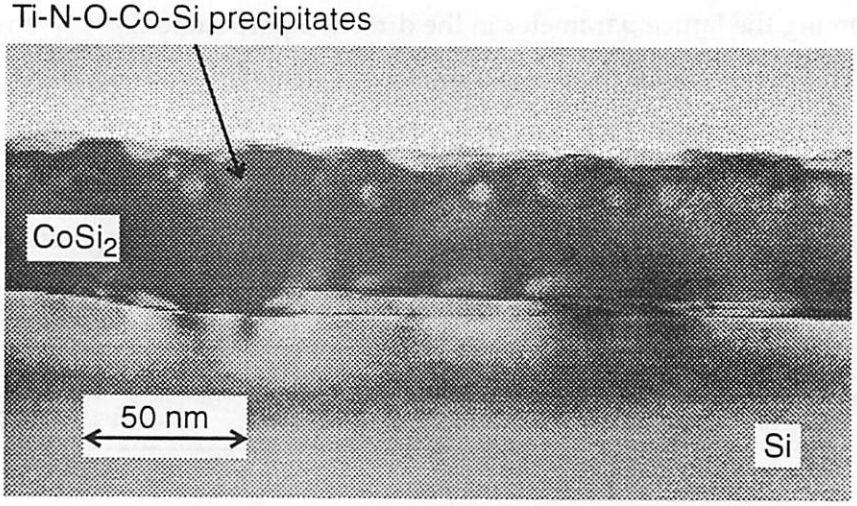

Figure 7-5. XTEM of epi-$CoSi_2$ made in 900°C, 30 s RTA

Cross-sectional transmission electron micrograph (XTEM) of 52 nm thick epitaxial $CoSi_2$ formed in 30 s, 900°C RTA cycle in forming gas. Facets edged by {111} planes are less than 5 nm deep. Amorphous precipitates in top 3 nm of film contain Ti-N-Co-Si-O.

20 s RTA annealing cycle (Figure 7-6) are thinner, about 41 nm. In addition, this film has a denser distribution of thicker facets than the film annealed in a longer RTA cycle. Films

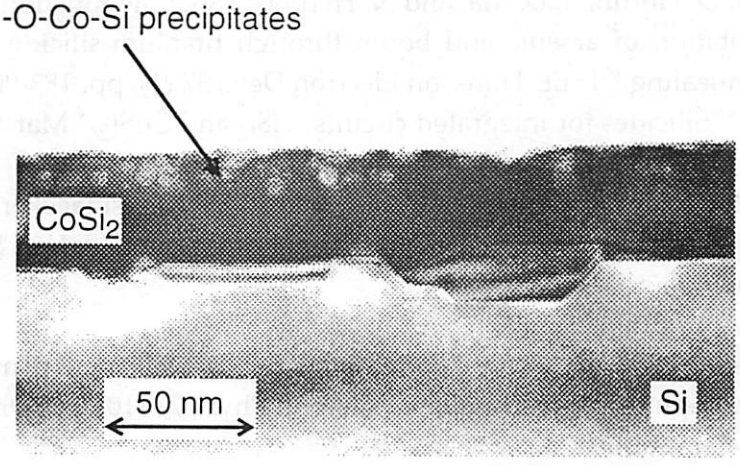

Figure 7-6. XTEM of epi-$CoSi_2$ made in 900°C, 20 s RTA

Cross-sectional transmission electron micrograph (XTEM) of epitaxial $CoSi_2$ formed in 20 s, 900°C, RTA cycle in forming gas. The shorter thermal cycle yields a thinner, 41 nm film, with greater variation in thickness. The ledges in this sample are larger, 7-8 nm thick.

used to make devices in the next chapter are all annealed for 30 s.

Another important feature in the epitaxially-grown $CoSi_2$ films are the precipitates (3-9 nm in diameter) in the top quarter of the epitaxial $CoSi_2$ film. These have been identified as amorphous Ti-N-Co-Si-O precipitates [7.14]. The precipitates, as will be shown in the next chapter, have a dramatic effect on the redistribution of dopant in the epitaxial $CoSi_2$ films. The polycrystalline $CoSi_2$ films have grain sizes on the order of 100 microns and no Ti-N-Co-Si-O precipitate layer, as the polycrystalline films were formed without Ti. The polycrystalline silicides are on average slightly thinner than the epitaxial films, about 50 nm.

7.7 References

[7.1] Q. Wang, C. M. Osburn, and C. A. Canovai, "Ultra-shallow junction formation using silicide as a diffusion source and low thermal budget," IEEE Trans. on Electron Dev., 39 (11), pp. 2486-2496, 1992.

[7.2] C. M. Osburn, Q. F. Wang, M. Kellam, and C. Canovai, "Incorporation of metal silicides and refractory metals in VLSI technology," Appl. Surf. Sci., 53, pp. 291-312, 1991.

[7.3] K. Maex, G. Ghosh, L. Delaney, and V. Probst, "Stability of As and B doped Si with respect to overlaying $CoSi_2$ and $TiSi_2$ thin films," J. Mat. Res., 4 (5), pp. 1209-1217, 1989.

[7.4] L. Rubin, D. Hoffman, D. Ma, and N. Herbots, "Shallow-junction diode formation by implantation of arsenic and boron through titanium-silicide films and rapid thermal annealing," IEEE Trans. on Electron Dev., 37 (1), pp. 183-90, 1990.

[7.5] K. Maex, "Silicides for integrated circuits: $TiSi_2$ and $CoSi_2$," Mat. Sci. Eng., R11 (2-3), pp. 53-153, 1993.

[7.6] L. Van den hove, R. Wolters, K. Maex, and R. De Keersmaecker, "A self-aligned cobalt silicide technology using rapid thermal processing," J. Vac. Sci. Tech., B4 (6), pp. 1358-63, 1986.

[7.7] E.C. Jones, unpublished.

[7.8] B-S. Chen and M.-C. Chen, "Formation of cobalt-silicided p^+n junctions using implant through silicide technology," J. Appl. Phys., 72 (10), pp. 4619-4626, 1992.

[7.9] S. Ogawa, unpublished.

[7.10] L.P. Hobbs and K. Maex, "Control of lateral overgrowth of $TiSi_2$ and $CoSi_2$ films in VLSI circuits," Appl. Surf. Sci., 53, pp. 321-327, 1991.

[7.11] J.S. Byun, S. B. Kang, H. J. Kim, and C. Y. Kim, "Epitaxial growth of $CoSi_2$ on Si wafer using Co/Ta bilayer," J. Appl. Phys., 74 (5), pp. 3156-3161, 1993.

[7.12] T.Y. Tan and G.E. McGuire, SRC Contract Review Presentation, June, 1993.

[7.13] C.-S. Wei, D.B. Fraser, M.L.A. Dass, and T. Brat, "Formation of self-aligned TiN/$CoSi_2$ bilayer from Co/Ti/Si and its applications in salicide, diffusion barrier and contact fill," in Proc. of VII VLSI Multilevel Interconnect Conf. (VMIC), pp. 233-239, 1990.

[7.14] S. Ogawa, M. Lawrence, A. Dass, and J. A. Fair, "Epitaxial $CoSi_2$ film formation on (100) Si by annealing of Co/Ti/Si structure in N_2." in *Common Themes and Mechanisms of Epitaxial Growth*, Pittsburgh: Mater. Res. Soc, pp. 193-199, 1993.

[7.15] S. Ogawa, J. A. Fair, T. Kouzaki, and R. Sinclair, "Direct solid state phase transformation from Co to epitaxial $CoSi_2$ in Co/thin Ti(100)/Si structure and its application for shallow junction formation," in *Silicides, Germanides, and Their Interfaces*, Pittsburgh: Mater. Res. Soc., pp. 355-360, 1994.

[7.16] P. Liu, B.-Z. Li, Z. Sun, and Z.-G. Gu, "Epitaxial growth of $CoSi_2$ on both (111) and (100) Si substrates by multistep annealing of a ternary Co/Ti/Si system," J. Appl. Phys., 74 (3), pp. 1700-1706, 1993.

[7.17] J.S. Byun, H.J. Cho, H.J. Kim, W.S. Kim, M.S. Choi, and D. Chun, "ZrN/$CoSi_2$ formation using the bilayer of Co/Zr for deep submicrometer devices," Proc. of X VLSI Multilevel Interconnect Conf. (VMIC), pp. 478-484, 1993.

[7.18] A.H. Reader, J. P. W. B. Duchateau, J. E. Crombeen, and E. P. Naburgh, "The formation of epitaxial $CoSi_2$ thin film on (001) Si from amorphous Co-W alloys," Appl. Surf. Sci., 53, pp. 92-102, 1991.

[7.19] S.L. Hsia, T. Y. Tan, P. Smith, and G. E. McGuire, "Formation of epitaxial $CoSi_2$ films on (001) silicon using Ti-Co alloy and bimetal source materials," J. Appl. Phys., 70 (12), pp. 7579-7587, 1991.

[7.20] M.J. Sherony, private communication.

[7.21] M.L.A. Dass, D.B. Fraser, and C.-S. Wei, "Growth of epitaxial $CoSi_2$ on (100) Si," Appl. Phys. Lett., 58 (12), pp. 1308-1310, 1991.

[7.22] S.L. Hsia, T.Y. Tan, P. Smith and G.E. McGuire, "Resistance and structural stabilities of epitaxial $CoSi_2$ films on (001) Si substrates," J. Appl. Phys., 72 (5), pp. 1864-1873, 1992.

[7.23] B.-S. Chen and M.-C. Chen, "Thermal stability of cobalt silicide thin films on Si(100)," J. Appl. Phys., 74 (2), pp. 1035-1039, 1993.

8 Epitaxial $CoSi_2$ as a shallow junction doping source

8.1 Using silicide as a dopant source

Silicided junctions have been widely evaluated for reducing the resistivity and contact resistance of ultra-shallow source/drains [8.1, 8.2]. Three processes are used to make silicide contacts to source/drain junctions (Figure 8-1). All three make use of the maskless, self-aligned silicide (salicide) process described in the previous chapter. The conventional approach is to diffuse the doped junction before forming the silicide. As the substrate is consumed during silicidation and a rough silicide with a non-planar growth front may easily grow all the way through the junction, this process is difficult to scale. For ultra-shallow junctions, "implantation through metal" (ITM) or "silicide as a doping source" (SADS, or implant through silicide, ITS) processes are advantageous [8.3 - 8.8]. In both ITM and SADS schemes, implant damage is contained in the metal or silicide, so a high temperature step to anneal implant damage in the Si is no longer necessary. Low temperatures (800°C or below) can be used for activation and drive-in of the dopant. Spiking through the junction is avoided, as conformal dopant outdiffusion occurs after the silicide is formed. SADS appears preferable, since metal atoms that are knocked into the Si during ITM implantation tend to make such devices very leaky [8.1].

There are two main difficulties when using metal layers or silicides as dopant sources: providing enough dopant supply to the interface so the dopant concentration can approach solid solubility, and ensuring the activation temperature is low enough that no agglomeration of the silicide occurs during processing. The following chapter describes the properties of shallow junction devices formed by B diffusion from epitaxial $CoSi_2$. Physical and electrical properties of junctions made with the SPE-grown epitaxial $CoSi_2$ are compared to devices made with standard, polycrystalline silicide.

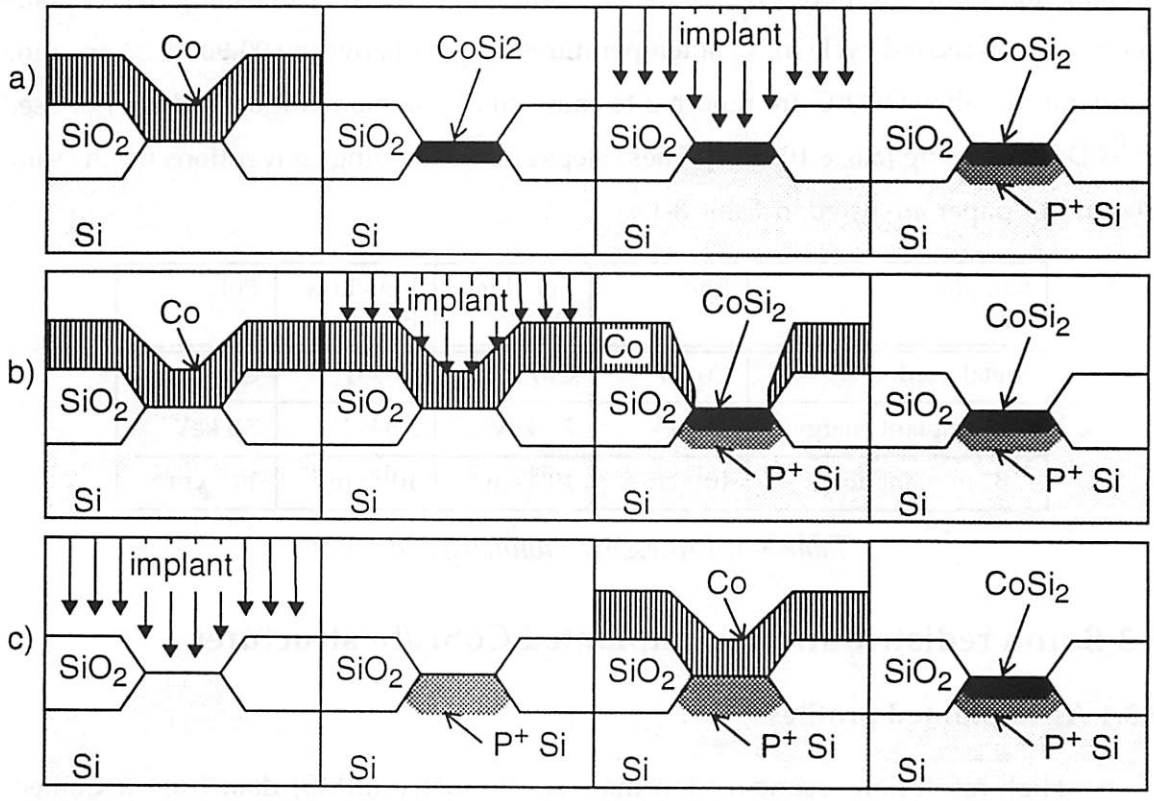

Figure 8-1. Silicided shallow junction fabrication.

Three methods for forming silicide-contacted shallow junctions: a) silicide as a doping source, b) implantation through metal, and c) the conventional process.

8.2 Experiment

Junction device structures were fabricated on 4-inch diameter, CZ-grown, (100) n-type wafers with resistivity 8-12 Ω-cm. Active diode areas were defined using the local-oxidation (LOCOS) process, as shown in Figure 6-10. The metal deposition and silicide formation were described in the previous chapter. Since BF_3 PIII was shown to cause enhanced removal of the silicide (Section 3.3.2.3), the silicides were doped by conventional implantation. $^{11}B^+$ ions were implanted at 3.5 keV and 7.5 keV at doses 10^{14} and 10^{15} cm^{-2} with an Applied Materials 9200XJ implanter. These energies were chosen to locate the B peak at 15% and 30%, respectively, of the silicide thickness [8.9]. Profile calculations show that the point where the dopant concentration falls to 1% of its peak value is 25 nm and 32 nm for these two energies, so it is expected that most of the dopant and implant damage will be contained in the silicide. Since there is no implant damage in the Si requiring high temperature removal, low temperatures (600-900°C) can be used for the dopant diffusion and activation. Transient enhanced diffusion is not expected in these samples. Post-

implant annealing was performed in the Heatpulse rapid thermal annealing (RTA) chamber, with a 30 second cycle in N_2 at temperatures varying between 600-900°C. Annealing temperatures above 900°C are reported to cause silicide agglomeration and are not used in SADS processing [8.6, 8.10, 8.11]. These steps and the naming conventions for the samples in this paper are listed in Table 8-1.

Sample	Epi	Epi - Low Dose	Epi - Low Energy	Poly
Metal used	Co/Ti	Co/Ti	Co/Ti	Co
$^{11}B^+$ implant energy	7.5 keV	7.5 keV	3.5 keV	7.5 keV
$^{11}B^+$ implant dose	10^{15} cm^{-2}	10^{14} cm^{-2}	10^{15} cm^{-2}	10^{15} cm^{-2}

Table 8-1. Processing Summary of devices

8.3 Boron redistribution in implanted $CoSi_2$/Si structures

8.3.1 As-implanted profiles

High-resolution secondary ion mass spectrometry (SIMS) data from a Cameca IMS4f spectrometer is used to monitor the as-implanted B depth profile and the B redistribution after annealing in device samples. SIMS analysis was performed with a 3 keV O_2^+ beam which hits the sample at 52° off normal incidence to improve depth resolution. Low energy O_2^+ is used to minimize ion beam mixing during depth profiling and minimize excessive spreading of the profiles [8.12 - 8.14]. The SIMS depth profiling and concentration calibration for these samples is discussed in Appendix C. Widening of the profiles is also caused by the non-planar $CoSi_2$/Si interfaces, introducing error in the depth scale on the order of the interface roughness. This error is greater for the polycrystalline samples. As the following figures will show, even with a total of approximately 8 nm error in the depth scale, distinct movement of the dopant with annealing can be seen in the SIMS data.

Figure 8-2 shows the as-implanted profiles of B in the $CoSi_2$/Si samples measured by SIMS. The $CoSi_2$/Si interface is defined for each sample as the depth where the Co signal falls to half its maximum value. The figure shows comparable B profiles in the epi and poly samples implanted with 7.5 keV, 10^{15}/cm^2 $^{11}B^+$. The profiles in both materials are deeper than expected from the simulation, due to random scattering of ions into channels in the textured silicides. Channeling occurs at these low energies even when the samples is intentionally tilted 7° off normal. The channeling of B through the epitaxial-$CoSi_2$

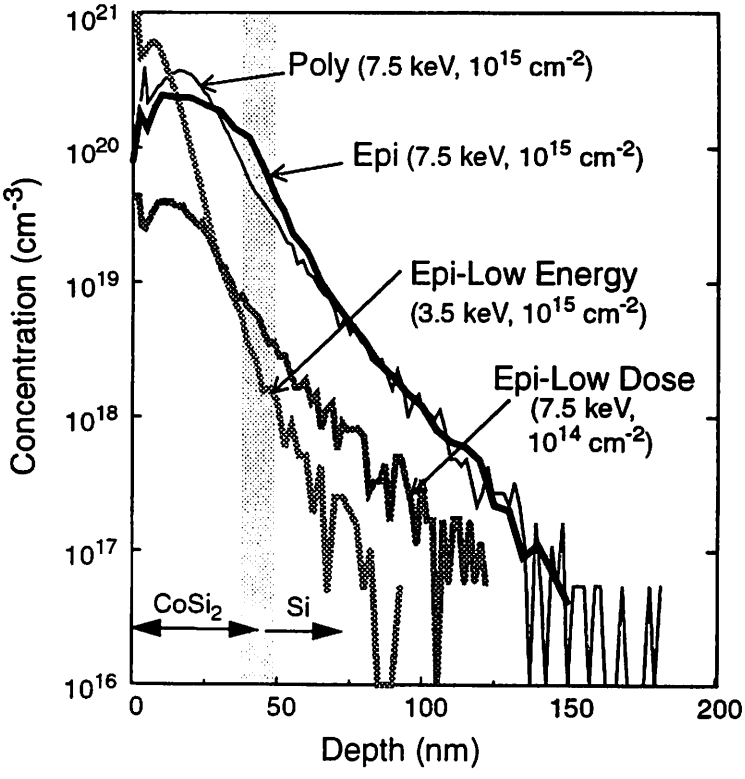

Figure 8-2. SIMS of as-implanted $CoSi_2$ samples

Secondary Ion Mass Spectrometer (SIMS) B profiles collected from as-implanted epitaxial and polycrystalline samples using 3keV O_2^+ primary beam. All samples implanted with $^{11}B^+$. Shaded region indicates variation in silicide thickness among samples.

is more severe, as expected. The profile for the low-dose epi sample (7.5 keV, $10^{14}/cm^2$ B implant) has the same shape as the higher dose implant. The low-energy epi sample (3.5 keV, $10^{15}/cm^2$ B implant) has a B peak closer to the surface and a steeper slope, as expected. The B is mostly contained in the silicide for all samples.

8.3.2 Epi sample (7.5kV, $10^{15}/cm^2$ B-implanted)

The dopant movement in the epi sample is measured by SIMS. The data in Figure 8-3a shows a buildup of B at the $CoSi_2$/Si interface and B movement into the Si. Both quantities increase with post-implant anneal temperature. Since TEM micrographs have not shown any roughening or agglomeration at the $CoSi_2$ interface during the annealing steps, the B movement seen in the SIMS cannot be attributed to interface roughening. The movement is larger than the expected cascade mixing error, so B diffusion into the Si is confirmed. According to values of diffusivity and activation energy listed in Ref. [8.15], bulk B diffusion in Si should vary from 0-1.5 nm for 600-900°C annealing. This indi-

cates that the 10-25 nm of B diffusion seen directly under the Si/$CoSi_2$ interface is enhanced by the high B concentration in that area. In the regions where the B concentration is below 10^{18} cm^{-3}, the B does not move significantly. If this process is used to make shallow junctions for deep sub-micron feature MOS devices with channel doping on the order of 10^{18} cm^{-3}, the junction depth will be independent of the annealing temperature for short RTA cycles in the range 600-900°C.

Another feature to notice is the buildup of B in the region of the Ti-containing precipitates that were shown in Figure 7-5. The precipitate layer acts as a dopant sink, very much like oxide capping layers used to avoid B loss from the silicide during annealing [8.13]. In all the samples made with epitaxial $CoSi_2$, the precipitate layer acts as a capping layer, and there is no net dopant loss in the structure with annealing. As shown by arrows in the inset of Figure 8-3a, B in the $CoSi_2$ can move both toward the $CoSi_2$/Si interface and towards the surface precipitate layer. In this sample, where the initial implant is high in dose and energy, the precipitate layer does not have a very strong effect on the junction properties. A sufficient amount of dopant diffuses into the Si to create a high-quality, pn diode after 700-900°C annealing.

8.3.3 Poly sample (7.5kV, 10^{15} cm^{-2} B-implanted)

The B redistribution in the poly sample (7.5 keV, 10^{15} cm^{-2} B) is shown in Figure 8-3b. The buildup of B at the $CoSi_2$/Si interface and B diffusion into Si are similar to the epi sample in Figure 8-3a. Like the epi sample, the value of x_j at low concentrations is independent of temperature, and high-concentration enhanced diffusion is observed. The dimensions of the p-layer under the silicide in the poly sample are averages, as the poly-$CoSi_2$ has a greater variation in silicide thickness and a non-planar interface. It is difficult to discern whether the slight increase in x_j from the epi to the poly sample is actually due to faster diffusion under the polycrystalline $CoSi_2$, SIMS measurement errors, or variable roughness of the $CoSi_2$/Si interface making the B appear to penetrate deeper. Taking into account these errors, the junction depths are indistinguishable. Buildup of B inside the polycrystalline $CoSi_2$ is different as there are no Ti-N-Co-Si-O precipitates in the material. TEM study has shown that coherent B-containing precipitate regions formed during annealing are responsible for the B peak in the center of the 900°C annealed poly sample (Figure 8-4). The presence of B in these regions is confirmed by energy-dispersive x-ray (EDX). The large B concentration in the precipitates is likely the source of their contrast.

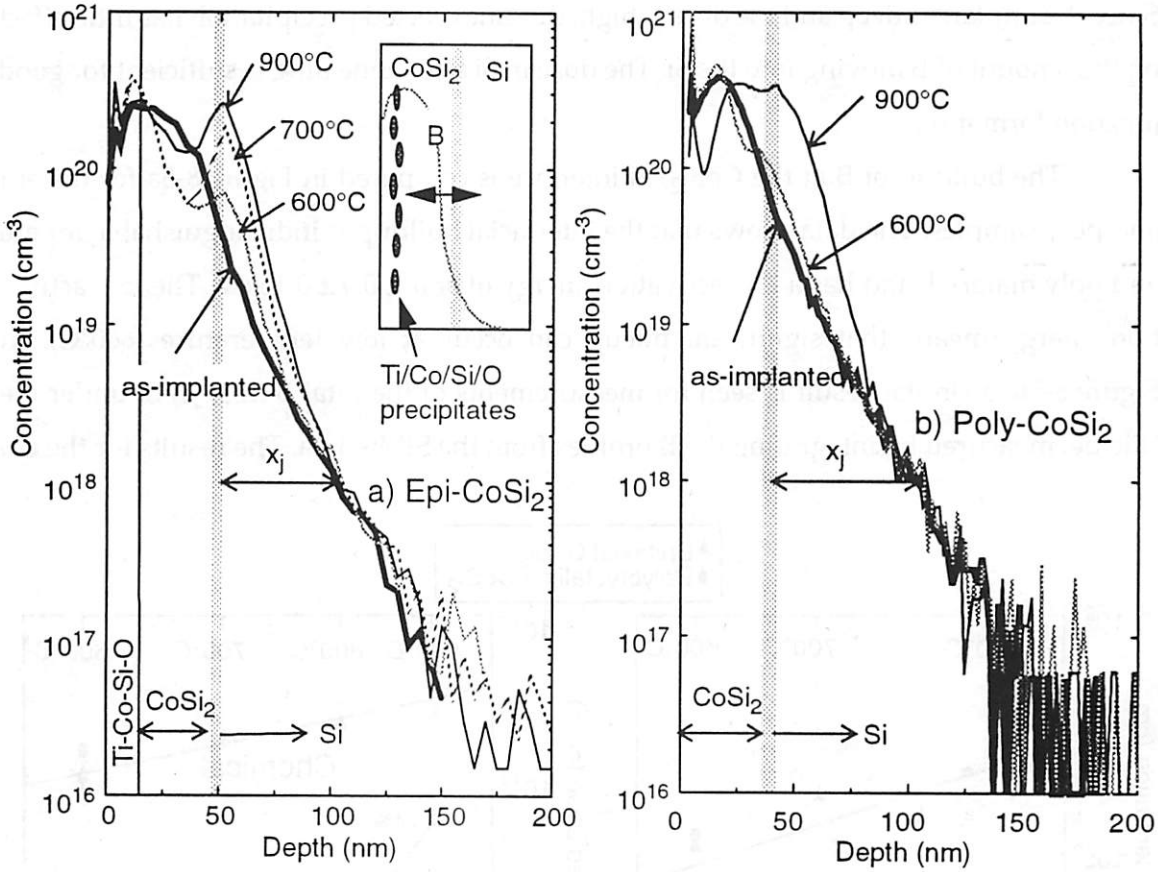

Figure 8-3. SIMS of annealed Epi-$CoSi_2$ and Poly-$CoSi_2$ samples

SIMS data collected from 7.5kV, 10^{15} cm^{-2} B implanted a) epi sample and b) poly sample before and after annealing for 30 s at 600°C, 700°C and 900°C. Annealed samples show marked B buildup at $CoSi_2$/Si interface. Epi sample shows additional buildup at location of precipitates near silicide surface. Junction depth below 10^{18} cm^{-3} does not move with annealing at these temperatures.

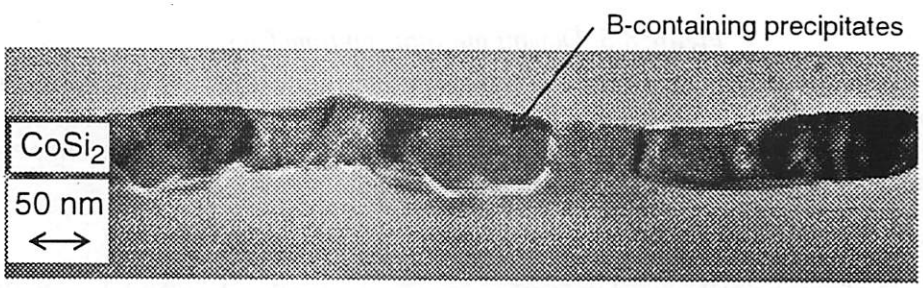

Figure 8-4. XTEM of poly-$CoSi_2$ after dopant annealing

XTEM micrograph of 7.5 keV, 10^{15} cm^{-2} B implanted polycrystalline $CoSi_2$ after 900°C annealing, showing circular regions with brighter intensity near the projected range of implant. These are identified as $CoSi_2$ regions containing high concentrations of boron.

Since the implant is deep and the dose is high, this unexpected precipitation has little effect on the amount of B moving into the Si. The dose in Si after annealing is sufficient for good junction formation.

The buildup of B at the $CoSi_2$/Si interface is compared in Figure 8-5a for the epi and poly samples. The data shows that the interfacial buildup is indistinguishable for epi and poly material, and has a low activation energy of about 0.4 ± 0.15 eV. The low activation energy means that significant pileup can occur at low temperature (600°C). In Figure 8-5b, a similar result is seen for measurements of the total B dose in Si under the silicide, measured by integrating the B profiles from the SIMS data. The results for the epi

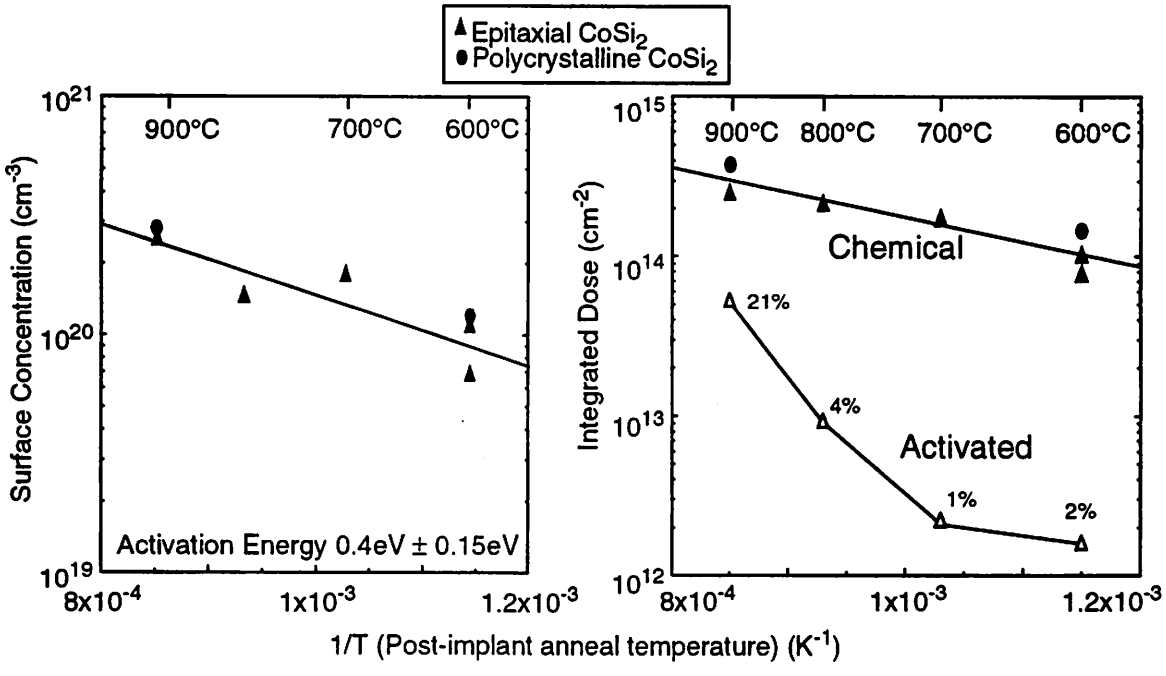

Figure 8-5. Dopant outdiffusion from $CoSi_2$

a) Arrhenius plot shows increase of B concentration at the $CoSi_2$/Si interface with post-implant annealing temperature. b) Arrhenius plot of chemical and active B doses incorporated in Si (under silicide) with post-implant annealing temperature.

and poly samples are similar, and the activation energy for the chemical dose in Si is found to be very low, 0.29 eV ± 0.05 eV. Also shown is the increase in dopant activation with annealing temperature for the epi-$CoSi_2$ sample. From this data, significant B incorporation on lattice sites requires annealing above 800°C. The activated B dose is calculated from spreading resistance profiling results. Since the first few readings under the silicide

must be disregarded due to the shunting influence of the silicide, and since error in the assumed bulk mobility values makes the calculated activated dose appear low, the values calculated here are lower bounds on the true activation and may contain errors of up to 100%.

8.3.4 Epi - low energy (3.5kV, 10^{15} cm^{-2} B-implanted)

The SIMS data from the low-energy epi sample in Figure 8-6a) shows that putting the dopant peak in the location of the Ti-N-Co-Si-O precipitate layer and starting with the dopant further away from the $CoSi_2$/Si interface lowers the dose accumulation in the Si. As shown in the figure and clarified by the magnitude and direction of the arrows in the inset, at 600°C annealing there is dopant movement into the Si, buildup at the interface, and buildup in the surface precipitate layer. At 900°C, the B flux toward the precipitate layer is much larger, depleting the B from the silicide/Si interface. Apparently, the Ti-containing precipitates require saturation by B before significant B motion into the Si is possible. At 600°C, the precipitates are saturated, and B diffusion into Si is observed. At 900°C, more B is needed to saturate the precipitates and little B is available for diffusion into Si. The presence and type of precipitate layer formed during bilayer epitaxial silicide growth must be considered when designing implant and annealing sequences for the SADS process.

8.3.5 Epi - low dose (7.5kV, 10^{14} cm^{-2} B-implanted)

Similar diffusion flux competition is seen in the low-dose epi sample in Figure 8-6b, where B is implanted at 7.5 keV energy, but at a dose of $10^{14}/cm^2$. Like the low-energy epi sample, the B flux into the Si is sizable at 600°C, and the familiar buildup of B at the interface is seen. The behavior of the low-dose epi and low-energy epi samples after 900°C annealing is similar as well. At 900°C, the B required to saturate the precipitates is larger, and the B flux toward the precipitates is dominant. In the low-dose epi case, the accumulated dose is an order of magnitude lower than the epi sample. Not enough dopant is present for saturation of the precipitates, and B is depleted from throughout the silicide to build up in the Ti-N-Co-Si-O precipitate location. There is still a B peak at the interface, but the interfacial concentration of B after the 900°C step is reduced from the as-implanted case. A threshold dose is therefore necessary to saturate the precipitates before there is a driving force for the excess B to diffuse into the Si.

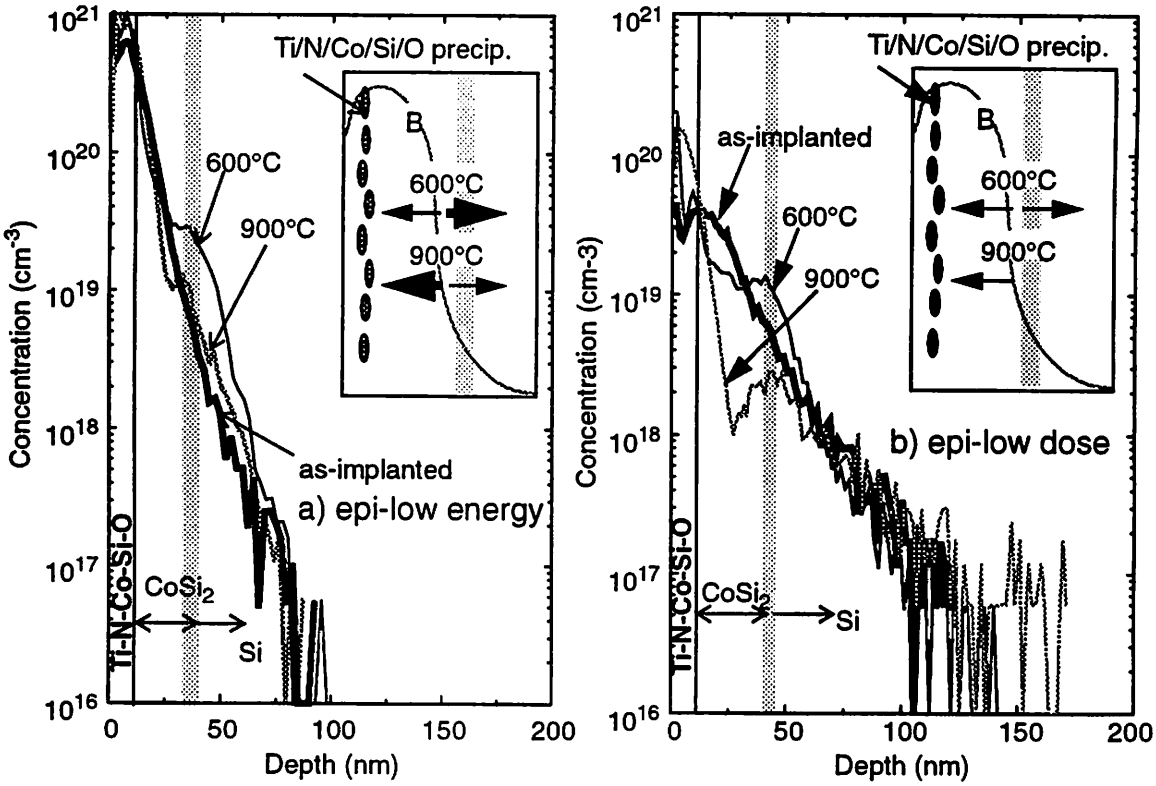

Figure 8-6. SIMS of annealed epi-low energy and low dose samples

SIMS data from a) epi - low energy and b) epi - low dose samples before and after post-implant annealing. In a), projected range of implant is very close to Ti-N-Co-Si-O precipitate layer, so most of the B is trapped there, and little diffuses into Si. In both cases, at 900°C most of the B is required for saturation of Ti-N-Co-Si-O precipitate layer, and dose in Si is small. Magnitude of arrows in inset shows relative sizes of B flux into Si and B flux toward precipitate layer at different temperatures. As in the epi and poly samples, the tail region is affected little by annealing.

The dopant gettering effect of the precipitate layer necessitates a higher energy, higher dose implant for sufficient B incorporation in the Si. Since the low-concentration implant tail defining the junction depth does not move with annealing in this temperature region, the junction depth is set by the implantation condition. As shown in Figure 8-7, the pn junction depth beyond the silicide is around 55-65 nm for the high-dose, high-energy implants at a background concentration of $10^{18}/cm^3$. From Figure 8-6a and Figure 8-6b, a pn junction depth of 20-30 nm beyond the silicide is found for the low-energy and low-dose implants. However, the lower x_j of the low-energy, low-dose implants is tied to lower surface concentrations and B doses in Si, which result in poor electrical characteristics of those samples.

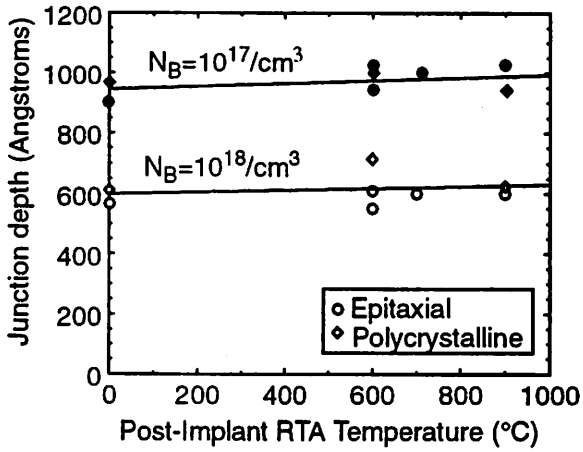

Figure 8-7. Junction depth sensitivity to background doping

Junction depth beyond silicide (x_j, as defined in Figure 8-3) is independent of annealing temperature and type of silicide for poly and epi samples (7.5kV, 10^{15} cm^{-2} dose). Total junction depth is silicide thickness plus outdiffusion depth.

8.4 Boron activation during post-implant annealing

Another factor involved in the electrical characteristics of the diodes is the dopant activation (Figure 8-5b). The dopant activation is calculated by integrating the curve of activated B in Si measured by spreading resistance profiling (SRP) in the epi sample. Little activation is seen for annealing at 600-700°C, and the Arrhenius plot slope in that region gives a low activation energy, around 0.2 eV. This activation energy is close to the activation energy of the B dose buildup in the Si (also in Figure 8-5b), suggesting that the activated B is proportional to the B diffusing into the Si: a certain fraction of the diffusing B finds substitutional lattice sites. Above 700°C, the activated dose in Si increases rapidly, faster than the total dose. The higher temperatures are needed to efficiently activate both the B present and B diffusing in. The increase in post-implant annealing temperature from 800°C to 900°C increases the activated B dose in Si by a factor of 5, from 9.4×10^{12} cm^{-2} to 5.4×10^{13} cm^{-2}, without increasing the junction depth.

8.5 Electrical characterization of diodes

Variation in the electrical properties of the diodes and silicide degradation are the main constraints on the annealing process window since the junction depth is constant.

8.5.1 Epi and poly samples (7.5kV, 10^{15} cm^{-2} B implant)

The *JV* curves of characteristic diodes from the epi and poly samples are shown in Figure 8-8a and b, respectively. The forward bias curves show that the diodes behave like pn diodes in the forward turn-on region, with forward saturation currents at least 4-6 orders of magnitude higher than the reverse leakage currents at all temperatures and diode ideality factors of 1.10 for epi samples and 1.04 for poly samples after 700°C post-implant anneal. The reverse characteristics show that the leakage improves as the post-implant annealing temperature is increased from 600-700°C, both by reducing the leakage current and by slightly reducing the slope of the *JV* curve (Section 1.2.5). The reverse leakage currents after 700°C and 800°C post-implant annealing are similar in magnitude for both the epi and poly sets of diodes. For the epi diodes, the slopes of the 800°C curves are lower, indicating lower carrier generation in the space-charge region. This indicates that the higher boron concentration and activation in the 800°C p^+ layer is shrinking the penetration of the space charge region into the p^+ layer. This reduces the effect of any deep-level centers in the region, and creates a thicker quasi-neutral p^+ region buffer between the depletion region and the $CoSi_2$ interface. When this quasi-neutral region is too thin, within a diffusion length of the space-charge region, majority carriers from the metal are able to diffuse to its edge and add to the leakage current [8.16].

After 900°C annealing, the reverse-biased *JV* slopes increase only slightly for both types of silicides, but the magnitude of leakage in the 900°C epi diode increases noticeably. The unchanged slope indicates that the depletion region itself is roughly comparable to the one after 800°C post-implant annealing. The cause of the increased leakage magnitude is probably silicide-related. Further inspection of the 900°C post-implant annealed polycrystalline silicide *JV* characteristics shows that although the poly diodes have a lower leakage in magnitude than the epi diodes, the slope of the characteristics is higher than the epi diodes and the curves contain a bump at -3V. This suggests an additional source of leakage current a small distance above the metallurgical junction in the p^+ region, likely due to the proximity of the rough poly-$CoSi_2$ interface. Another possible explanation is that residual implant damage is created in regions where the silicide is thin and the boron entirely penetrates through to the silicon during implantation.

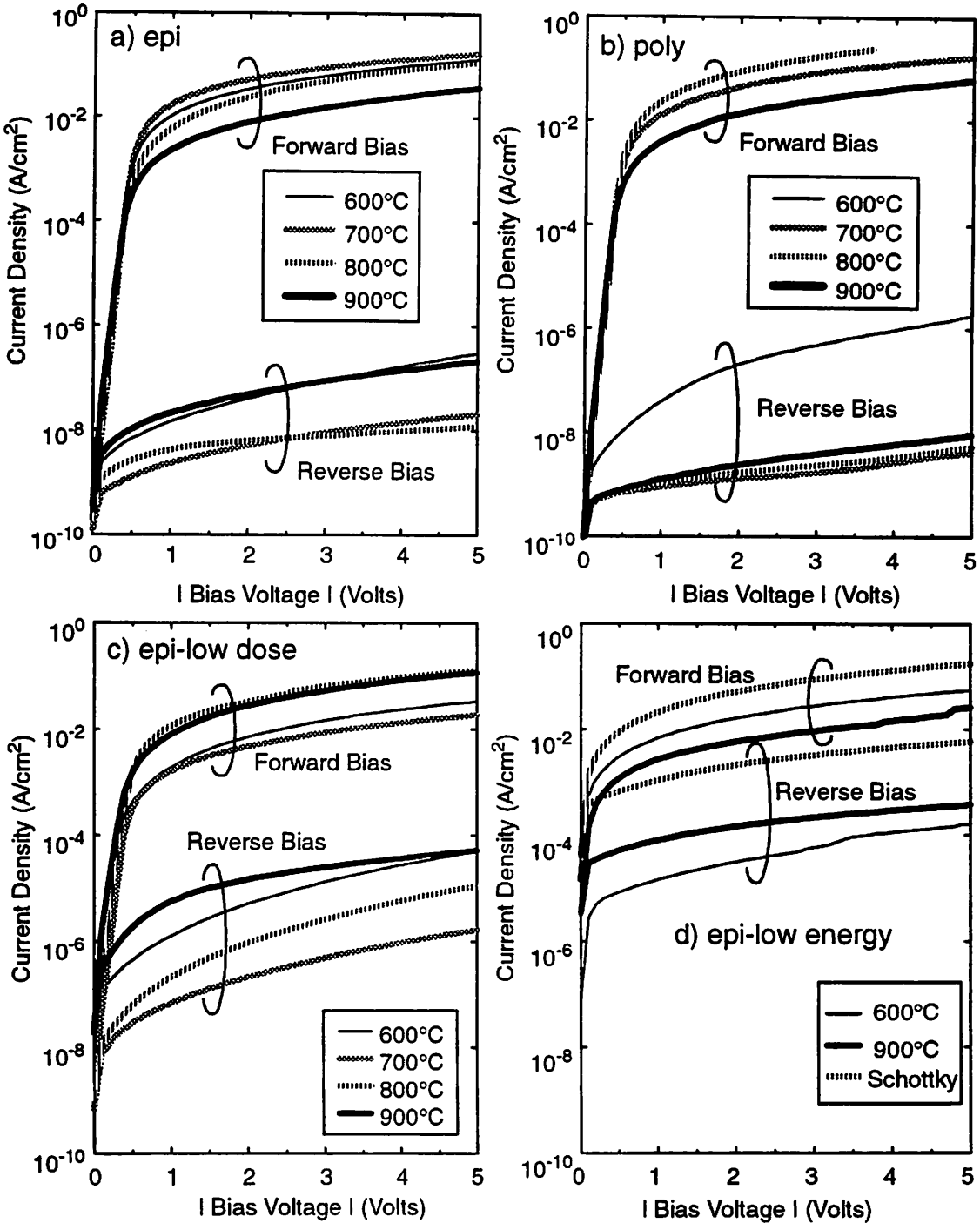

Figure 8-8. Current density-voltage characteristics of $CoSi_2$ diodes

Forward and reverse current density-voltage curves with varying anneal temperatures. a) epi diodes with minimum reverse leakage current density 12 nA/cm^2, and minimum slope among the curves observed after 800°C anneal. b) poly sample diodes have minimum reverse leakage current density at 700°C, and smaller leakage for 700°C-900°C than epi-$CoSi_2$ diodes. c) epi-low dose diodes. d) epi-low energy diodes.

8.5.2 Low-dose epi (7.5 keV, 10^{14} cm^{-2} B implant) and low-energy epi (3.5 keV, 10^{15} cm^{-2} B implant)

For the low-dose epi diode, excessive leakage currents are observed (Figure 8-8c). The slope of the reverse-biased JV characteristics after post-implant anneal at 600-800°C is similar to the steep rise in the epi and poly diode leakage current densities at 600°C. After 900°C annealing the curve flattens out, indicating that a junction of better quality has been formed under the silicide, although the proximity of the metal to the junction keeps the current high. The behavior of low-energy epi diode shown in Figure 8-8d, implanted with boron at 3.5kV, behaves even more like a Schottky contact (i.e., a device with no B implant). The low-energy diode JV curves have been compared with the curves for a Schottky diode made with the same silicide. The low-energy epi diode currents follow the contours of the Schottky diode currents closely, but the magnitude of the reverse leakage current is 10-100 times lower. The same comparison to the contours of the Schottky diode can be made for the low-dose epi diodes, although in the low-dose epi case the current is reduced by factors of 10^2-10^4. The Schottky-like behavior of the low-dose epi and low-energy epi diodes may be explained by considering them as camel diodes with the small amounts of boron present under the silicide increasing the effective barrier height of the contact [8.17, 8.18].

For the camel diodes, a very small change in the barrier height can cause a large change in the reverse leakage current, like the factor of 10-10^4 reduction in currents seen in these samples. The camel diode model explains the difference between the low-dose and low-energy epi samples: the low-dose epi sample shows lower leakage because its boron layer is thicker while the surface concentrations of the two samples are comparable. As seen for the low-energy epi samples, even the small amount of dopant present and activated after 600°C annealing is able to raise the barrier and lower the leakage an order of magnitude. However, the low-dose epi and low-energy epi diodes do not have pn diode characteristics, and have reverse leakage currents more than 100 times larger than the epi and poly samples. A summary of the diode types and ideality factors after 700°C annealing is shown in Table 2. The camel behavior is discussed fully in the next chapter.

Sample	Epi	Epi-Low Dose	Epi-Low Energy	Poly
B dose in Si from SIMS	high	low	low	high
Junction type	pn junction	camel diode	camel diode	pn junction
n, diode ideality factor	1.11	1.37	5.3 at 600°C	1.04
Total leakage current density	21 nA/cm^2	1700 nA/cm^2	175 μA/cm^2 at 600°C	4 nA/cm^2

Table 8-2. Summary of diode physical and electrical properties after 700°C post-implant annealing.

8.6 Discussion

The variation of leakage current magnitude with post-implant anneal temperature is shown for the epi and poly diodes in Figure 8-9. Each point is an average of 5 or more diodes tested at the given post-implant anneal condition. The curves show that it is preferable to activate the dopant in the range of 700°-800°C to achieve the lowest possible leakage currents. The post-implant anneal of 600°C is clearly insufficient to promote adequate dopant movement and activation. As the junction depth is independent of the temperature of this post-implant anneal, a 700°C anneal may be chosen to keep the thermal budget at a minimum, or an 800°C anneal may be chosen to minimize reverse leakage current while promoting dopant activation. The curves show that the poly process creates low leakage junctions that are thermally stable up to a 900°C, 30 s RTA step. The epi samples

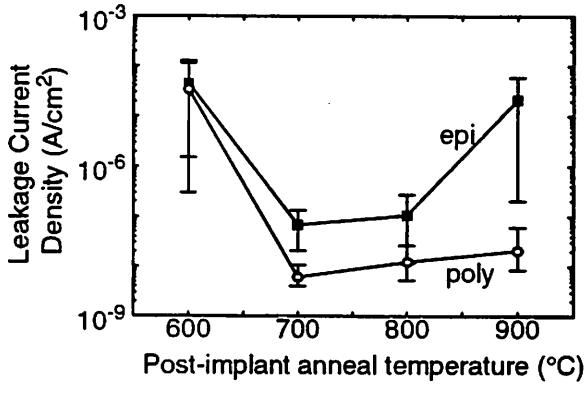

Figure 8-9. Effect of dopant activation temperature on $CoSi_2$ diode leakage

Leakage current density measured at -5V bias of epi and poly samples with variation in annealing temperatures. 700°C-800°C is the ideal range for the epitaxial $CoSi_2$ diodes, as the epi sample current increases after 900°C annealing. Error bars show highest and lowest leakage current measured for the sample.

also produce good diodes that are thermally stable up to 800°C. As there is no evidence of large-scale morphology changes in the silicide after 900°C annealing, the increased leakage of the 900°C post-implant annealed epi samples is attributed to local defect failures, perhaps due to thermal-mechanical stresses in the bilayer-formed epitaxial silicide. The U-shaped curve of Figure 8-9 has been seen previously for poly-$CoSi_2$ diodes, where the increase in current after 900°C annealing was attributed to silicide agglomeration [8.1]. As mentioned, the slopes of the JV curves after 900°C annealing (in Figure 8-8) support the idea that the increase in leakage is not pn-junction related, but rather a property of the silicide. In these samples, however, a sheet resistivity increase has not been detected in these silicides after the anneal, as is usually the way agglomeration is quantified in absence of TEM data [8.10, 8.11]. More unexpected is the fact that the poly diode is unaffected by the high-temperature anneal while the epi diode leakage has increased, since previous work reports that epitaxial silicides are more resistant to agglomeration [8.10]. Perhaps relaxation of high strains in small-area epitaxial silicide diodes causes agglomeration which is not seen in large- area blanket films.

The total leakage current of devices depends highly on the perimeter current density, which is more a function of the interfacial structure of the device than a property of the diffused junction being studied. As in Section 6.7, devices with varying area and perimeter are used to distinguish the area (J_a) and perimeter (J_p) components of the reverse leakage currents. A graph of I_{total}/L versus L is shown for the 700°C post-implant annealed nominal poly and epi diodes (Figure 8-10). The slopes provide areal leakage density of 2 nA/cm^2 for poly after a 700°C post-implant anneal. The areal leakage density of the epi appears larger from the three largest samples in the plot, but the areal and perimeter leakage densities of the epi diodes are masked by a sharp increase in the leakage current density as the diode size decreases. This increase may be due to either an area-dependent metallurgical effect like stress, a different morphology of the epitaxial silicide in smaller area contacts, or a significant contribution from the corners of the diode. The areal leakage of the poly diode is comparable to diodes made by direct implantation into Si. The perimeter leakage of the poly diodes was calculated at 170 pA/cm, and is almost twice the value found of 90-95 pA/cm found in Section 6.7 for 100 nm junctions formed by implantation directly into Si and 1060°C annealing. The higher value of perimeter leakage may indicate that lateral diffusion of dopant out of the silicide or silicide growth at the edges can be sig-

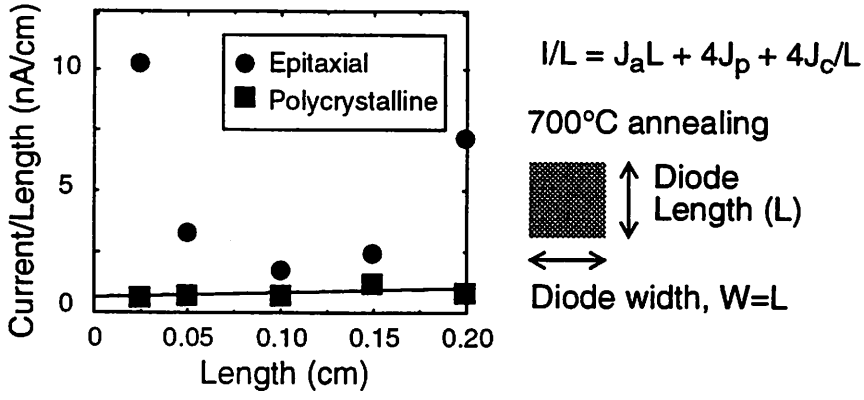

Figure 8-10. Area and perimeter leakage currents of Epi and Poly-$CoSi_2$ diodes
Plot shows variation of bulk leakage current density (J_a) and perimeter leakage current density (J_p) among Epi and Poly diodes annealed at 700°C. Points are averages of diode leakage for a certain size diode.

nificantly different than in the bulk region, and will be the limiting factor in producing low-leakage 100 nm junctions with the SADS process. Again, as shown in Table 8-3, it is seen that the leakage of the low-energy epi diode is an order of magnitude better than the Schottky diode, and the low-dose implant is two orders of magnitude lower in leakage.

Sample	J_a	J_p
Epi-Low Dose	33 μA/cm^2	1 μA/cm
Epi-Low Energy	357 μA/cm^2	26 μA/cm
Schottky	1.1 mA/cm^2	295 μA/cm

Table 8-3. Area and perimeter leakage of diodes after 900°C dopant activation annealing.

Figure 8-11 shows the correlation between physical junction properties and electrical characteristics. The graph correlates the leakage current density to the concentration of boron at the $CoSi_2$/Si interface. A similar relation is observed by plotting the leakage current density versus the B dose incorporated in the Si. The clustering of most of the points around a single line regardless of annealing confirms that the implant profile is the most important parameter to optimize to achieve a low-leakage diode. For epi-$CoSi_2$, this is due to the Ti-N-Co-Si-O precipitates which restrict the dopant movement into the Si in the low-energy and low-dose implant cases, and make it necessary to use a higher-dose, deeper implant to get enough B under the silicide to make a pn junction. The 900°C, low-dose implanted diode is the only sample which does not follow the trend. As explained previ-

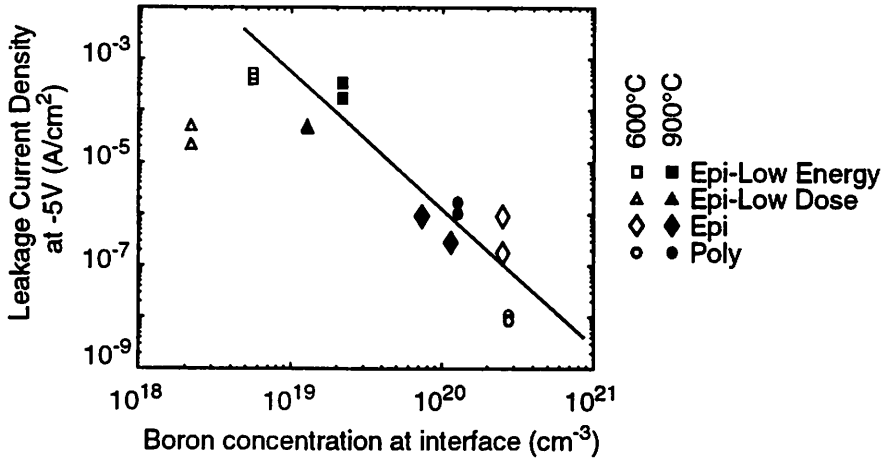

Figure 8-11. Correlation of B interface concentration and diode leakage

ously, it is a camel diode contact whose leakage is dependent on the depth of the p layer. In this case, the leakage current is lower than expected from the curve because the dopant layer is thick (due to the 7.5kV implant) although the B interface concentration is low.

8.7 Conclusion

When shallow junctions are formed with the SADS process using a Co/Ti bilayer to form an epitaxial $CoSi_2$ contact, the use of a thin Ti interlayer which helps the film grow epitaxially can radically affect the dopant redistribution. Since the Ti bilayer used in the epitaxial silicide formation creates a layer of dopant gettering precipitates. A threshold dose of B is required to saturate the precipitates before sufficient B diffusion into the Si can occur. These effects are seen clearly in electrical characteristics, where samples implanted with low-dose or low-energy dopant have high leakage. The low-energy and low-dose implanted diodes are best described as camel diode contacts, whose reverse leakage is a sensitive function of the doping levels. The low-dose epi diodes are slightly better, owing to the deeper penetration of B into the Si. A sufficiently high-dose, high-energy implant and annealing in the 700-800°C range is the best choice for creating a low-leakage, good quality pn junction with this process. As shown by SIMS data, the resulting junction depth of these low-leakage diodes is constrained in the area of 100 nm, including the silicide thickness. Shallower junctions will require either thinner silicides or acceptance of leakage currents in excess of the $1nA/cm^2$ ULSI benchmark.

8.8 References

[8.1] C.M. Osburn, Q.F. Wang, M. Kellam, C. Canovai, P.L. Smith, G.E. McGuire, Z.G. Xiao, and G.A. Rozgonyi, "Incorporation of metal silicides and refractory metals in VLSI technology," Appl. Surf. Sci., 53, pp. 291-312, 1991.

[8.2] D.B. Scott, R.A. Chapman, C. Wei, S.S. Mahant-Shetti, R.A. Haken, and T.C. Holloway, "Titanium disilicide contact resistivity and its impact on 1- mu m CMOS circuit performance," IEEE Trans. on Elec. Dev., 34 (3), pp. 562-574, 1987.

[8.3] C.M. Osburn, S. Chevacharoenkul, Q.F. Wang, K. Markus, G.E. McGuire, and P.L Smith, "Materials and device issues in the formation of sub-100-nm junctions," Nucl. Instr. & Meth. in Phys. Res., B74, (1-2), pp. 53-9, 1993.

[8.4] H. Jiang, C.M. Osburn, P. Smith, Z.-G. Xiao, D. Griffis, G. McGuire, and G.A. Rozgonyi, "Ultra shallow junction formation using diffusion from silicides. I. Silicide formation, dopant implantation and depth profiling," J. Electrochem. Soc., 139 (1), pp. 196-206, 1992.

[8.5] H. Jiang, C.M. Osburn, Z.-G. Xiao, G. McGuire, G.A. Rozgonyi, B. Patnaik, N. Parikh, and M. Swanson, "Ultra shallow junction formation using diffusion from silicides.II. Diffusion in silicides and evaporation," J. of the Electrochem. Soc., 139 (1), pp. 206-11, 1992.

[8.6] Q. Wang, C.M. Osburn, and C.A. Canovai, "Ultra-shallow junction formation using silicide as a diffusion source and low thermal budget," IEEE Trans. on Elec. Dev., 39 (11), pp. 2486-2496, 1992.

[8.7] V. Probst, H. Schaber, A. Mitwalsky, H. Kabza, L. Van den hove, and K. Maex, "WSi_2 and $CoSi_2$ as diffusion sources for shallow-junction formation in silicon," J. Appl. Phys., 70 (2), pp. 708-719, 1991.

[8.8] O. Thomas, P. Gas, F.M. d'Heurle, F.K. LeGoues, A. Michel, and G. Scilla, "Diffusion of boron, phosphorus, and arsenic implanted in thin films of cobalt disilicide," J. Vac. Sci. Tech., A6 (3, pt. 2), pp. 1736-1739, 1988.

[8.9] J.F. Ziegler and J.P. Biersack, *The Stopping and Range of Ions in Solids*, New York: Pergamon Press, 1985.

[8.10] S.L. Hsia, T.Y. Tan, P. Smith and G.E. McGuire, "Formation of epitaxial $CoSi_2$ films on (001) silicon using Ti-Co alloy and bimetal source materials," J. Appl. Phys., 70 (12), pp. 7579-7587, 1991.

[8.11] B.-S. Chen and M.-C. Chen, "Thermal stability of cobalt silicide thin films on Si (100)," J. Appl. Phys., 74 (2), pp. 1035-1039, 1993.

[8.12] W. Eichammer, K.Maex, K. Elst, and W. Vandervorst, "Boron outdiffusion from poly- and monocrystalline $CoSi_2$,"Appl. Surf. Sci., 53, pp. 171-179, 1991.

[8.13] K. Maex, "Silicides for integrated circuits: $TiSi_2$ and $CoSi_2$," Mater. Sci. and Eng., R11, pp. 53-153, 1993.

[8.14] W. Vandervorst and F.R. Shepherd, "Secondary ion mass spectrometry profiling of shallow, implanted layers using quadrupole and magnetic sector instruments," J. Vac. Sci. Tech., A5 (3), pp. 313 -320, 1987.

[8.15] C. Zaring, Ph.D. Thesis, Royal Institute of Technology, 1993.

[8.16] R. Liu, D.S. Williams, and W.T. Lynch, "A study of the leakage mechanisms of silicided n^+/p junctions," J. Appl. Phys., 63(6), pp. 1990 -1999, 1988.

[8.17] L.C. Zhang, C.L. Liang, S.K. Cheung, and N.W. Cheung, "Refractory metal nitride rectifying contacts on GaAs," J. Vac. Sci. Tech. B5 (6), pp. 1716-22, 1987.

[8.18] G.P. Schwartz and G.J. Gualtieri, "Schottky barrier height enhancement on M-P^+-N structures including free-carriers," J. Electrochem. Soc. 133 (7), pp. 1266-1268, 1986.

9 Ultra-shallow junction scaling

9.1 Introduction

In standard implant and rapid thermal anneal processes, junction depth is reduced by lowering implant energy and thermal budget. For p-type doping, this lower thermal budget may lower the active boron concentrations below $2x10^{19}$ cm^{-3}. Junctions made by diffusion from a solid or gaseous dopant source may have higher activation, but will have steep, error-function shaped profiles. When these junctions are deep, they exhibit ideal pn junction leakage due to hole and electron generation in the junction depletion region and minority carrier diffusion across the junction. When they become very shallow, below several hundred Angstroms, the junctions may become fully depleted and behave as camel diode contacts [9.1]. A camel diode is a Schottky metal-semiconductor contact with a barrier height enhanced by a thin layer of carrier-depleted Si doped oppositely to the substrate under the metal. When the junction becomes shallow enough to be described as a camel diode contact, its leakage current due to thermionic emission of carriers from the metal into Si increases rapidly. Since a camel diode is fully or partially depleted, it has no quasi-neutral region and cannot behave as a minority carrier device. This chapter investigates the electrical behavior of junctions as they become very shallow, using the simple analytical model of Shannon [9.1], 1-D device simulations, and the $CoSi_2$ diodes fabricated in the previous chapter. A *CV* method for detecting the camel to pn junction crossover point in devices is developed.

9.2 Camel diode barrier height and leakage current

9.2.1 Barrier height calculation

A schematic of the doping profile and band diagram of a camel diode (i.e., Shannon contact) is shown in Figure 9-1. The thin p-layer of thickness d has an arbitrary net

doping profile of concentration $N_A(x)$, which is assumed to be completely depleted in this simple analysis. The thermionic emission barrier height is then the sum of the barrier height of the metal contact to n-Si (Φ_B) and the enhancement due to the p-layer, $\Delta\Phi(V)$:

$$\Phi_B(V) = \Phi_{BO} + \Delta\Phi(V) \tag{9-1}$$

where the enhancement $\Delta\Phi$ is a function of the p-layer doping, junction depth, substrate doping, temperature, and applied voltage. The metal contact is assumed to be the epitaxial $CoSi_2$ material described in the previous chapters, with workfunction 4.789 eV.

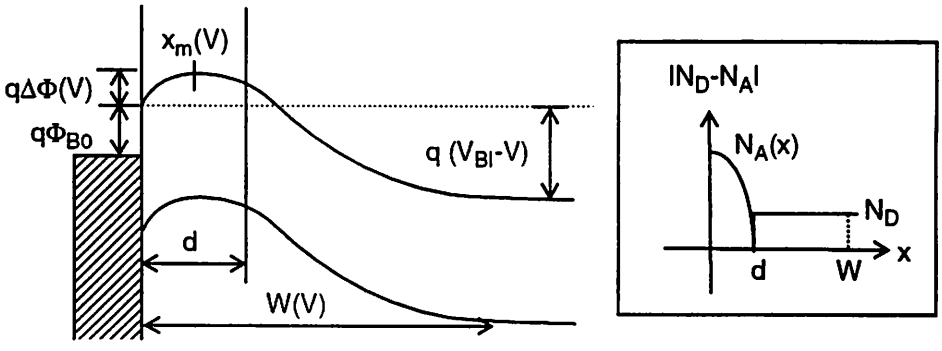

Figure 9-1. Schematic drawing of camel diode contact band diagram

$q\Phi_{B0}$ is the barrier height of the Schottky diode (with no p-type doping layer) at zero bias. $q\Delta\Phi(V)$ is the voltage-dependent enhancement in the effective barrier height due to the dopant profile shown in the inset. $N_A(x)$ and N_D are net dopant concentrations.

In this model, when the p-layer doping and thickness are increased, the total barrier height to *n*-Si will saturate. Saturation occurs when the band bending between the p-Si and n-Si reaches its maximum value, $E_g - \Phi_n - \Phi_p$, at thermal equilibrium, where Φ_n is $E_c - E_f$ in the quasi-neutral *n*-type substrate, and Φ_p is $E_f - E_v$ in the quasi-neutral region of the diffused layer. When the barrier height saturates, holes begin to build up in the area of the peak potential, and the layer is no longer fully depleted. This is one measure determining when the device begins to behave like a pn junction.

The barrier height enhancement is calculated from Poisson's equation, assuming complete depletion of the surface layer of thickness *d* [9.2]. The second derivative of the potential is related to the ionized dopant profiles:

$$\frac{d^2\Psi}{dx^2} = \frac{-q}{\varepsilon_s} N_A(x) \quad \text{for } 0 \le x \le d, \tag{9-2}$$

$$\text{and } \frac{d^2\Psi}{dx^2} = \frac{-q}{\varepsilon_s} N_D \quad \text{for } d \le x \le W, \tag{9-3}$$

where W is the total thickness of the depletion layer, q is the electron charge, ε_s is the permittivity of silicon, and N_D is the uniform doping concentration of the substrate. Equation 9-2 and Equation 9-3 are integrated once to find the electric field, $d\Psi/dx = -E(x)$, and integrated again to find the potential, $\Psi(x)$. The calculation uses the following boundary conditions: the electric field and potential are continuous at the boundary between the n- and p-type doping layers ($x = d$), the electric field at the edge of the depletion region ($x = W$) is zero, and the potential at the surface is $\Psi\ (x=0) = \Phi_{B0}$ if image-force lowering is ignored. The potential is then found:

$$\Psi(x) = \Phi_{B0} + \left[\frac{q}{\varepsilon_s} N_D (d - W)\right] x + \frac{q}{\varepsilon_s}\int_0^x x N_A(x')\,dx' + \frac{q}{\varepsilon_s} x \int_x^d N_A(x')\,dx' \quad \text{for } d \le x \le W, \tag{9-4}$$

$$\text{and} \quad \Psi(x) = \Phi_{B0} + \frac{q}{\varepsilon_s} N_D \left(\frac{d^2}{2} + \frac{x^2}{2} - dW\right) + M \quad \text{for } d \le x \le W. \tag{9-5}$$

The quantity M is the spatial moment of the p-type doping profile:

$$M = \frac{q}{\varepsilon_s}\int_0^d x \cdot N_A(x)\,dx\ . \tag{9-6}$$

The total depletion width W is then found from setting the potential in the bulk, $\Psi\ (x = W) = \Phi_{B0} - (V_{BI} - V)$, as described in Figure 9-1.

$$W(V) = \left[\frac{2\varepsilon_S}{qN_D}\cdot (V_{BI} - V) + d^2\left(1 + \frac{M}{d^2 N_D/2}\right)\right]^{1/2} \tag{9-7}$$

The total barrier height is then found by finding the maximum value of $\Psi(x)$, which occurs where the electric field $(-d\Psi/dx)$ equals zero. This gives an expression for the position (x_m) where the potential is maximum:

$$\int_0^{x_m} N_A(x)\,dx = N_D(d - W) + \int_0^d N_A(x)\,dx \tag{9-8}$$

Once x_m and W are found from Equation 9-8 and Equation 9-7, the total barrier height $\Phi(V)$ is equal to $\Psi(x_m)$:

$$\Psi(x_m) = \Phi_{B0} + \frac{q}{\varepsilon_S}\left(N_D x_m (d - W) + x_m \int_{x_m}^d N_A(x)\,dx + \int_0^{x_m} x \cdot N_A(x)\,dx\right) - \frac{q^2}{16\pi\varepsilon_s}\frac{1}{x}\ . \tag{9-9}$$

Image force lowering of the barrier is included in the last term in Equation 9-9, as the image force correction can be large in lowly doped layers: for a layer with 10^{19} cm^{-3}, the correction is only 0.3%, but for a 10 nm layer with constant doping of 10^{18} cm^{-3}, the correction is 60%. The voltage dependence in W and x_m in Equation 9-9 causes the maximum barrier height to fall when the magnitude of the applied reverse bias is increased. For an arbitrary doping profile, the equations can be solved numerically.

9.2.2 IV Characteristics

The current density-voltage characteristic of the camel diode contact is dominated by thermionic emission current, like a Schottky contact, but with enhanced barrier height:

$$J_{SC} = A^* T^2 exp\left(\frac{-q\Phi_B(V)}{kT}\right)\left[exp\left(\frac{qV}{kT}\right)-1\right] \qquad (9\text{-}10)$$

where A* is the effective Richardson constant for n-type Si, 252 $A/cm^2/K$. An example of the current density-voltage plots expected from these relations is plotted in Figure 9-2, assuming constant doping in the p-layer. As shown in Ref. [9.1], for moderate doping levels the magnitude of the current density is sensitive to very small changes in the junc-

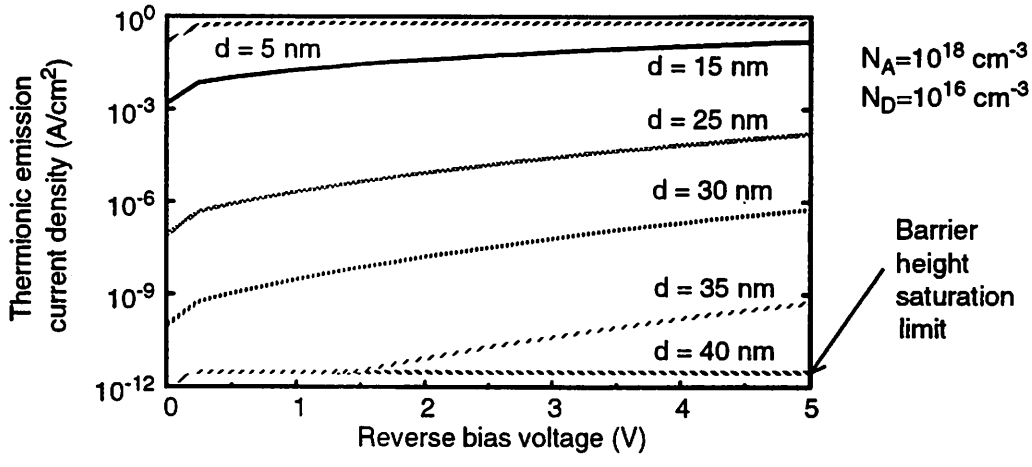

Figure 9-2. Current density-voltage curves for camel diode contacts

Simulated current density-voltage curves show rapid variation in current magnitude with p-type layer thickness variation for constant doping: N_A=10^{18} cm^{-3}, N_D=10^{16} cm^{-3}. 40 nm curve shows barrier height saturation current level of $3x10^{-12}$ A/cm^2.

tion depth. As the barrier height lowers, the leakage climbs rapidly. A small, 5 nm thickness variation causes a factor of 1000 increase in leakage at -3.3 V of a 30 nm junction with

junction doping of 10^{18} cm^{-3} and background doping of 10^{16} cm^{-3}. In the 35 nm p-layer curve, the slope of the characteristic changes at -1.5 V where the increasing bias lowers the barrier height from the saturation value seen at low bias values. When the barrier height saturates, and the band bending reaches its maximum, the thermionic emission leakage drops to the pA/cm^2 level according to this model.

To determine how shallow a junction can be tolerated at different doping levels, the leakage current density is plotted as a function of the p-layer thickness while varying the constant p-layer doping concentration, N_A, in Figure 9-3. The figures show the pn junc-

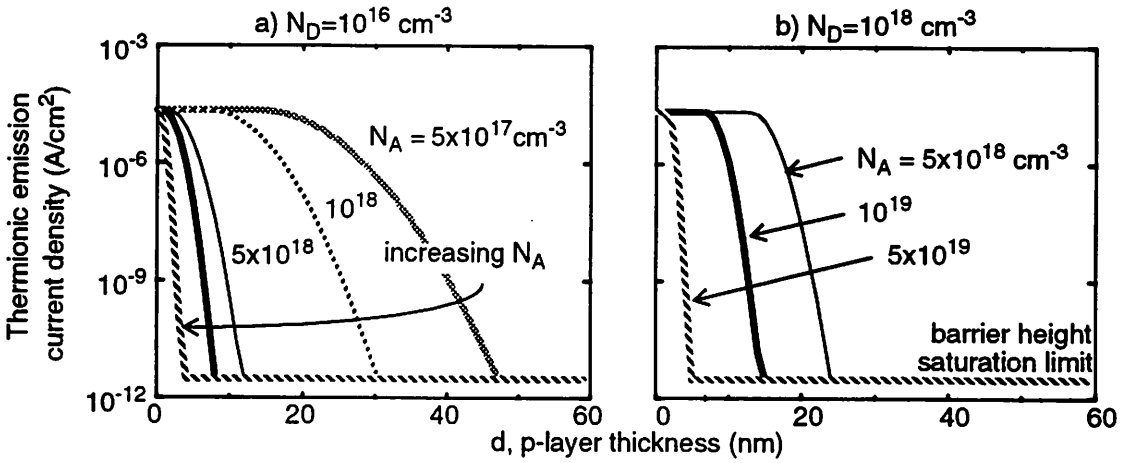

Figure 9-3. Variation in thermionic emission currents with substrate doping
Simulated current density at -3.3 V reverse bias for $CoSi_2/p$-Si/n-Si camel diode contacts with a) 10^{16} cm^{-3} and b) 10^{18} cm^{-3} substrate doping and uniform doping of surface dopant layers.

tion depth required to avoid thermionic emission leakage. According to this model, a shallow junction abutting a MOSFET channel region with doping near 10^{18} cm^{-3} requires more than 25 nm of material doped $5x10^{18}$ cm^{-3} or more to avoid thermionic emission leakage. If activation above 10^{19} cm^{-3} is possible, a 15 nm layer may be sufficient to meet the leakage requirement. The current is exponentially dependent on the barrier height enhancement, which is proportional to the spatial moment, or $N_A d^2$ in the case of constant doping; therefore, the leakage current of the camel diodes is very sensitive to doping profile. Diodes fabricated with doping that puts them near the camel regime exhibit large fluctuations in leakage with minor process variations.

9.2.3 Effect of profile shape on barrier height

As discussed above, the profile of a shallow junction in the camel diode regime influences its electrical behavior. In Figure 9-4, the equations from Section 9.2.1 are used to calculate the barrier heights for different profiles with the same surface concentration and dose of active dopant. In this example, the exponential profile, with the highest spatial moment, has the highest barrier height. Figure 9-5 shows the variation in barrier height when the junction depth is 10 nm and the surface concentration is varied to keep the doses constant. A more box-like profile is shown to be preferable for meeting a junction goal. To make a 10 nm junction with constant dose, the surface concentration of the exponential

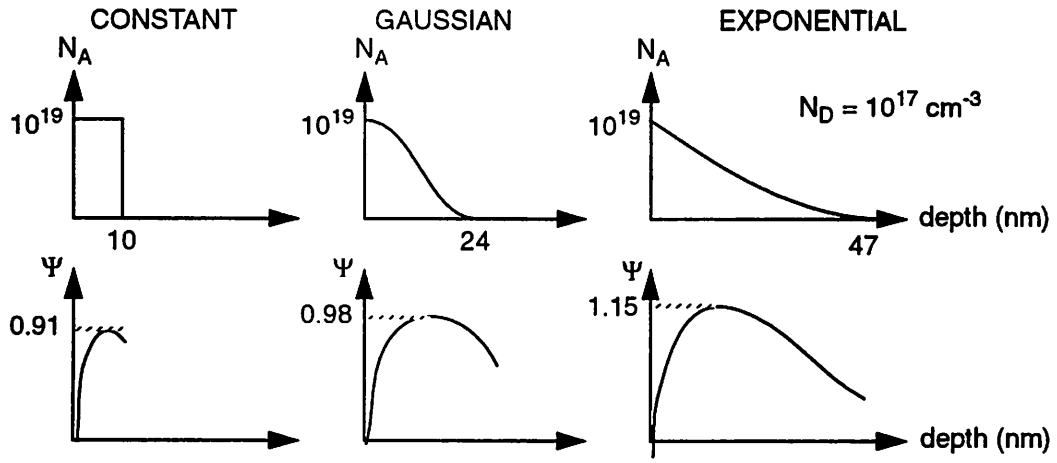

Figure 9-4. Barrier height with varying profile but constant surface concentration
Surface concentration is kept constant while junction depth is varied with profile shape to keep dose constant. Exponential case, with highest spatial moment (M), has largest barrier.

profile is increased a factor of 6.5 over the constant profile with hardly any increase in the total barrier. This is why it is difficult to make ultra-shallow junctions by rapid thermal diffusion from a gaseous or oxide dopant source, when the dopant profile is constrained to follow an error function. Exponential profiles have to be deeper than the more uniform profiles made by laser doping to act electrically as ideal pn junctions.

9.2.4 Camel diode leakage of $CoSi_2$ diodes

The scaling difficulties described in the preceding sections are observed in the epitaxial $CoSi_2$/p-Si/n-Si diode structures fabricated in Chapter 8. To review, the naming

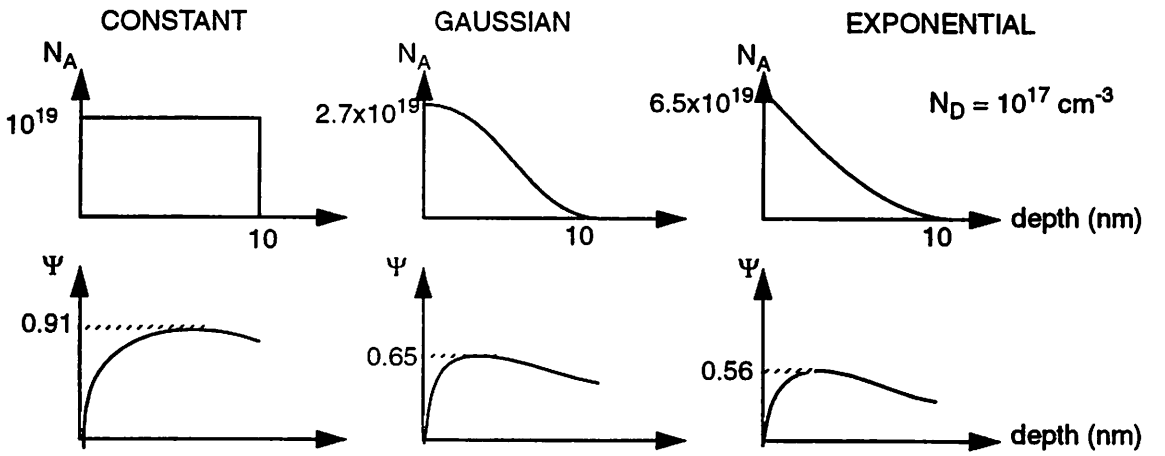

Figure 9-5. Barrier height with varying profile but constant junction depth

Dose and junction depth are constant, and surface concentration is varied. In this case, constant profile has highest spatial moment (*M*), and highest barrier.

conventions of the samples are summarized in Table 9-1. Reverse-biased *JV* characteris-

Sample	High-Energy	Low-Energy	Low-Dose
$^{11}B^+$ Implant Energy	7.5 keV	3.5 keV	7.5 keV
Implant Dose	10^{15} cm^{-2}	10^{15} cm^{-2}	10^{14} cm^{-2}

Table 9-1. Summary of boron implants in $CoSi_2$ used as a dopant source

tics are shown for the diode samples after 900°C annealing in N_2 RTA in Figure 9-6. Orders-of-magnitude variation is observed in the reverse leakage currents, despite secondary ion mass spectroscopy and spreading resistance profile data indicating that significant quantities of B are present under the silicide for all the samples. Diodes implanted with $^{11}B^+$ at 7.5 keV and 10^{15} cm^{-2} dose show leakage current near 100 nA/cm^2 at -5V and behave like ideal pn junctions after a 900°C, 30 s post-implant anneal. Diodes implanted at 3.5 keV with 10^{15} cm^{-2} dose or at 7.5 keV with a 10^{14} cm^{-2} dose display higher leakage currents like Schottky diodes that were made in the same silicide processing sequence but without B implantation and annealing steps. The low-energy *JV* curve shows similar curve shape but large difference in leakage magnitude from the Schottky diode curve.

9.2.5 PN junction / camel diode phase space

Figure 9-7 summarizes the shallow junction scaling criterion based on thermionic emission leakage. The lines in the graph give the doping and junction depth necessary for

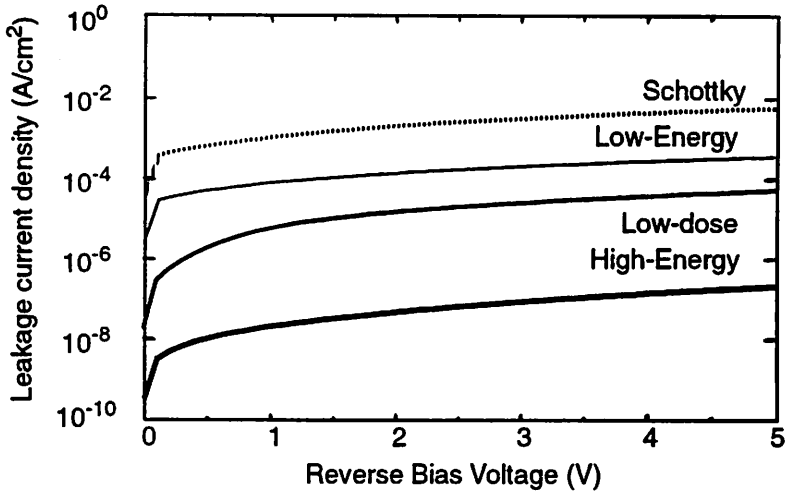

Figure 9-6. Reverse current density of $CoSi_2$ diodes with implant condition

Reverse-biased current density-voltage curve for $CoSi_2$ diodes implanted with boron after 900°C post-implant anneal, showing Schottky-like behavior of diodes implanted at a low-dose or low-energy condition.

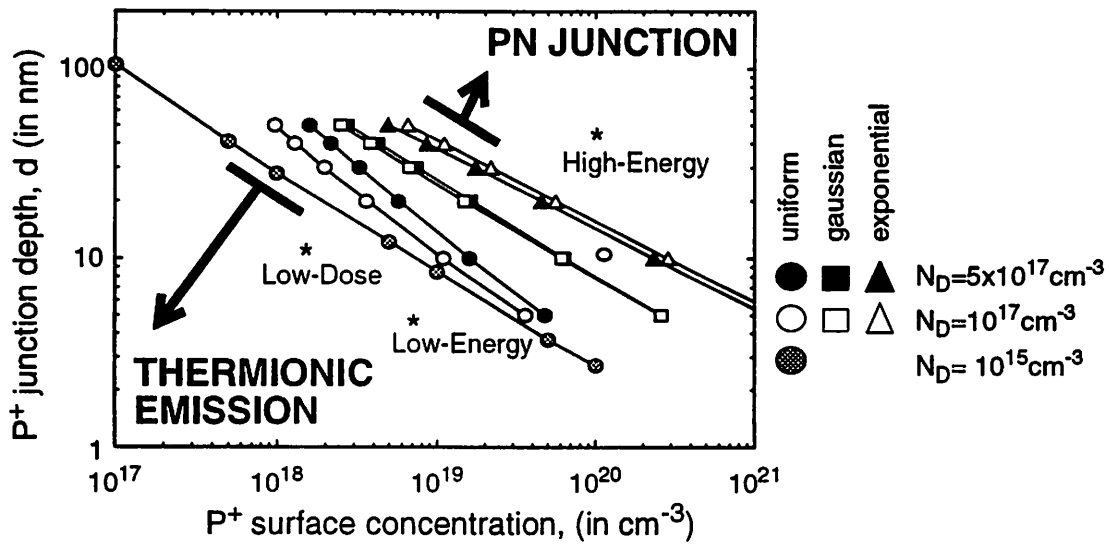

Figure 9-7. Camel diode/pn junction phase space

Lines indicate surface concentration (N_{A0}) and junction depth (d) necessary for barrier height saturation, including effect of barrier height lowering. Position of fabricated $CoSi_2$ device parameters in camel/pn junction phase space assumes constant doping in p-type diffused layer.

barrier height saturation of constant, Gaussian, and exponential doping profiles. As the junctions become shallower, the doping needed to meet the leakage requirement for the different profiles diverges. With an active surface concentration of $5x10^{19}$ cm^{-3}, a constant profile of less than 5 nm is sufficient. For an exponential profile, more than 20 nm is

needed. P-layer peak doping and thickness values from spreading resistance profiling of the epitaxial $CoSi_2$ diodes are shown in the pn junction/camel diode phase space. The position in the diagram of the $CoSi_2$ diodes' thickness and doping data correlates very well with the leakage characteristics shown in Figure 9-6. The low-energy and low-dose samples with high leakage and Schottky-like characteristics are located in the region where thermionic emission is the dominant leakage mechanism. The high-energy sample with leakage current density near 100 nA/cm^2 at -5V is located above the cutoff line, in the region where diffusion and generation dominate, and therefore can be described as a pn junction.

9.3 Camel diode capacitance

9.3.1 CV method for determining camel/pn crossover point

The camel diode behavior of shallow junctions is also observed in capacitance-voltage (*CV*) measurements, where the presence of the depleted p-type layer makes the depletion region larger, and the capacitance smaller, than a pure Schottky contact. Such capacitance-voltage measurements have been used to monitor the progression of dopant into semiconducting material, by observing the increase in the *V*-axis intercept of the $1/C^2$ vs. *V* diagram after increasing thermal cycles [9.3]. Likewise, the change in $1/C^2$ values as a camel diode turns into a pn junction diode can be monitored to find the crossover point, and so determine the minimum junction depth that behaves as pn junction for a particular process.

The depletion width of the camel diode contact is given by Equation 9-7. Since $C=\varepsilon_s A/W$, the intercept of the $1/C^2$ plot ($1/C^2 = 0$) occurs at $W^2 = 0$:

$$V_i = V_{BI} + \frac{q}{2\varepsilon_s}(2M + N_D d^2) \tag{9-11}$$

where $V_{BI} = \Phi_{B0} - \Phi_n$. V_i for the pn diode is the built-in potential of the pn junction, which varies slowly for N_A in the degenerate doping regime. The variation in the $1/C^2$ plot with varying junction depth (d) is shown in Figure 9-8. For simplicity, the p-layer doping is kept constant. At $d=0$, the intercept is at the Schottky value. As d increases, the magnitude of the $1/C^2$ curve increases but the slope remains constant so the $1/C^2$ plot intercept increases, as shown in the line for $d_c > d > 0$. The intercept increases until the barrier height saturates. When the saturation point is reached, the slope of the $1/C^2$ curve ($2\varepsilon_s/qN_D$) increases to the

pn junction value $\frac{2\varepsilon_s}{q}\left(\frac{1}{N_A}+\frac{1}{N_D}\right)$, and the intercept falls to the pn junction built-in potential (the line with $d > d_c$). For layers thicker than this, the pn junction intercept will be roughly constant. As shown in Figure 9-8, if high enough voltage is applied, the p-type

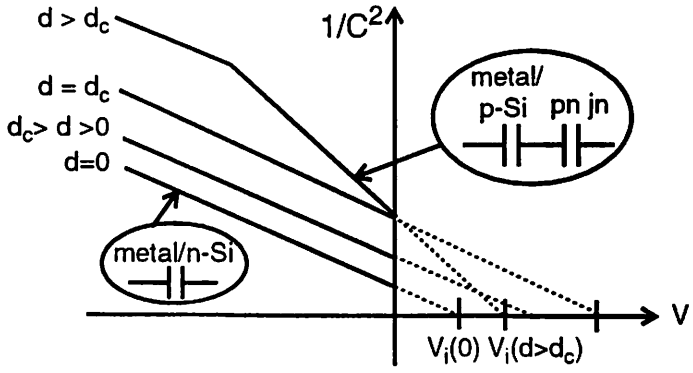

Figure 9-8. Monitoring PN junction evolution with CV

Variation of the $1/C^2$ graph with increasing junction depth, d, for constant diode doping. $d=0$ is a Schottky contact, d_c is the crossover thickness. Diodes with p-layer thickness larger than d_c are pn junctions at $V=0$.

layer will be depleted. At the voltage where this occurs the camel diode slope will again be observed, and the slope on the $1/C^2$ plot will change. A good pn junction will exhibit pn junction behavior up to the supply voltage.

Figure 9-9 shows the increase of the $1/C^2$ plot intercept as the dopant dose in Si increases. When the barrier height saturates, and the diode begins to act as a pn junction with a quasi-neutral region in the p-type layer, the intercept decreases to the built-in potential of the pn junction. Observation of this $1/C^2$ intercept curve is a useful method for finding the minimum drive-in necessary to create a diode with pn behavior, for which leakage current is not sensitive to changes in junction depth and doping.

9.3.2 Observation of camel diode behavior in 1-D simulation

The simple analytical model of camel diode behavior from the previous sections is tested in the device simulator TMA MEDICI, version 2.1.2. The simulator allows second-order effects like incomplete depletion of the p-layer to be taken into account. Diodes are simulated with a uniformly doped p-layer (N_A=10^{18} cm^{-3}) or with a Gaussian profile (at surface N_{A0}=10^{19} cm^{-2}). The background doping is 10^{17} cm^{-3} in both cases. Contacts to the p-layer are $CoSi_2$ and contact to the substrate is assumed to be n^+ poly-Si. The simulation

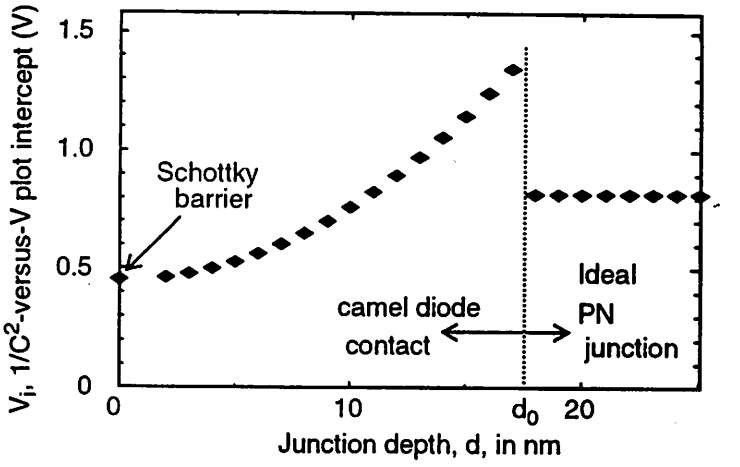

Figure 9-9. Variation of $1/C^2$ plot intercept with doping

Increase with doping of the intercept of the $1/C^2$ diagram, showing intercept steadily increasing as junction depth increases and then snapping back to the pn junction value when pn junction is formed.

mesh is very fine in the shallow doping areas, with grid points every 1-5 Angstroms. High frequency ac analysis at 1 MHz is used to extract the capacitances of the simulated diodes.

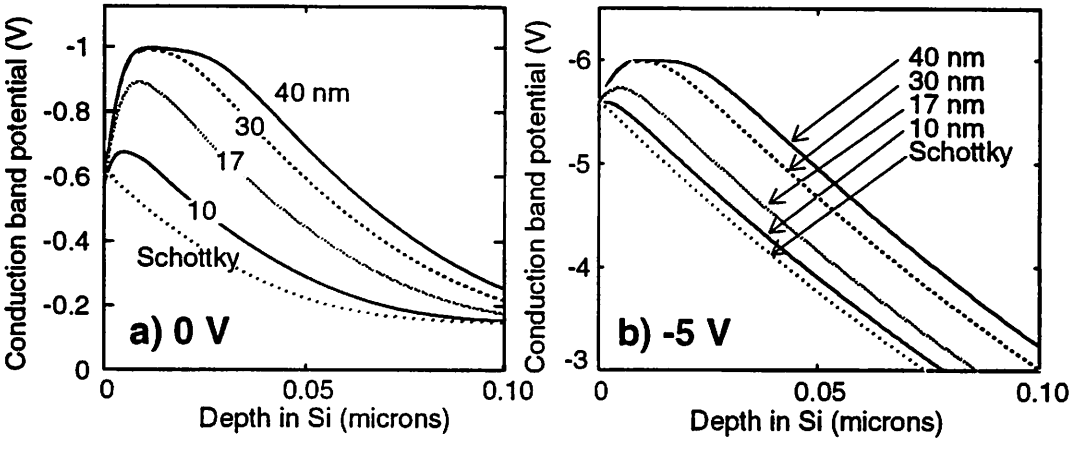

Figure 9-10. Simulated barrier height saturation of Gaussian junctions

Barrier height enhancement and saturation of Gaussian pn junctions with junction depth 0-40 nm, surface concentration 10^{19} cm^{-3}, and background doping 10^{17} cm^{-3}. a) 0V applied bias, b) -5 V reverse bias.

Figure 9-10 shows conduction band contours for the Schottky diode case and for Gaussian profiles with junction depth 10-40 nm, with 0 V and -5 V reverse bias applied. The 30 and 40 nm junctions both reach the saturation barrier height even under -5 V reverse bias. The 10 and 17 nm layers both show the reduction of barrier height under

reverse bias, in Figure 9-10b. From these plots, a junction more than 20 nm is needed to reach barrier height saturation under -5 V bias.

9.3.3 Confirmation of CV method with 1-D simulation

Figure 9-11 shows $1/C^2$ values simulated at 0 V and -5 V for both the uniformly doped and Gaussian profile diodes. The figure shows the impact of incomplete depletion on the diode capacitances. Here, the plots all show a bump in the $1/C^2$ values around the crossover region. As expected, the crossover from camel to pn junction occurs at a higher junction depth when a higher voltage is applied ($d_2 > d_1$ in Figure 9-11a and b). The changes in capacitance are correlated to the increasing barrier height enhancement, shown in Figure 9-11c and d. $1/C^2$ is seen to reach its peak as the barrier height enhancement is half-way to saturation, at junction depth d_1 at 0V and d_2 at -5V. Beyond these values, the fully-depleted approximation begins to break down, holes in the p-layer begin to respond to the bias, and the effective depletion width decreases. At the bottom of the hump, at junction depth d_3 (-5V), a quasi-neutral region is established and barrier height saturation occurs. Beyond the peak, the $1/C^2$ values are roughly constant, as the pn junction capacitance should not change with junction depth. This is true for the constant doping profile in Figure 9-11b. In the Gaussian profile in Figure 9-11a, the depletion width increases slowly as the Gaussian profile is stretched, and the doping gradient in the tail becomes smaller.

The same set of features can be observed in the plot of $1/C^2$ intercepts (V_i) in Figure 9-11e and f. The intercepts plotted here are found using the 0 V and -5 V points to define a slope as in Figure 9-8. The intercept increases from the Schottky value to a peak at d_1, falls to a valley at d_2, and then rises to the saturation value at d_3. As shown in Figure 9-11, for a highly doped, non-uniformly doped diode, the valley may be difficult to resolve. As the ideal pn junction condition is at the end of the valley (d_3), comparing results from the reverse-biased $1/C^2$ plot (Figure 9-11a) and the intercept plot (Figure 9-11e) may be necessary to identify the correct point. The minimum junction depths for pn junction behavior determined by this simulation are 30 nm for the Gaussian profile with peak concentration 10^{19} cm^{-3}, and 60 nm for the uniform doping profile with doping 10^{18} cm^{-3}.

9.3.4 Confirmation of CV method with $CoSi_2$ diodes

Figure 9-12 shows the measured $1/C^2$ plot intercept of the $CoSi_2$ diode samples. The data is plotted versus junction depth from SIMS data, which is somewhat misleading,

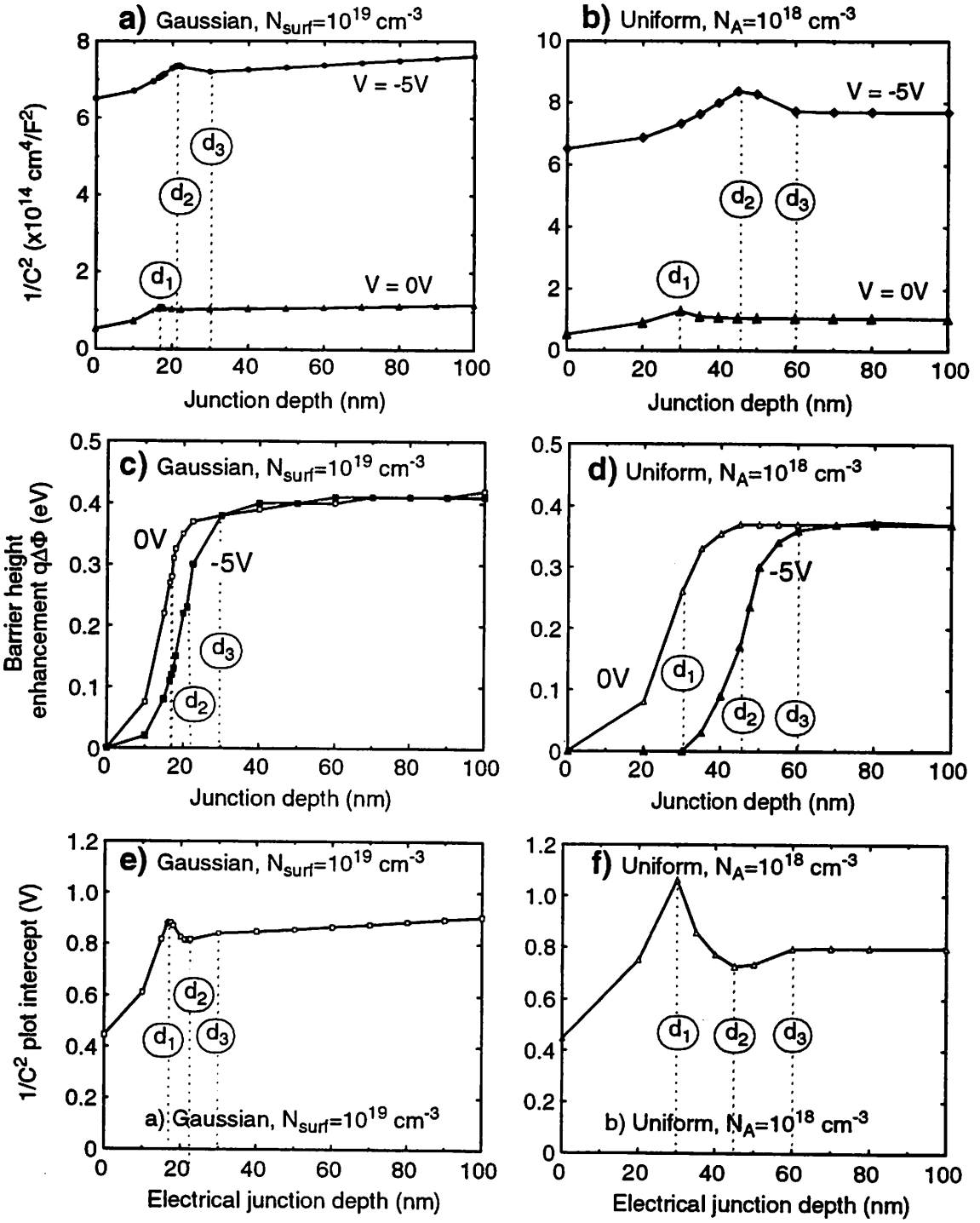

Figure 9-11. Simulation of CV method for finding minimum pn junction depth

Bump in $1/C^2$ values seen as junction changes from camel to pn junction diode for Gaussian profile in a) and constant profile in b). Actual barrier height enhancement $q\Delta\Phi$ (defined in Figure 9-1) shown in c) and d). Peak at 0 V at d_1, when 0 V barrier height halfway to saturation. Peak in -5V at d_2, when -5 V barrier height halfway to saturation. -5 V peak ends at d_3, where -5V barrier height saturation reached. e) and f) show variation in $1/C^2$ plot intercepts (V_i) with increasing junction depth using values from 0V and -5V to define the slope. Background doping 10^{17} cm^{-3}.

as the dopant doses and interface B concentrations vary among these samples. The measured values correlate well with the leakage behavior in Figure 9-6 and with the barrier heights calculated using the equations in Section 9.2.1 and the SIMS dopant data. The

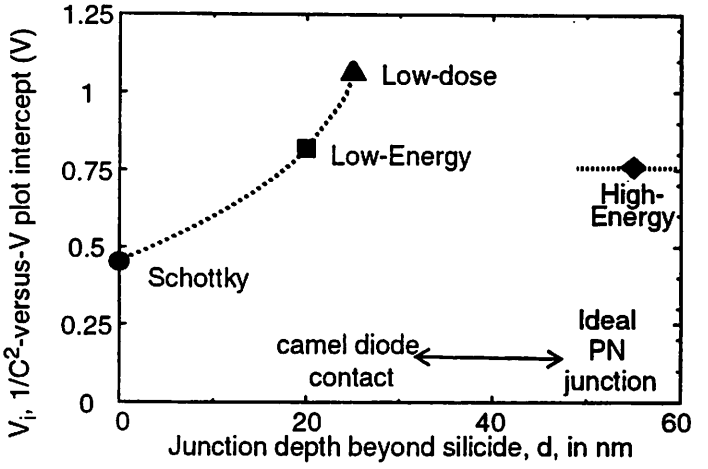

Figure 9-12. CV identification of $CoSi_2$ diode contact type

results are summarized in Table 9-2. The low-energy diode shows a barrier height higher than the Schottky junction and reduced leakage. The low-dose diode shows an increased barrier height, but on average, no reduction in the leakage, due to a very large spread in leakage among the low-dose samples, as expected from Figure 9-2. The SIMS data of the

Sample	High-Energy	Low-Dose	Low-Energy	Schottky
V_i, measured *CV* intercept (V)	0.76	1.07	0.82	0.45
V_i, calculated *CV* intercept (V)	pn jn value	1.34-1.55	0.81-0.83	
Best leakage current density	100 nA/cm^2	22 μA/cm^2	350 μA/cm^2	2.3 mA/cm^2
DIODE TYPE	PN JN	CAMEL	CAMEL	

Table 9-2. Summary of epitaxial $CoSi_2$ diode type

best, lowest-leakage low-dose samples showed that those had a similar dose but higher junction depth of B in the Si than the low-energy samples. This correlates with the trend seen in Figure 9-4, where deeper junction depths are seen to be most effective for reducing leakage. For the high-energy diode, the barrier decreases and the leakage decreases further, showing it has reached the pn junction regime.

The progressive increase, peak, and saturation of the $1/C^2$ plot intercept has also been observed in the $CoSi_2$ diodes. Figure 9-13 shows such a curve for the Low-Energy sample with successive annealing steps at 700°C. The peak and decline signalling barrier

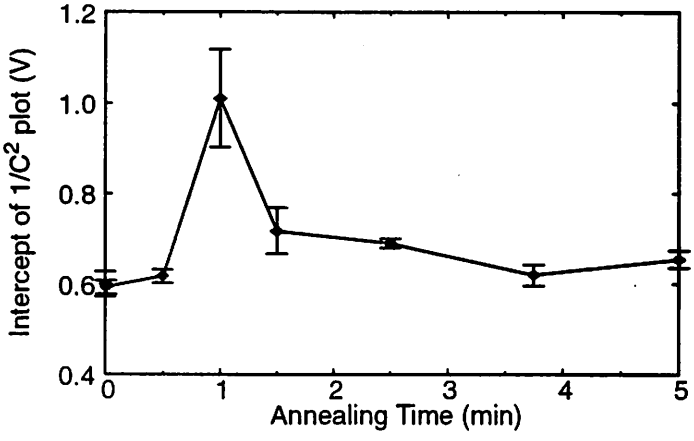

Figure 9-13. Variation of $1/C^2$ plot intercept for $CoSi_2$ diode on annealing
Sample implanted with 3.5 keV B^+, 10^{15} cm^{-2} dose, annealed at 700°C. Intercept increases to a peak, decreases, and saturates. Ideal junction forms after 5 min.

height saturation at 0 V bias are seen after 1 - 1.5 min. annealing. The dip is not pronounced because the $1/C^2$ intercept was found using points at 0 V and -1 V to find slope. Ideal junction is formed after 5 min. of annealing, when dip ends.

9.4 Conclusions

The high leakage currents of ultra-shallow junctions formed by B diffusion out of solid-phase epitaxially grown $CoSi_2$ contacts grown from Co/Ti bilayers on Si are explained by the camel diode contact model. Depending on implant condition, the diodes behave either as pn diodes or Schottky diodes with barrier height enhanced by the p-type diffusion. Camel diode contacts, with barrier height that depends on the spatial moment of the doping and thermionic leakage current that depends exponentially on the barrier height, have electrical characteristics that are very sensitive to process variation. Therefore, for reproducible junction *IV* characteristics, shallow junctions to be used in critical devices must be fabricated deep enough or highly doped enough to behave as ideal pn junctions. Capacitance measurements are shown to be useful in finding the point where a leaky, majority-carrier camel diode becomes a low-leakage, minority-carrier p*n* junction.

This point defines the minimum junction that can be made with a process which will behave electrically as a pn junction.

9.5 References

[9.1] J.M. Shannon, "Control of Schottky barrier height using highly doped surface layers," Solid-State Electron., 19 (6), pp. 537-543, 1976.

[9.2] S.M. Sze, *Physics of Semiconductor Devices*, New York: J. Wiley and Sons, 1981.

[9.3] L.C. Zhang, C.L. Liang, S.K. Cheung, and N.W. Cheung, "Refractory metal nitride rectifying contacts on GaAs," J.Vac. Sci. Technol., B5 (6), pp. 1716-1722, 1987.

A Appendix: Optical emission spectroscopy peaks

A.1 Introduction

Optical emission peaks for species expected in BF_3 plasma are compiled so that peaks in measured OES spectra may be analyzed in Chapter 3. In Section A.2, the OES peaks are listed. In Section A.3, a calibrated OES spectrum from a BF_3 plasma is shown.

A.2 OES peaks

λ(nm)	Species	Intensity	Ref.	λ(nm)	Species	Intensity	Ref.
089.0	BF_3		[A.1]	221.7	Si		[A.4]
094.0	BF_3		[A.2]	222.0	B^+	70	[A.6]
126.1	Si^+		[A.3]	222.0	BF_3^+		[A.1]
136.2	B^+		[A.3]	229.1	Si		[A.4]
162.4	B^+		[A.3]	229.5	Si		[A.4]
180.8	Si^+		[A.3]	232.3	B^+	40	[A.6]
182.6	B		[A.3]	232.9	B^+	40	[A.6]
196.0	BF		[A.3]	239.3	B^+	40	[A.6]
200.8	Si		[A.4]	239.5	B^+	220	[A.6]
201.1	Si		[A.4]	243.5	Si		[A.7]
205.5	Si		[A.4]	243.8	Si		[A.4]
206.0	B		[A.5]	244.3	Si		[A.4]
206.1	Si		[A.4]	245.0	B		[A.5]
206.5	Si		[A.3]	245.0	BF_3		[A.3]
206.6	B	250	[A.6]	245.2	Si		[A.4]
206.7	B	300	[A.6]	246.0	B^+	40	[A.6]
208.9	B	500	[A.4]	249.7	B	1000	[A.4]
209.0	B	500	[A.4]	249.8	B		[A.4]
211.5	Si		[A.4]	249.8	B		[A.8]
212.1	Si		[A.4]	250.7	Si		[A.4]
215.0	BF_3		[A.3]	251.4	Si		[A.4]
217.9	B^+		[A.6]	251.6	Si		[A.4]
220.7	Si		[A.4]	251.9	Si		[A.4]
220.8	Si		[A.3]	252.0	Si		[A.9]
221.1	Si		[A.4]	252.4	Si		[A.4]

λ(nm)	Species	Intensity	Ref.	λ(nm)	Species	Intensity	Ref.
252.4	Si		[A.7]	312.4	BF		[A.10]
252.9	Si		[A.7]	315.3	F^+	140	[A.6]
253.0	SiF		[A.8]	320.3	F^+	170	[A.6]
253.2	Si		[A.4]	322.3	BF		[A.10]
253.9	SiF		[A.8]	325.5	BF		[A.10]
255.6	F^+	100	[A.6]	326.4	F^+	140	[A.6]
256.4	Si		[A.4]	332.3	B^+	110	[A.6]
256.5	Si		[A.4]	332.4	B^+	110	[A.6]
257.0	BF_3^+		[A.1]	334.0	Si^+		[A.7]
258.4	SiF		[A.8]	334.6	SiF		[A.8]
259.5	SiF		[A.8]	336.0	BF		[A.10]
263.1	BF		[A.10]	336.3	SiF		[A.8]
263.1	Si		[A.4]	339.7	BF		[A.10]
264.1	SiF		[A.8]	341.5	F^+	140	[A.6]
265.3	SiF		[A.8]	341.6	F^+	150	[A.6]
272.5	BF		[A.10]	341.7	F^+	160	[A.6]
275.0	BF_3		[A.3]	345.0	B^+		[A.5]
278.0	BF_3^+		[A.1]	345.1	B^+	450	[A.6]
280.0	SiF		[A.8]	347.3	F^+	150	[A.6]
281.3	SiF		[A.8]	347.5	F^+	170	[A.6]
282.4	BF		[A.10]	350.1	F^+	190	[A.7]
284.2	Si		[A.4]	350.2	F^+	200	[A.6]
284.5	BF		[A.10]	350.3	F^+	210	[A.7]
287.1	F^+	100	[A.6]	350.5	F^+	170	[A.6]
288.0	Si		[A.9]	350.6	F^+	220	[A.6]
288.1	SiF		[A.8]	352.3	F^+	160	[A.6]
288.2	Si		[A.7]	353.7	F^+	150	[A.6]
289.4	SiF		[A.8]	354.2	F^+	160	[A.6]
290.0	Si		[A.9]	355.0	BF		[A.10]
290.4	Si^+		[A.7]	359.1	F^+	160	[A.6]
290.6	Si^+		[A.7]	359.4	F	6	[A.6]
291.8	B^+	160	[A.6]	359.9	F^+	170	[A.6]
292.7	F_2		[A.12]	360.1	F^+	180	[A.6]
295.3	SiF		[A.8]	360.3	F^+	190	[A.6]
296.0	SiF_4		[A.3]	370.5	F^+	180	[A.6]
296.7	SiF		[A.8]	371.0	F^+	160	[A.6]
297.0	Si		[A.4]	374.0	F^+	160	[A.6]
297.5	BF		[A.10]	380.6	F^+	140	[A.6]
298.8	Si		[A.4]	384.7	F^+	270	[A.6]
300.0	BF_2		[A.2]	385.0	F^+	260	[A.6]
301.0	SiF_4		[A.3]	385.2	F^+	250	[A.6]
302.8	SiF		[A.8]	385.6	Si^+		[A.7]
303.2	B^+	110	[A.6]	389.8	F	5	[A.6]
304.2	SiF		[A.8]	389.9	F^+	190	[A.6]
305.7	F^+	6	[A.7]	390.0	SiF_2		[A.9]
305.8	F^+	7	[A.7]	390.2	F^+	180	[A.6]
306.0	F^+	100	[A.6]	390.4	F^+	170	[A.6]
306.0	SiF_4		[A.3]	390.6	Si		[A.8]
311.8	BF		[A.10]	393.1	F	8	[A.6]
312.0	BF		[A.10]	393.4	F	5	[A.6]
312.1	BF		[A.10]	394.9	F	5	[A.6]
312.2	BF		[A.10]	397.2	F^+	150	[A.6]

λ(nm)	Species	Intensity	Ref.	λ(nm)	Species	Intensity	Ref.
397.3	F^+	160	[A.6]	504.1	Si^+		[A.7]
397.5	F^+	170	[A.6]	505.6	Si^+		[A.7]
401.0	SiF_2		[A.9]	510.2	F_2		[A.12]
401.2	SiF		[A.8]	517.3	F^+	150	[A.6]
402.5	F^+	240	[A.6]	520.2	Si^+		[A.7]
405.0	SiN		[A.9]	521.0	BF_3^+		[A.1]
408.4	F^+	160	[A.6]	523.0	F	15	[A.6]
410.3	F^+	190	[A.7]	527.9	F	12	[A.6]
410.3	Si		[A.4]	539.4	F_2		[A.12]
410.4	F^+	200	[A.6]	545.7	BF		[A.10]
410.9	F^+	170	[A.6]	546.0	BF		[A.10]
411.7	F^+	160	[A.6]	546.6	Si^+		[A.7]
411.9	F^+	150	[A.6]	546.7	Si^+		[A.7]
412.2	B^+	285	[A.6]	547.1	BF		[A.10]
413.1	Si^+		[A.7]	551.6	F_2		[A.12]
418.3	SiF		[A.8]	554.1	F	18	[A.6]
419.5	B^+	110	[A.6]	555.2	F	12	[A.6]
420.0	BF_2		[A.2]	557.7	F	10	[A.6]
420.7	F^+	140	[A.6]	558.9	F^+	160	[A.6]
422.5	F^+	170 h	[A.6]	562.4	F	20	[A.6]
423.0	SiF		[A.8]	562.7	F	12	[A.6]
424.4	F^+	150 h	[A.6]	565.9	F	15	[A.6]
424.6	F^+	200	[A.7]	566.4	BF		[A.10]
424.7	F^+	180	[A.6]	566.8	F	40	[A.6]
427.0	SiF		[A.8]	567.0	Si^+		[A.7]
427.5	F^+	170 h	[A.6]	567.2	F	90	[A.6]
427.8	F^+	160 h	[A.6]	568.9	F	18	[A.6]
427.9	F^+	160 h	[A.6]	570.1	F	25	[A.6]
429.9	F^+	200	[A.6]	570.7	F	25	[A.6]
433.4	SiF		[A.8]	573.1	F_2		[A.12]
436.8	SiF		[A.8]	580.4	BF		[A.10]
440.1	SiF		[A.8]	580.7	BF		[A.10]
441.0	SiN		[A.9]	581.5	BF		[A.10]
443.0	SiF		[A.8]	582.2	BF		[A.10]
444.4	BF		[A.10]	582.6	BF		[A.10]
444.7	F^+	180	[A.7]	585.1	F_2		[A.12]
446.1	BF		[A.10]	595.0	F	12	[A.6]
446.2	SiF		[A.8]	595.8	Si^+		[A.7]
446.5	BF		[A.10]	595.9	F	25	[A.6]
447.2	B^+	110	[A.6]	596.5	F	70	[A.6]
447.3	B^+	110	[A.6]	597.9	Si^+		[A.7]
449.6	SiF		[A.8]	598.4	BF		[A.10]
453.0	B^+		[A.5]	599.4	BF		[A.10]
453.2	SiF		[A.8]	599.4	F	50	[A.6]
473.4	F^+	140	[A.6]	601.6	F	150	[A.6]
478.4	B^+	70	[A.6]	603.8	F	80	[A.6]
485.1	SiF		[A.8]	604.8	F	900	[A.6]
485.9	F^+	170	[A.6]	606.6	Si		[A.4]
493.3	F^+	160	[A.6]	608.0	B^+	110	[A.6]
494.0	B^+	110	[A.6]	608.0	F	100	[A.6]
496.1	F	6	[A.6]	610.3	F_2		[A.12]
500.2	F^+	140	[A.6]	615.0	F	800	[A.6]

λ(nm)	Species	Intensity	Ref.	λ(nm)	Species	Intensity	Ref.
621.1	F	400	[A.6]	742.6	F	4000	[A.6]
624.0	F	13000	[A.4]	748.3	F	2200	[A.6]
624.8	F^+	140	[A.6]	748.5	BF_3^+		[A.13]
627.0	SiF		[A.8]	748.5	BF_2^+		[A.13]
628.5	B^+	70	[A.6]	748.9	F	2500	[A.6]
633.9	BF_3^+		[A.13]	751.5	F	900	[A.6]
634.7	Si^+		[A.7]	755.2	F	5000	[A.6]
634.9	F	10000	[A.4]	757.3	F	5000	[A.6]
637.0	BF_3^+		[A.13]	759.0	BF_3^+		[A.13]
639.7	SiF		[A.8]	759.0	BF_2^+		[A.13]
640.2	BF_3^+		[A.13]	760.7	F	7000	[A.6]
641.4	F	8000	[A.6]	762.5	BF_3^+		[A.13]
641.6	SiF		[A.8]	762.5	BF_2^+		[A.13]
643.3	BF_3^+		[A.13]	767.1	Si^+		[A.7]
646.4	BF_3^+		[A.13]	773.5	BF_3^+		[A.13]
648.9	F_2		[A.12]	775.5	F	18000	[A.4]
649.2	SiF		[A.8]	777.5	BF_3^+		[A.13]
649.7	BF_3^+		[A.13]	780.0	F	15000	[A.4]
651.9	F_2		[A.12]	784.9	Si^+		[A.7]
653.2	BF_3^+		[A.13]	785.0	Si^+		[A.7]
657.0	F	450	[A.6]	787.9	F	300	[A.6]
658.0	F	300	[A.6]	789.9	F	500	[A.6]
659.4	SiF		[A.8]	793.2	Si		[A.7]
665.0	F	400	[A.6]	793.6	F	350	[A.6]
669.0	F	1800	[A.6]	794.4	Si		[A.7]
670.8	F	400	[A.6]	795.6	F	300	[A.6]
677.4	F	7000	[A.6]	801.6	F^+	80	[A.6]
679.6	F	1500	[A.6]	804.1	F	1000	[A.6]
683.4	F	9000	[A.6]	807.6	F	900	[A.6]
685.6	F	50000	[A.8]	807.8	F	350	[A.6]
687.0	F	8000	[A.6]	812.7	F	350	[A.6]
690.2	F	15000	[A.4]	812.9	F	600	[A.6]
691.0	F	6000	[A.6]	816.0	F	300	[A.6]
696.6	F	4000	[A.6]	817.9	F	600	[A.6]
697.7	F_2		[A.12]	819.1	F	300	[A.6]
703.0	B^+	40	[A.6]	821.5	F	2500	[A.7]
703.7	F	45000	[A.4]	866.8	B		[A.6]
712.8	F	30000	[A.4]	866.9	B	70	[A.6]
718.0	F^+	130	[A.6]	873.0	BF_3^+		[A.1]
720.2	F	15000	[A.6]				
721.2	F	130 h	[A.6]				
724.2	BF_3^+		[A.13]				
728.9	Si		[A.7]				
730.2	B^+		[A.6]				
730.9	F	1000	[A.6]				
731.1	F	15000	[A.4]				
731.4	F	700	[A.6]				
733.2	F	5000	[A.4]				
739.9	F	10000	[A.4]				
740.6	Si		[A.7]				
741.6	Si		[A.7]				
742.3	Si		[A.7]				

A.3 OES spectra from BF_3 and Ar plasmas

The following pages show measured spectra from BF_3 and Ar plasmas run in the ECR system. Plasmas are run at 700W, 1 mtorr gas pressure, and 220 A magnet current. The relative intensity of lines in the Ar plasma follow closely the intensities listed in Ref. [A.14]. Quartz windows in the ECR chamber attenuate the optical signal below 300 nm.

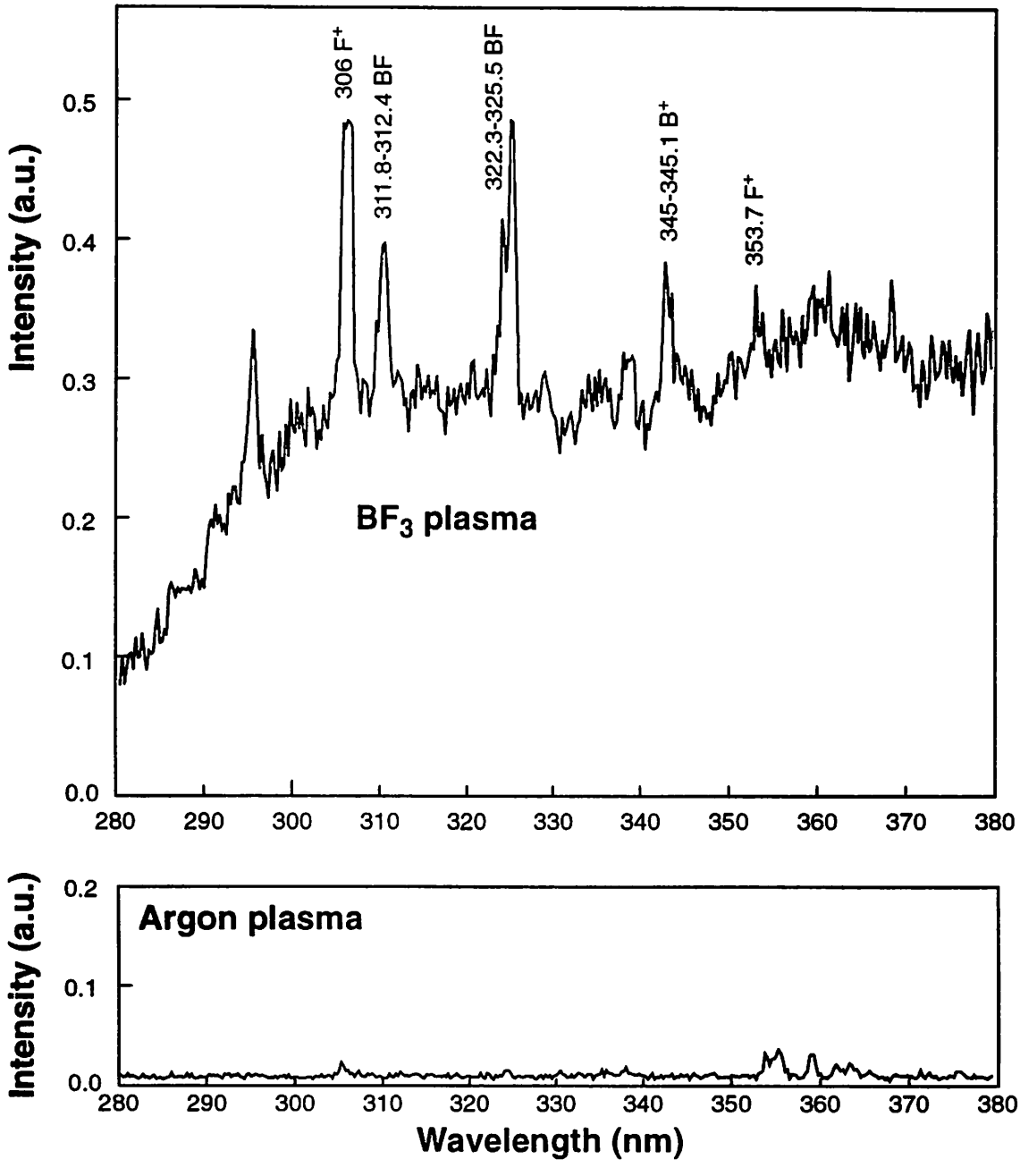

Figure A-1. OES spectra of BF_3 and Ar plasmas from 280 - 380 nm

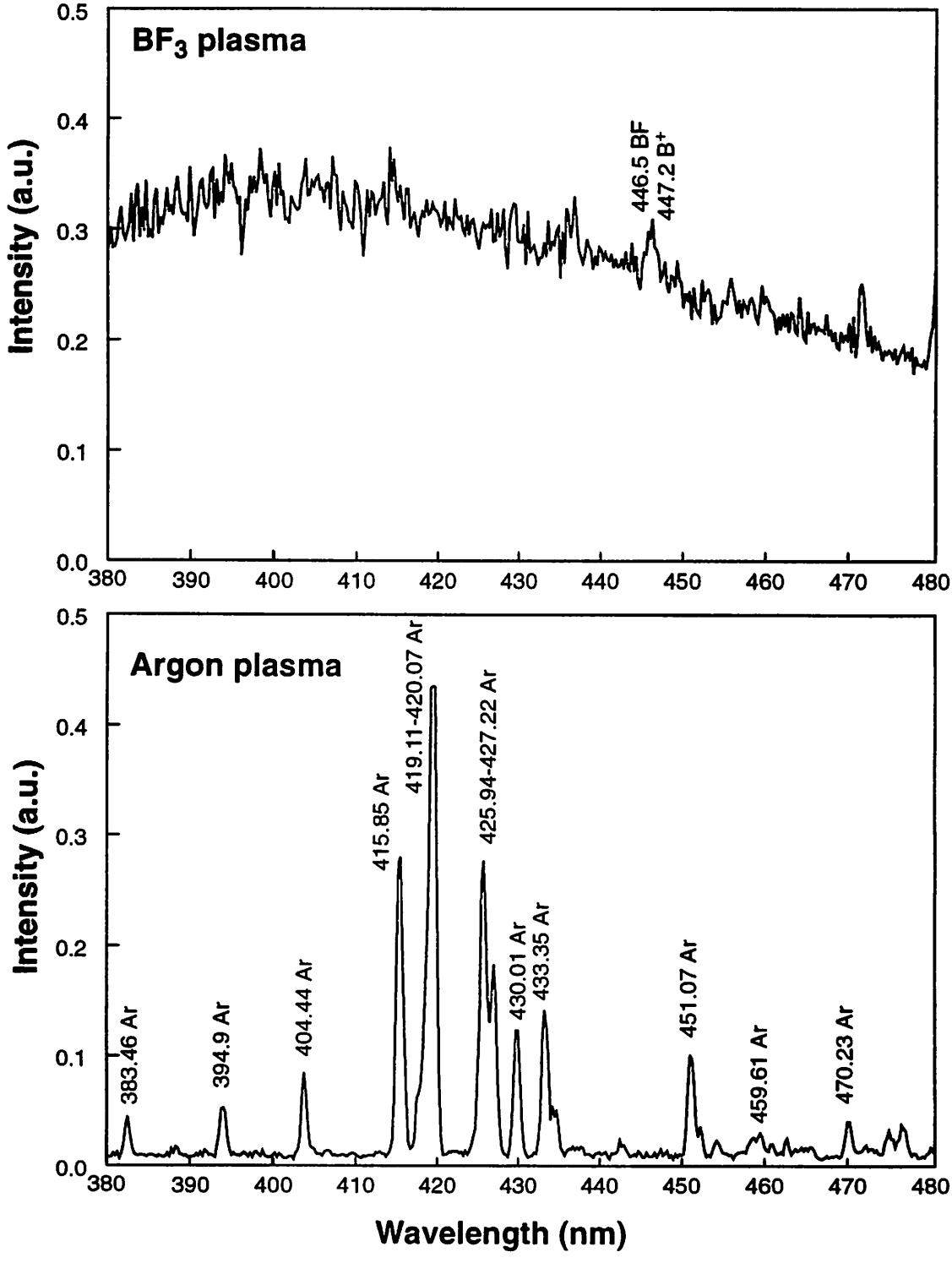

Figure A-2. OES spectra of BF_3 and Ar plasmas from 380 - 480 nm

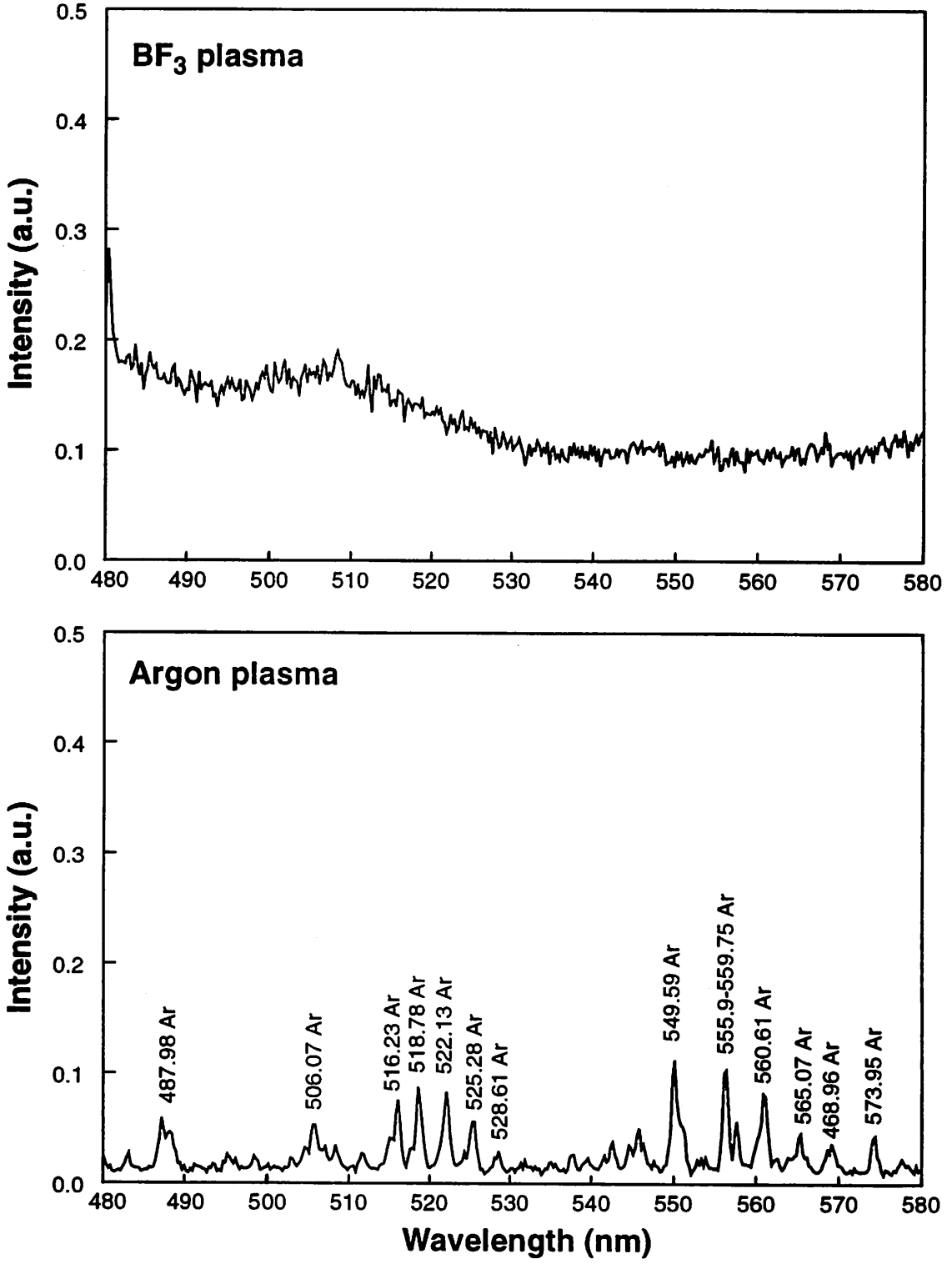

Figure A-3. OES spectra of BF_3 and Ar plasmas from 480 - 580 nm

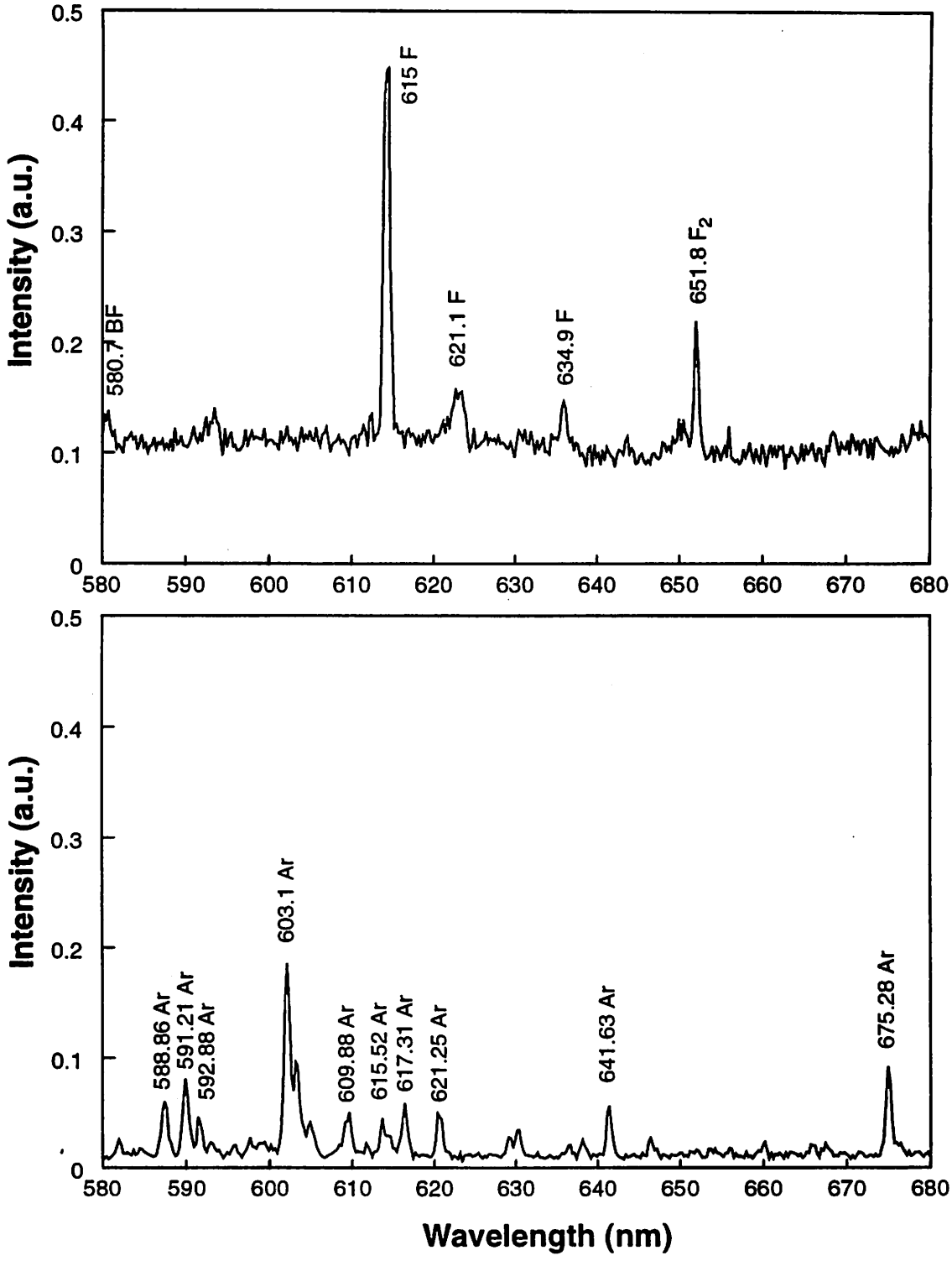

Figure A-4. OES spectra of BF_3 and Ar plasmas from 580 - 680 nm

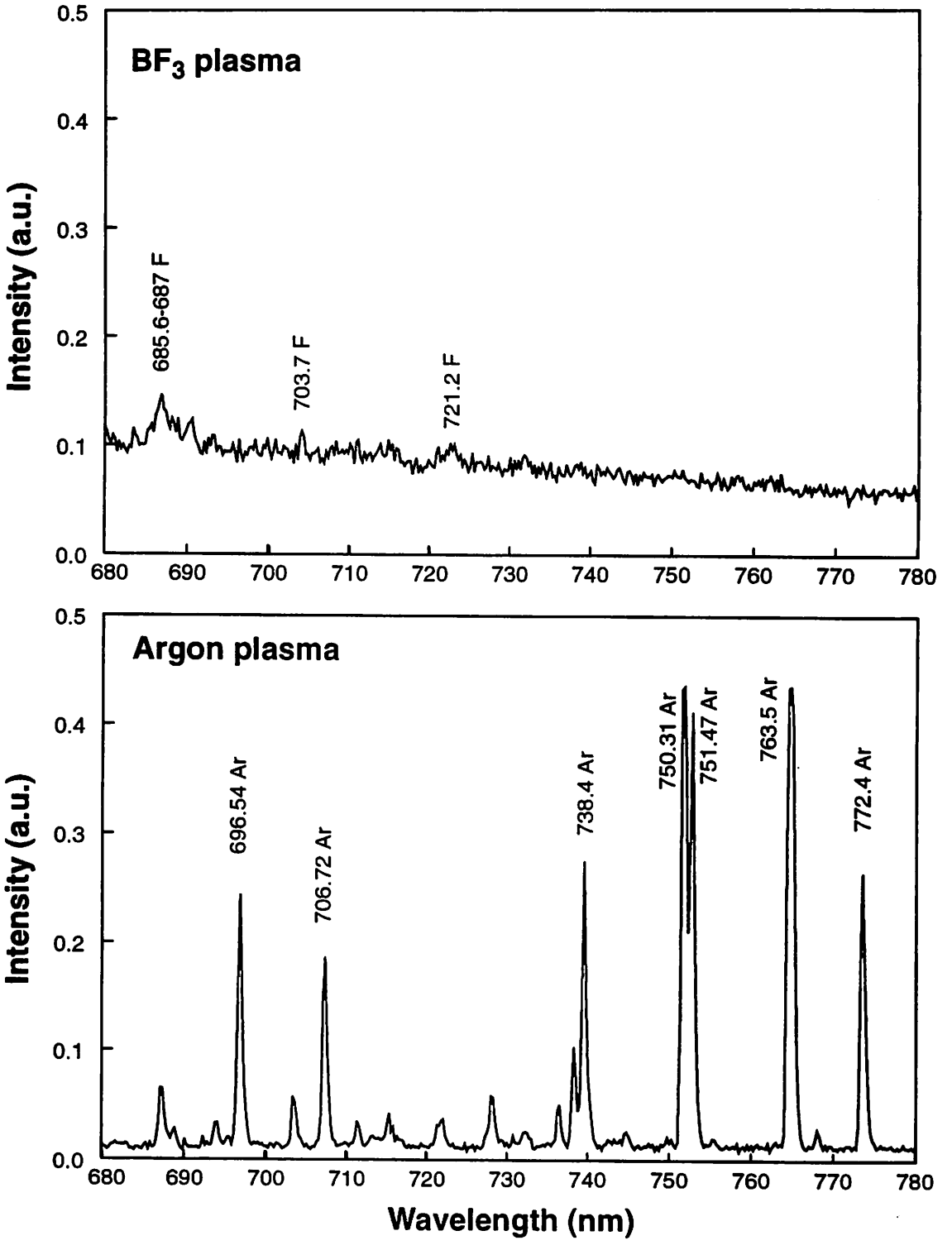

Figure A-5. OES spectra of BF_3 and Ar plasmas from 680 - 780 nm

A.4 References

[A.1] J.C. Creasey, P.A. Hatherly, H.M. Jones, I.R. Lambert, et al, "Vacuum UV fluorescence excitation spectroscopy of BF_3 in the range 45-125 nm. Observation of new electronic transitions in the BF_2 free radical," Molecular Phys., 78 (4), pp. 837-854, 1993.

[A.2] M. Suto, C. Ye, and L.C. Lee, "Photoabsorption and fluorescence spectroscopy of BF_3 in the extreme-vacuum-ultraviolet region," Phys. Rev. A, 42 (1), pp. 424-431, 1990.

[A.3] J.E. Hesser and K. Dressler, "Radiative Lifetimes of Ultraviolet Emission Systems Excited in BF_3, CF_4 and SiF_4," J. Chem. Phys., 47 (9), pp. 3443-3450, 1967.

[A.4] C. Candler, *Atomic spectra and the vector model*, Princeton, NJ: D. van Nostrand Co., Inc., 1964.

[A.5] Th. Glenewinkel-Meyer, A. Kowalski, B. Muller, Ch. Ottinger, and W.H. Breckenridge, "Emission Spectra and electronic structure of group IIIa monohalide cations," J. Chem. Phys., 89 (12), pp. 7112-7125, 1988.

[A.6] J. Reader and C.H. Corliss, *Wavelengths and transition probabilities for atoms and atomic ions*, Washington: U.S. Govt. Print. Off., 1980.

[A.7] A.R. Striganov and N.S. Sventitskii, *Tables of spectral lines of neutral and ionized atoms*, Washington: IFI/Plenum, 1968.

[A.8] R.W.B. Pearse and A.G. Gaydon, *The identification of molecular spectra*, New York: J. Wiley & sons, inc., 1941.

[A.9] D.L. Flamm, V.M. Donnelly, and J.A. Mucha, "The reaction of fluorine atoms with silicon," J. Appl. Phys., 52 (5), pp. 3633-3639, 1981.

[A.10] Dull, Phys. Rev., 47, p. 458, 1935.

[A.11] Strong, Phys. Rev., 49, p. 740, 1936.

[A.12] Gale, Astrophys. J., 59, p.77, 1929.

[A.13] C.F. Batten, J.A. Taylor, B.P. Tsai, and G.G. Meisels, "Photoionization processes at threshold. II. Threshold photoelectron photoionization, and coincidence ion-threshold photoelectron spectra of BF_3," J. Chem. Phys., 69 (6), pp. 2547-2552, 1978.

[A.14] A.N. Zaidel, *Tables of spectral lines*, New York: IFI/Plenum, 1970.

B Appendix: Implant profile generation and extraction programs

B.1 General

The following programs were written for Matlab, version 4.2c, distributed by MathWorks, Inc.

B.2 Per-pulse profile generation from implanter IV waveforms

Generation of a per-pulse profile from the implanter IV waveform requires two programs: Ivtospec.m, which creates an energy spectrum for the implant from the implanter waveforms, and Specboth.m, which creates the implanted profiles from the energy spectrum.

B.2.1 Generation of energy spectrum

Program Ivtospec.m takes two 2-column input files which contain the implanter current and voltage waveforms. The first column is expected to contain the time in seconds, and the second column, voltage or current. The program will extend the fall-time of the voltage waveform to the end of the pulse period, and will extrapolate for more points in the voltage rise-time. The current is converted to current density, and current due to secondary electron emission is extracted. For accurate simulation, the parameter 'step' must be small. This is the width of each energy bin. Another parameter that may be changed is the minimum implant energy. In this version, it is assumed that any ion with less than 50 eV of energy is deposited or reflected, but not implanted.

```
% ------------------BEGIN PROGRAM--------------------------------------
% PROGRAM IVTOSPEC.m takes [time | I] and [time | V] files and yields
% 2-column outfile containing energy and # ions implanted at that energy.
% This is the energy spectrum of implant, assuming collisionless sheath

% ------------------INPUT DATA IN THIS SECTION-----------------------
ma = 5000;  % energy of highest bin
```

```
step = 100; % energy range in each bin
nb = ma/step;% number of bins
bins = [step:step:ma];

% READ IN DATA: files expected are 2-column: 1. time, 2. voltage/current
vinfile='voltages.txt';
fid1 = fopen(vinfile,'r+');
[volt,countdat] = fscanf(fid1,'%g %g',[2 inf]);
l1 = length(volt);
iinfile='currents.txt';
fid2 = fopen(iinfile,'r+');
[curr,countdat] = fscanf(fid2,'%g %g',[2 inf]);
l2 = length(curr);

frequency=5000;                 % frequency of implant pulses,
                                % to give length of fall time between them
area=.0078539816;               % implant target area in m^2
outfile='outbins';              % outfile name for energy spectrum

%CORRECT SECONDARY ELECTRON YIELD MODEL FOR ION SPECIES USED:
%for 7.5% B, 7.5% F, 85% BF2 : sey=0.0026 * energy ^ 0.86
%for 80% B, 20% BF2 : sey=0.001 * energy ^ 0.965 (both for 20% Si exposed )
%for Ar, use 0.004*energy^0.82
seypf=0.0026;
seyex=0.86;
%Used Rocca data for Ar yield on Al in 1-5kV range, Used Alonso data to
%switch ion species from Ar to B/F, Used En data to adjust for % of Al,
%Si and SiO2 exposed

%-------------------------------------------------------------------
curr(2,:)=curr(2,:) ./ area;        % convert to current density
dt=curr(1,2)-curr(1,1);             % timestep must be constant for all
                                    % data
if ~(dt==volt(1,2)-volt(1,1)) % timescales must be the same for i and v
   error('timestep must be equal for voltage and current')
end
if ~(curr(1,1)==volt(1,1))
   error('starting time must be equal for voltage and current waveforms')
end
curr(1,:)=[curr(1,1):dt:curr(1,1)+(l2-1)*dt];
volt(1,:)=[curr(1,1):dt:curr(1,1)+(l2-1)*dt];
volt(2,:)=volt(2,:)-max(volt(2,:)); % remove dc offsets
curr(2,:)=curr(2,:)-max(curr(2,1));
%-------------------------------------------------------------------
% IMPLANT PER PULSE
%implanted ions=(pulse on?=volt>50eV?)*current*dt/secondary e- current
%only consider ions implanted after pulse begins
%divide out secondary e- current using SE yield from input model
temp1=-dt*(real(volt(2,:)<=-50).*curr(2,:))./(seypf*(abs(volt(2,:))).^-
seyex+1);
%-------------------------------------------------------------------
% RISE TIME / FALL TIME
%This Section splits energy profile into rise time/on time/fall time
%rtv, rise time is time to get to 0.85 of max voltage
```

```
%on, on time is time when voltage falls below 0.85 of max voltage
%st, start time is time when voltage above 0.05 of maximum
maxvolt= min(volt(2,:)) % maximum implant voltage
rtv=min(find((volt(2,:)-0.85*maxvolt)<0));% timeindex to 85% max. voltage
st =min(find((volt(2,:)-0.05*maxvolt)<0));% timeindex when pulse began
on =max(find((volt(2,:)-0.85*maxvolt)<0));% time index of pulse end

% FALL TIME: EXTRAPOLATE FROM WAVEFORM TO COMPLETE FALL TIME
%assume exponential fall in voltage or current, fit log plot to find slope
%add 500 points from end of data, ft1, to point where ion energy too low
%to implant (-50eV), at ftend
ft2 = 1/frequency;              % 1/frequency, set in input section
ft1 = curr(1,l2);               % last timevalue of measured data
ft0 = curr(1,on+1);             % timevalue at beginning of fall-time
voltg=log(-volt(2,on+1:l2));
slope=sum(gradient(voltg))/length(voltg)/dt;
yo=volt(2,l2);
ftend=ft1+(log(-50/yo))/slope;
steps=500;                      % # of timesteps in extrapolated waveform
dtg=(ftend-ft1)/steps;          % timestep in extrapolated waveform
timeh=[ft1+dtg:dtg:ftend];
volth=yo*exp((timeh-ft1)*slope);
tci=l2-250;                 % timeindex range used for curr fit: tci to l2
tc=curr(1,tci);             % timevalue range used for curr fit: tc to ft1
currg=log(-curr(2,tci:l2));
slc=sum(gradient(currg))/length(currg)/dt;
co=curr(2,tci); currh=co*exp((timeh-tc)*slc);
currk=curr(2,tci)*exp((curr(1,tci:l2)-tc)*slc);
lenh=length(timeh);
temp3 = -dtg*(real(volth<=-50).*currh)./(seypf*(abs(volth)).^seyex+1);
                        % implanted ions during end of fall time

% RISE TIME: INTERPOLATE FOR MORE POINTS
f=50;                       % add f points between every point in rise time
dtf=dt/f;                   % timestep in rise time
time=[curr(1,st):dtf:curr(1,rtv)]';
curr2=interp1(curr(1,:), curr(2,:), time);
volt2=interp1(volt(1,:), volt(2,:), time);
len=length(time);
temp2 = -dtf*(real(volt2<=-50).*curr2)./(seypf*abs(volt2).^seyex+1);
                        % implanted ions during rise time
%-------------------------------------------------------------------------
% TOTAL DOSE AND MEAN ENERGY OF IMPLANT SPECIES
                    % for dose/pulse add up all the dose/time steps,
                    % convert to cm-2
dose=-1*(sum(temp1(rtv:l2))+sum(temp2)+sum(temp3))*1e-4/1.6e-19
                    % mean implant energy = Sum(Energy*dose)/(total dose)
meanen=(sum(volt(2,rtv:l2).*temp1(rtv:l2))+sum(volt2.*temp2)+sum(volth.*
temp3))/(sum(temp1(rtv:l2))+sum(temp2)+ sum(temp3))
%-------------------------------------------------------------------------
% ENERGY DISTRIBUTION
% split implant voltage into discrete bins and sum up all ions which match
% each bin  (temp1-temp3 from above)
      % RISE TIME
```

```
for x=1:nb
energy1a(x)= sum(temp2(find(abs(floor(volt2./step)) == x)));
end;
      % ON TIME
for x=1:nb
energy1b(x)=sum(temp1(rtv-1+(find(abs(floor(volt(2,rtv:on)./
step))==x))));
end;
      % FALL TIME
      % count ions from fall time and extrapolated fall time
for x=1:nb
energy1c(x) = sum(temp1(on+(find(abs(floor(volt(2,on+1:12)./step)) ==
x)))) + sum(temp3(find(abs(floor(volth./step)) == x)));
end;
% TOTAL
energy1=energy1a+energy1b+energy1c;
%-----------------SAVING DATA-----------------------------------------
A=[bins',(energy1a/1.6e-19*1e-4)'];
B=[bins',(energy1b/1.6e-19*1e-4)'];
C=[bins',(energy1c/1.6e-19*1e-4)'];
D=[bins',(energy1/1.6e-19*1e-4)'];
fid4=fopen(outfile, 'w');
fprintf(fid4, '# Output from Ivtospec.m, Energy spectrum of implant\n');
string=['# Current Input file was: ' iinfile ' \n'];
fprintf(fid4, string);
string=['# Voltage Input file was: ' vinfile ' \n'];
fprintf(fid4, string);
fprintf(fid4, '# SEY model used:seypf=%2.6f, seyex=%2.6f\n',seypf,seyex);
fprintf(fid4, '# \n');
fprintf(fid4, '# Energy spectrum of Rise time \n');
fprintf(fid4, '%g %g \n', A');
fprintf(fid4, '# \n');
fprintf(fid4, '# Energy spectrum of On time \n');
fprintf(fid4, '%g %g \n', B');
fprintf(fid4, '# \n');
fprintf(fid4, '# Energy spectrum of Fall time \n');
fprintf(fid4, '%g %g \n', A'); fprintf(fid4, '# \n');
fprintf(fid4, '# TOTAL Energy spectrum \n');
fprintf(fid4, '%g %g \n', A'); fclose(fid4);
'program "done'"
outfile
%------------------END PROGRAM-----------------------------------------
```

B.2.2 Generation of per-pulse profile from energy spectrum

Spectoprof.m takes the output from Ivtospec.m. Using the dose of ions implanted per energy given by that program, Spectoprof.m generates a per-pulse implant profile (concentration versus depth). Two files be set up which contain the projected range and straggle data for the atomic species whose implant is being monitored (i.e., B or F). These files are two-column, energy in eV and projected range or straggle in A.The program also

requires as input the ion species fraction of the implant (db, dbf, dbf2 and df). The SIMS per-pulse profiles in Chapter 4 were fit by varying these parameters. Output file is total concentration versus depth of monitored atom. The program below is set up to monitor B.

```
%--BEGIN PROGRAM-------------------------------------------------------
% SPECTOPROF.M : Takes as input an output file from Ivtospec.m, [bin dose],
% and fraction of ion flux due to each ion species (B+, BF+, BF2+ and F+).
% Program plots the depth profile assuming Gaussian profiles and using
% range and straggle data from TRIM 90.05. This program gives
% PROFILES FOR BORON implanted during BF3 PIII.
% Must set up files brp.dat and bdrp.dat, 2-column files containing
% [energy(in eV) | range_or_straggle(in A)].

% INPUT DATA IN THIS SECTION---------------------------------------
infile='outbins';
fid1 = fopen(infile,'r+');
[bins,countdat] = fscanf(fid1,'%g %g',[2 inf]);
fclose(fid1);
nb = length(bins);
ma = max(bins(1,:));
step = bins(1,1);
outfile='binspp'; % Output filename

% ion species fractions
% 11 B +; 30 BF +; 49 BF2+; 19 F +
db=.075; dbf=0; dbf2=0.85; df=0.075;

%-TOTAL DOSES EXPECTED-------------------------------------------------
expdose=sum(bins(2,:));              % dose from input file
bdose=(db+dbf+dbf2)*expdose;         % total boron dose

%-BORON PROFILE--------------------------------------------------------
% table of projected ranges for boron from TRIM 90.05, in Angstroms
fid2 = fopen('Brp.dat','r+');
[brp,countdat] = fscanf(fid2,'%g %g',[2 inf]);
fclose(fid2);
% table of straggle in projected range for boron TRIM 90.05, in Angstroms
fid3 = fopen('Bdrp.dat','r+');
[bdrp,countdat] = fscanf(fid3,'%g %g',[2 inf]);
fclose(fid3);
% energy of different ion species after impact
ebb=1;
ebbf=11/30;
ebbf2=11/49;

xmax=1000;              % maximum depth of constructed profile, in A
xstep=5;                % depth resolution in Angstroms
depth=[0:xstep:xmax];   % set depth matrix

profilebb=zeros(1,xmax/xstep+1);    % intitalize concentration matrix
profilebbf=zeros(1,xmax/xstep+1);   % intitalize concentration matrix
profilebbf2=zeros(1,xmax/xstep+1);  % intitalize concentration matrix
%----------------------------------------------------------------------
```

```
for i=1:nb
% B FROM B+
      xi=interp1(brp(1,:), brp(2,:), bins(1,i)*ebb);
                                    % proj. range = peak location
      dxi=interp1(bdrp(1,:), bdrp(2,:), bins(1,i)*ebb);
                                    % drp = gaussian width
      ai=bins(2,i)/(dxi*1e-8*sqrt(pi/2)*(1+erf(xi/dxi/sqrt(2))));
                                    % set peak concentration
      profilebb=profilebb+ai*db*exp(-(depth-xi).^2/(2*dxi^2));
                                    % Gaussian profile
% B FROM BF+
if bins(1,i)*ebbf > 10;
      xi=interp1(brp(1,:), brp(2,:), bins(1,i)*ebbf);
      dxi=interp1(bdrp(1,:), bdrp(2,:), bins(1,i)*ebbf);
      ai=bins(2,i)/(dxi*1e-8*sqrt(pi/2)*(1+erf(xi/dxi/sqrt(2))));
      profilebbf=profilebbf+ai*dbf*exp(-(depth-xi).^2/(2*dxi^2));
end;
% B from BF2+
if bins(1,i)*ebbf2 > 10;
      xi=interp1(brp(1,:), brp(2,:), bins(1,i)*ebbf2);
      dxi=interp1(bdrp(1,:), bdrp(2,:), bins(1,i)*ebbf2);
      ai=bins(2,i)/(dxi*1e-8*sqrt(pi/2)*(1+erf(xi/dxi/sqrt(2))));
      profilebbf2=profilebbf2+ai*dbf2*exp(-(depth-xi).^2/(2*dxi^2));
end;
end;
profileb=profilebb+profilebbf+profilebbf2;

bdose
calc_b_dose=trapz(depth,profileb)*1e-8
           % dose in profile (check that they're equal)
%-SAVING DATA--------------------------------------------------------

fid4=fopen(outfile, 'w');
fprintf(fid4, '# Output from SPECBOTH.M, F and B IV-constructed per-pulse
profiles\n');
string=['# Input file was: ' infile '\n'];
fprintf(fid4, string);
fprintf(fid4, '# Boron flux fraction %2.3f\n',db);
fprintf(fid4, '# BF flux fraction %2.3f\n',dbf);
fprintf(fid4, '# BF2 flux fraction %2.3f\n',dbf2);
fprintf(fid4, '# F flux fraction %2.3f\n',df);
fprintf(fid4, '#\n');
fprintf(fid4, '# Calculated B dose=%.3e, Expected B dose=%.3e\n', bdose,
calc_b_dose);
fprintf(fid4, '# Boron implant profile\n');
fprintf(fid4, '# Depth(Angstrom)  Concentration(cm-3)\n');
B=[depth', profileb'];
count=fprintf(fid4, '%g %g \n', B');
fclose(fid4);
'program done'
outfile
%-END PROGRAM--------------------------------------------------------
```

B.3 Per-pulse profile extraction from SIMS data

As described in Chapter 3 and 4, simultaneous implantation and etching during plasma immersion ion implantation cause the final concentration profile to be a convolution of a per-pulse implant profile with a function that takes into account the pulse rate and surface erosion rate. Secondary ion mass spectrometry of the B profile gives the final concentration profile. The program Rev.m takes that concentration profile and performs the deconvolution. Input data that are needed are the etching rate (in A/sec), the pulse frequency (in Hz), the implant length (in s). If input data has depth resolution of 1 Angstrom (one point per Angstrom), then program will determine an optimal depth removal increment (x_{inc}) to make the etch rate in the program as close as possible to the real etch rate. Since it is assumed in the program that all pulses implanted in the time (t_{inc}) it takes to remove x_{inc} Angstroms of material are implanted at the same depth, the etch rate will be rounded so that the t_{inc} is an integer. A warning is given if x_{inc} of the input data is not optimal.

The deconvolution is described by the equation C=Ag, where C is the final concentration vector read in from SIMS data, and g is the per-pulse concentration vector. A contains the information on the deconvolution. The vector equation will resemble the following:

$$\begin{bmatrix} c(x_1) \\ c(x_2) \\ c(x_3) \\ c(x_4) \\ c(x_5) \\ c(x_6) \\ c(x_7) \\ c(x_8) \\ c(x_9) \end{bmatrix} = \begin{bmatrix} 1 & 0 & 0 & 0 & 0 \\ 1 & 1 & 0 & 0 & 0 \\ 1 & 1 & 1 & 0 & 0 \\ 1 & 1 & 1 & 1 & 0 \\ 1 & 1 & 1 & 1 & 1 \\ 0 & 1 & 1 & 1 & 1 \\ 0 & 0 & 1 & 1 & 1 \\ 0 & 0 & 0 & 1 & 1 \\ 0 & 0 & 0 & 0 & 1 \end{bmatrix} \begin{bmatrix} g(x_1) \\ g(x_2) \\ g(x_3) \\ g(x_4) \\ g(x_5) \end{bmatrix} = Ag \qquad \text{(B-1)}$$

where the values in A will vary with etch rate, frequency and implant time. Even using sparse matrices for the calculation, the size of the matrices becomes large for etch rates larger than 8 nm/min and long implant times. In these cases, a lower x_{inc} should be used.

After the matrix A is constructed, the deconvolution is a single, inverse matrix multiplication step. This same program can be used to make a per-pulse profile into a final implant profile by inputting the per-pulse profile, setting all the implant parameters, and simply substituting a forward matrix multiplication step.

```
%--BEGIN PROGRAM-------------------------------------------------------
% PIII implantation during etching, given:
% ** final profile in matrix C[] (one point per r angstrom depth)
% ** etch rate v in Angstroms per second (may be fractional)
% ** implant pulse frequency in Hz
% ** length of implant in seconds
% GIVES PER PULSE PROFILE

%--DATA INPUT IN THIS SECTION-----------------------------------------
% Setting up matrix for final implant profile
% Cs0(x) is as-implanted profile from SIMS, csl0 is number of points
% Expects 2-column file X values and Concentration
% X-values must be evenly spaced.
% If X spacing=1 Angstrom, program can set optimal resolution

filename='bf3_55/5kv5khz.txt';
optfilename=[filename 'opt'];
fid=fopen(optfilename);
 if fid==-1;
      fid=fopen(filename);
 end
Cs0=fscanf(fid, '%g %g', [2 inf]);
fclose(fid);
Cs0=Cs0';
csl0=length(Cs0);

% IMPORTANT INPUT DATA
v=77.5/60; % Exact etch rate in Angstrom/sec
t=600; % Length of implant in seconds
f=5000; % Implant pulse frequency
%-----------------------------------------------------------------------
% find optimal resolution for profile, r
% resolution is lowered to r for best fit to etch rate
% real etch rate is v*60 Angstrom/sec
% etch rate used is r*60/round(r/v) Angstrom/sec

real_etch_rate=v*60
rm=[1:1:5];              % maximum depth step 5 Angstrom
choices=(rm*60./round(rm/v));
rm2=abs(choices-60*v);
r=min(find(rm2-min(rm2)==0));
optimal_r=r
optimal_etch_rate=r*60/round(r/v)

% check that data in proper form, either one point per Angstrom
% (in which case resolution will be reduced to optimal r)
% or that resolution is properly set to optimal r
```

```
% if not, warning will be displayed and calculation continues
rdat=Cs0(2,1)-Cs0(1,1);
if rdat==1
      csl=ceil(csl0/r);
      Cs=zeros(csl, 2);

      for i=1:csl
       Cs(i,1)=Cs0((i-1)*r+1,1);
       Cs(i,2)=Cs0((i-1)*r+1,2);
      end

      fid=fopen(optfilename,'w');
      count=fprintf(fid, '%g %g \n', Cs');
      fclose(fid);
      'made new file with optimal depth spacing, suffix "opt"'
      Cs=Cs(:,2);
else
      if ~(r==rdat)
       current_etch_rate=(rdat*60/round(rdat/v))
       current_r=rdat
       q=input('WARNING: depth step is not optimal. Continue? (y/n)
','s');
       if q=='n'
       error('Program terminated due to incorrect r & etch rate values')
       else
       r=rdat;
       Cs=Cs0(:,2);
       end
      else
       'data already properly scaled'
       Cs=Cs0(:,2);
       csl=csl0;
      end
end

% Time step: 1 second. Resolution lowered to r Angstroms.
% If etch rate lower than r Angstrom per second, so
% many seconds go by without r Angstrom removal, then
% dt is time that passes before new layer considered.
if v/r<1
      dt=round(r/v); vi=1;
else
      dt=1; vi=v/r;
end

% dimensions of conversion matrix
cl=csl;
gl=csl;

% Time indecies (n and m). Need two to deal with etch rates
% which are fractions of an Angstrom per second (1/v not integer).
n=floor(t/dt);
m=ceil(t/dt);
```

```
% Implant description
a=sparse(cl,gl);

if dt>t
      b=f*t*ones(gl,1);
      a=spdiags(b,[0],cl,gl);
else
      if m==n
            b=f*dt*ones(gl,n);
            bl=[1-n:0];
            bl=-vi*bl;
            a=spdiags(b,bl,cl,gl);
      else
            b=f*dt*ones(gl,n);
            c=f*rem(t,dt)*ones(gl,1);
            b=[b,c];
            bl=[-n:0];
            bl=-vi*bl;
            a=spdiags(b,bl,cl,gl);
      end
end
clear b bl Cs0;

% REVERSING CALCULATION
Cs=sparse(Cs);
Gs=zeros(gl,2);
Gs(:,2)=a\Cs;      % change this line to perform forward calculation,
                   % to find final profile from per-pulse profile

% depth matrix (X)
Gs(:,1)=r*[0:gl-1]';

% extinguish negative values
for i=1:length(Gs);
 if Gs(i,2)<0;
      Gs(i,2)=10;
 end
 if Gs(i,2)==0;
      Gs(i,2)=10;
 end
end

% Saving data in two columns, x values and G values
ppfilename=[filename 'pp'];
fid=fopen(ppfilename,'w');
count=fprintf(fid, '%g %g \n', Gs');
fclose(fid);
'made output file with per-pulse profile, suffix pp'
'done'
%--END PROGRAM-----------------------------------------------------------
```

C Appendix: Shallow junction and thin film characterization techniques

C.1 Introduction

This appendix contains introduction, background, and calculations for a number of the characterization techniques that have been used in this work. Secondary ion mass spectrometry (SIMS, section C.2) is used to determine the depth of implanted dopant profiles and to estimate dopant diffusion during annealing cycles. This section contains the penetration depth calculations for the SIMS analysis used. X-ray diffraction (XRD, section C.3), and Rutherford backscattering (RBS, section C.4) are used to measure film thicknesses, determine structural information about metal and silicide films, and to look at implantation-induced structural damage. These sections contain the table of XRD peaks used to identify $CoSi_2$ and the kinematic factors and stopping powers used for RBS of $CoSi_2$.

C.2 SIMS

Secondary ion mass spectrometry is used to find the concentration versus depth profiles of impurity atoms in silicon and cobalt silicide materials. The technique uses a low energy (1-10 keV) ion beam to slowly sputter away the material being analyzed (Figure C-1). The ion beam sputtering creates a secondary particle plume consisting of neutrals and positive and negative ions. The particles in the plume are mostly generated within the penetration depth of the primary ion. A mass spectrometer is used to collect either positive or negative ions. Electronic gating is used so ions are only collected from the center of the crater, to avoid edge effects. The SIMS work in this paper was performed in Cameca IMS-3f, IMS-4f and IMS-4.5f high mass resolution magnetic sector ion microanalyzers at sites at Intel, SEMATECH and Charles Evans.

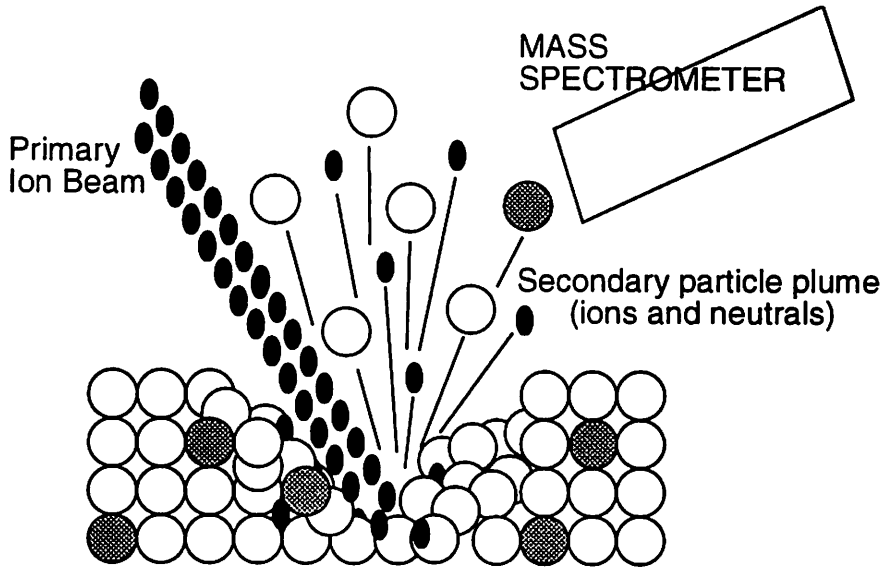

Figure C-1. Secondary Ion Mass Spectrometry

Successful profiling of shallow dopant profiles by SIMS requires attention to the experimental conditions. Care is taken in choosing the primary ion species, energy, sputter rate, and ambient. Most important is the primary ion species. Reactive ion beams, namely O_2^+ and Cs^+, are used to enhance the fraction of sputtered atoms which are positively and negatively ionized, respectively. Using these beams rather than an inert beam like Xe^+ or Ar^+ will increase the secondary ion yield by orders of magnitude. For boron in Si, the secondary ion measured is either $^{11}B^+$ or $^{10}B^+$, so the ion used is O_2^+. It has been found that the ionized secondary B concentration is further enhanced when the surface matrix is SiO_2, after the O_2^+ has impinged on the surface long enough to convert it to oxide. At the beginning of a SIMS measurement on a B-doped Si sample, when the matrix at the surface is changing from Si to SiO_2, the B secondary yield will vary by orders of magnitude. This surface transient time is lowered by using a lower energy primary ion beam. Using a lower energy beam, the ion penetration depth is lowered, and the amount of Si that must be converted to SiO_2 before reaching steady-state is reduced. In magnetic sector instruments like the CAMECA IMS series, lowering the ion beam energy is tied to raising the incidence angle of the beam. As the sputter rate increases with angle faster than it decreases with energy, this can lead to a reduction in the steady state O concentration in the matrix, and lower the secondary ion signal of B [C.1]. One of the methods developed to compensate is the use of an oxygen bleed, backfilling the SIMS vacuum chamber with a low flow rate of oxygen. This oxygen helps establish the stoichiometry of the SiO_2 surface layer quickly, so

the B yield is well defined and the surface transient is minimized [C.1, C.2]. This helps maintain the stoichiometry regardless of the sputtering rate, and helps keep the bottom of the sputtered trench smooth. In addition, since the oxide formed is thicker than the Si consumed, the sputtering rate of the original material is effectively reduced. The problem of the technique is that oxide grown on walls in the system can attract B, leading to system memory, higher background B concentrations, and an erroneously longer decay length of the measured B tail.

Conversion of the secondary ions per second recorded by the mass spectrometer to a concentration versus depth profile requires two steps: conversion of the sputter rate to a depth scale, and conversion of the ion counts to concentration. The depth scale is set by measuring the depth of the eroded crater afterwards, assuming a constant etch rate during the measurement, and directly converting the time scale to a depth scale. For measurement of a Si sample, the etch rate is only in doubt during the surface transient, when the stoichiometry is changing. This small error is minimized by using lower energy ions and oxygen bleed to reduce the transient. For multi-layer systems, like $CoSi_2$ on Si layers, the depth scale is harder to set. There may be different etch rates in the two materials, and interface roughness may cause both materials to be exposed and etched at once [C.3, C.4]. To calibrate the depth in this case, both etch rates must be measured and the depth scales calculated on both sides of a carefully chosen interface location. Although it has been reported previously that Si and $CoSi_2$ sputter rates are close [C.5], for this work, the sputter rates of 0.24 nm/sec for $CoSi_2$ and 0.28 nm/sec for Si were measured for a 7.5 keV primary O_2^+ beam at 52° off normal. These values were used to set the depth scales.

The concentration is set by relative sensitivity factors (RSF) determined by measurement of calibration standards [C.5, C.6]. Once RSF values are determined, the concentration is calculated from the intensity of the secondary ion signals from the matrix (I_m) and the impurity (I_i):

$$C_i = RSF\frac{I_i}{I_m} = \left(C_m\frac{\alpha_m}{\alpha_i}\right)\frac{I_i}{I_m} \quad . \tag{C-1}$$

where C_m is the concentration of the matrix ion being measured in the matrix, and α are the ion yields. C_m, α_m and α_i are all matrix-dependent quantities. The RSF is usually calculated from measurement of a doping standard from

$$RSF = \frac{\Phi c I_m t}{z\,(\Sigma I_i - I_b c)} \qquad \text{(C-2)}$$

where Σ is the total dose of the dopant, c is the number of data cycles measured, t is the analysis time per cycle, z is the total sputter depth, and I_b is the background counts measured per cycle. The RSF calculated this way will contain errors due to roughness of the crater impeding correct interpretation of z, measurement of I_m, I_b and I_i, and local geometry near or on the sample that can alter ion paths. RSF values reported for the same implant standards in industry can vary more than 50%. The concentrations reported are no better than these RSF values. For $CoSi_2$, since no standard existed, the RSF values used in those samples had to be calculated. As described in Ref. [C.5], the RSF for B in Si and $CoSi_2$ is almost the same because the C_m values for Si in Si and $CoSi_2$ are close, and the ratio α_{Si}/α_B is almost the same in the two materials. Using the same RSF for B in Si and $CoSi_2$ is estimated to cause an error of only 15%. This is especially fortuitous in the transition and interface region between Si and $CoSi_2$, where the composition exposed may be part Si and part $CoSi_2$. For this work, the RSF factor for B in $CoSi_2$ was determined separately, by calibrating the RSF so the SIMS dose matched the reported implant dose.

The last factor that has to be examined is the errors introduced in the SIMS profiles due to interface roughness. Since dopant outdiffused from silicide is expected to be conformal with the interface, interface roughness will cause spreading of the SIMS profiles. Elst reported decay lengths of the Co^+ signal from mono-crystalline and polycrystalline $CoSi_2$, finding that for the lowest O_2^+ impact energy (2 keV), the Co signal decays in about 5 nm. The decay was longer than 15 nm for polycrystalline $CoSi_2$. That work showed the correlation of the decay depths to the penetration depth of the primary ion. Ref. [C.1] gives the penetration depth as $R\cos\theta$, where R in nm is $2.15 * E$ for O_2^+ and $1.838 * E^{0.68}$ for Cs^+ in Si, if E is in keV. As the simulator TRIM [C.7] shows that the nuclear stopping energy of O in $CoSi_2$ is higher than in Si or SiO_2, the values of penetration depth calculated below for $CoSi_2$ are upper bounds. The primary ion penetration depths used in this work are listed in Table C-1. The depth error due to the signal decay will be related to this parameter. Error due to interface roughness is additional. Therefore, in interpreting the SIMS data of the $CoSi_2$ samples, interface roughness must be taken into account.

Vendor	Ion	Matrix	Final Impact Energy (keV)	Angle off normal	Penetration depth (nm)	Reported accuracy of RSF/dose
Charles Evans, 10/1995 (IMS-4.5f)	Cs^+	Si	5.5	24	5.4	x2
Charles Evans, 2/1994 (IMS-4f)	O_2^+	$CoSi_2$, Si	3	52	4.0	x2
SEMATECH, 11/1995 (IMS-4f)	O_2^+	Si	2	64	1.9	50%
Charles Evans, 9/1993 (IMS-3f)	O_2^+	Si	5.5	42	8.8	x2

Table C-1. Penetration depths of primary ions in SIMS

C.3 XRD

X-ray diffraction is a fast, non-destructive technique for identifying the phase and orientation of materials present in a sample [C.8]. In this work, XRD data was one of the clues used to determine whether cobalt disilicide films were epitaxially oriented on Si substrates. X-ray diffraction is the result of incident X-ray radiation being scattered by the regular array of scattering centers formed by atoms in the stacked crystal planes in the target material. The spacing of these atoms and planes is close to the wavelength of the Cu-Kα_1 radiation used, 0.15405 nm. Diffraction occurs when beams scattered off adjacent crystal planes are in phase, as described in Figure C-2. The Bragg law describes the condition necessary for the beams to be in phase:

$$n\lambda = 2d\sin\theta \tag{C-3}$$

where n is the order of the diffraction, λ is the wavelength and the other parameters are defined in Figure C-2. For the cubic materials studied in the following work, the space (d) between adjacent planes is a simple function of the Miller indices of the plane (hkl):

$$d_{hkl} = \frac{a}{\sqrt{h^2 + k^2 + l^2}}. \tag{C-4}$$

An X-ray diffraction spectrum that can be used to identify the crystal structure present in a sample can be made by varying the wavelength in a Laue camera, or by tilting the sample to vary the angle θ in an X-ray diffractometer. In the latter technique, a 2θ scan, the incident and diffracted beam angles are varied to yield a plot of diffracted beam inten-

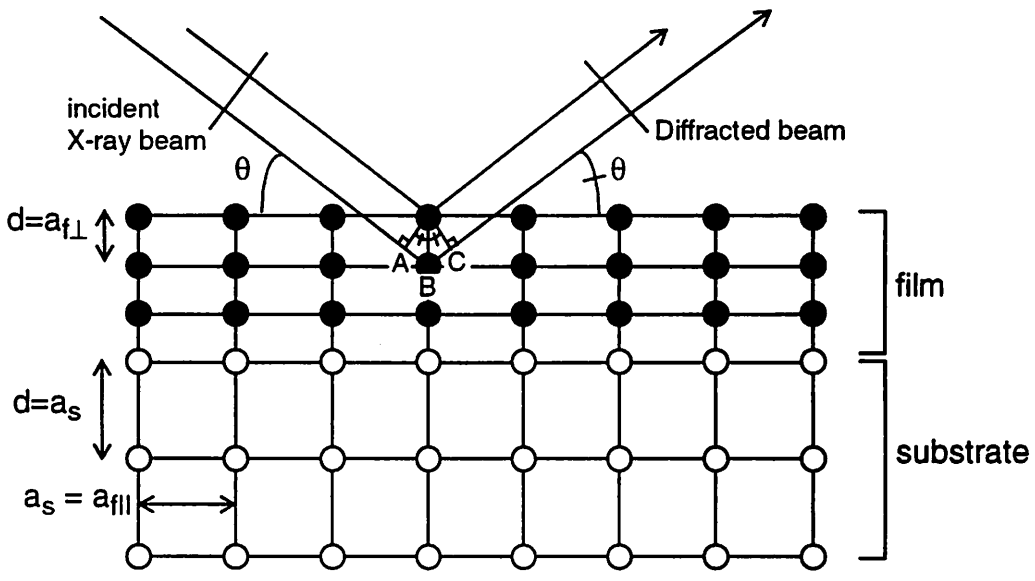

Figure C-2. Diffraction in strained thin film

Bragg law predicts constructive interference when line segment AB+BC=2dsinθ. Film grown epitaxially on Si will stretch or contract to match Si lattice parameter in lateral direction, leading to a change in the perpendicular plane spacing, $a_{f\perp}$.

sity versus diffraction angle, 2θ. Equation C-3 and Equation C-4 can then be used to translate the angle 2θ at which diffracted beams occur into the Miller indices of the planes that caused the diffraction. For Si and cobalt disilicide, which have structures based on the non-primitive face-centered cubic (fcc) crystal structure, certain planes that would show diffraction in a simple cubic structure are not expected to cause intensity peaks. In fcc structures, diffraction peaks are only expected for planes whose Miller indices are all even or all odd.

X-ray diffraction can provide information on a strained thin film grown on Si. As shown in Figure C-2, if a film grows epitaxially on Si, its lattice parameter in the plane of the interface ($a_{f||}$) must be equal to the lattice parameter of Si (a_s). The unit cell will then distort according to Poisson's ratio, forcing the lattice parameter in the perpendicular direction ($a_{f\perp}$) to either contract or expand. Since the x-ray penetration into a Si substrate is on the order of microns, intensity peaks can be seen for both the substrate, where plane spacing is based on a_s, and the thin film, where plane spacing is based on $a_{f\perp}$. The difference between measured values of $a_{f\perp}$ and the expected value of $a_{f\perp}$ in an unstrained film gives a measure of the strain in the film [C.9]. For an epitaxially grown $CoSi_2$ film on (100) Si, only planes of the {100} family are expected to be seen in the measurement. Films that

show a number of other planes are likely to be polycrystalline. Table C-2 lists peaks that fall in the measured diffraction angle range of 25-75°. This table is used in Chapter 7 to analyze XRD data.

ANGLE (°)	Spacing, d (A)	Plane (hkl)	Material	ANGLE (°)	Spacing, d (A)	Plane (hkl)	Material
28.441	3.1355	(111)	Si	47.920	1.8967	(220)	$CoSi_2$
28.492	3.13	(110)	CoSi	48.648	1.87	(002)	Co_2Si
28.812	3.096	(111)	$CoSi_2$	49.209	1.85	(311)	Co_2Si
32.531	2.75	(111)	Co_2Si	50.461	1.807	(211)	CoSi
33.393	2.681	(200)	$CoSi_2$	53.544	1.71	(320)	Co_2Si
34.880	2.57	(111)	CoSi	56.118	1.6375	(311)	Si
39.489	2.28	(211)	Co_2Si	56.890	1.6171	(311)	$CoSi_2$
40.475	2.21	(200)	CoSi	59.680	1.5480	(222)	$CoSi_2$
42.399	2.13	(310)	Co_2Si	64.674	1.44	(420)	Co_2Si
44.139	2.05	(021)	Co_2Si	66.437	1.406	(312)	Co_2Si
44.830	2.02	(220)	Co_2Si	68.363	1.371	(222)	Co_2Si
45.303	2.00	(301)	Co_2Si	67.127	1.3577	(400)	Si
45.884	1.976	(210)	CoSi	70.718	1.331	(311)	CoSi
46.032	1.97	(121)	Co_2Si	70.119	1.3409	(400)	$CoSi_2$
47.300	1.9201	(220)	Si				

Table C-2. Possible diffraction peaks in Co/Si system

Using the values of perpendicular and parallel lattice parameter calculated from the XRD peak locations, values of strain are calculated from:

$$\text{In-plane strain} = \quad \varepsilon_{//} = (a_{//} - a_f)/a_f \tag{C-5}$$

$$\text{Perpendicular strain} = \quad \varepsilon_{//} = (a_{f\perp} - a_f)/a_f \tag{C-6}$$

$$\text{Tetragonal strain} = \quad \varepsilon_{//} = |a_{f\perp} - a_{//}|/a_f \quad . \tag{C-7}$$

C.4 RBS and Channeling

Rutherford backscattering and channeling monitor the energy and intensity of the elastically backscattered portion of an incident ion beam to characterize an unknown

sample [C.10]. Typically a H or He ion beam with energy in the MeV range is used, as these ions have a de Broglie wavelength small enough that the ions will collide with target atoms, not be diffracted. RBS is a uniquely informative non-destructive technique, which can provide quantitative information on chemical composition, layer thicknesses, and depth profiles without specimen preparation or calibration standards. Its weaknesses are low resolution for masses lower than the substrate and for low concentrations of impurities, poor lateral resolution (~1 mm), and artifacts in the data when the surface or material interfaces are rough. Ion channeling is a related technique where the ion beam is aligned with a low index crystallographic direction, like the Si <100> direction. In a crystalline material the number of backscattered ions will fall sharply when the beam. High backscattering yield during channeling can indicate high concentrations of crystalline damage, interstitial dopants, or poly-crystallinity.

A schematic of the RBS geometry used in this work is shown in Figure C-2. A number of quantities must be calculated before analyzing RBS data. First is the kinematic

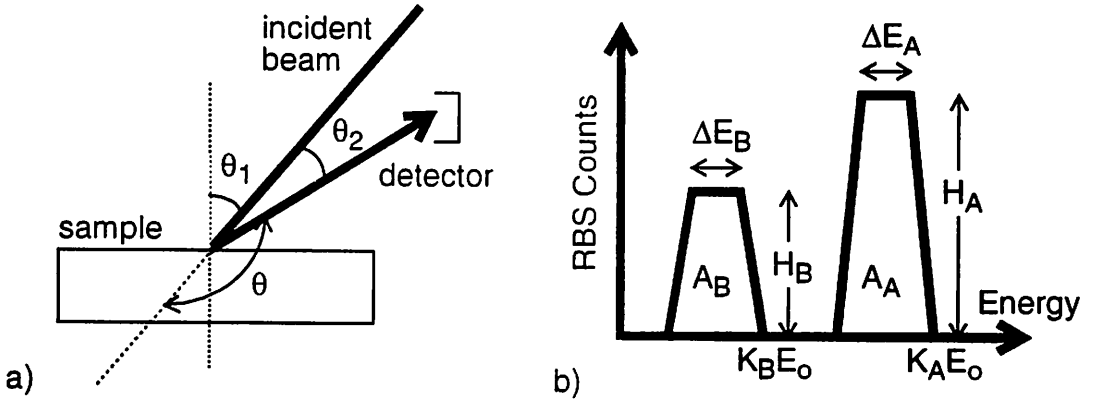

Figure C-3. Rutherford backscattering geometry

factor, the ratio of the measured energy of backscattered ions (KE_0) to the incident ion energy (E_0), calculated from the conservation of mass and momentum expressions:

$$K_{M_2} = \left[\frac{(1 - (M_2/M_1)^2 \sin^2\theta)^{1/2} + (M_2/M_1)\cos\theta}{1 + (M_2/M_1)} \right]^2 \qquad \text{(C-8)}$$

where M_1 is the incident ion mass, M_2 is target mass, and θ is the backscattering angle shown in the figure. The composition of a material can be found by calculating the differ-

ential scattering cross section of the ion-atom collision ($d\sigma/d\Omega$), which is proportional to the squares of the atomic numbers divided by the square of the ion energy, $(Z_1Z_2/E)^2$. The area of an RBS peak, A_A or A_B in Figure C-2, is then equal to $A = Q \cdot \frac{d\sigma}{d\Omega} \cdot d\Omega \cdot Nt$, where $d\Omega$ is the solid angle of the detector, Q, the total number of incident ions, and Nt the areal density of target atoms.The composition of a film A_mB_n can then be found within a few percent accuracy from the ratio of backscattered ions in a peak to incident ions:

$$\frac{m}{n} = \frac{(Nt)_A}{(Nt)_B} \equiv \left(\frac{A_A}{A_B}\right)\left(\frac{Z_B}{Z_A}\right)^2 \qquad \text{(C-9)}$$

Calculation of the film thickness requires calculation of the effective stopping energy of ions in the material, and knowledge of the expected atomic density of the material (N). The effective stopping energy is also a function of the incident energy, angles θ_1 and θ_2 from Figure C-2, and the kinematic factor of the collision:

$$[\varepsilon_o] = [S_o]N = \frac{K\varepsilon(E_{..})}{\cos\theta_1} + \frac{\varepsilon(KE_o)}{\cos\theta_2} \quad . \qquad \text{(C-10)}$$

If the layer being measured is a compound, Bragg's rule may be used to estimate the contributions of the different species to the total stopping energy: $\varepsilon^{AmBn} = m\varepsilon^A + n\varepsilon^B$. Once the effective stopping energy due to species A in layer AB is known, the layer thickness may be calculated from the width of the energy peak, ΔE_A or ΔE_B, from the figure:

$$\Delta E_A = [\varepsilon_o]_A^{AB} N t_{AB} \quad . \qquad \text{(C-11)}$$

Table C-3 and Table C-4 report calculated values for the effective stopping energy for Si and Co atoms in Si, Co and $CoSi_2$ materials for the conditions used in the experiments in this paper.

Target material	Kinematic factor	Atomic density (cm^{-3})
Si	0.5694	$5x10^{22}$
Co	0.7657	$8.97x10^{22}$
Ti	0.7197	$5.66x10^{22}$
$CoSi_2$		$7.7622x10^{22}$

Table C-3. Kinematic factor and atomic density for target materials studied by 1.8 MeV $^4He^+$ RBS. Backscattering angle θ=165°.

Target material	ε for Si in target ($x10^{-15}$ eVcm^2/atom)	ε for Co in target ($x10^{-15}$ eVcm^2/atom)	ε for Ti in target ($x10^{-15}$ eVcm^2/atom)
Co	570.58	584.36	584.36
Ti			629.1
$CoSi_2$	489.51	484.16	
$CoSi_{2.1}$	488.20	482.54	
$CoSi_{2.2}$	486.97	481.02	

Table C-4. Effective stopping energies for RBS performed with 1.8 MeV $^4He^+$ primary beam, with θ_1=65° and θ_2=80°.

C.5 References

[C.1] W. Vandervorst and F.R. Shepherd, "Secondary ion mass spectrometry profiling of shallow, implanted layers using quadrupole and magnetic sector instruments," J. Vac. Sci. Tech. A, A5 (3) pp. 313-320, 1987.

[C.2] J.W. Erickson and R. Brigham, "Improved sensitivity and depth resolution for analyses of shallow p-n junctions in silicon with secondary ion mass spectrometry," J. Vac. Sci. Tech. B, B14 (1) pp. 353-357, 1996.

[C.3] J.Y. Tsai, C. Canovai, C.M. Osburn, and Q.F. Wang, "Solid source diffusion from agglomerating silicide sources. I. Measurement and modeling," J. Vac. Sci. Tech. B, B12 (1) pp. 219-229, 1994.

[C.4] B. Mohadjeri and B.G. Svensson, "Secondary ion mass spectrometry measurements of shallow boron profiles in cobalt, silicon, and cobalt disilicide," J. Vac. Sci. Tech. B, B12 (1) pp. 209-213, 1994.

[C.5] K. Elst, W. Vandervorst, T. Clarysse, and W. Eichhammer, "Secondary ion mass spectrometry-spreading resistance profiling study on the outdiffusion from poly- and monocrystalline cobalt silicide," J.Vac.Sci.Tech.B, B10 (1) pp. 524-532, 1992.

[C.6] D.S. Simons and S.F. Corcoran, "Quantitative aspects of SIMS: Precision, Accuracy and Reproducibility," in Proc. of the Third Int. Workshop on Meas. Char. of Ultra-Shallow Doping Profiles in Semiconductors, (NC, 20-22 March1995), insert, 1995.

[C.7] J.F. Ziegler, J.P. Biersack, and U. Littmark, *The stopping and range of ions in solids*, New York : Pergamon, 1985.

[C.8] B.E. Warren, *X-ray diffraction*, Reading, Mass., Addison-Wesley Pub. Co., 1969.

[C.9] K.N. Tu, J.W. Mayer, and L.C. Feldman, *Electronic thin film science : for electrical engineers and materials scientists*, New York : Macmillan, 1992.

[C.10] J.W. Mayer and E. Rimini, *Ion beam handbook for material analysis*, NewYork: AcademicPress, 1977.